

Advancing the understanding of neurotoxicity
and mitigation strategies for α -dicarbonyl
precursors of advanced glycation end products
through new approach methodologies

Liang Zheng



Propositions

1. Proteomics-based identification of methylglyoxal-induced protein modifications provides insights into the cellular effects of endogenously formed versus externally added MGO.
(this thesis)
2. In risk assessment of methylglyoxal it is important to consider endogenously formed levels.
(this thesis)
3. When using AI as an assistant in scientific research one should not become an assistant to AI.
4. Risk assessment of the effects of nuclear wastewater discharge from Fukushima on marine and human health is needed.
5. Addressing stereotypes associated with different cultural groups is vital to increase mutual understanding among them.
6. Human emotions are universally similar in the face of war.

Propositions belonging to the thesis, entitled

Advancing the understanding of neurotoxicity and mitigation strategies for α -dicarbonyl precursors of advanced glycation end products through new approach methodologies

Liang Zheng

Wageningen, 19 November 2024

**Advancing the understanding of neurotoxicity
and mitigation strategies for α -dicarbonyl
precursors of advanced glycation end products
through new approach methodologies**

Liang Zheng

Thesis committee

Promotor

Prof. Dr IMCM (Ivonne) Rietjens
Professor of Toxicology
Wageningen University & Research

Co-Promotor

Dr E (Edoardo) Saccenti
Associate Professor, Systems and Synthetic Biology
Wageningen University & Research

Other members

Prof. Dr V (Vincenzo) Fogliano, Wageningen University & Research
Prof. Dr MAJS (Tiny) van Boekel, Wageningen University & Research
Prof. Dr TMCM (Theodorus) de Kok, Maastricht University
Dr A (Agnieszka) Blanchet – Smolinska, Maastricht University

This research was conducted under the auspices of the Graduate School VLAG (Biobased, Biomolecular, Chemical, Food and Nutrition Sciences)

**Advancing the understanding of neurotoxicity
and mitigation strategies for α -dicarbonyl
precursors of advanced glycation end products
through new approach methodologies**

Liang Zheng

Thesis

submitted in fulfilment of the requirements for the degree of doctor
at Wageningen University
by the authority of the Rector Magnificus,
Prof. Dr C. Kroeze,
in the presence of the
Thesis Committee appointed by the Academic Board
to be defended in public
on Tuesday 19 November 2024
at 3.30 p.m. in the Omnia Auditorium.

Liang Zheng

Advancing the understanding of neurotoxicity and mitigation strategies for α -dicarbonyl precursors of advanced glycation end products through new approach methodologies, 238 pages.

PhD thesis, Wageningen University, Wageningen, the Netherlands (2024)

With references, with summary in English

ISBN: 978-94-6510-255-9

DOI: <https://doi.org/10.18174/673793>

Table of contents

Chapter 1	General introduction	7
Chapter 2	The influence of intracellular glutathione levels on the induction of Nrf2-mediated gene expression by α -dicarbonyl precursors of advanced glycation end products	31
Chapter 3	Comparison of the methylglyoxal scavenging effects of kaempferol and glutathione and the consequences for the toxicity of methylglyoxal in SH-SY5Y cells	53
Chapter 4	Proteomics-based identification of biomarkers reflecting endogenous and exogenous exposure to the advanced glycation end product precursor methylglyoxal in SH-SY5Y human neuroblastoma cells	75
Chapter 5	An integrated proteomics and metabolomics analysis of methylglyoxal-induced neurotoxicity in a human neuroblastoma cell line	107
Chapter 6	Physiologically based kinetic modeling-facilitated reverse dosimetry to predict neurotoxicity and genotoxicity of methylglyoxal in humans from <i>in vitro</i> data	135
Chapter 7	General discussion	167
References		191
Summary		217
Acknowledgments		225
About the author		233
	Curriculum Vitae	235
	List of publications	236
	Overview of completed training activities	237

1



Chapter 1

General Introduction

1.1 Background

The past century has seen a substantial increase in life expectancy, leading to a rise in age-related diseases that have introduced new burdens on society¹. Among these, neurodegenerative diseases are particularly concerning not only due to the devastating consequences they have on the quality of life of patients and their families but also because of their complex pathophysiology, which remains inadequately addressed by current treatments^{2, 3}. Neurodegenerative diseases such as Alzheimer's disease (AD) and Parkinson's disease (PD) are characterized by hallmark features such as pathological protein aggregation, altered energy homeostasis, DNA and RNA defects, inflammation, and neuronal cell death, driven by a complex interplay of genetic, molecular, and environmental factors^{4, 5}.

Advanced glycation end products (AGEs), also known as "glycotoxins," have attracted increasing attention over the past years due to mounting evidence of their role in various pathophysiological processes and their association with diseases such as diabetes and many neurodegenerative disorders⁶⁻⁸. Exposure of humans to AGEs may originate from exogenous sources (food) but also from endogenous formation (formation inside the body)⁹. α -Dicarbonyl compounds, particularly methylglyoxal (MGO), glyoxal (GO), and 3-deoxyglucosone (3-DG), are the representative and most studied highly reactive precursors for AGE formation^{10, 11}. These compounds are present in various foods and can also form endogenously as metabolic byproducts^{10, 11}.

α -Dicarbonyl compounds are interesting and relevant to investigate in the context of neurotoxicity and neurodegenerative diseases for several reasons. Firstly, they readily modify free amino acids and biomacromolecules such as DNA and proteins within the body, forming AGEs^{10, 12}. This process can lead to structural and functional changes in these molecules, resulting in cell and tissue dysfunction, which may contribute to neurotoxicity^{10, 12}. Secondly, dicarbonyl-derived AGEs can bind to the receptor for AGEs (RAGE), triggering oxidative stress and inflammation, which may further promote the development of neurodegeneration¹³. However, despite their critical implications, the specific hotspot modification targets within neuronal cells, as well as the physiological impacts of these modifications, remain poorly understood. Exploring these aspects is essential, as it is expected to not only lead to the identification of potential biomarkers and therapeutic targets but also enhance our understanding of the specific mode of action by which α -dicarbonyl compounds contribute to neurotoxicity and their role in the progression of neurodegenerative diseases, offering new insights into diagnostic and treatment strategies for related conditions¹⁴. Lastly, AGEs and their precursors can also be ingested through the diet, potentially increasing exposure to these harmful compounds and elevating the risk of developing related health conditions¹⁵.

Understanding how to effectively control the amount of these compounds in food products could potentially block AGE formation and reduce human exposure to these precursors and the resulting AGEs¹⁶. However, the extent to which the neurotoxicity of these compounds can be attributed to exogenous versus endogenous sources remains to be established.

The studies presented in this thesis aimed to advance the understanding of neurotoxicity and mitigation strategies for α -dicarbonyl precursors of AGEs. Specifically, this research compared the reactivity of three common dicarbonyl precursors—MGO, GO, and 3-DG—in *vitro* (**Chapter 2**), further focused mainly on MGO to investigate its mitigation both endogenously and in food (**Chapter 3**), and explored and evaluated its neurotoxicity in *in vitro* neuronal cells using new approach methodologies (NAMs), including cell-based proteomics and metabolomics and physiologically based kinetic (PBK) modeling-based reverse dosimetry to obtain further insight into modes of action and dose-response curves for the potential adverse effects (**Chapters 4-6**). A detailed overview of each chapter will be provided in **Section 1.8**.

The current chapter will further introduce the key components of the thesis, including the introduction to α -dicarbonyl compounds and AGEs and their formation in **Sections 1.2 and 1.3**; the scavenging of exogenous dietary dicarbonyl compounds especially by flavonoids in **Section 1.4**; endogenous pathways for the metabolism of α -dicarbonyl compounds in **Section 1.5**; dicarbonyl stress and its role in neurodegenerative diseases in **Section 1.6**; and the NAMs employed in this thesis in **Section 1.7**. Finally, **Section 1.8** will provide an overview of the entire thesis.

1.2 α -Dicarbonyl compounds and their formation

α -Dicarbonyl compounds (dicarbonyls) are a special class of low molecular weight electrophiles known for their role as precursors in the formation of AGEs, with MGO, GO, and 3-DG (structures can be found in **Figure 1.1A**) being the most reported^{17, 18}. Exposure to these compounds results from both dietary intake and endogenous metabolic processes.

1.2.1 Exogenous formation of α -dicarbonyl compounds

Dicarbonyls are predominantly formed during the thermal processing of food and can also accumulate during long-term storage, particularly in carbohydrate and protein-rich foods¹⁹. Their formation involves non-enzymatic reactions including the Maillard reaction, caramelization, and lipid peroxidation, as well as enzymatic reactions in microorganisms found in fermented foods^{18, 19}. The primary non-enzymatic pathway for their formation is the Maillard reaction (**Figure 1.1A**), which proceeds effectively at temperatures above 50 °C and is favored at a pH range of 4 to 7^{18, 20, 21}. The Maillard reaction initiates when a reducing sugar's

reactive carbonyl group (e.g., glucose) condenses with the amino group of an amino acid, peptide, or protein, forming a Schiff base²⁰. This Schiff base then rearranges into an Amadori product, which can undergo enolization to form 1,2-enaminol or 2,3-enaminol, subsequently leading to the generation of long-chain dicarbonyls such as 3-DG and 1-deoxyglucosone (1-DG)²⁰. These longer chains can then fragment into shorter-chain dicarbonyls like MGO and GO²⁰.

Caramelization also contributes to α -dicarbonyl formation during high-temperature processes (above 120 °C) like baking and roasting, particularly through the degradation of carbohydrates in the absence of amino-containing compounds (**Figure 1.1B**)²². This process involves tautomerism reactions that lead to the formation of 1,2-enediol or 2,3-enediol, part of the Lobry de Bruyn–Alberda van Ekenstein rearrangement, followed by dehydration or oxidation steps²². The oxidation process generates glucosone, while dehydration reactions produce compounds such as 1-DG and 3-DG²².

In addition to the above-mentioned non-enzymatic pathways as major sources, dicarbonyls can also arise from the oxidation of lipids, particularly in foods rich in polyunsaturated fatty acids (PUFAs)^{18, 23}. The formation of dicarbonyls through lipid peroxidation involves complex mechanisms. The basic process of lipid peroxidation is initiated by reactive oxygen species (ROS), leading to the formation of free radicals such as peroxy radicals²³. Once these radicals are formed, lipid peroxidation advances, producing a variety of secondary oxidation products, including aldehydes, ketones, and dicarbonyls^{18, 23}. Lastly, dicarbonyls can also be formed through enzymatic reactions by different microorganisms in fermented foods, which are responsible for the distinctive aromas and flavors of these products^{19, 24, 25}.

The impact of the formation of dicarbonyls in food is dual-faceted: dicarbonyls play important roles in the color, flavor, and aroma formation during the thermal processing of some baked and fried foods²⁶. However, they can also form potentially harmful substances like AGEs, posing health risks and affecting the nutritional value of food products^{27, 28}.

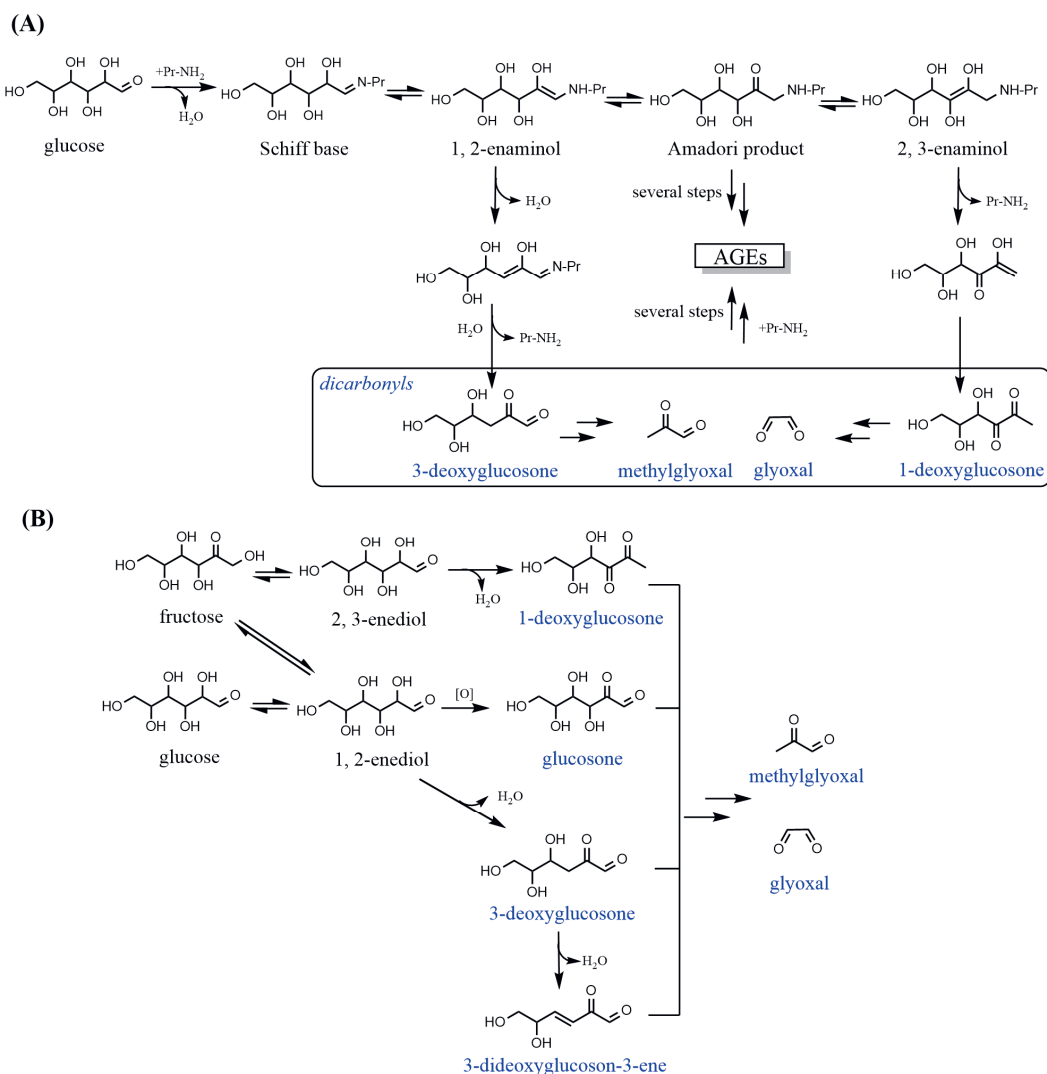


Figure 1.1. Simplified scheme for the exogenous formation of α -dicarbonyl compounds: (A) Maillard reaction via reaction of glucose and a protein amine (Pr-NH₂) as an example (adapted from Lund and Ray 2017)²⁰, and (B) degradation of monosaccharides (e.g., fructose and glucose) in caramelization (adapted from Helliwig et al. 2018)²². Names of dicarbonyl compounds are highlighted in blue. For further details see text. Structure formulas were created using ChemDraw 20.

1.2.2 Endogenous formation of α -dicarbonyl compounds

MGO, GO, and 3-DG are the primary α -dicarbonyl compounds produced endogenously, with typical intracellular concentrations ranging from 1–4 μM ¹⁰. MGO is the most reactive among these and has the highest endogenous flux, estimated at 3 mmol per day in a healthy adult^{29–31}. These compounds are formed as byproducts during various metabolic processes.

The endogenous formation of dicarbonyls, including MGO, GO, and 3-DG, involves mechanisms like those described in the Maillard reaction (**Figure 1.1A**), though occurring at lower rates due to the lower physiological temperatures¹⁵. These dicarbonyls can also arise through the endogenous degradation of monosaccharides via autooxidation and retro-aldol reactions³², processes less intense than those occurring in exogenous caramelization.

The primary source for endogenous MGO is the non-enzymatic degradation of triosephosphate intermediates in the glycolytic pathways (**Figure 1.2**)³³. In this pathway, aldolase catalyzes the reverse aldol conversion of fructose-1,6-bisphosphate into two triose phosphates: glyceraldehyde-3-phosphate (GA3P) and dihydroxyacetone phosphate (DHAP). An enediol intermediate, formed from GA3P and DHAP, frequently eludes enzymatic control and non-enzymatically loses a phosphate group, thereby generating MGO. Triosephosphate esters can also spontaneously decompose into MGO likely through similar mechanisms^{34, 35}. Inhibiting downstream enzymes in the glycolytic pathway may lead to an accumulation of these intermediates, thereby further increasing MGO production³⁶.

The polyol pathway, which is particularly active under hyperglycemic conditions, plays an important role in the formation of 3-DG^{37, 38}. In this pathway, glucose is converted to sorbitol by aldose reductase and then oxidized to fructose by sorbitol dehydrogenase. Subsequently, fructose is metabolized to fructose-3-phosphate, which can decompose to form 3-DG³⁷.

Additionally, ROS-induced lipid peroxidation of PUFAs in biological membranes also contributes to the endogenous formation of dicarbonyls, especially GO³⁹.

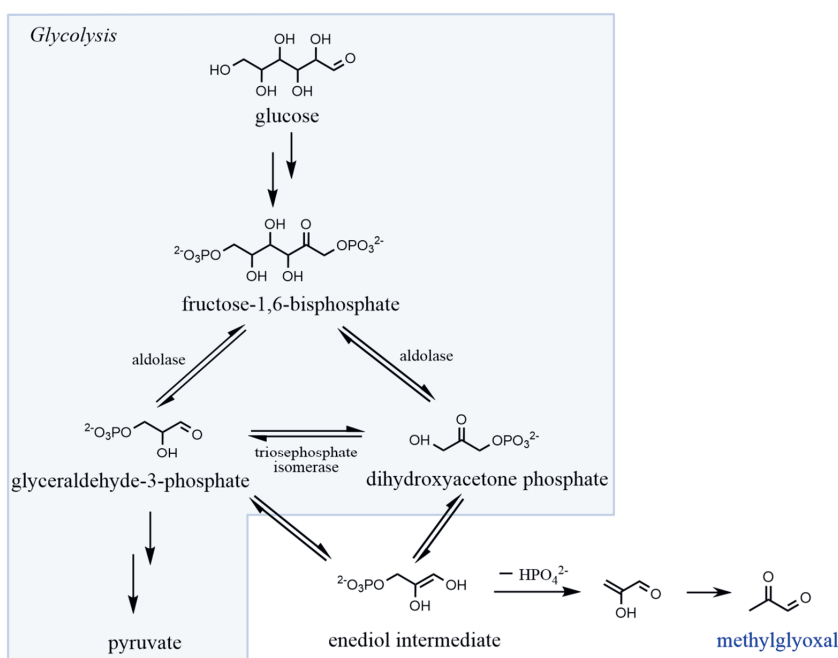


Figure 1.2. Non-enzymatic degradation of triosephosphate intermediates during glycolytic pathways to form methylglyoxal (adapted from Sibbersen and Johannsen 2020)³³. Structure formulas were created using ChemDraw 20.

1.3 The formation of advanced glycation end products

The primary pathways of AGE formation involve reactions between reducing sugars (e.g., glucose) or reactive carbonyl compounds, particularly dicarbonyls, and various nucleophiles such as free amino acids, proteins, and nucleic acids⁴⁰. AGEs are a heterogeneous group of compounds, distinguished by the involvement of different reactants and characterized by both cross-linked and non-crosslinked types⁴¹.

Amadori products, which form from reducing sugars and the primary amino groups of amino acid residues in non-enzymatic Maillard reactions (as described in **Section 1.2.1** and **Figure 1.1**), can undergo non-oxidative and oxidative cleavage reactions to transform into AGEs⁴². During food processing at high temperatures, Maillard reactions occur rapidly, whereas at body or room temperature, these reactions take place over a relatively long time, spanning weeks or months⁸.

The dicarbonyl-dependent pathway of AGE formation, which bypasses Amadori product formation, occurs directly through the reaction of dicarbonyls with nucleophiles such as amino acid residues especially lysine, arginine, and cysteine residues, as well as nucleic acids⁴⁰.

Dicarbonyls are intrinsically far more electrophilic compared to glucose, and it was reported that dicarbonyls are between 200–50,000 times more reactive than glucose in glycation reactions⁴³, making them the most reactive physiologically relevant glyating agents.

The reactions between dicarbonyls and nucleophiles yield a great variety of AGEs, including those bound to free amino acids, peptides, proteins, free nucleosides, DNA, and RNA^{44, 45}. In amino acids, peptides, and proteins, dicarbonyl-mediated modifications predominantly target lysine, arginine, and cysteine residues^{41, 46}. Dicarbonyls react with the amino groups of lysine or arginine residues non-enzymatically, generally forming reversible hemiaminals as the first step (**Figure 1.3A**)^{41, 47}. Further reactions with lysine residues can result in the formation of irreversible AGEs such as *N*^ε-carboxyethyl lysine (CEL) from MGO, *N*^ε-carboxymethyl lysine (CML) from GO or 3-DG, and pyrraline from 3-DG (**Figure 1.3B**)^{46, 48}. Further reactions with arginine residues lead to the formation of AGEs like hydroimidazolones (MG-H1, G-H1, and 3-DG-H1), *N*⁷-carboxyethyl arginine (CEA), and *N*⁷-carboxymethyl arginine (CMA) (**Figure 1.3B**)^{41, 49}.

Furthermore, the reactions between dicarbonyls and cysteine residues are considered reversible, forming hemithioacetals (**Figure 1.3A**), which may act as a “depot” of bound dicarbonyls *in vivo*^{41, 50}. *S*-carboxyethyl cysteine (CEC) and *S*-carboxymethyl cysteine (CMC) are considered AGEs resulting from the reactions of MGO and GO with cysteine residues *in vivo*, respectively (**Figure 1.3B**)⁵¹; however, limited studies have reported their formation. The formation of irreversible thiol-derived MGO adducts in cells through enzymatic mediation has also been proposed⁵².

Additionally, dicarbonyls can react with the amines of nucleic acids to form DNA/RNA-bound AGEs. Using free guanosine or 2'-deoxyguanosine as model compounds in incubations with dicarbonyls has identified several possible DNA adducts, such as *N*²-(1-carboxyethyl)-2'-deoxyguanosine (CEdG) from MGO, *N*²-(1-carboxymethyl)-guanosine (CMG) from GO, and *N*²-(1-oxo-2,4,5,6-hydroxyhexyl)-2'-deoxyguanosine from 3-DG (**Figure 1.3B**)⁴⁵.

When dicarbonyls react with multiple amino acid residues, this can lead to the formation of cross-linked AGEs, such as methylglyoxal-lysine dimer (MOLD), methylglyoxal-derived lysine-arginine crosslinks (MODIC), and methylimidazole crosslinks between proximal cysteine and arginine residues (MICA) from MGO (**Figure 1.3B**)^{48, 49, 53}.

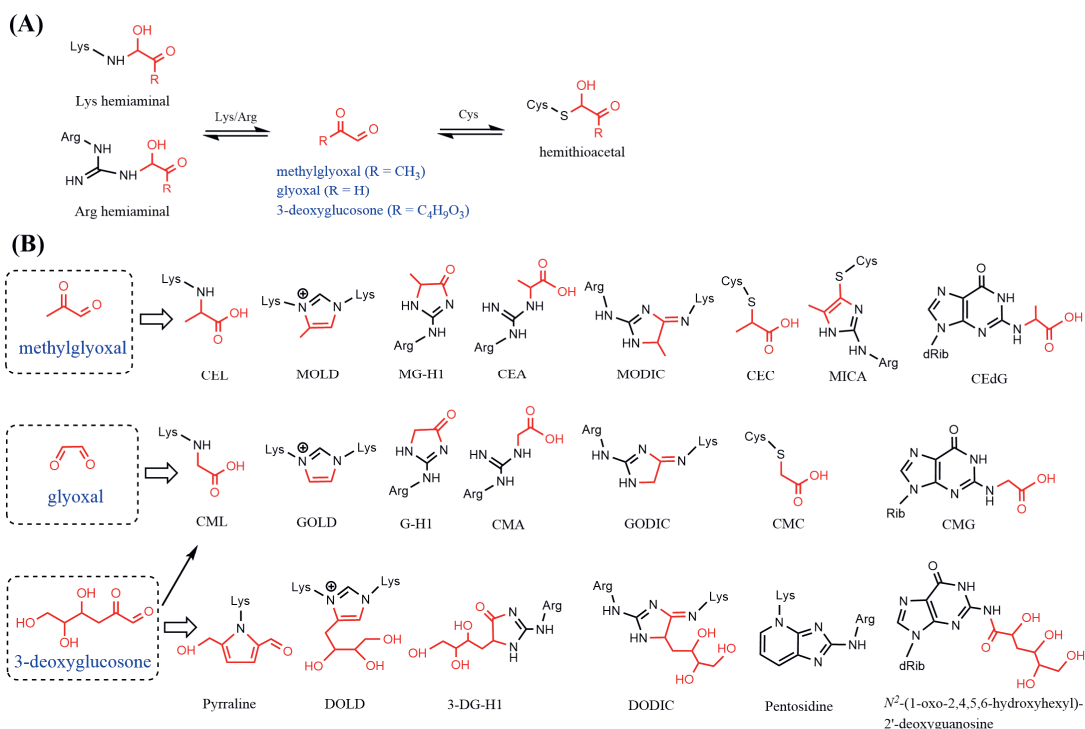


Figure 1.3. Structural formulas of reversible adducts (A) and typical AGEs (B) derived from methylglyoxal, glyoxal, and 3-deoxyglucosone. Lys: lys residue; Arg: arg residue; Cys: cys residue; dRib: 2-deoxyribose; Rib: ribose; CEL: N^ϵ -carboxyethyl lysine; CML: N^ϵ -carboxymethyl lysine; MOLD: methylglyoxal-lysine dimer; GOLD: glyoxal-lysine dimer; DOLD: 3-deoxyglucosone-lysine dimer; MG-H1: methylglyoxal-derived hydroimidazolone 1; G-H1: glyoxal-derived hydroimidazolone 1; 3-DG-H1: 3-deoxyglucosone-derived hydroimidazolone 1; CEA: N^γ -carboxyethyl arginine; CMA: N^γ -carboxymethyl arginine; MODIC: methylglyoxal-derived lysine-arginine crosslinks; GODIC: glyoxal-derived lysine-arginine crosslinks; DODIC: 3-deoxyglucosone-derived lysine-arginine crosslinks; CEC: S-carboxyethyl cysteine; CMC: S-carboxymethyl cysteine; MICA, methylimidazole crosslink between proximal cysteine and arginine residues; CedG: N^2 -(1-carboxyethyl)-2'-deoxyguanosine; CMG: N^2 -(1-carboxymethyl)-guanosine. Note that CML can be formed from both glyoxal and 3-deoxyglucosone. Structure formulas were created using ChemDraw 20.

1.4 Exogenous scavengers of α -dicarbonyl compounds inhibiting AGE formation

Dicarbonyl compounds are widely present in various foods and beverages such as biscuits, bread, fried potatoes, roasted meat, honey, coffee, and beer^{11, 54}. In some food products, like bread and roasted meats, the Maillard-derived aroma changes are often desirable²⁶. However, they generally negatively impact the sensory attributes of foods such as dairy products and may reduce the nutritional value of foods by inducing protein modifications to form AGEs^{16, 28}. Additionally, although a direct link between dietary dicarbonyls, resulting AGEs, and specific health outcomes has not been conclusively established, several studies suggest that high

intake of dietary AGEs may contribute to risk factors, especially inflammation and oxidative stress, which are associated with chronic diseases such as type 2 diabetes mellitus and chronic kidney disease^{28, 55, 56}. Given the possible impact of dicarbonyls on food quality and human health, controlling the amount of MGO in foods is crucial. One proposed strategy to mitigate these effects is the scavenging of dicarbonyls using various agents in foods^{16, 57}.

Plant polyphenols, particularly flavonoids, have shown significant efficacy as dicarbonyl scavengers^{58, 59}. The scavenging of MGO by different flavonoids has been extensively studied *in vitro*. Flavonoids like quercetin, genistein, naringenin, and epicatechin can trap MGO through electrophilic substitution reactions to form mono- and di-MGO adducts, primarily at the C6 and C8 positions of the A ring under physiological conditions^{27, 58, 60, 61}. **Figure 1.4** illustrates the major adducts formed between genistein and MGO in an *in vitro* cell-free system.

The use of flavonoids in food products, such as baked foods, for control of dicarbonyl and inhibition of AGE formation is considered a reasonable approach, provided their solubility and the impact on the background flavor and color of the foods do not compromise their utility^{16, 62}. Considering that the dicarbonyls can also react with the amino acid residues in the food matrix, it is of interest to study the possible competition between flavonoids and amino acid residues. For instance, a study simulated the competitive reaction between MGO and nucleophilic amino acid residues (N α -acetyl forms of lysine, arginine, and cysteine) and naringenin in milk²⁷. Results predicted that 84% of total MGO was trapped by naringenin after 24 hours of incubation at concentrations that do not compromise sensory qualities in milk, while almost all cysteine- and lysine-derived MGO adducts were depleted, and the arginine-derived adducts accounted for only 10% of the reaction²⁷. This study indicates that flavonoids might be a preferred target for MGO and could compete with amino acid residues, thereby preventing MGO from reacting with these residues to form AGEs.

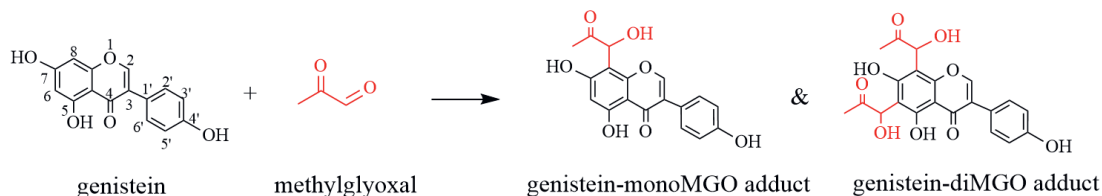


Figure 1.4. Formation of monoMGO and diMGO adduct between genistein and methylglyoxal in PBS (pH 7.4, 37 °C) (adapted from Lv et al. 2011)⁶¹. Structure formulas were created using ChemDraw 20.

1.5 Endogenous pathways for the metabolism of α -dicarbonyl compounds

In healthy individuals, concentrations of dicarbonyl compounds are kept low due to relatively low levels of endogenous formation and efficient detoxification by several pathways¹⁰. The glutathione (GSH)-dependent glyoxalase system, consisting of glyoxalase 1 (Glo1) and glyoxalase 2 (GLO2), is the primary pathway for the metabolism of MGO and GO⁶³. Glo1 is the rate-limiting enzyme in this pathway⁶⁴.

In the initial step of the detoxification process, MGO and GO react with the nucleophilic thiol group of GSH non-enzymatically or through a reaction catalyzed by glutathione-S-transferases (GSTs), forming a hemithioacetal^{63, 65}. The hemithioacetal is then converted by Glo1 and Glo2 into the corresponding α -hydroxy acids (**Figure 1.5A**)⁶³. Additionally, aldoketo reductases (AKRs) and aldehyde dehydrogenases (ALDHs) also contribute to the detoxification of these compounds, albeit to a lesser extent^{10, 66}. 3-DG is mainly metabolized to 3-deoxyfructose by AKRs, and to a lesser degree, to 2-keto-3-deoxygluconic acid by ALDH (**Figure 1.5B and C**)^{10, 66}.

It is important to note that the transcription factor Nrf2 plays a crucial role in regulating dicarbonyl metabolism⁶⁷. Nrf2 binds to the electrophile-responsive element (EPRE), which is responsible for inducing transcription of a range of antioxidant genes, including those for Glo1 and AKRs, as well as enhancing GSH synthesis and proteasome activity, thereby protecting cells from both electrophilic and oxidative stress^{36, 68}. Small electrophilic compounds are known to bind to Kelch-like ECH-associated protein 1 (Keap1), enabling the release of Nrf2 from Keap1 and its translocation into the nucleus⁶⁹. It has been reported that excessive cellular MGO modifies Keap1 to form a methylimidazole crosslink (MICA) between proximal cysteine and arginine residues, leading to Keap1 dimerization, subsequent release of Nrf2, and activation of the Nrf2 transcriptional program (**Figure 1.6**)⁵³. The activation of the Nrf2 pathway by MGO is considered a hormetic response, resulting in enhanced cellular detoxification of MGO³⁶. Additionally, pretreatment with Nrf2 activators such as carnosic acid and naringenin has been shown to protect against MGO-induced cytotoxicity by promoting GSH synthesis through the Nrf2 signaling pathway, critical for the detoxification mechanism of MGO^{70, 71}.

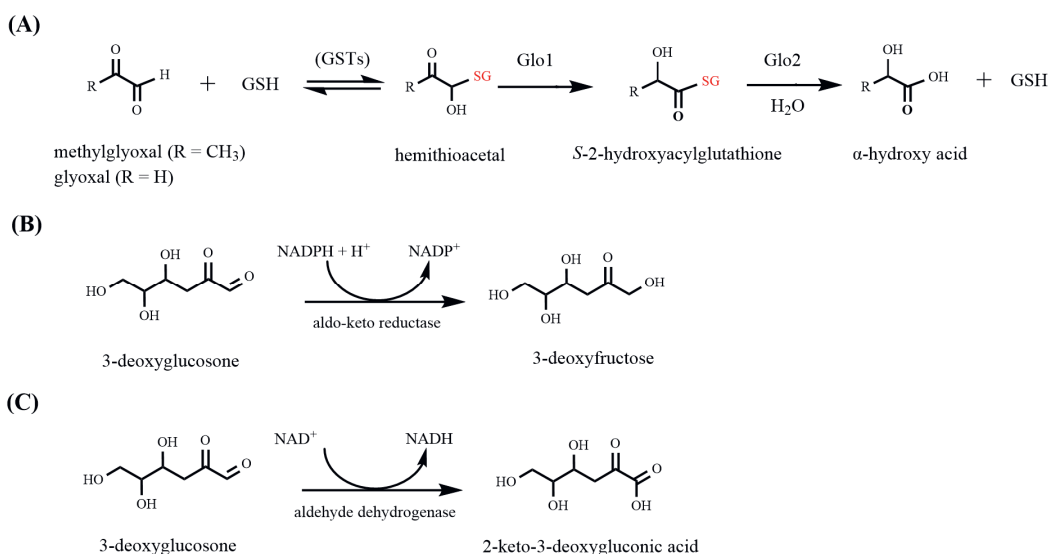


Figure 1.5. Intracellular metabolic pathways for α -dicarbonyl compounds. (A) Metabolism of methylglyoxal and glyoxal by the GSH-dependent glyoxalase system. (B) and (C) Metabolism of 3-deoxyglucosone by aldo-keto reductases and aldehyde dehydrogenases (adapted from Rabbani and Thornalley 2015)¹⁰. GSH: glutathione; GST: glutathione-S-transferases; Glo1: glyoxalase 1; Glo2: glyoxalase 2. Structure formulas were created using ChemDraw 20.

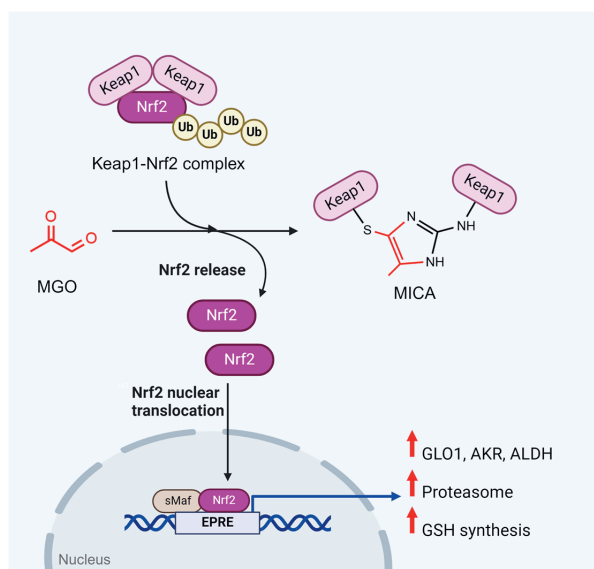


Figure 1.6. Activation of the Keap1-Nrf2-EPRE signaling pathway induced by methylglyoxal modification of Keap1 to form cross-linked AGE-Keap1 dimers (adapted from Kold-Christensen and Johannsen 2020)³⁶. AKR: aldo-keto reductase; ALDH: aldehyde dehydrogenase. Figure created with BioRender.com.

1.6 Dicarbonyl stress and neurodegenerative diseases

1.6.1 Dicarbonyl stress

Dicarbonyl stress is a dysfunctional metabolic state characterized by an increase in the steady-state levels of reactive dicarbonyls *in vivo*, leading to increased modifications of free amino acids and biomacromolecules, including proteins and DNA^{10, 72}. Dicarbonyl stress results from an imbalance between their production and metabolism, commonly occurring under pathological conditions such as hypoxia, inflammation, oxidative stress, and hyperglycemia^{10, 73, 74}. Under these conditions, there is typically an increase in glycolysis and/or impairments in the dicarbonyl detoxification system, such as decreased Glo1 expression and/or activity^{73, 75}. Dicarbonyl stress has been associated with many diseases, including diabetes and its complications, cardiovascular diseases, chronic kidney diseases, and neurodegenerative diseases^{74, 76-78}. The potential role of dicarbonyl stress in neurodegenerative diseases will be briefly discussed in **Section 1.6.2**.

Elevated endogenous dicarbonyl levels may also result from increased exposure to exogenous dicarbonyls. Although little is known about the contribution of exogenous dicarbonyls to the overall *in vivo* dicarbonyl exposome, some animal studies have shown increased plasma concentrations of MGO in mice after high oral MGO administration^{79, 80}. Additionally, upon a single oral consumption of honey containing a dietary amount of 3-DG by human volunteers, elevated amounts of 3-DG and its metabolite (3-deoxyfructose) were excreted in the urine, with 10-15% of the ingested 3-DG dose being recovered⁸¹. However, similar studies for MGO did not seem to increase the urinary excretion of MGO and its metabolite D-lactate⁸². This disparity suggests that MGO may have a lower bioavailability and/or be rapidly metabolized upon absorption due to its higher reactivity compared to 3-DG.

1.6.2 The role of dicarbonyl stress in neurodegenerative diseases

Neurodegenerative diseases such as AD and PD share many common pathological features, including the deposition of aggregated proteins, altered energy homeostasis, progressive loss of neurons, oxidative stress, and inflammation^{4, 83}. In AD, the hallmark pathological deposits are extracellular amyloid- β plaques and intracellular neurofibrillary tangles formed by tau protein⁸⁴. On the other hand, PD is characterized by the presence of Lewy bodies, which are cytoplasmic inclusions predominantly composed of α -synuclein⁸⁵.

Clinical research has revealed that higher serum MGO levels are associated with poorer memory, executive function, and lower grey matter volume in older individuals⁸⁶. Additionally, increased levels of protein-bound CML and protein-bound 3-DG-derived hydroimidazolones

have been found in the cerebrospinal fluid (CSF) proteins of AD patients, along with elevated levels of MGO- and GO-derived hydroimidazolone free adducts in the CSF ultrafiltrate⁸⁷. Similarly, increased levels of MGO-derived hydroimidazolones have been detected in the nigral neurons of PD patients. More importantly, increased levels of AGEs were detected in amyloid plaques and neurofibrillary tangles in AD patients^{88, 89}, and key proteins associated with neurodegeneration, such as tau and α -synuclein, were also found to be glycated in patients^{90, 91}. Glycation is believed to increase protein stability by forming crosslinks that stabilize pathological protein aggregates, thereby promoting their accumulation and persistence⁷. These clinical findings suggest that dicarbonyl stress may be a feature and play a role in the pathogenesis of neurodegenerative diseases.

Dicarbonyls, as mentioned above, readily react with free amino acids, proteins, and DNA. This interaction can cause damage to the metabolome, proteome, and genome, leading to cell and tissue dysfunction, which may ultimately play a role in neurodegeneration. The mechanisms by which dicarbonyl stress drives neurodegeneration are still largely unknown; however, activation of the RAGE signaling pathway has been proposed as an important mechanism⁹². Dicarbonyl-derived AGEs can bind to RAGE, leading to an increase in oxidative stress and inflammation through the production of ROS and the induction of NF- κ B, forming a positive feedback loop that augments oxidative and inflammatory damage in the brain¹³. The expression of RAGE is upregulated in the brain of AD patients⁹³, and early and persistent activation of MGO/AGE/RAGE/NOX-2 was previously observed in rats with streptozotocin-induced AD⁹⁴.

Moreover, *in vitro* studies using different neuronal cell models, such as the human SH-SY5Y neuroblastoma cell line and neuronal-like cells transdifferentiated from human mesenchymal stem cells, have revealed the cytotoxicity of dicarbonyl compounds^{76, 95-98}. Most of the research to date has focused on the most reactive dicarbonyl, MGO. Exposure of cells to MGO leads to increased ROS production, loss of mitochondrial membrane potential, and apoptosis⁹⁵⁻⁹⁸. These toxic effects may result from potential damage to the metabolome, proteome, and/or genome, which needs further clarification. For example, one proposed mechanism is that dicarbonyl glycation damage to the mitochondrial proteome may precede mitochondrial dysfunction, leading to oxidative stress⁴³, based on the observation that overexpression of Glo1 in *Caenorhabditis elegans* decreased dicarbonyl glycation of mitochondrial proteins and reduced ROS formation⁹⁹.

Given that dicarbonyls target amino acids and biomacromolecules, forming AGEs, which in turn may play a role in neurodegeneration, AGEs may be utilized as biomarkers of these

diseases, but there is a need to further identify the hotspot modification targets in neuronal cells.

1.7 New approach methodologies (NAMs) used in the thesis

NAMs encompass various non-animal-based testing approaches, including *in silico* and *in vitro* methods such as quantitative structure-activity relationship (QSAR) models, read-across, physiologically-based kinetic (PBK) models, quantitative *in vitro* to *in vivo* extrapolations (QIVIVE), high-throughput cell-based omics technologies, and advanced 3D human cell models, all designed to provide mechanism-based insights with improved ethics and human-relevant safety data¹⁰⁰. The use of NAMs in the risk assessment of chemicals and food has received growing attention, primarily because they align with the 3R principle (replacement, reduction, and refinement) of animal testing, enhancing the mechanistic understanding of chemical toxic effects on biological systems, and facilitating the extrapolation of results from *in vitro* studies to humans^{101, 102}.

The NAMs used in this thesis primarily include cell-based omics technologies and PBK modeling-facilitated reverse dosimetry. Cell-based omics technologies were employed to characterize protein modifications and neurotoxicity induced by MGO, using the human SH-SY5Y neuroblastoma cell line—a widely recognized model for investigating the pathological effects of neurotoxic compounds¹⁰³. Meanwhile, PBK modeling-facilitated reverse dosimetry was utilized for the risk assessment of MGO from daily dietary intake and endogenous formation. These approaches will be briefly introduced below.

1.7.1 A Proteomic strategy used for identifying MGO-induced protein modifications in cells

To understand better the role of modifications by dicarbonyl compounds and to define potential biomarkers for exposure and effects, efforts have been made to identify proteins and their specific sites susceptible to dicarbonyl modifications¹⁰⁴⁻¹⁰⁸. Given the relatively low abundance and the heterogeneity of these modifications, mass spectrometry-based proteomics is an effective, high-throughput method that provides a comprehensive assessment of a large number of proteins and their modifications. Previous studies have employed mass spectrometry-based proteomics to identify protein modifications caused by dicarbonyls in several cell types including WIL2-NS B lymphoblastoid cells, HMEC-1 microvascular epithelial cells, and HEK293T kidney cells^{104, 106, 107}.

In this thesis, a bottom-up proteomics approach was employed to characterize protein modifications induced by MGO exposure in SH-SY5Y neuroblastoma cells. After 24 hours of incubation with either no MGO or increasing concentrations of MGO, proteins were extracted

from the cells, digested into peptides using trypsin, then separated by nano-liquid chromatography (nano-LC), and identified and quantified through mass spectrometry analysis. Peptides modified by MGO were then mapped back to their source proteins for further data analysis.

The intensity data of MGO-modified peptides were analyzed using the Jonckheere-Terpstra test to identify potential biomarkers for endogenous and exogenous MGO exposure. This non-parametric method is particularly adept at identifying ordered differences among groups¹⁰⁹, making it suitable for assessing concentration-dependent increases in peptide modifications. This test is especially useful when expecting a trend across ordered treatment concentrations¹⁰⁹.

Proteins with peptides that exhibited a concentration-dependent increase in modification levels were considered potential exogenous biomarkers for MGO exposure. Conversely, proteins where peptides showed comparable or higher modification levels in the control compared to exogenous MGO-treated cells were defined as biomarkers of endogenous exposure.

Building on these findings, bioinformatics tools were employed to delve deeper into the biological implications of protein modifications induced by MGO. Enrichment analysis, a common approach in proteomics, often incorporates methodologies such as Gene Ontology (GO), KEGG pathway, and WikiPathways analyses to annotate proteins with specific biological functions, processes, and pathway involvements¹¹⁰.

Similarly, protein-protein interaction (PPI) network analysis, also widely used in proteomics, can help identify critical connections that can significantly influence cellular functions and stability¹¹¹. For the proteins modified by MGO in this study, KEGG pathway and PPI network analyses were applied to identify potential biological pathways and interaction networks these modifications could be involved in, helping to pinpoint the mechanisms through which these modifications could potentially affect cellular processes and contribute to the observed phenotypic outcomes.

1.7.2 An integrated proteomics and metabolomics approach for the analysis of MGO-induced neurotoxicity in cells

High-throughput omics strategies are now widely used in toxicology to explore the molecular mechanisms underlying the toxicological effects of chemicals¹¹². Serving as exploratory tools, these techniques provide insights into the modes of action and guide directions for future in-depth studies. Traditional toxicological methods often focus on limited endpoints and may not

fully capture the broader biological or toxicological impacts of substances like MGO, which is known to interact complexly with free cellular amino acids and biomacromolecules, causing widespread damage to the cellular metabolome, proteome, and genome⁷². In contrast, omics techniques such as transcriptomics, proteomics, and metabolomics offer a more comprehensive view, enabling the simultaneous analysis of thousands of molecules in a single biological sample, thereby uncovering intricate molecular interactions and systemic effects¹¹³.

In this thesis, the global protein expression in cells after exposure to MGO was assessed using the bottom-up proteomics approach described in **Section 1.7.1**. The unmodified peptides identified were mapped back to their source proteins, with subsequent data analysis including univariate and multivariate analysis methods to identify differential protein expression patterns and their biological significance.

In univariate analysis, each variable is analyzed independently to assess its individual effect on the outcome; techniques such as the *t*-test were employed to determine the statistical significance of differences observed in protein expression between treated and control groups. Meanwhile, multivariate analysis involves examining multiple variables simultaneously to understand the relationships and interactions among them; methods like principal component analysis (PCA) were utilized to identify patterns and trends that might not be apparent from univariate analysis alone.

Further analysis of the differentially expressed proteins, leveraging the enrichment methodologies and PPI network analysis already described in **Section 1.7.1**, was conducted to extend our understanding of the biological impact of MGO exposure. Specifically, advanced algorithms were applied within the PPI network framework to identify key functional modules and hub proteins, enhancing the insights gained from the initial analysis. An example of a key functional module identified in the PPI network from the present study revealed a connection to oxidative stress responses involving the Nrf2 pathway, with critical proteins such as NQO1, HMOX1, TXN, and GCLM being upregulated, emphasizing the role of MGO in the activation of Nrf2-mediated pathway (**Figure 1.7**).

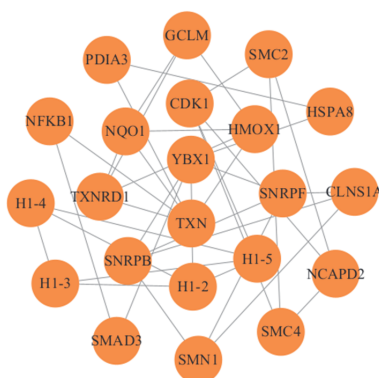


Figure 1.7. One of several key functional modules identified in the protein-protein interaction network in this study (Chapter 5), revealing a connection to oxidative stress responses via the Nrf2-mediated pathway upon MGO exposure.

A targeted LC/MS/MS-based metabolomics approach was applied to analyze metabolites extracted from cells after the same exposure steps as used for the proteomics study. This method facilitated the precise quantification and identification of MGO-induced changes in key metabolites such as amino acids, organic acids, nucleosides, and nucleotides, which are crucial components of central cellular pathways, including the glycolytic system, the tricarboxylic acid (TCA) cycle, and amino acid metabolism. Analysis methodologies like those used in proteomics, such as univariate and multivariate analysis, were employed to define the biological significance of differential metabolites.

Additionally, to understand better the interactions between proteins and metabolites, an integrated analysis of metabolomics and proteomics data was conducted. This analysis included correlation analysis using Spearman's index to assess the strength and direction of associations between differentially expressed proteins and differential metabolites. Joint pathway analysis was also employed to identify shared pathways affected by MGO exposure, thereby linking changes in metabolite levels and protein expressions to specific biological processes.

This integrated approach provides a holistic view of the phenotypic changes and the complex molecular interactions triggered by MGO exposure, facilitating a deeper understanding of the disrupted cellular pathways and their contributions to MGO's neurotoxic effects.

1.7.3 Use of PBK modelling-based reverse dosimetry in the risk assessment of MGO

Many *in vitro* studies have demonstrated that exposure to exogenous MGO can lead to cellular injury and toxicity in a variety of animal and human neuronal cell models^{95, 96, 114, 115}. However, these findings cannot be directly applied to human risk assessment. The concentration-

response data derived from these studies need to be converted into human-relevant dose-response data to establish safe exposure levels. This conversion is possible through quantitative *in vitro* to *in vivo* extrapolation (QIVIVE), utilizing PBK modeling-based reverse dosimetry¹¹⁶. These methods have proven effective in predicting *in vivo* toxicity for a range of compounds across multiple endpoints, thus contributing to the development of non-animal testing methods¹¹⁷⁻¹²⁰.

A PBK model comprises mathematical differential equations that describe the change in a compound or its metabolite over time in a body compartment of interest due to absorption, distribution, metabolism, and excretion (ADME) characteristics of the compound within the organism^{119, 121}. It utilizes three primary types of parameters: physiological and anatomical, physicochemical, and kinetic¹²¹. By modeling these ADME processes, the PBK model can predict the time course of the compound or its metabolites in blood or other tissues of interest at a given dose level, also called forward dosimetry^{116, 121}.

In reverse dosimetry, the PBK model is used inversely to determine the dose required to achieve specific concentrations of a chemical in blood or other tissues¹¹⁶. Here, *in vitro* concentrations of the chemical are set equal to blood levels in the PBK model, allowing *in vitro* toxicity data to be translated into *in vivo* equivalents^{116, 121}.

In this thesis, a human PBK model for MGO was developed, translating *in vitro* data on MGO-induced neurotoxicity and genotoxicity from the literature^{95, 122} into *in vivo* dose-response curves. These curves facilitate the establishment of a BMDL₁₀ (benchmark dose lower confidence limit causing 10% extra effect above background levels) for MGO, which is crucial for risk assessment¹²³. Reflecting MGO's known genotoxic potential for DNA adduction and its well-documented neurotoxic effects, we have adopted the margin of exposure (MOE) approach used for evaluating the risk of compounds that are genotoxic and carcinogenic by the European Food Safety Authority (EFSA)^{124, 125}.

This MOE approach does not make implicit assumptions of a “safe” intake but rather indicates whether there is a concern and a priority for risk management¹²⁵. For estimating MOEs for MGO resulting from exogenous and endogenous exposure, MOEs were calculated by dividing the BMDL₁₀ obtained from PBK model-predicted *in vivo* dose-response curves for neurotoxicity and genotoxicity, by the estimated daily intake or the estimated endogenous formation of MGO.

For neurotoxicity endpoints, which are thresholded, an MOE of 100 or above was considered safe. This margin accounts for uncertainties and variability within the human population (default uncertainty value of 10) and the incorporation of NAMs (assumed uncertainty value

of also 10). The default factor of 10 for interspecies differences was considered not necessary given that the BMDL₁₀ value for neurotoxicity was derived based on human data. For genotoxicity endpoints, an MOE of 10,000 or higher was deemed to be of no concern, accounting for interindividual variability (value of 10), the use of NAMs (value of 10), uncertainties related to the carcinogenic processes (value of 10), and use of the BMDL₁₀ value (value of 10). Also, here use of the default factor of 10 for interspecies differences was considered unnecessary.

1.8 Aim and outline of the thesis

The aim of this thesis was to advance the understanding of neurotoxicity and mitigation strategies for α -dicarbonyl precursors of AGEs. This research compared the reactivity of three representative dicarbonyl precursors—MGO, GO, and 3-DG—*in vitro*. It further focused mainly on MGO to investigate its mitigation both endogenously and in food, as well as explored and evaluated MGO's neurotoxicity in *in-vitro* neuronal cells using NAMs, including cell-based proteomics and metabolomics and PBK model-based reverse dosimetry to obtain further insight into modes of action and dose-response curves for the potential adverse effects.

In **Chapter 1**, background information, an introduction to the key components of the thesis, and the aims and outline of the thesis are presented.

In **Chapter 2**, the differences in the role of GSH in protection against the three representative dicarbonyls (MGO, GO, and 3-DG) and their induction of Nrf2-mediated gene expression were investigated. This included comparing the scavenging of these dicarbonyls by GSH in cell-free incubation experiments. Additionally, the capability of these compounds to induce Nrf2-mediated gene expression and the role of intracellular GSH in counteracting this effect were investigated through a cell-based reporter gene assay.

In **Chapter 3**, the MGO scavenging capacity of GSH and kaempferol were characterized in more detail with special emphasis on the possible reversible nature of the adduct formation and their competition for MGO in *in vitro* cell-free incubations. Moreover, the safety consequences of their MGO-scavenging effects in food were evaluated in human SH-SY5Y neuroblastoma cells.

In **Chapter 4**, MGO-induced protein modifications were qualitatively and quantitatively characterized in SH-SY5Y cells incubated with and without exogenous MGO, using a proteomics approach, to identify potential biomarkers for its exposure and toxicity.

In **Chapter 5**, an integrated proteomics and metabolomics approach was used to explore the molecular and biochemical changes induced by MGO exposure in SH-SY5Y cells and how these changes contribute to neurotoxicity.

In **Chapter 6**, a human PBK model was defined based on a newly developed and validated mouse PBK model. *In vitro* neurotoxicity and genotoxicity data from the literature were translated into quantitative human *in vivo* toxicity data using PBK modeling-facilitated reverse dosimetry. A risk assessment was further conducted using the MOE approach to evaluate the risks from dietary and endogenous MGO.

Finally, in **Chapter 7**, General discussion, the main results from the previous chapters are discussed in more detail, and further recommendations or possibilities for future research are explored.

2



Chapter 2

The Influence of Intracellular Glutathione Levels on the Induction of Nrf2-Mediated Gene Expression by α -Dicarbonyl Precursors of Advanced Glycation End Products

This chapter is based on:

Liang Zheng, Katja C. W. van Dongen, Wouter Bakker, Ignacio Miro Estruch, Ivonne M. C. M. Rietjens. The influence of intracellular glutathione levels on the induction of Nrf2-mediated gene expression by α -dicarbonyl precursors of advanced glycation end products.

Published in: Nutrients. 2022 Mar 24;14(7):1364.

DOI: 10.3390/nu14071364

Abstract

α -Dicarbonyl compounds, particularly methylglyoxal (MGO), glyoxal (GO), and 3-deoxyglucosone (3-DG), are highly reactive precursors for the formation of advanced glycation end products (AGEs). They are formed *in vivo* and during food processing. This study aimed to investigate the role of intracellular glutathione (GSH) levels in the induction of Nrf2-mediated gene expression by α -dicarbonyl compounds. The reactions between α -dicarbonyl compounds (MGO, GO, and 3-DG) and GSH were studied by LC-MS in a cell-free system. It was shown that these three α -dicarbonyl compounds react instantaneously with GSH, with the GSH-mediated scavenging decreasing in the order MGO > GO > 3-DG. Furthermore, in a cell-based reporter gene assay MGO, GO, and 3-DG were able to induce Nrf2-mediated gene expression in a dose-dependent manner. Modulation of intracellular GSH levels showed that the cytotoxicity and induction of the Nrf2-mediated pathway by MGO, GO, and 3-DG was significantly enhanced by depletion of GSH, while a decrease in Nrf2-activation by MGO and GO but not 3-DG was observed upon an increase of the cellular GSH levels. Our results reveal subtle differences in the role of GSH in protection against the three typical α -dicarbonyl compounds and in their induction of Nrf2-mediated gene expression, and point at a dual biological effect of the α -dicarbonyl compounds, being reactive toxic electrophiles and -as a consequence- able to induce Nrf2-mediated protective gene expression, with MGO being most reactive.

Keywords: α -dicarbonyl compounds; glutathione; methylglyoxal; glyoxal; 3-deoxyglucosone; Nrf2

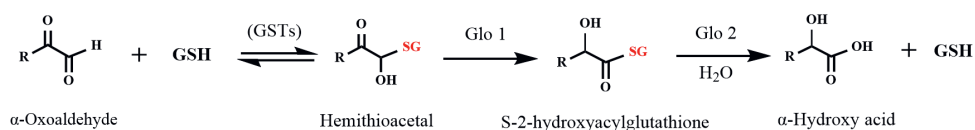
2.1 Introduction

α -Dicarbonyl compounds are by-products from cellular metabolism formed *in vivo* by glycation, degradation of glycolytic intermediates, and lipid peroxidation^{34, 126}. They are also found in various foods and beverages, in which they are mainly formed by caramelization and Maillard reactions during thermal processing and storage of food^{54, 127}. Among the α -dicarbonyl compounds, also so-called α -oxoaldehydes, methylglyoxal (MGO), glyoxal (GO), and 3-deoxyglucosone (3-DG) are the major precursors for advanced glycation end products (AGEs), the formation of which has been associated with many chronic diseases^{128, 129}. Typical concentrations of MGO, GO, and 3-DG are 1-4 μ M in cells, but these concentrations are elevated under pathological circumstances such as metabolic disorders^{10, 12}. The production of α -dicarbonyl compounds during thermal processing and storage of food further increases human exposure to these compounds or the resulting AGEs via dietary intake. Increased *in vivo* concentrations of these α -dicarbonyl compounds may result in a dysfunctional metabolic state also called dicarbonyl stress, which causes an increase in the production of reactive oxygen species (ROS) and proinflammatory cytokines and induces loss of mitochondrial membrane potential in different cell types^{97, 130, 131}. Especially, under dicarbonyl stress, the pronounced electrophilic reactivity of the α -dicarbonyl compounds facilitates their spontaneous reactions with nucleophilic reaction sites of proteins to form AGEs causing protein damage and aggregation, which contributes to cell and tissue dysfunction and eventually may play a role in the development of diabetes mellitus, cardiovascular diseases, and a variety of age-related diseases, such as Parkinson's disease and Alzheimer's disease^{22, 132, 133}. Understanding the underlying mechanisms by which cells are affected by or can be protected against α -dicarbonyl compounds is therefore of particular importance.

Several metabolic pathways in human cells are known to antagonize the formation of AGEs mediated by α -dicarbonyl compounds. The glyoxalase system, which is highly dependent on glutathione (GSH), has been reported to provide a major detoxification pathway for MGO and GO in cells⁶⁸. MGO and GO can react with the nucleophilic thiol group of GSH both non-enzymatically and in a reaction catalyzed by glutathione-S-transferases (GSTs) to form a hemithioacetal which can be further converted by glyoxalase 1 and 2 (Glo1 and Glo2) to the corresponding α -hydroxy acid (**Figure 2.1A**)^{65, 134, 135}. 3-DG is mainly detoxified to 3-deoxyfructose by NADPH-dependent aldo-keto reductases (**Figure 2.1B**)¹⁰. Previous studies have confirmed that GSH plays a crucial role in the detoxification of MGO and GO^{135, 136}, while for 3-DG this role remains uncertain. The aim of the present study was to compare the role of intracellular GSH in counteracting the cellular effects of the three reactive α -dicarbonyls,

including cytotoxicity and the induction of the nuclear factor erythroid 2 p45-related factor 2 (Nrf2)-mediated gene expression.

(A)



(B)

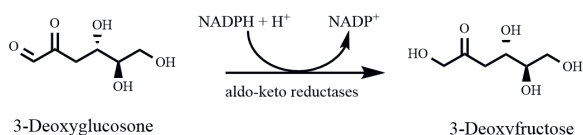


Figure 2.1. Major intracellular detoxification pathways for α -dicarbonyl compounds including (A) detoxification of the α -dicarbonyl compounds (mainly MGO and GO) by the glyoxalase system and (B) detoxification (mainly for 3-DG) by NADPH-dependent aldol-keto reductases. GSH: glutathione, GSTs: glutathione-S-transferases, MGO: methylglyoxal, GO: glyoxal, 3-DG: 3-deoxyglucosone, Glo1: glyoxalase 1, Glo2: glyoxalase 2.

Nrf2 is an essential transcription factor regulating the expression of genes containing an electrophile-responsive element (EpRE) responsible for the induction of a wide range of protective enzymes involved in the synthesis of GSH and protection of cells against electrophilic as well as oxidative stress^{68, 137}. Due to the reactive electrophilic activity of the α -dicarbonyl compounds, possible reversible binding of the dicarbonyls to reactive cysteine residues in the regulatory inhibitory protein Keap1 (Kelch-like erythroid-cell-derived protein with CNC homology-associated protein 1), the major regulator of Nrf2, may result in the release of Nrf2 from Keap1, leading to nuclear translocation of Nrf2 and the activation of EpRE-mediated gene transcription¹⁰. Some studies have reported that pretreatment of cells with Nrf2 activators, such as carnosic acid and naringenin, promoted the levels of intracellular GSH by increasing the expression of cystine/glutamate transporter and glutamyl-cysteine ligase (GSH synthesis rate-limiting enzyme) via the Nrf2 signaling pathway, contributing to the attenuation of MGO-induced cytotoxicity in SH-SY5Y cells^{70, 71}. However, the direct involvement of Nrf2 in the adaptive cellular response to exposure to α -dicarbonyl compounds has not been fully elucidated, and the potential differences in the induction of the Nrf2-mediated transcriptional pathway by the three α -dicarbonyl compounds and the influence on this process by cellular GSH levels still need to be clarified. In this study, the scavenging efficacy of GSH on the three α -dicarbonyl compounds was evaluated in an *in vitro* cell-free system. Furthermore, the influence of intracellular GSH levels on cytotoxicity and on the Nrf2-mediated gene expression induced by the selected α -dicarbonyl compounds was studied using

the U2OS Nrf2 reporter gene cells¹³⁸, either without or upon modulation of their intracellular GSH levels.

2.2 Materials and methods

2.2.1 Chemicals and reagents

MGO (40% in water), GO (40% in water), L-glutathione reduced (GSH, purity \geq 98%), L-glutathione oxidized (GSSG, purity \geq 98%), N-acetyl-L-cysteine (NAC, purity \geq 99%), L-buthionine-sulfoximine (BSO, purity \geq 97%), 2',7'-dichlorofluorescein diacetate (DCFDA, purity \geq 97%), and *tert*-butyl hydroperoxide (TBHP, 70% in water) were purchased from Sigma-Aldrich (St. Louis, MO, USA). 3-Deoxyglucosone (3-DG, purity $>$ 99%) was obtained from Toronto Research Chemicals (Toronto, ON, Canada). Trichloroacetic acid (TCA, purity \geq 98%) and acetic acid (purity \geq 99%) were purchased from Merck (Darmstadt, Germany). Acetonitrile (LC-MS grade) was purchased from Biosolve BV (Valkenswaard, The Netherlands). Formic acid (purity \geq 99%) was purchased from VWR CHEMICA (Amsterdam, The Netherlands). WST-1 reagent was obtained from Roche (Mannheim, Germany). Dulbecco's Modified Eagle Medium/Nutrient Mixture F-12 (DMEM/F-12) with GlutaMAX supplement cell culture medium (with and without phenol red), penicillin/streptomycin, Hanks' balanced salt solution (HBSS) and phosphate buffered saline (PBS) were purchased from Gibco (Paisley, UK). Foetal calf serum (FCS) was obtained from Bodinco (Alkmaar, The Netherlands). Trypsin, nonessential amino acids (NEAA), and geneticin (G418) were obtained from Invitrogen Corporation (Breda, The Netherlands). Ultrapure water was prepared by a Milli-Q system (Millipore, MA, USA). All other reagents in this study were of analytical grade or purer.

2.2.2 Cell lines

The Nrf2 CALUX cells (BioDetection Systems, Amsterdam, The Netherlands) are human osteosarcoma U2OS cells, which were stably transfected with a reporter construct carrying a luciferase reporter gene under transcriptional control of four EpREs¹³⁸.

The Cytotox CALUX cells (BioDetection Systems, Amsterdam, The Netherlands) are human osteosarcoma U2OS cells stably transfected with a reporter construct carrying a luciferase reporter gene under transcriptional control of a constitutive promoter¹³⁹. The reporter construct was generated by inserting the luciferase gene into the multiple cloning site of the pSG5-neo vector¹⁴⁰. These cells have an invariant luciferase expression and a decrease in luciferase activity therefore indicates a cytotoxic effect. Besides, an increased luciferase activity in these cells may indicate stabilization of luciferase reporter protein without underlying increased expression of the gene¹⁴¹.

Both cell lines were cultured in DMEM/F12 GlutaMAX medium containing 7.5% FCS, 1% NEAA, and 0.3% penicillin/streptomycin in a humidified incubator of 5% CO₂ at 37 °C. 200 µg/mL G418 was added to the culture medium once a week to maintain the selection pressure¹³⁸.

2.2.3 Kinetic study of the reaction between α -dicarbonyl compounds and GSH

Stock solutions of MGO, GO, 3-DG, GSH, and GSSG were all prepared in 25 mM potassium phosphate (pH = 7.4). To a starting solution of GSH (final concentration 0.5 mM) were added different volumes of the stock solution of MGO, GO, or 3-DG to give a final concentration of 0.5 mM or 5 mM, followed by incubation of the resulting solution at 37 °C in a water bath for 0 h, 0.5 h, 1 h, 2 h, 4 h, and 6 h. At each time point, 4 µL acetic acid was added to the collected samples (196 µL) to stabilize GSH and its related adducts. Samples were immediately stored at -80 °C until analysis by LC-MS as further described in **Sections 2.2.4 and 2.2.5**.

2.2.4 LC-TOF-MS analysis

An Agilent 1200 LC system coupled with a Bruker micro-TOF mass spectrometer was used to qualitatively detect the reaction products between α -dicarbonyl compounds and GSH. A Phenomenex Luna Omega Polar C18 (100 mm \times 2.1 mm, 1.6 µm) column was employed during the experiment with a flow rate of 0.18 mL/min. The mobile phase was composed of A (ultrapure water with 0.1% formic acid) and B (acetonitrile with 0.1% formic acid) with the following gradient elution: 0–2 min, 100%A; 2–7 min, 100–40%A; 7–8.5 min, 40–20%A; 8.5–8.7 min, 20–100%A; 8.7–24 min, 100%A. The injection volume was 1 µL. Mass spectrometric analysis was performed in the positive electrospray ionization mode with mass spectra acquired from m/z 100 to 1500. The mass parameters were: capillary voltage, -4500 V; nebulizing gas pressure, 1.2 bar; drying gas flow, 8 L/min and drying temperature, 200 °C.

2.2.5 LC-TQ-MS analysis

A Shimadzu Nexera XR LC-20AD XR UHPLC system coupled with a Shimadzu 8040 triple quadrupole mass spectrometer with electrospray ionization (ESI) interface was applied for quantification of GSH in the samples. Chromatographic separation was achieved using the same column as used in the LC-TOF-MS analysis. Ultrapure water containing 0.1% formic acid (A) and acetonitrile with 0.1% formic acid (B) were used as mobile phase at a flow rate of 0.2 mL/min. The following gradient was used: 0–1 min, 100%A; 1–5 min, 100–35%A; 5–7.5 min, 35%A; 7.5–7.6 min, 35–100%A; 7.6–18 min, 100%A. The instrument was operated in positive ionization mode with multiple reaction monitoring (MRM) for quantification. The mass parameters were: nebulizing gas flow, 3.0 L/min; drying gas flow and heating gas flow, 10.0 L/min; interface temperature, 300 °C; and heat block temperature, 400 °C. GSH was monitored

at the $[M + H]^+$ of precursor to product ion transitions of m/z 307.90 \rightarrow 179.05 (collision energy (CE) = -12 eV), 307.90 \rightarrow 76.10 (CE = -25 eV), 307.90 \rightarrow 162.05 (CE = -16 eV), and 307.90 \rightarrow 84.05 (CE = -21 eV). GSSG was monitored at the $[M + H]^+$ of precursor to products of m/z 613.15 \rightarrow 355.05 (CE = -22 eV), 613.15 \rightarrow 231.00 (CE = -22 eV), 613.15 \rightarrow 484.15 (CE = -22 eV) and 613.15 \rightarrow 177.10 (CE = -30 eV). Quantification of GSH in the samples was achieved via calibration curves made using the reference compound. The remaining GSH (%) was calculated using the following equation: Remaining GSH (%) = detected amount of GSH in test samples / original amount of GSH in the samples \times 100.

2.2.6 Nrf2 CALUX assay

The induction of Nrf2-mediated gene expression by α -dicarbonyl compounds was tested by measuring the luciferase activity in the Nrf2 CALUX cells. Briefly, Nrf2 CALUX cells (2×10^4 cells/well) were seeded into white opaque 96-well plates (Greiner Bio-one) and incubated for 24 h. Next, the culture medium was refreshed and cells were incubated for another 24 h to allow them to form a confluent monolayer. The culture medium was then replaced by assay medium (DMEM/F12 without phenol red and supplemented with 5% dextran-coated charcoal-stripped FCS (DCC-FCS)¹³⁸) containing different concentrations of each α -dicarbonyl compound for a continuous 24 h exposure. Eight final concentrations (100, 250, 500, 750, 1000, 1250, 1500, and 1750 μ M) of each compound were tested. The three α -dicarbonyl compounds were all dissolved in sterile ultrapure water and added to the cells from 200 times concentrated stock solutions in water. Curcumin at 25 μ M was used as the positive control in each plate. After 24 h exposure, cells were carefully washed with $\frac{1}{2}$ PBS and lysed by low salt buffer¹⁴². Subsequently, the plates were placed on ice for 15 min and then frozen at -80 °C overnight. Afterward, the plates were thawed and the luciferase activity in relative light units (RLU) was measured using a luminometer (GloMax-Multi Detection System-Promega) after the addition of flash mix¹⁴² to each well. The results were expressed as induction factor (IF) compared to the medium control.

2.2.7 Cytotox CALUX assay

To investigate whether cytotoxicity or stabilization of the luciferase enzyme (false positive) occurred during the exposure to α -dicarbonyl compounds, a parallel Cytotox CALUX assay was carried out using Cytotox CALUX cells¹⁴¹. The assay was performed in the same way as the Nrf2 CALUX assay described above.

2.2.8 Cell viability assay

A WST-1 assay was used to evaluate the cytotoxicity of the α -dicarbonyl compounds towards the Nrf2 CALUX cells. In brief, after the same seeding and exposure steps as applied in the Nrf2 CALUX assay, 5 μ L of WST-1 solution was added to each well of the 96-well plates. The plates were then further incubated for 1 h after which the absorbance at 440 nm and a reference wavelength at 620 nm was measured using a plate spectrophotometer (Molecular Devices, San Jose, CA, USA, Spectra Max M2). The cell viability was expressed as a percentage of medium control set at 100%.

2.2.9 Measurement of intracellular ROS levels

The intracellular ROS levels in Nrf2 CALUX cells were measured using the cell-permeant fluorogenic dye 2',7'-dichlorofluorescein diacetate (DCFDA)¹⁴³. Briefly, Nrf2 CALUX cells (3×10^4 cells/well) were seeded into the wells of black 96-well plates (Greiner Bio-one) and incubated for 24 h. Next, the culture medium was removed and cells were loaded with DCFDA by incubation for 45 min at 37 °C with 25 μ M DCFDA in HBSS containing 0.4% FCS. The DCFDA-containing medium was then replaced by assay medium containing different concentrations of each α -dicarbonyl compound for a continuous 6 h exposure. TBHP at 50 μ M was used as the positive control in each plate. After 6 h exposure, the levels of 2',7'-dichlorofluorescein (DCF), reflecting ROS formation, were measured using a fluorescence microplate reader (Molecular Devices, Spectra Max M2) at an excitation wavelength of 485 nm and an emission wavelength of 535 nm. The results were expressed as fold induction compared to the medium control.

2.2.10 Investigation of the effects of altered intracellular GSH levels on the induction of Nrf2-mediated gene expression by the α -dicarbonyl compounds

To study the effect of intracellular GSH levels on the induction of Nrf2-mediated gene expression by the α -dicarbonyl compounds, the intracellular GSH level was modulated by the addition of NAC, a precursor of GSH able to increase intracellular levels of GSH¹⁴⁴, and by the addition of BSO to decrease the levels of GSH in cells¹⁴⁵. Cells were seeded and incubated for 24 h as described above for the Nrf2 CALUX assay. For NAC pre-treatment, after 24 h incubation, the culture medium was replaced by fresh medium and incubated for another 20 h, followed by incubation of the cells with 10 mM NAC for 4 h to allow an increase in GSH in the cells. After 4 h of pre-incubation with NAC, the culture medium was removed and cells were carefully washed by PBS to remove all extracellular NAC residues before the addition of assay medium containing different concentrations of each α -dicarbonyl compound for a continuous 24 h exposure. Co-exposure of the cells to NAC and α -dicarbonyl compounds was

not applied since NAC is known to scavenge α -dicarbonyl compounds⁴¹. For BSO pre-treatment, after 24 h incubation, the culture medium was replaced by medium containing 100 μ M of BSO and incubated for 24 h to decrease the intracellular GSH level. After 24 h of pre-incubation with BSO, the culture medium was removed and assay medium containing 100 μ M of BSO and different concentrations of each α -dicarbonyl compound were added to cells for 24 h of exposure.

After 24 h of exposure, cells were washed and lysed and the luciferase activity was measured as described above. The WST-1 assay was also carried out in parallel to evaluate the cell viability.

2.2.11 Quantification of the intracellular GSH levels

The intracellular levels of GSH were quantified by LC-TQ-MS for control cells and after pre-incubation of cells with 10 mM NAC or 100 μ M BSO. Briefly, after the same seeding and pre-incubation steps as described above, the medium in plates was removed and cells were washed with cold PBS, followed by adding 200 μ L 2% TCA to stabilize the GSH. The plates were first placed on ice for 15 min and then frozen at -80°C for more than 6 h before cells were mechanically scraped from the plates. Next, cell lysate from each well was transferred to a centrifuge tube. After being vortexed and centrifuged at 12,000 rpm ($13,523\times g$) for 30 min, the supernatant was collected and analyzed by LC-TQ-MS. The intracellular GSH levels were normalized to protein concentrations as quantified by BCA protein assay kits according to the manufacturer's instructions (Pierce, Thermo Scientific, Waltham, MA, USA).

2.2.12 Statistical analysis

Data are presented as means \pm standard error of the mean (SEM) from at least three independent experiments. An independent-samples *t* test for normally distributed data and a Mann-Whitney U test for non-normally distributed data were applied to compare between any two groups (normality was assessed using the Shapiro-Wilk test) using SPSS 25.0 software (SPSS Inc., Chicago, IL, USA). Statistical significance was defined as $p < 0.05$. Figures were prepared using GraphPad Prism 9 software (San Diego, CA, USA). Chemical structures were drawn by ChemDraw 20.0 (PerkinElmer, Waltham, MA, USA).

2.3 Results

2.3.1 Identification of reaction products between α -dicarbonyl compounds and GSH by LC-TOF-MS

The reaction mixtures of MGO, GO, or 3-DG with GSH were analyzed by LC-TOF-MS. Typical base peak chromatograms are shown in **Figure 2.2**. Due to the poor ionization efficiency and stability of dicarbonyls in the ESI source¹⁴⁶, these compounds were not detected. The adducts formed by the reactions between MGO, GO, or 3-DG and GSH at a molar ratio of 10:1 were identified and their mass spectra are shown in **Figure 2.3**. After incubation of GSH with MGO for 1 h, a new peak (at 5.7 min) appeared in the chromatogram (**Figure 2.2A**) with the molecular ion m/z 380 $[M + H]^+$, which was 72 mass units greater than the molecular ion of GSH m/z 308 $[M + H]^+$, indicating that this peak was GSH conjugated MGO (denoted as MGO-GSH adduct). The fragment ion of this peak m/z 308 $[M - 72 + H]^+$, suggesting the loss of one MGO molecule, further corroborated the formation of the MGO-GSH adduct. Two new reaction products (at 2.7 min and 4.2 min) were observed after the incubation of GSH and GO for 1 h (**Figure 2.2B**). The peak at 4.2 min had the molecular ion m/z 366 $[M + H]^+$ and fragment ion m/z 308 $[M - 58 + H]^+$, indicating the loss of one GO molecule, suggesting this product was a GSH adduct of GO (denoted as GO-GSH adduct). The peak at 2.7 min had the molecular ion m/z 384 $[M + H]^+$, which was 18 mass units higher than the m/z of the GO-GSH adduct (m/z 366 $[M + H]^+$), suggesting a possible hydration of the GO-GSH adduct (denoted as hydrous GO-GSH adduct). By losing a molecule of H_2O , the fragment ion m/z 366 $[M - 18 + H]^+$ was produced. A previous study showed that the hydrated GO is the dominant form of GO in aqueous solutions¹⁴⁷. Similarly, a new peak was observed at 2.9 min (**Figure 2.2C**) with the molecular ion m/z 470 $[M + H]^+$ and fragment ion m/z 308 $[M - 162 + H]^+$ after incubation of GSH with 3-DG, suggesting it lost one molecule of 3-DG, indicating that this product was a GSH adduct of 3-DG (denoted as 3-DG-GSH adduct).

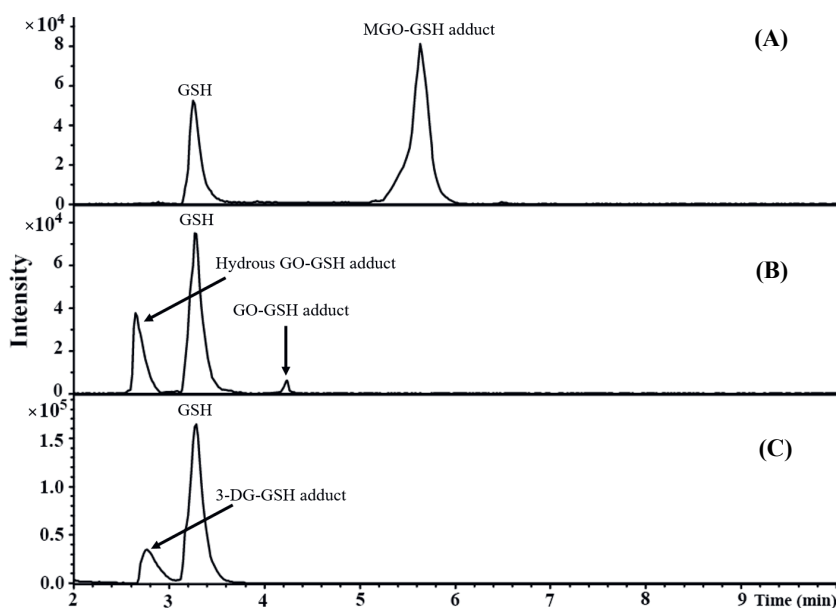


Figure 2.2. Typical LC-TOF-MS base peak chromatograms of incubations of MGO (A), GO (B), or 3-DG (C) with GSH at a molar ratio of 10:1 for 1 h.

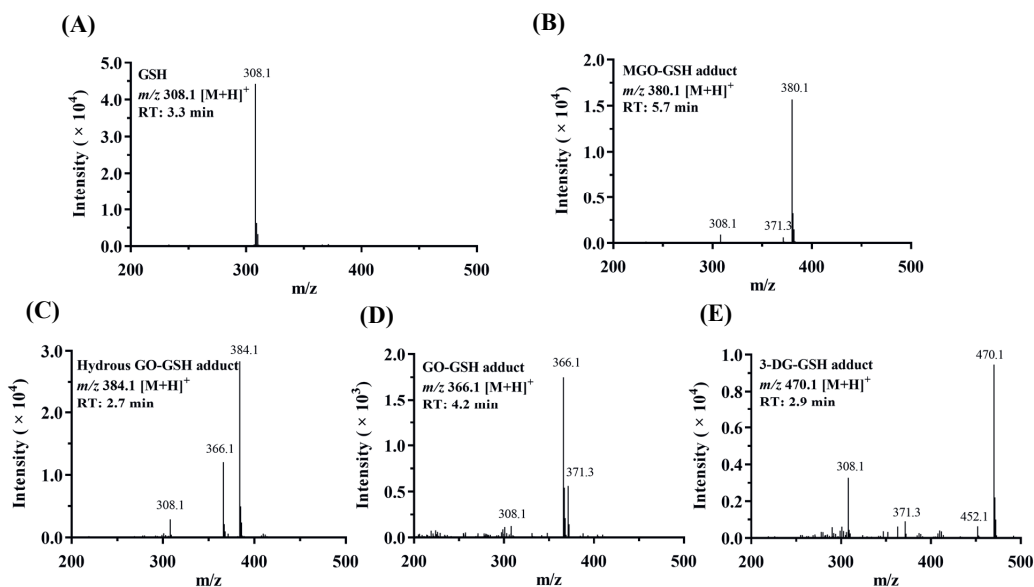


Figure 2.3. LC-TOF-MS spectra of GSH (A), MGO-GSH adduct (B), hydrus GO-GSH adduct (C), GO-GSH adduct (D), and 3-DG-GSH adduct (E).

2.3.2 Kinetic study of the reaction between α -dicarbonyl compounds and GSH

We further evaluated and compared the kinetics of the scavenging effects of GSH on the three α -dicarbonyl compounds at a molar ratio of 1:1 in 25 mM potassium phosphate (pH = 7.4) at 37 °C. These reactions were monitored for 6 h during which the formation of GSSG from GSH was limited as confirmed by LC-TQ-MS (data not shown). The results shown in **Figure 2.4** suggest that GSH reacted instantaneously with the three α -dicarbonyl compounds, and the scavenging of the α -dicarbonyls by GSH did not continue during the subsequent 6 h of incubation, during which only a small further decrease in GSH was observed likely due to some autoxidation of GSH. At equimolar concentrations of MGO and GSH resulted in the highest level of GSH scavenging (ca. 18.1% reduction of GSH immediately at the start), as compared with GO (ca. 8.6% reduction of GSH) and 3-DG (ca. 1.7% reduction of GSH).

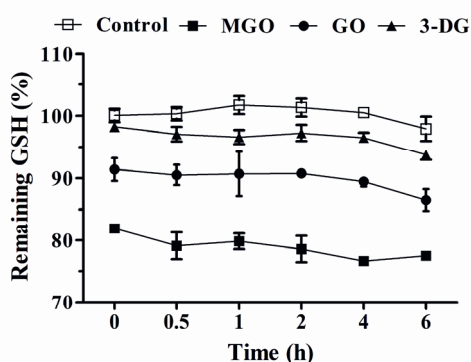


Figure 2.4. The change in GSH content after incubation of GSH (0.5 mM) with MGO (0.5 mM), GO (0.5 mM) or 3-DG (0.5 mM) in 25 mM potassium phosphate (pH = 7.4, 37 °C) for 0, 0.5, 1, 2, 4, and 6 h. Data are presented as mean \pm SEM of three independent replicates.

2.3.3 Effects of α -dicarbonyl compounds on the viability of Nrf2 CALUX cells and induction of Nrf2-mediated gene expression

The WST-1 assay was used to assess the effects of MGO, GO, and 3-DG on the viability of Nrf2 CALUX cells. As shown in **Figure 2.5**, none of the individual compounds (MGO, GO, and 3-DG) caused cytotoxic effects at concentrations from 100 to 1750 μ M on Nrf2 CALUX cells after 24 h exposure, except for MGO that exhibited some cytotoxicity (66.6% cell viability remaining) at the maximum concentration tested (1750 μ M).

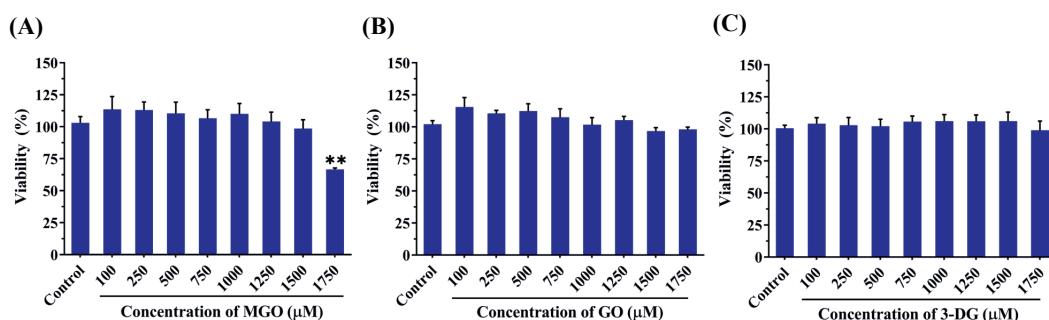


Figure 2.5. Effects of MGO (A), GO (B), and 3-DG (C) on the viability of Nrf2 CALUX cells as evaluated with the WST-1 assay. Data are presented as mean \pm SEM of three independent replicates. ** $p < 0.01$ compared with the solvent control (0.5% nano pure water).

Figure 2.6 shows the concentration-dependent luciferase induction by each α -dicarbonyl compound at concentrations up to 1750 μM in the Nrf2 CALUX assay and the Cytotox CALUX assay. The Cytotox CALUX results corroborate the minor effects on cell viability as also observed in the WST-1 assay for the three compounds by showing no substantial reduction (**Figure 2.5**). Furthermore, no increase in luciferase activity was observed after exposure of the Cytotox CALUX cells to the α -dicarbonyl compounds, indicating that the observed induction in the Nrf2 CALUX assay does not reflect false positive results due to the stabilization of the luciferase enzyme. The results of the Nrf2 CALUX assay presented in **Figure 2.6** show that MGO, GO, and 3-DG significantly induced Nrf2-mediated luciferase expression in a concentration-dependent manner compared to the solvent control, with the induction becoming statistically significant at concentrations $\geq 750 \mu\text{M}$ MGO, $\geq 750 \mu\text{M}$ GO, and $\geq 500 \mu\text{M}$ 3-DG, respectively ($p < 0.05$). 3-DG showed a luciferase induction at a lower concentration (500 μM), potentially reflecting its less efficient scavenging by GSH (**Figure 2.4**). In terms of fold induction, however, at higher concentrations ($\geq 1250 \mu\text{M}$) MGO appeared to be the most potent Nrf2 inducer, followed by 3-DG and lastly GO. GO showed the lowest induction capacity of Nrf2-mediated gene expression at all concentrations tested among the three compounds.

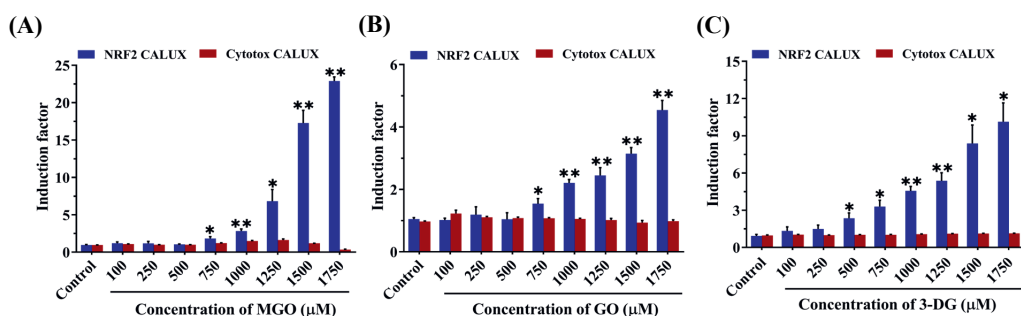


Figure 2.6. Induction of Nrf2-mediated luciferase gene expression in the Nrf2 CALUX cells (blue bars) and fold change in luciferase activity in the Cytotox CALUX assay (red bars) after 24 h exposure to MGO (A), GO (B), and 3-DG (C). Note the different sizes of the Y-axes. Data are presented as mean \pm SEM of three independent replicates. * $p < 0.05$ and ** $p < 0.01$ compared with the solvent control (0.5% nano pure water).

2.3.4 Effects of α -dicarbonyl compounds on the production of intracellular ROS

Intracellular ROS production induced by MGO, GO, and 3-DG at concentrations from 500 to 1750 μM was measured using the oxidation-sensitive probe DCFDA. As shown in **Figure 2.7**, incubation of the Nrf2 CALUX cells for 6 h with MGO, GO, and 3-DG induced a concentration-dependent increase in ROS production compared to the solvent control, with the induction becoming statistically significant at concentrations ≥ 500 μM MGO, ≥ 1250 μM GO, and ≥ 1250 μM 3-DG, respectively ($p < 0.05$). This effect appeared to decrease in the order MGO > GO \approx 3-DG.

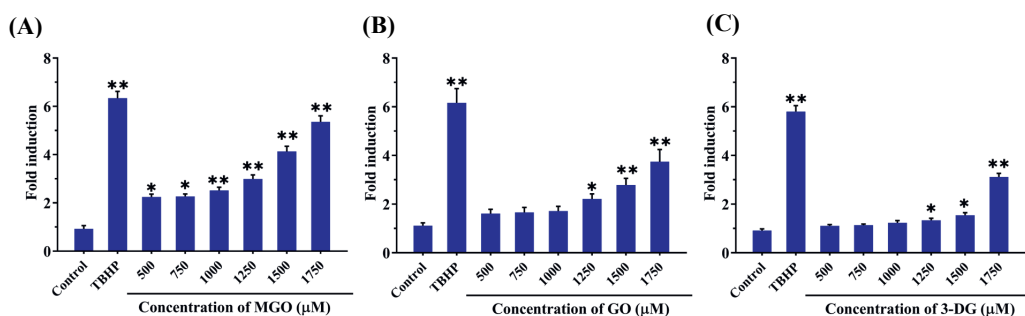


Figure 2.7. Effects of MGO (A), GO (B), and 3-DG (C) on the reactive oxygen species (ROS) production in Nrf2 CALUX cells. *tert*-Butyl hydroperoxide (TBHP) at 50 μM was used as the positive control. Data are presented as mean \pm SEM of three independent replicates. * $p < 0.05$ and ** $p < 0.01$ compared with the solvent control.

2.3.5 Effects of altered intracellular GSH levels on the viability of Nrf2 CALUX cells and the induction of Nrf2-mediated gene expression by α -dicarbonyl compounds

Intracellular GSH levels were measured by LC-TQ-MS in control and NAC or BSO treated cells to validate the effectiveness in the modulation of GSH levels in the Nrf2 CALUX cells (**Figure 2.8**). After treatment with 10 mM NAC for 4 h, intracellular GSH levels were increased 1.4-fold compared to the solvent control. In contrast, intracellular GSH levels in cells treated with 100 μ M BSO for 48 h were 18.4-fold lower than what was detected in untreated control cells.

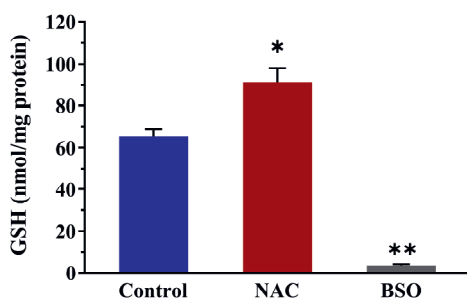


Figure 2.8. Changes in intracellular GSH levels after exposure of Nrf2 CALUX cells to NAC or BSO only. Data are shown as mean \pm SEM of three independent replicates. * $p < 0.05$ and ** $p < 0.01$ compared with the solvent control. NAC: N-acetyl-L-cysteine, BSO: L-buthionine-sulfoximine.

Figure 2.9 shows the effect of pre-incubation of Nrf2 CALUX cells with NAC or BSO on the cytotoxicity of the three α -dicarbonyl compounds. The selected concentrations in this assay for MGO, GO and 3-DG were not toxic to the cells with unmodified GSH levels. Upon pre-treatment of the cells with 10 mM NAC, MGO, GO, and 3-DG also showed no significant toxic effect on the cells. Treatment with BSO alone showed some cytotoxicity (89.5% cell viability remaining), while co-exposure of the cells to 100 μ M BSO and the α -dicarbonyl compounds at increasing concentrations that were not toxic by themselves (**Figure 2.5**) resulted in a considerable dose-dependent additional decrease in the cell viability. Upon reduction of cellular GSH levels by BSO, MGO, GO, and 3-DG showed significantly increased toxicity at concentrations that were shown non cytotoxic towards cells with unmodified GSH levels. This effect appeared to decrease in the order 3-DG > MGO > GO.

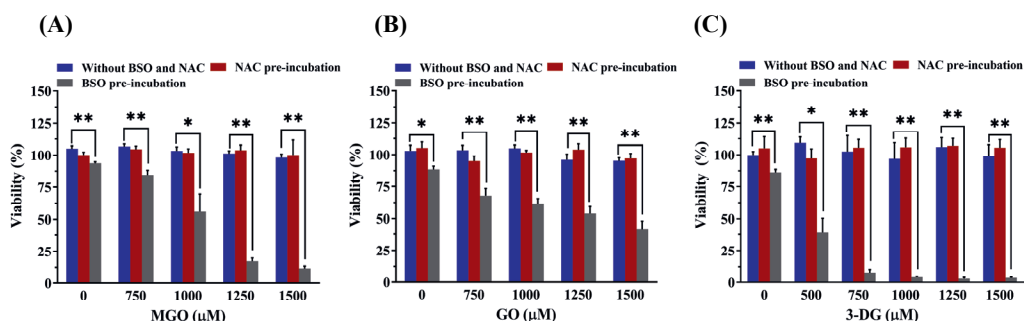


Figure 2.9. Effects of altered intracellular GSH levels on the cell viability upon exposure of Nrf2 CALUX cells to MGO (A), GO (B), and 3-DG (C) for 24 h. Data are presented as mean \pm SEM of at least three independent replicates. * $p < 0.05$ and ** $p < 0.01$.

The effects of changes in intracellular GSH levels on the α -dicarbonyl-mediated induction of Nrf2-mediated gene expression are shown in **Figure 2.10**. Although treatment with NAC alone did not show any effect on basal luciferase induction, it significantly attenuated Nrf2-mediated induction of gene expression by MGO (at concentrations $\geq 1000 \mu\text{M}$) and GO (at $1500 \mu\text{M}$) but not 3-DG. Upon pre-treatment of the Nrf2 CALUX cells with NAC, the induction factor for the Nrf2-mediated induction of gene expression of MGO at 1000, 1250, $1500 \mu\text{M}$ decreased from 3.8- to 1.9-fold (50% decrease), 9.1- to 5.0-fold (45% decrease), and 23.1- to 9.1-fold (61% decrease), respectively, while the induction factor of GO at $1500 \mu\text{M}$ decreased from 2.9- to 2.1-fold (28% decrease).

The addition of BSO leads to the opposite effect causing a substantial increase in luciferase induction by MGO (750 and $1000 \mu\text{M}$), GO (750 and $1000 \mu\text{M}$), and 3-DG ($500 \mu\text{M}$). The induction factor of MGO at 750 and $1000 \mu\text{M}$ increased from 1.9- to 33.7-fold and 3.8- to 51.5-fold, respectively. The luciferase induction of GO at 750 and $1000 \mu\text{M}$ increased from 1.9- to 15.4-fold and 1.8- to 11.5-fold, respectively. For 3-DG, an increase in induction from 2.7- to 8.9-fold at $500 \mu\text{M}$ was observed. In addition, a decrease in luciferase induction was observed at higher concentrations of the three compounds in the presence of BSO, due to the increased cytotoxic effects caused by each α -dicarbonyl compound in the presence of BSO (**Figure 2.9**). BSO itself showed an induction factor of 4.0-fold compared to the untreated control. However, the luciferase induction response by the three α -dicarbonyl compounds with the addition of BSO is considerably higher than the sum of the responses induced by each α -dicarbonyl compound and BSO separately. This indicates that the reduction of cellular GSH levels by BSO resulted in a more than additive enhancement of Nrf2-mediated gene expression by the α -dicarbonyl compounds.

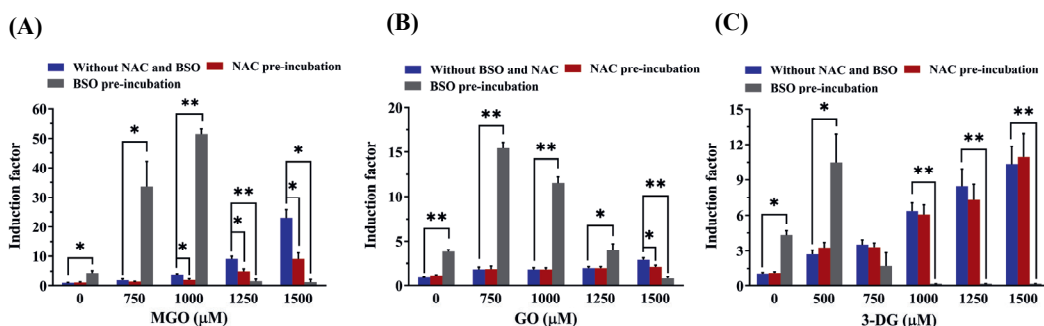


Figure 2.10. Effects of altered intracellular GSH levels on the induction of Nrf2-mediated gene expression upon 24 h exposure to MGO (A), GO (B), and 3-DG (C). Note the different sizes of the Y-axes. Data are shown as mean \pm SEM of at least three independent replicates. * $p < 0.05$ and ** $p < 0.01$.

2.4. Discussion

The scavenging of GO and MGO by GSH in cells is a well-known phenomenon that occurs non-catalytically or is catalyzed by GSTs, leading to the subsequent further detoxification of GO and MGO by Glo1 and Glo2 in the glyoxalase system^{10, 65, 148}. Our results demonstrate that 3-DG can form adducts with GSH as well. In addition, we found that, unlike what was observed for MGO, for GO also a hydrated GSH adduct was detected. The results also indicate that the three compounds react instantaneously with GSH and that the reactions reach equilibrium rapidly. In the present study, the amount of GSH scavenged by an equimolar concentration of the three α -dicarbonyl compounds decreased in the order MGO > GO > 3-DG. This difference may be related to the occurrence of their various chemical forms in aqueous solution (**Figure 2.11**)¹⁴⁹. 3-DG tends to exist in a cyclic form in aqueous solutions resulting in relatively lower levels of the form that tends to react with GSH¹⁵⁰. Similarly, MGO is present in aqueous solutions in a monohydrate (71%), dihydrate (28%), and unhydrated form (1%), while GO exists mainly as dihydrate followed by dimers (1–2%), monohydrate (0.5%), and an unhydrated form (0.005%)^{151, 152}. This difference in hydration between GO and MGO can be related to the fact that GO is a dialdehyde and therefore probably exists in doubly hydrated form, in which upon GSH adduct formation one hydrated moiety remains, while the keto group of MGO is less susceptible to hydration explaining why no hydrated adduct is formed from MGO and GSH. In addition, the fact that less unhydrated GO exists in buffer solutions and also that the monohydrate of GO tends to polymerize more rapidly than that of MGO may result in a lower level of GSH adduct formation with GO compared to MGO¹⁵².

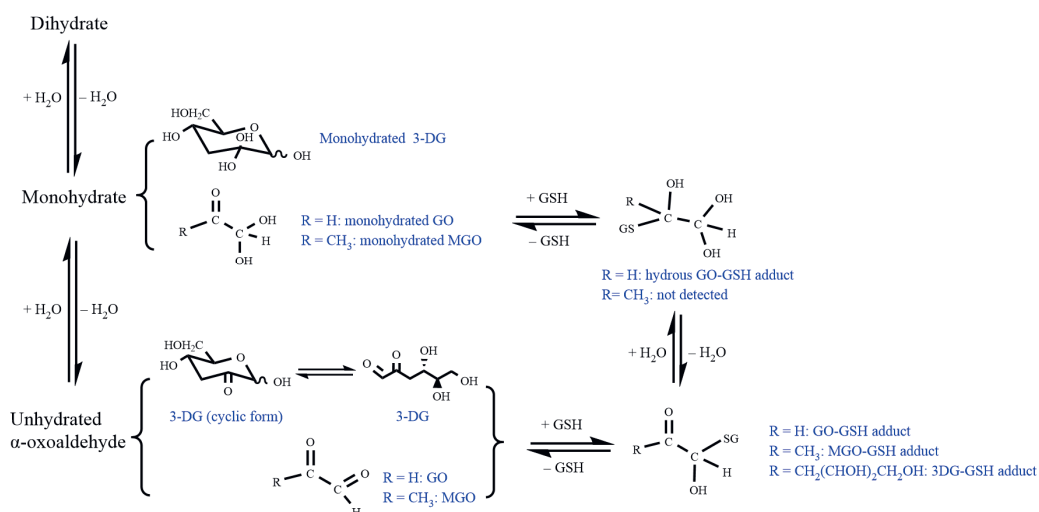


Figure 2.11. Schematic presentation of the formation of MGO-GSH, hydrous GO-GSH, GO-GSH, and 3-DG-GSH adducts.

Apart from the primary GSH-dependent detoxification pathway through direct scavenging with or without GSTs mediation followed by the further metabolism via Glo1 and Glo2 in the glyoxalase system for MGO and GO, aldehyde dehydrogenases (ADHs) and aldo-keto reductases (AKRs) also contribute to the detoxification of MGO and GO to a lesser degree¹⁰. 3-DG is reported to be mainly metabolized by AKRs, with minor metabolism by ADH¹³⁵. Despite that 3-DG did form an adduct with GSH in this study, a previous study reported that Glo1 overexpression did not result in decreased 3-DG levels and thus 3-DG was considered as not sensitive to Glo1¹⁵³. The expression of Glo1, AKRs, and ADHs, as well as the synthesis of GSH are known to be controlled by the transcription factor Nrf2 through regulatory EpRE-mediated gene expression, with the activation of Nrf2-mediated gene expression enhancing the expression of enzymes for metabolism of α-dicarbonyl compounds leading to the prevention of so-called dicarbonyl stress within cells³⁶. MGO, as a highly reactive electrophilic compound is known to trigger the Nrf2-mediated adaptive cellular response¹⁵⁴, while studies on the induction of the Nrf2 pathway by GO and 3-DG are still absent. In the present study we compared the ability of the three α-dicarbonyl compounds to induce Nrf2-mediated gene expression using the Nrf2 CALUX reporter gene assay, which provides a powerful tool to measure Nrf2-mediated gene expression. Our results show that all three compounds are able to induce the Nrf2-mediated pathway in a dose-dependent manner, suggesting the potential role of α-dicarbonyl compounds in cellular signaling function despite the fact that they are also known as contributing factors to many diseases. It was reported that 3-DG is less reactive than MGO and GO, with for example 200-fold lower reactivity with arginine residues than MGO and GO³², which is in line with our results that show that 3-DG has the lowest reactivity towards GSH. However, 3-DG appeared able to activate the Nrf2-mediated transcriptional

program already at somewhat lower concentrations compared to MGO and GO. In terms of fold induction, at higher concentrations ($\geq 1250 \mu\text{M}$) the induction factors for the three dicarbonyls decreased in the order $\text{MGO} > 3\text{-DG} > \text{GO}$. One possible explanation is that 3-DG was less efficiently scavenged by GSH, resulting in higher cellular concentrations, and thus induction of Nrf2-mediated gene expression at a lower concentration, while the potential of MGO to activate Nrf2 pathway is higher. Besides, due to the high abundance and kinetic constants of Glo1 for the metabolism of MGO and GO in comparison to the essential detoxifying enzymes AKRs for 3-DG⁷⁴, a slower metabolism of 3-DG in cells can be expected which may also result in the higher induction capacity of 3-DG as compared to GO. In addition, the underlying mode of action by which the three α -dicarbonyl compounds mediate Nrf2 induction may be related to either (i) ROS production and/or (ii) their electrophilicity and reaction with amino acid moieties of Keap1 resulting in the release of Nrf2. With respect to ROS production, these three compounds were shown in the present study to be able to induce ROS production, with the fold induction decreasing in the order $\text{MGO} > \text{GO} \approx 3\text{-DG}$. In addition, α -dicarbonyl compounds may react reversibly with cysteine residues of Keap1, and/or may also form irreversible adducts with other nucleophilic amino acid residues such as arginine and lysine, leading to the Nrf2 release. A previous study discovered that MGO was able to modify Keap1 to form a crosslinking AGE between a cysteine and arginine residue of Keap1, resulting in the dimerization of Keap1 followed by the release of Nrf2 and activation of the Nrf2 transcriptional program⁵³. The irreversible adduct formed by MGO may cause prolonged activation of Nrf2 in comparison to reversible binding to its cysteine moieties. Therefore, the reactivity of dicarbonyls towards GSH may not be the only indicative parameter of their Nrf2 induction capacity.

We further studied the role of intracellular GSH levels in the Nrf2-mediated gene expression. The intracellular GSH levels were modulated by the addition of NAC and BSO, which resulted in a 1.4-fold increase and an 18.4-fold decrease in cellular GSH levels, respectively. This difference in the degree of intracellular GSH level modulation may explain the more pronounced influence on the Nrf2-mediated luciferase induction by the α -dicarbonyl compounds upon the addition of BSO than upon pre-treatment with NAC in our cell model. Pre-treatment of the cells with NAC to increase intracellular GSH levels resulted in a decrease in the Nrf2-mediated gene expression by MGO and GO, but not by 3-DG. This difference is ascribed to the lower level of scavenging of 3-DG with GSH, for which apparently available levels of GSH are adequate and a further increase in cellular GSH levels does not provide extra protection. However, the addition of BSO to decrease the intracellular GSH levels resulted in enhanced cytotoxicity as well as increased induction of Nrf2-mediated gene transcription by MGO, GO, and also by 3-DG. The effects of GSH depletion on the Nrf2 induction by the three compounds appeared to decrease in order of $\text{MGO} > \text{GO} > 3\text{-DG}$. These results indicate the

difference in the role of GSH in the protection against cytotoxicity and in the activation of Nrf2-mediated gene expression by MGO, GO, and 3-DG. For MGO and GO, the depletion of cellular GSH can be expected to result in the inhibition of the formation of the hemithioacetal via the reaction of MGO and GO with GSH, leading to less efficient detoxification of MGO and GO in the cells, thereby increasing their cytotoxicity and Nrf2 inducing activity. In the meanwhile, the depletion of GSH may also increase the oxidative stress in the cells which may contribute to the increased cytotoxic effects and Nrf2 inducing activity. For 3-DG, the enhanced Nrf2 induction activity may be mainly due to the increased oxidative stress in cells caused by 3-DG and the depletion of GSH. A quite unexpected finding was the highest cytotoxic effects by 3-DG in the presence of BSO. Besides the increased oxidative stress which may contribute to the cytotoxic effects to some extent, another possible explanation for the results is that the depletion of GSH may lead to the decrease in the cellular NADPH levels in the regeneration of GSH from GSSG in oxidative stress, which would further cause the decrease of the activity of AKRs leading to the inhibition of the detoxification of 3-DG in the cells^{135, 155}. The exact mode of action underlying this discrepancy for 3-DG, however, remains to be elucidated.

α -Dicarbonyl compounds have traditionally been considered toxic metabolites leading to pathological disorders and many diseases^{10, 36}. However, some recent studies proposed that a hormetic effect can be induced by lower levels of reactive carbonyl species resulting in biological beneficial effects¹⁵⁶. In a healthy human body, a lower level of dicarbonyls may induce adaptive responses such as induction of Nrf2 mediated gene expression leading to the prevention or repair of the adverse effects of the dicarbonyls. However, overwhelming of the protective mechanisms by elevated levels of dicarbonyls and accompanying decreased GSH levels may play a role in some chronic diseases for example neurodegenerative diseases and diabetes^{157, 158}. The augmented and persistent activation of the Nrf2 pathway by dicarbonyl stress can be considered to counteract the related potential adverse effects at least to some extent.

By using U2OS reporter cell lines, our study revealed the potential of the selected α -dicarbonyl AGE precursors to activate Nrf2 mediated gene expression and the role of intracellular GSH in counteracting this effect. The results also revealed subtle differences between the three α -dicarbonyls with MGO being the most potent in terms of scavenging by GSH, ROS production, induction of Nrf2-mediated gene expression, and the effects of GSH depletion on this potential. It is of interest to note that other studies report the toxicity of MGO to other cell lines^{70, 159}. Comparison of the toxicity data from these studies to the results of the present study reveals that U2OS cells appear less sensitive to the adverse effects of MGO. Nevertheless, these cells were used to create the Nrf2 reporter cell model because generally U2OS cells are considered suitable for this purpose given their lack of high levels of endogenous receptors,

reducing chances on receptor cross talk^{138, 160}. For all of these *in vitro* toxicity data reported in the present study it holds that the concentrations of the dicarbonyls at which they cause toxicity are beyond expected physiological concentrations. Nevertheless, the results of the present study reveal information relevant for the mode of action underlying cellular effects of these dicarbonyls and show that endogenous GSH levels play a role in the protection against dicarbonyl stress. Future studies in cell lines representing tissues known to be sensitive towards glycation products and/or dicarbonyl stress, for example kidney or neuronal cells^{161, 162}, may use different or additional read outs, such as PCR or proteomics, to quantify the induction of Nrf2-mediated gene and protein expression. The results of the present study reveal that for such studies MGO is the preferred model compound.

In conclusion, this study elucidated subtle differences in the induction of Nrf2-mediated gene expression by the three typical α -dicarbonyl compounds and their scavenging by GSH, and pointed at a dual biological effect of the α -dicarbonyl compounds, being reactive toxic electrophiles and -as a consequence- able to induce Nrf2-mediated protective gene expression, with MGO being the most reactive.

Acknowledgments

Liang Zheng is grateful for the financial support from the China Scholarship Council (No. 202008510115). The authors acknowledge Biodetection Systems (BDS, Amsterdam) for the use of the U2OS Cytotox and Nrf2 CALUX cells. Especially, we also would like to thank Professor Jacques Vervoort who passed away in July 2021 and offered a lot of assistance with instrumental analysis for this article.

3



Chapter 3

Comparison of the Methylglyoxal Scavenging Effects of Kaempferol and Glutathione and the Consequences for the Toxicity of Methylglyoxal in SH-SY5Y Cells

This chapter is based on:

Liang Zheng, Wouter Bakker, Ignacio Miro Estruch, Frances Widjaja, Ivonne M. C. M. Rietjens. Comparison of the methylglyoxal scavenging effects of kaempferol and glutathione and the consequences for the toxicity of methylglyoxal in SH-SY5Y cells.

Published in: Food Chemistry: X. 2023 Dec 30;20:100920.

DOI: 10.1016/j.fochx.2023.100920

Abstract

This study aimed to characterize the methylglyoxal (MGO) scavenging capacity of glutathione (GSH) and kaempferol in more detail with special emphasis on the possible reversible nature of the adduct formation and their competition for MGO, and the safety consequences of their MGO-scavenging effects. GSH showed immediate and concentration-dependent MGO-scavenging effects, while the scavenging effects by kaempferol appeared concentration- but also time-dependent, with stable adducts formed over time. The GSH adduct gradually disappeared in a competition reaction with kaempferol, and kaempferol became the preferred scavenger over time. Furthermore, the scavenging of MGO by kaempferol provided better protection than GSH against extracellular MGO of SH-SY5Y cells. It is concluded that flavonoids like kaempferol provide better scavengers for food-borne MGO than thiol-based scavengers such as GSH, while, given the endogenous concentrations of both scavengers and the detoxification of the GSH-MGO adduct by the glyoxalase system, GSH will be dominant for intracellular MGO protection.

Keywords: methylglyoxal; kaempferol; glutathione; adduct formation; cytotoxicity

3.1 Introduction

Methylglyoxal (MGO) is a highly reactive α -dicarbonyl compound formed endogenous but also widely distributed in various foods and beverages such as roasted meat, cookies, bread, honey, coffee, milk, and beer^{11, 54}. It can be formed during food processing and storage due to the autoxidation of sugars, the Maillard reaction, lipid degradation, and/or enzymatic reactions of microorganisms in fermented foods^{22, 24}. MGO plays an essential role in the color and aroma formation during thermal processing of some baked and fried foods²⁸. However, MGO can react with nucleophilic sites on proteins to form advanced glycation end products (AGEs), which may result in reduced nutritional value of foods⁵⁸. Moreover, increasing evidence has indicated that higher intake of dietary AGEs may promote oxidative stress and inflammation, contributing to the development of some diseases such as chronic kidney disease and neurodegenerative diseases^{56, 163}. Considering the possible impact of MGO on food quality and human health, controlling the amount of MGO in foods is of importance, and the scavenging of MGO by different agents in foods has been suggested as a potential strategy to prevent the formation of AGEs and their adverse effects^{60, 164, 165}.

To this end, previous studies have reported the reactions of MGO with a variety of compounds, of which amino acids, thiol compounds, and plant polyphenols, especially flavonoids, have been proven to be efficient scavengers for MGO^{59, 166}. For instance, MGO reacts with amino groups of lysine to form reversible hemiaminals and stable AGEs including N ϵ -(carboxyethyl)lysine (CEL) and methylglyoxal-lysine dimer (MOLD)¹⁶⁷, while the reaction with guanidine groups in arginine residues results in the irreversible formation of hydroimidazolones and argpyrimidines^{168, 169}. MGO can also react reversibly with the thiol group of N-acetylcysteine and glutathione (GSH) to form hemithioacetals⁴¹. Especially, the hemithioacetals formed by GSH and MGO can be further detoxified into D-lactate by glyoxalase enzymes in biological systems^{41, 148}. This GSH conjugation is a well-known phenomenon identified before as a primary endogenous detoxification mechanism for MGO¹²⁶. Compared to some free amino acids such as lysine, arginine, and histidine, which may react with MGO to produce AGEs, the addition of biological thiols in foods may be a reasonable choice to be used as the competitive target for MGO inhibiting the formation of AGEs. Lastly, natural polyphenols, especially flavonoids, have been regarded as efficient scavengers of MGO and suggested for MGO control in food systems such as milk and cookies, provided their solubility and background flavor would not hamper this use^{16, 20, 27, 58, 62}. Studies have shown that flavonoids such as quercetin and genistein can trap MGO by forming mono- and di-MGO adducts under physiological conditions^{60, 61}. Although the MGO scavenging capacity of flavonoids is extensively studied in in-vitro cell-free systems, the extent to which the resulting adduct formation is reversible and/or is preferred over a reaction with thiol compounds such

as GSH remains to be established. In addition, to what extent the scavenging effects of both GSH and flavonoids contribute to the detoxification of food-borne exogenous MGO is still unknown.

In the present study, a representative thiol compound GSH, and kaempferol, a typical flavonoid widely present in fruits and vegetables, were chosen as model compounds. The study aimed to characterize their MGO scavenging capacity in more detail with special emphasis on the possible reversible nature of the adduct formation and their potential competition for MGO, as well as the consequences of their MGO-scavenging effects both endogenously and in food for MGO-induced cytotoxicity. To this end, product formation in *in-vitro* incubations of MGO with GSH and/or kaempferol, and incubations of purified adducts formed were characterized in time using an LC-MS based method. Furthermore, the influence of MGO scavenging by GSH and kaempferol on MGO-induced cytotoxicity was evaluated, using the SH-SY5Y human neuroblastoma cells, representing neuronal cells known to be sensitive towards dicarbonyl stress and/or AGEs^{162, 170}.

3.2 Materials and methods

3.2.1 Chemicals and reagents

MGO (40% in water), L-glutathione reduced (GSH, $\geq 98\%$), L-glutathione oxidized (GSSG, $\geq 98\%$), 3-(4,5-dimethylthiazol-2-yl)-2,5-diphenyltetrazolium bromide (MTT, 98%), dimethyl sulfoxide (DMSO, $\geq 99\%$), ethanol ($\geq 99\%$), and acetic acid ($\geq 99\%$) were purchased from Merck (Darmstadt, Germany). Kaempferol ($> 99\%$) was purchased from MedChemExpress (Monmouth Junction, NJ, USA). Acetonitrile (LC-MS grade) and methanol (LC-MS grade) were purchased from Biosolve BV (Valkenswaard, The Netherlands). Formic acid ($\geq 99\%$) was obtained from VWR CHEMICA (Amsterdam, The Netherlands). Dulbecco's Modified Eagle Medium/Nutrient Mixture F-12 with GlutaMAX supplement cell culture medium (DMEM/F12 GlutaMAX), penicillin/streptomycin, phosphate buffered saline (PBS), Hanks' balanced salt solution (HBSS), trypsin-EDTA and nonessential amino acids (NEAA) were bought from Gibco (Paisley, UK). Foetal calf serum (FCS) was purchased from Bodinco (Alkmaar, The Netherlands). Ultrapure water was prepared by a Milli-Q system (Millipore, MA, USA).

3.2.2 Kinetic study of the reaction between GSH and kaempferol with MGO

Stock solutions of MGO, GSH, and GSSG were prepared (5 mM) in 100 mM sodium phosphate buffer (pH = 7.4), and a stock solution of kaempferol (5 mM) was prepared in DMSO. To a starting solution of GSH or kaempferol (final concentration of 0.25 mM) in 100 mM phosphate buffer (pH = 7.4, with 1.5% DMSO for each incubation) were added different volumes of MGO

stock solution to give a final concentration of 0.5, 1.25, or 2.5 mM (GSH or kaempferol, each with MGO in the molar ratios of scavenger : MGO of 1:2, 1:5, and 1:10). The resulting solutions were incubated at 37 °C in a water bath for 0, 1, 2, 4, 8, 24, and 48 h. At each time point, 100 μ L stop solution (ethanol containing 2% acetic acid) was added to the equal volume of collected samples to stop the reaction. Samples were immediately stored at -80 °C until analysis. LC-TOF-MS was applied for the analysis of kaempferol and its adducts with MGO as further described in **Section 3.2.5**, and LC-TQ-MS was used for the quantification of GSH, GSSG, and the GSH adduct with MGO as described in **Section 3.2.6**.

3.2.3 Reversibility of the MGO-kaempferol adducts

The purified monoMGO adduct of kaempferol was incubated (final concentration 5 μ M) in 100 mM phosphate buffer (pH = 7.4) at 37 °C in a water bath for 24h. After the same sampling step as applied in **Section 3.2.2**, the samples were stored at -80 °C until analysis for free kaempferol by LC-TQ-MS as described in **Section 3.2.6**.

3.2.4 Investigation of the competition between GSH and kaempferol for MGO adduct formation

To a starting solution of GSH and kaempferol (final concentration of 0.25 mM) in 100 mM phosphate buffer (pH = 7.4, with 1.5% DMSO in the incubation) was added MGO stock solution to a final concentration of 0.25 mM. The resulting solutions were incubated at 37 °C in a water bath for 0, 1, 2, 4, 8, 24, and 48 h. Samples were collected in the same way as described in **Section 3.2.2**, after which they were immediately stored at -80 °C until further analysis for kaempferol, GSH, GSSG, and the adducts formed between GSH and kaempferol with MGO by LC-TQ-MS as described in **Section 3.2.6**.

3.2.5 LC-TOF-MS analysis

An Agilent 1200 LC system coupled with a Bruker micro-TOF mass spectrometer was used to analyze kaempferol and its MGO conjugates in the incubation mixtures of kaempferol with MGO, which enabled the identification and quantification of the diverse kaempferol adducts with MGO. An Acquity UPLC BEH C18 (50 mm \times 2.1 mm, 1.7 μ m) column was employed during the experiment with a flow rate of 0.18 mL/min. The mobile phase was composed of A (ultrapure water with 0.1% formic acid) and B (acetonitrile with 0.1% formic acid) with the following gradient: 0–5 min, 100–65%A; 5–15 min, 65–40%A; 15–18 min, 40–20%A; 18–19 min, 20–100%A; 19–30 min, 100%A. Mass spectrometric analysis was performed in the negative electrospray ionization mode with mass spectra acquired from m/z 100 to 1500. The

instrument parameters were: capillary voltage, + 3200 V; nebulizing gas pressure, 2 bar; drying gas flow, 8 L/min and drying temperature, 200 °C.

3.2.6 LC-TQ-MS analysis

A Shimadzu Nexera XR LC-20AD XR UHPLC system coupled with a Shimadzu 8050 triple quadrupole mass spectrometer with electrospray ionization (ESI) interface was applied for the kinetic study of the reaction between GSH and MGO by quantification of GSH, GSSG, and the GSH-MGO adduct. The m/z ratio of the GSH-MGO adduct for the LC-TQ-MS method was obtained by LC-TOF-MS in our previous study³¹. LC-TQ-MS methods were also developed for the quantification of kaempferol and its reaction products with MGO based on the identification information obtained by LC-TOF-MS in the current study, which also enabled simultaneous quantification of GSH, kaempferol, and the reaction products in a co-incubation of GSH and kaempferol with MGO. Chromatographic separation was achieved using a Supelco Discovery HS F5-3 column (15 cm×2.1 mm, 3 µm). Ultrapure water containing 0.1% formic acid (A) and acetonitrile with 0.1% formic acid (B) were used as mobile phase at a flow rate of 0.25 mL/min. The following gradient was used: 0–2 min, 100%A; 2–5 min, 100–40%A; 5–11 min, 40%–5%A; 11–14 min, 5%A; 14–14.1 min, 5%–100%A; 14.1–24 min, 100%A. The instrument parameters were as follows: nebulizing gas flow, 3.0 L/min; drying gas flow and heating gas flow, 10.0 L/min; interface temperature, 300 °C; and heat block temperature, 400 °C. Multiple-reaction monitoring (MRM) and selected-ion monitoring (SIM) modes with ionization polarity switching were utilized for the simultaneous determination of GSH, kaempferol, and the reaction products. The optimized acquisition parameters for these compounds are summarized in **Table S3.1 (Supporting information)**.

3.2.7 Cell culture

The SH-SY5Y (ATCC CRL-2266) human neuroblastoma cell line was purchased from the American Type Culture Collection (ATCC, Manassas, VA, USA). The cells were cultured in DMEM/F12 GlutaMAX medium containing 10% FCS, 1% NEAA, and 1% penicillin/streptomycin in a humidified incubator at 5% CO₂ at 37 °C. Cells were subcultivated at a ratio of 1:20 upon confluency, using 0.05% trypsin-EDTA solution. The medium was changed every 4 to 7 days.

3.2.8 Cell viability assay

To study the consequences of MGO scavenging by GSH and kaempferol for the toxicity of MGO, two types of experiments were performed. First, concentration-response curves were made for the cytotoxicity of MGO preincubation without or with a fixed concentration (0.25 mM) of GSH or kaempferol. Second, a fixed concentration (2 mM) of MGO was mixed with increasing

concentrations of GSH (0.05-0.25 mM, final concentration) or kaempferol (0.05-0.25 mM, final concentration) either with or without subsequent pre-incubation after which cytotoxicity was quantified.

Pre-incubations were performed for 48 h at 37 °C in a cell-free HBSS system before exposure. The cell viability assay was performed using the MTT method. Briefly, SH-SY5Y cells (1.5×10^4 cells/well) were seeded into 96-well plates (Greiner Bio-one) and incubated for 24 h. The culture medium was then replaced by the pre-incubated or non-preincubated solutions described above which were further supplemented with 10% FCS. After 24 h exposure, the cells were carefully washed with HBSS and incubated for 3 h in fresh HBSS containing 10% FCS and 0.5 mg/mL MTT. Subsequently, the produced formazan crystals were dissolved in 100 μ L DMSO, after which the absorbance at 562 nm and at a reference wavelength of 620 nm was measured using a plate spectrophotometer (Molecular Devices, San Jose, CA, USA, Spectra Max M2). Corrected absorbance values were calculated by subtracting the values at 620 nm from the corresponding values at 562 nm. The cell viability was further expressed as a percentage relative to solvent control set at 100%.

3.2.9 Statistical analysis

Data are expressed as mean \pm standard error of the mean (SEM) from at least three independent experiments. Statistical analyses and visualization of the results were conducted using GraphPad Prism 9 software (San Diego, CA, USA). EC50 values were determined by non-linear regression analysis, and statistical differences between the EC50 values were analyzed using student's *t*-tests. A two-way ANOVA was employed to assess the cytotoxic effects induced by exposure to different concentrations of MGO, under pre-incubation conditions without or with a fixed amount of GSH or kaempferol, and their interactions. A Dunnett's post hoc test was performed to compare the differences between the experimental groups and the control group (MGO pre-incubated alone group). Additionally, the effects of pre-incubation and non-preincubation of a fixed amount of MGO with increasing concentrations of GSH or kaempferol on the cytotoxicity of MGO were assessed using a two-way ANOVA, followed by a Tukey post hoc test for pairwise comparisons between any two groups. Results with *p*-values less than 0.05 were considered statistically significant.

3.3 Results

3.3.1 Characterization of reaction products between kaempferol and MGO by LC-TOF-MS

Our previous study already confirmed that a GSH-MGO adduct is formed upon incubation of GSH and MGO in phosphate buffer³¹. In the current study, we qualitatively analyzed the

reaction products between kaempferol and MGO by LC-TOF-MS. Nine major reaction products were detected after incubation of kaempferol (0.25 mM) with MGO (2.5 mM) for 48 hours. The identification information for kaempferol and its MGO adducts is summarized in **Table S3.2**, and typical extracted ion chromatograms are shown in **Figure S3.1 (Supporting information)**. The peak at 12.0 min (**Figure S3.1B**) had the molecular ion m/z 357.1 $[M - H]^-$, which was 72 mass units higher than the molecular ion of kaempferol m/z 285.1 $[M - H]^-$, indicating this peak represented a mono-MGO conjugated kaempferol (denoted as kaem-monoMGO). The peaks at 11.1, 11.5, and 12.1 min (**Figure S3.1C**) had identical molecular ions of m/z 429.1 $[M - H]^-$ with 72 mass units higher than the m/z of the kaem-monoMGO adduct (m/z 357.1 $[M - H]^-$) indicating that they were isomers of diMGO adducts of kaempferol (denoted as kaem-diMGOa, kaem-diMGOb, and kaem-diMGOc), with kaem-diMGOa being the dominant isomer. The molecular ions of the peaks at 12.0, 13.0, and 14.0 min (m/z 355.1 $[M - H]^-$, **Figure S3.1D**) were 2 mass units lower than that of the kaem-monoMGO (m/z 357.1 $[M - H]^-$), indicating a possible loss of two protons after the formation of kaem-monoMGO, and thus these peaks were proposed as the isomers of oxidized kaem-monoMGO (denoted as oxidized kaem-monoMGOa, oxidized kaem-monoMGOb, and oxidized kaem-monoMGOc). Similarly, the peaks at 11.5 and 12.0 min (**Figure S3.1E**) had molecular ions of m/z 427.1 $[M - H]^-$ with 2 mass units lower than the m/z of diMGO adduct of kaempferol (m/z 429.1 $[M - H]^-$), suggesting the loss of two protons after the conjugation of two molecules of MGO to kaempferol (denoted as oxidized kaem-diMGOa and oxidized kaem-diMGOb).

3.3.2 Kinetic study of the reaction between GSH and kaempferol with MGO

The kinetics of the scavenging effects of GSH on MGO were evaluated under three molar ratios of GSH : MGO (1:2, 1:5, and 1:10) keeping the concentration of GSH constant. LC-TQ-MS was applied for the targeted determination of GSH, GSSG, and the GSH-MGO adduct. **Figure 3.1** shows the time-dependent changes in the contents of GSH, GSSG, and the GSH-MGO adduct during the incubation of GSH with MGO for 48 h. The concentrations of GSH and GSSG were determined via calibration curves using their commercially available reference compounds, while the amount of GSH-MGO adduct was expressed as peak area due to a lack of reference compounds. As shown in **Figure 3.1A**, an average of 19.4% (0.05 mM), 26.0% (0.07 mM), and 34.7% (0.09 mM) loss of GSH occurred immediately at the start of incubation at the molar ratios of GSH : MGO of 1:2, 1:5, and 1:10, respectively. A further continuous decrease in GSH levels accompanied by an increase in GSSG content during the subsequent 48 h was observed likely mainly due to the autooxidation of GSH to GSSG (**Figure 3.1A and B**). The content of GSH-MGO adducts detected in the samples showed a slight tendency to increase in the first few hours followed by a decrease, the latter potentially related to the reversible nature of the adduct formation combined with the autooxidation of GSH (**Figure 3.1C**). The amount of GSH-

MGO adduct detected at the start of the incubations appeared to vary depending on the amount of MGO added, indicating the adduct formation to be instantaneous on the time scale used.

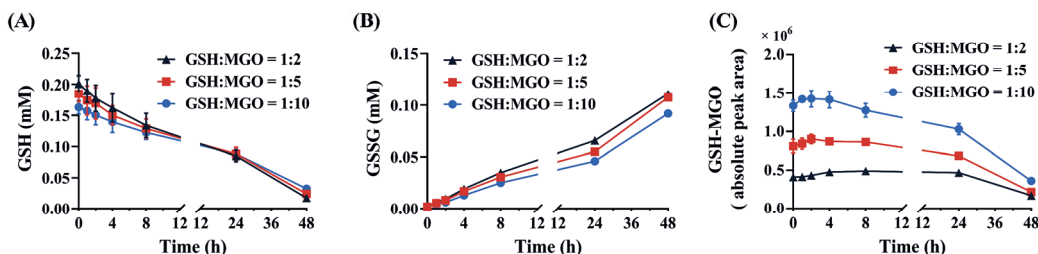


Figure 3.1. Time-dependent changes in the contents of GSH (A), GSSG (B), and GSH-MGO adduct (C) during incubation of GSH (0.25 mM) with MGO (0.5, 1.25, or 2.5 mM) at three different molar ratios of 1:2, 1:5, and 1:10 in 100 mM sodium phosphate buffer (pH=7.4) at 37 °C. The contents for GSH and GSSG were expressed as molar concentrations, while the content for GSH-MGO was expressed as absolute peak area. Data are presented as the means \pm SEM of three replications.

The kinetics of MGO scavenging by kaempferol were evaluated under the same incubation conditions as what was used for the incubations of GSH with MGO. Due to the more diverse formation of the reaction products between kaempferol with MGO compared to what was formed during incubation of GSH with MGO, LC-TOF-MS in full-scan acquisition mode was used for the analysis of the samples which enabled the comprehensive detection and quantification of the different reaction products. Kaempferol was quantified using its reference compound, and its reaction products were quantified using kaempferol as the reference in extracted ion mode. Using this approach the total mass recoveries for kaempferol and its reaction products ranged from 91.2% to 107.6%. As shown in **Figure 3.2**, the concentration of kaempferol decreased with increasing reaction time, with 47.7%, 24.1%, and 6.9% of kaempferol remaining after 48 h of incubation at the molar ratios of kaempferol : MGO of 1:2, 1:5, and 1:10, respectively. The content of kaem-monoMGO increased rapidly with incubation time in the first eight hours at all three ratios, and a slight decrease was observed after 24 h for the ratios of 1:5 and 1:10. The levels of the diMGO adducts of kaempferol increased with increasing incubation time during the 48 h of incubation, with kaem-diMGOa being the most abundant. Besides, the oxidized reaction products were also found to be slowly formed during the entire incubation period. At the start of the incubations kaempferol appeared to be present in its unmodified form.

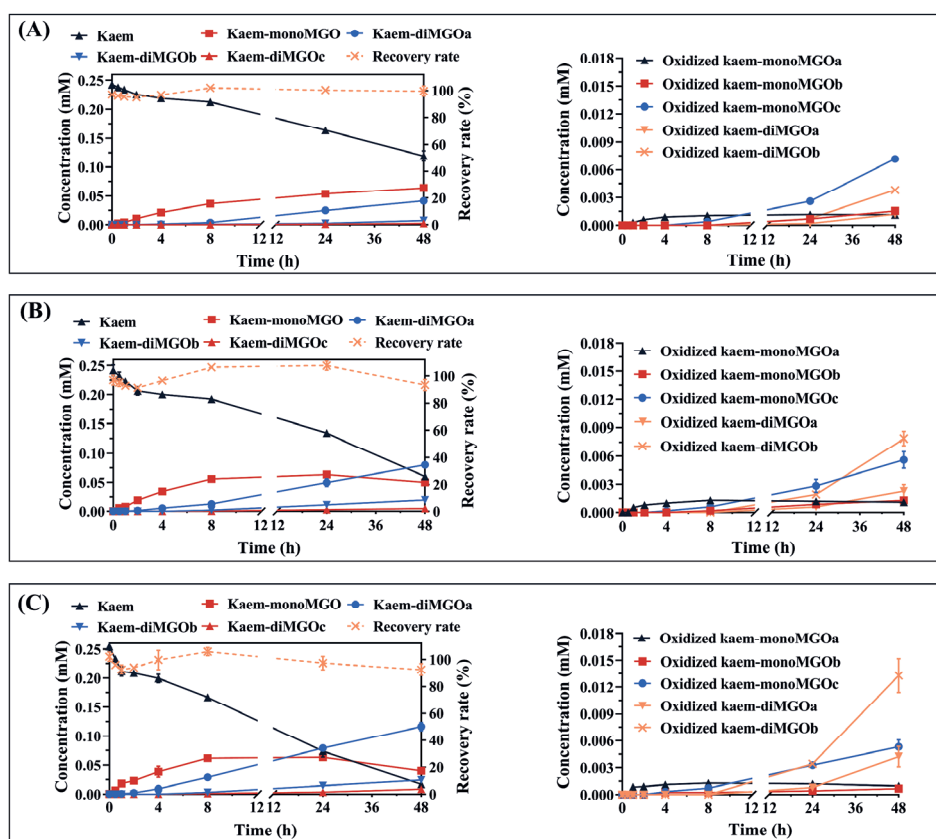


Figure 3.2. Time dependent changes in the concentrations of kaempferol (kaem), its reduced reaction products (left graph), and oxidized reaction products (right graph) after incubation of kaempferol (0.25 mM) with MGO (0.5, 1.25, or 2.5 mM) at three different molar ratios of 1:2 (A), 1:5 (B), and 1:10 (C) in 100 mM sodium phosphate buffer (pH=7.4) at 37 °C. Data are presented as mean \pm SEM of three replications.

3.3.3 Reversibility of MGO adducts of kaempferol

A previous study has reported the reversibility of the adduct formation between GSH with MGO¹⁷¹. In this section of the study, we evaluated the reversibility of the adducts formed between kaempferol with MGO by incubation of kaem-monoMGO which was isolated and purified by preparative LC. The incubation mixtures were analyzed by LC-TQ-MS by monitoring the changes in the peak areas of kaem-monoMGO, its potential oxidized products, and kaempferol in SIM mode. Incubation of kaem-monoMGO for 24 h resulted in a decrease in its content by 22.3%, while significant increases in the isomer of kaem-monoMGO and oxidized products were observed (**Figures 3.3A and B**). In addition, the amount of kaempferol remained at < 0.8 % and no significant change in its content was found during and after 24 h incubation. This result indicates that the monoMGO adduct formation of kaempferol was not reversible

and that the reduction in the monoMGO adduct after 24 h is likely due to its oxidation and the formation of the isomer.

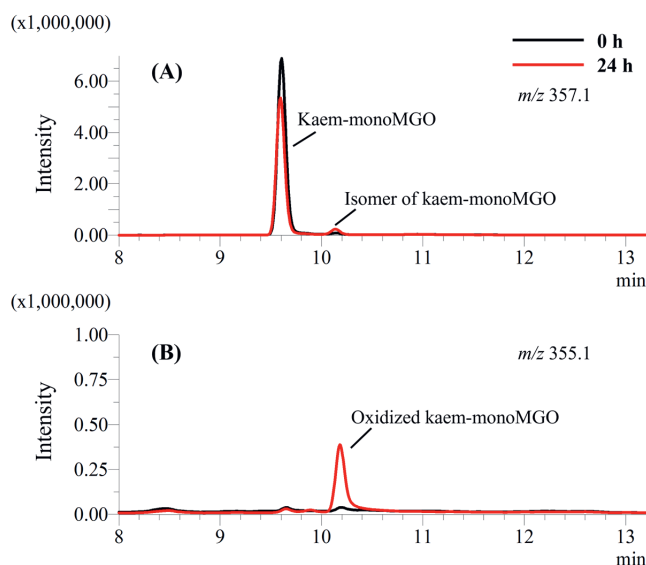


Figure 3.3. Typical LC-TQ-MS extracted ion chromatograms of kaempferol-monoMGO (A) and oxidized kaempferol-monoMGO (B) after incubation of kaempferol-monoMGO in 100 mM sodium phosphate buffer (pH=7.4) at 37 °C for 0 and 24 h.

3.3.4 Competition between GSH and kaempferol for MGO adduct formation

GSH and kaempferol were co-incubated with MGO to study the potential competition between GSH and kaempferol for MGO. **Figure 3.4** shows the changes in the contents of the GSH-MGO adduct and kaem-monoMGO (the main MGO adduct of kaempferol under this incubation condition) upon incubation of GSH and kaempferol with MGO for 48 hours. Instantaneous formation of the GSH-MGO adduct at the start was observed. The content of the GSH-MGO adduct started to decrease after 8 h incubation, with 16.2% of the GSH-MGO adduct remaining after 48 h relative to the starting point. However, the kaempferol-monoMGO adduct showed a constant increase in its concentration. The changes in the concentrations of GSH, GSSG, and kaempferol in this incubation of GSH and kaempferol with MGO can be found in **Figure S3.2**. The GSH levels reduced by 17.9% at the start followed by a rapid decrease (**Figure. S3.2A**). The reductions in GSH levels during the subsequent 48 h of the incubations were mainly due to the formation of GSSG from GSH (**Figure S3.2B**). **Figure S3.2C** shows that the concentration of kaempferol decreased gradually with increasing incubation time, with a 16.3% decrease in kaempferol concentration after 48 h. The results show that kaempferol still exhibited time-dependent scavenging effects towards MGO in a co-incubation with GSH and MGO, and it can be expected that the remaining MGO would continually be

scavenged by kaempferol over time, whereas the GSH-MGO would eventually be fully deconjugated with the resulting MGO being scavenged by kaempferol. As a result, in incubations of MGO with both GSH and kaempferol the adducts of MGO with kaempferol would become the preferred adducts over time due to their irreversible nature.

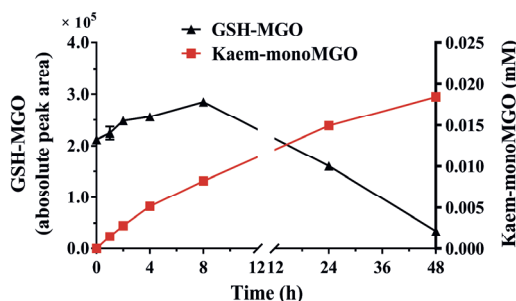


Figure 3.4. Changes in the contents of GSH-MGO adduct and kaem-monoMGO after incubation of GSH (0.25 mM) and kaempferol (0.25 mM) with MGO (0.25 mM) in 100 mM sodium phosphate buffer (pH=7.4) at 37 °C for 48 h. The content of GSH-MGO was expressed as absolute peak area, and the content for kaem-monoMGO was expressed as molar concentration. Data are presented as mean ± SEM of three replications.

3.3.5 Influence of MGO scavenging by GSH and kaempferol on the cytotoxicity of MGO in SH-SY5Y cells

The effects of different concentrations of GSH (0.05-0.25 mM) and kaempferol (0.05-0.25 mM) on the cell viability of SH-SY5Y cells were evaluated by the MTT assay. **Figure S3.3** shows that GSH and kaempferol at all concentrations tested up to 0.25 mM did not affect the cell viability of SH-SY5Y cells. To assess the effects of the scavenging of MGO by GSH and kaempferol on the MGO-induced cytotoxicity, MGO at different concentrations was pre-incubated in the absence and presence of 0.25 mM GSH or kaempferol for 48 h before exposure of cells to the resulting incubation mixtures. The difference in cell viability between the exposed groups is shown in **Figure 3.5**. Two-way ANOVA analysis of this data confirmed a significant effect of treatment ($p < 0.001$), concentration ($p < 0.001$), and their interaction ($p < 0.001$). Post hoc analysis using Dunnett's test revealed that pre-incubation of MGO with GSH and kaempferol both resulted in protection against MGO-induced cytotoxicity, with cell viability being statistically significantly higher upon preincubation of MGO with both scavengers than what was observed for MGO alone. Pre-incubation of MGO with GSH or kaempferol resulted in a statistically significant ($p < 0.01$) increase in the EC₅₀ values (1.68 and 2.05 mM, respectively) compared to the EC₅₀ of MGO pre-incubated alone (1.37 mM). In addition, the mean EC₅₀ value of MGO pre-incubated with 0.25 mM kaempferol was significantly higher than the EC₅₀

value of MGO pre-incubated with 0.25 mM GSH ($p < 0.05$), indicating kaempferol to be a better scavenger under the conditions employed.

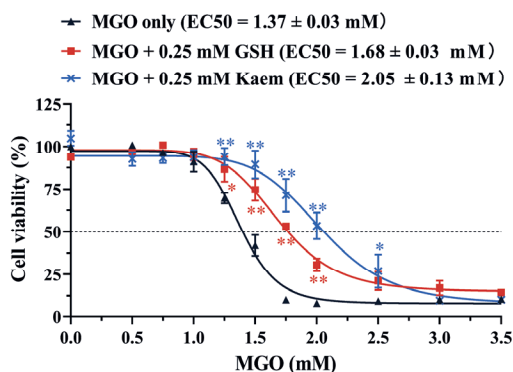


Figure 3.5. Effects of pre-incubation of MGO with GSH or kaempferol on the reduction of cell viability induced by increasing concentrations of MGO in SH-SY5Y cells as assessed by MTT assay. Data are presented as mean \pm SEM of at least four replications. * $p < 0.05$ and ** $p < 0.01$ compared with the MGO pre-incubated alone group.

The consequences of scavenging of MGO by GSH or kaempferol for MGO-induced cytotoxicity were further investigated. As shown in **Figure 3.6A**, protection against MGO-induced cytotoxicity by GSH appeared independent of preincubation. Testing with or without pre-incubation did not significantly influence the protective effects of GSH against MGO-induced reduction in cell viability. In contrast, **Figure 3.6B** shows that without pre-incubation kaempferol did not significantly influence the MGO-induced effects on cell viability, while the viability was significantly increased after 48 h pre-incubation of MGO with kaempferol at concentrations ≥ 0.15 mM. Thus, these results corroborate, in line with what was observed in the cell-free indications, that scavenging of MGO by kaempferol is, unlike the scavenging by GSH, not instantaneous, and requires some preincubation to display the protective effect whereas, in line with the instantaneous nature of its reaction with MGO, scavenging by GSH was protective without a need for preincubation.

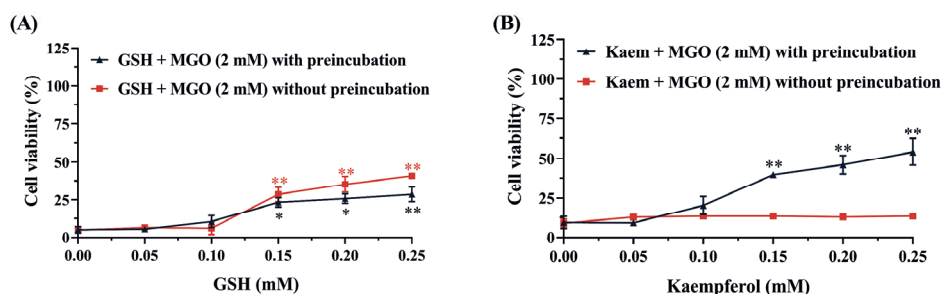


Figure 3.6. Comparison of the effects of pre-incubation and non-preincubation of MGO (2 mM) with increasing concentrations of GSH (A) or kaempferol (B) on the decrease of cell viability induced by MGO in SH-SY5Y cells as assessed by MTT assay. Data are all presented as mean \pm SEM of at least three replications. * $p < 0.05$ and ** $p < 0.01$ compared with the MGO-only group.

3.4. Discussion

The present study compared the MGO scavenging behavior of a representative thiol compound (GSH) and a typical dietary flavonoid (kaempferol) in more detail with special emphasis on the reversible nature of the adducts formed and the resulting potential for protection against MGO-induced cytotoxicity. The scavenging of MGO by GSH to form GSH-MGO hemithioacetals is a well-known phenomenon that occurs spontaneously and immediately and is known to be reversible leading to an equilibrium^{65, 171}. The kinetic results in this study also indicate that an increase in the proportion of MGO relative to GSH (GSH : MGO = 1:2, 1:5, and 1:10) shifted the equilibrium towards the GSH-MGO adduct formation. In contrast, kaempferol presented a different scavenging behavior towards MGO. Results obtained show that kaempferol can form various adducts with MGO, including mono- and di-MGO adducts in both reduced and oxidized forms. The structures of reduced mono- and di-MGO adducts of various flavonoids have been previously reported^{60, 61, 172}. The C6 and C8 positions of the A ring in the flavonoids are identified as the trapping sites of MGO⁶¹. In a study of the reaction between naringenin and MGO, C8 was reported to be the site with the highest reactivity due to its highest electron density among all the carbon atoms, and the mono-MGO adduct can be formed by reacting with one molecule of MGO at the C8 position followed by the formation of the di-MGO adduct by reacting at C6 with a second molecule of MGO²⁷. The MGO adducts of flavonoids were found to exist in several isomeric forms. For example, Liu et al.¹⁷³ observed two isomers of the mono-MGO adduct and four isomers of the di-MGO adduct of quercetin by LC-MS/MS. A study by Zhu et al.¹⁶ detected two mono-MGO adducts and one di-MGO adduct of kaempferol by LC-MS/MS, while one mono-MGO adduct and three di-MGO adducts of kaempferol were detected by LC-TOF-MS in the present study. The differences between these studies could be due to the different chromatographic conditions leading to

different resolutions for separating the isomers. Besides, some isomers may be present in the solution at a concentration that is below the detection limit. This would also explain the detection of the other isomer of kaem-monoMGO when LC-TQ-MS, which is more sensitive than LC-TOF-MS, was applied for the detection of the reversibility of kaem-monoMGO. With respect to the oxidized MGO adducts of the flavonoids, studies on their structures are still limited. A recent study identified the structures of several oxidized di-MGO adducts of rutin¹⁷⁴. The oxidation was reported to occur at the hydroxy group in the MGO moiety after the formation of the di-MGO adduct of rutin¹⁷⁴. Besides, a study investigating the quercetin-MGO adducts in a lysine/glucose aqueous system, suggested that the oxidation of the adducts may occur at the hydroxy group of quercetin to form mono- and di-MGO adducts of quercetin quinone, while the exact oxidation sites on the quercetin moiety remained unknown¹⁷³. For oxidized MGO adducts of kaempferol, the oxidation in the kaempferol moiety may also be possible due to the presence of the hydroxyl moieties at the C3, C4'-position which are sensitive sites to oxidation¹⁷⁵. Based on the above, the proposed structures of the MGO adducts of kaempferol detected in this study are shown in **Figure. S3.4**. The kinetic results obtained show that the MGO-scavenging effect of kaempferol is time-dependent, and an increase in the MGO proportion in the cell-free incubations of MGO with kaempferol (kaempferol : MGO = 1:2, 1:5, and 1:10) resulted in a more rapid loss of kaempferol during 48 h with an increasing relative concentration of MGO.

A previous study quantified the apparent second order rate constants for the reaction between four selected polyphenols (including kaempferol) and MGO¹⁶. The apparent second order rate constant for the reaction of MGO with kaempferol amounted to $6.3 \times 10^{-2} \text{ M}^{-1}\text{s}^{-1}$. The second order rate constant for the reaction of MGO with N-acetylcysteine as a thiol scavenger was reported to amount to $4.1 \times 10^4 \text{ M}^{-1}\text{s}^{-1}$ ⁴¹. These data corroborate that the initial scavenging of MGO by a thiol reagent like N-acetylcysteine or GSH will be highly favored over that by kaempferol. However, the reversible nature of the thiol adduct formation with a reverse first order rate constant of $7.5 \times 10^{-3} \text{ s}^{-1}$ ⁴¹ explains why in the longer term the irreversible scavenging by kaempferol dominates over scavenging by GSH. These kinetic constants are in line with the observed adduct formation and competition between kaempferol and GSH in the present study.

We further evaluated and compared the consequences of the MGO-scavenging effects of GSH and kaempferol for the cytotoxicity of MGO. Pre-incubation of MGO with kaempferol for 48 h resulted in a higher protection against MGO-induced cytotoxicity than its pre-incubation with GSH. The results also show that pre-incubation is not needed for GSH to display protective effects due to its instantaneous reaction with MGO. In contrast, the protective effects of kaempferol against MGO-induced cytotoxicity were shown to be dependent on a pre-

incubation time, which can be ascribed to the substantially lower second order rate constant ($6.3 \times 10^{-2} \text{ M}^{-1}\text{s}^{-1}$) for its reaction with MGO¹⁶ combined with the irreversible nature of the adduct formed as shown in the present study. It is of interest to note that a previous study evaluated the toxicity of oxidized MGO rutin adducts (oxidation at the MGO moiety) in comparison with rutin and MGO and suggested that the formation of these oxidized adducts significantly decreased the MGO-induced cytotoxicity in several cell types¹⁷⁴. In contrast to this and also to our study results, another study reported that the mono-MGO and di-MGO adducts of quercetin were found to have higher cytotoxic effects than MGO itself¹⁷⁶. To what extent these differences are due to the biological effects of different types of adducts, the different flavonoids, or different experimental conditions used needs further investigation. In addition, it is of interest to note that some studies have reported that the protective effects of several polyphenols against MGO-induced toxicity are correlated to their activation of Nrf2-mediated protective gene expression^{71, 177, 178}. However, this may be related to a mode of action where pre-treatment of cells with these compounds for a few hours to a day results in an increase in intracellular GSH levels via the activation of the Nrf2-mediated pathway prior to MGO exposure, as intracellular GSH plays an essential role in the detoxification of MGO³¹.

Given that intracellular levels of GSH are generally high and in the mM range¹⁷⁹, while physiological levels of flavonoids are generally in the low μM range^{180, 181}, it may be concluded that for protection against endogenous MGO, GSH will be more relevant. However, the results of the present study reveal that for scavenging food-borne MGO use of kaempferol and other flavonoids would be preferred over the use of GSH and other thiol-based scavengers, as the GSH adduct would eventually lose the adduct formation with MGO in a competition reaction with kaempferol. Our study reveals that the scavenging of MGO by kaempferol is not reversible and that the MGO scavenging mediated by kaempferol would lead to the detoxification of MGO, while the protective effects of GSH against MGO-induced cytotoxicity via extracellular MGO scavenging were less substantial. This conclusion would also hold when considering scavenging food-borne MGO. When considering scavenging of intracellular MGO however, GSH would be more efficient than kaempferol, not only because of its higher intracellular concentrations but also because of the fact that within the cell the reversibility of the adduct formation will be less problematic given that the GSH-MGO adducts are further detoxified by the glyoxalase system¹⁴⁸. Thus, taking all together it is concluded that for scavenging food-borne MGO kaempferol would be preferred over thiol scavengers, while for endogenous protection against MGO, the role of scavenging by GSH will be dominant.

Acknowledgments

Liang Zheng is grateful for the financial support from the China Scholarship Council. Grant Number: 202008510115.

Supporting information

Table S3.1. LC-TQ-MS acquisition parameters.

Compounds	Scan mode (Polarity)	Precursor ion (<i>m/z</i>)	Product ion (<i>m/z</i>)	Collision energy (V)
GSH	MRM (+)	308.0	179.1	-13
GSSG	MRM (–)	611.1	306.0, 143.1	24, 48
GSH-MGO adduct	MRM (+)	380.2	308.3, 162.0	-13, -26
Kaempferol (Kaem)	SIM (–)	285.1	/	/
	MRM (–)	285.1	257.2, 239.1	19, 27
Kaem-monoMGO	SIM (–)	357.1	/	/
	MRM (–)	357.1	285.1, 205.0, 151.0	35, 35, 35
Kaem-diMGO	SIM (–)	429.1	/	/
	MRM (–)	429.1	357.1, 295.0, 285.1	35, 35, 35
Oxidized kaem-monoMGO	SIM (–)	355.1	/	/
Oxidized kaem-diMGO	SIM (–)	427.1	/	/

Table S3.2. LC-TOF-MS identification of kaempferol and its reaction products with MGO.

Category	Compounds	Precursor ion (<i>m/z</i>)	Retention time (min)
Parent compound	Kaempferol (Kaem)	285.1	13.6
Reduced products	Kaem-monoMGO	357.1	12.0
	Kaem-diMGOa	429.1	11.1
	Kaem-diMGOb	429.1	11.5
	Kaem-diMGOc	429.1	12.1
	Oxidized kaem-monoMGOa	355.1	12.0
Oxidized products	Oxidized kaem-monoMGOb	355.1	13.0
	Oxidized kaem-monoMGOc	355.1	14.0
	Oxidized kaem-diMGOa	427.1	11.5
	Oxidized kaem-diMGOb	427.1	12.0
	Oxidized kaem-diMGOb	427.1	12.0

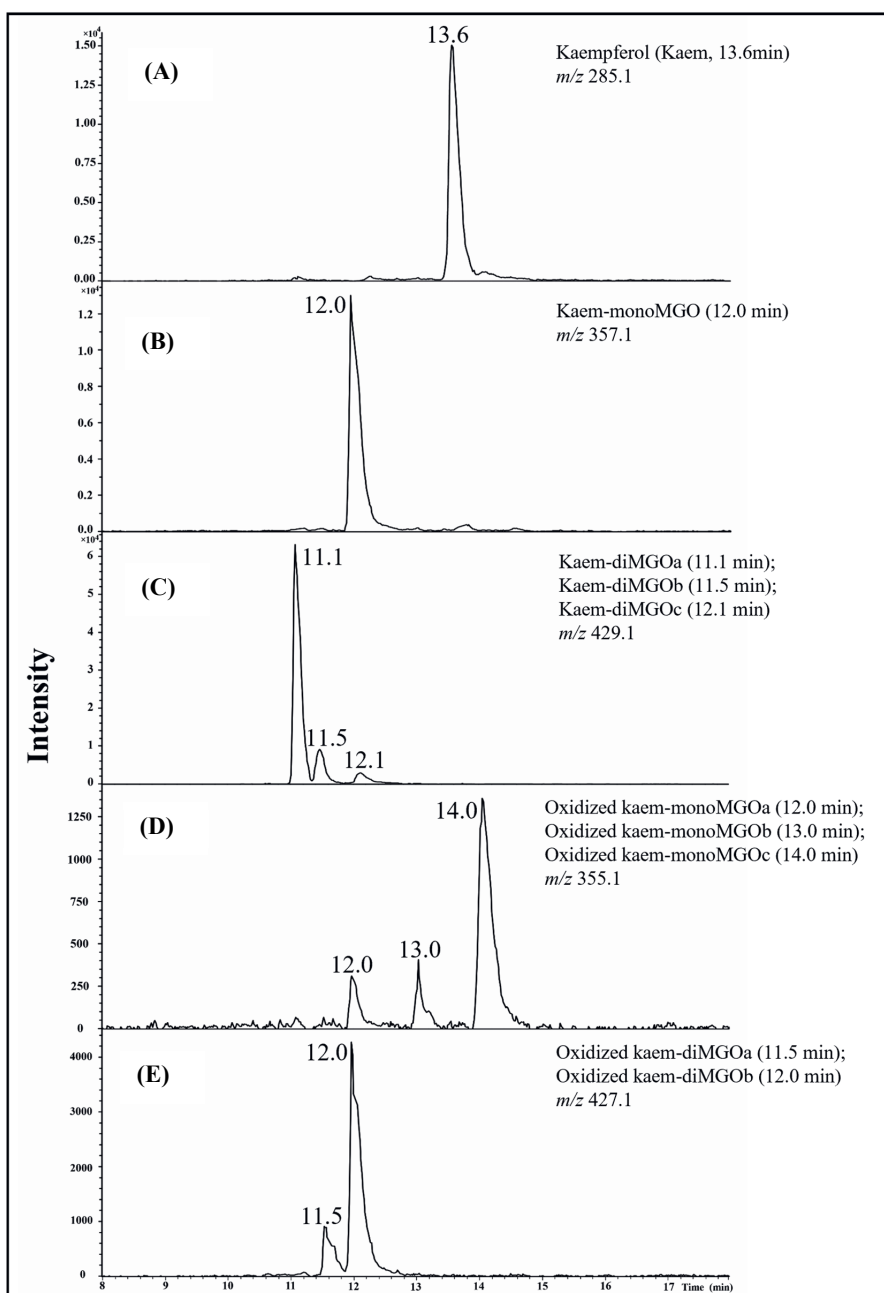


Figure. S3.1. Typical LC-TOF-MS extracted ion chromatograms of incubations of kaempferol (0.25 mM) with MGO (2.5 mM) for 48 h: (A) kaempferol (kaem, m/z = 285.1); (B) kaem-monoMGO (m/z = 357.1); (C) kaem-diMGOa, kaem-diMGOb; and kaem-diMGOb (m/z = 429.1); (D) oxidized kaem-monoMGOa, oxidized kaem-monoMGOb, and oxidized kaem-monoMGOb (m/z = 355.1); (E) oxidized kaem-diMGOa and oxidized kaem-diMGOb (m/z = 427.1).

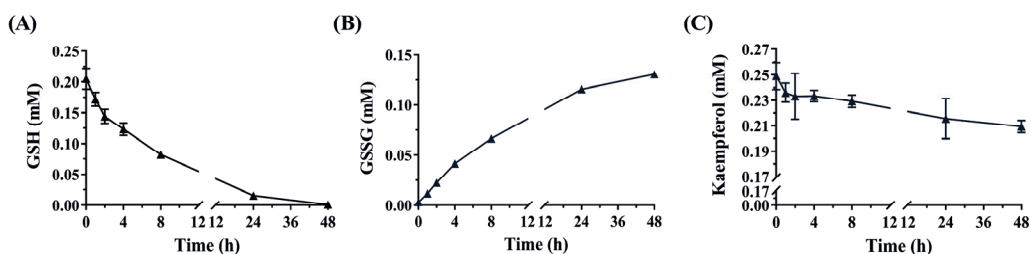


Figure S3.2. Changes in the contents of GSH (A), GSSG (B), and kaempferol (C) after incubation of GSH (0.25 mM) and kaempferol (0.25 mM) with MGO (0.25 mM) in 100 mM sodium phosphate buffer (pH=7.4) at 37 °C for 48 h. Data are presented as mean \pm SEM of three replications.

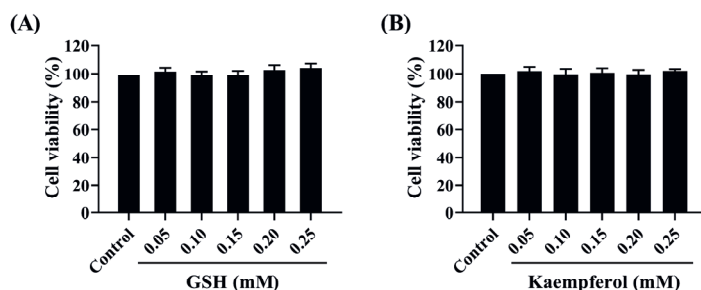
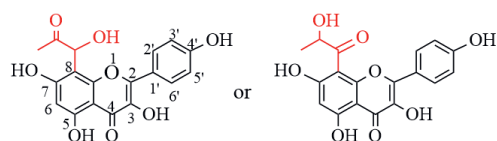
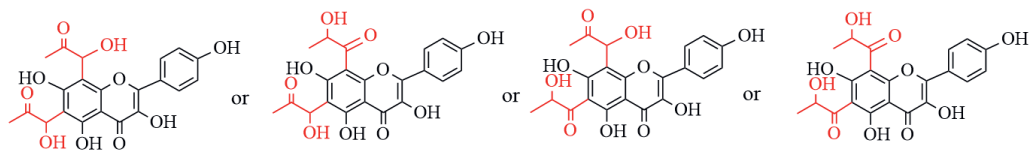


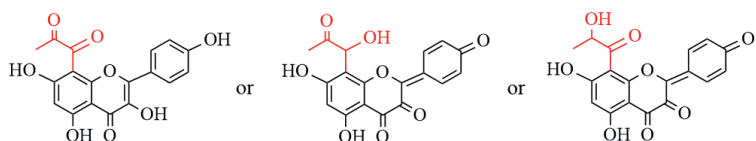
Figure S3.3. Effects of GSH (A) and kaempferol (B) on the cell viability of SH-SY5Y cells. The results were calculated relative to solvent control and are presented as mean \pm SEM of three replications.



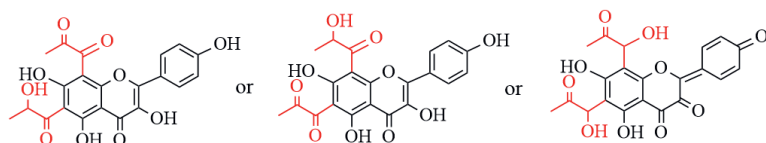
Kaem-monoMGO



Kaem-diMGO



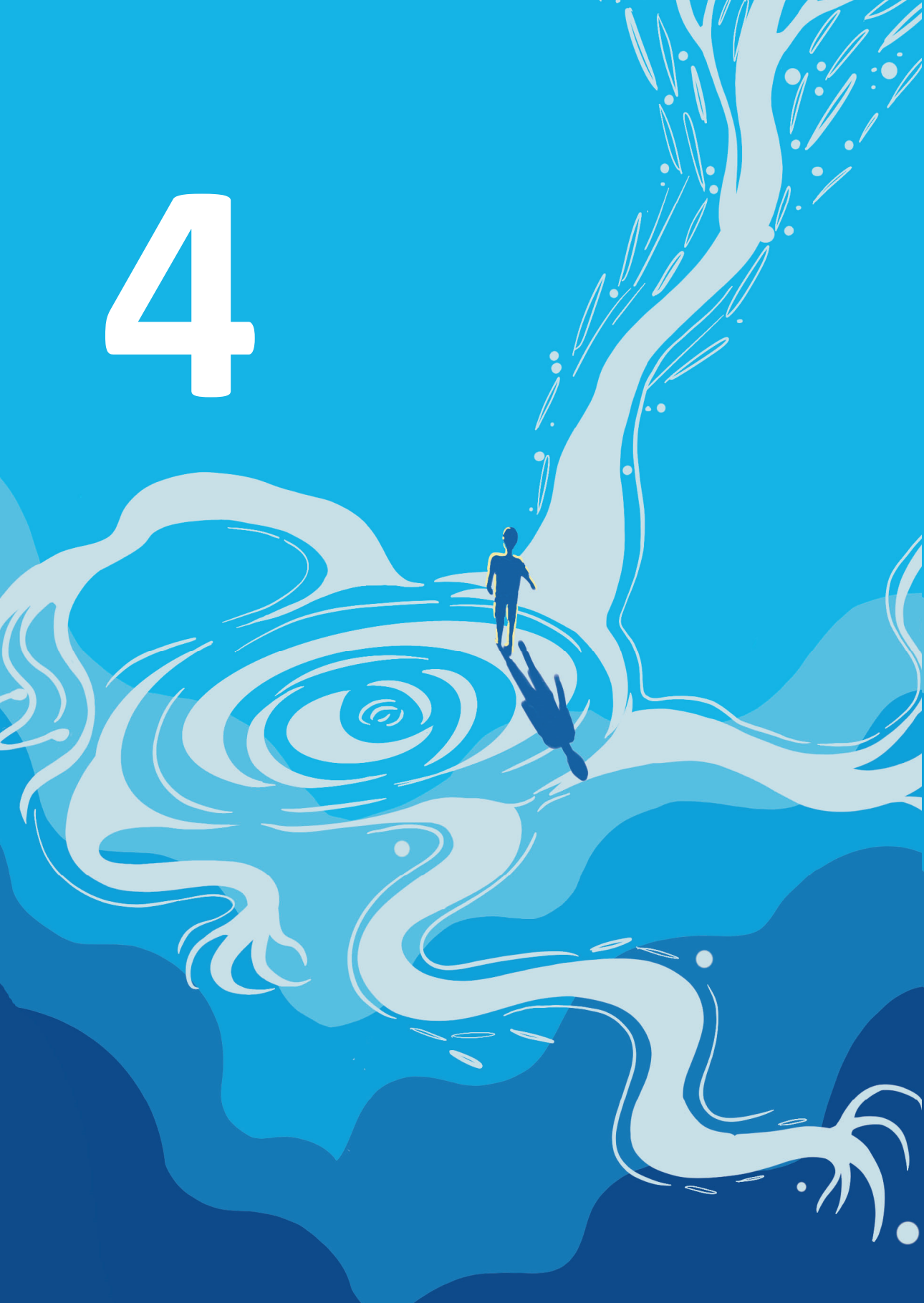
Oxidized kaem-monoMGO



Oxidized kaem-diMGO

Figure. S3.4. Proposed structures of MGO adducts of kaempferol. Other isomeric forms for oxidized kaem-diMGO are also possible.

4



Chapter 4

Proteomics-based Identification of Biomarkers Reflecting Endogenous and Exogenous Exposure to the Advanced Glycation End Product Precursor Methylglyoxal in SH-SY5Y Human Neuroblastoma Cells

This chapter is based on:

Liang Zheng, Sjeff Boeren, Chen Liu, Wouter Bakker, Haomiao Wang, Ivonne M. C. M. Rietjens, Edoardo Saccenti. Proteomics-based identification of biomarkers reflecting endogenous and exogenous exposure to the advanced glycation end product precursor methylglyoxal in SH-SY5Y human neuroblastoma cells.

Published in: International Journal of Biological Macromolecules. 2024 Jun 3:132859.

DOI: 10.1016/j.ijbiomac.2024.132859

Abstract

Methylglyoxal (MGO), a highly reactive precursor of advanced glycation end products, is endogenously produced and prevalent in various food products. This study aimed to characterize protein modifications in SH-SY5Y human neuroblastoma cells induced by MGO and identify potential biomarkers for its exposure and toxicity. A shot-gun proteomic analysis was applied to characterize protein modifications in cells incubated with and without exogenous MGO. Seventy-seven proteins were identified as highly susceptible to MGO modification, among which eight, including vimentin and histone H2B type 2-F, showing concentration-dependent modifications by externally added MGO, were defined as biomarkers for exogenous MGO exposure. Remarkably, up to 10 modification sites were identified on vimentin. Myosin light polypeptide 6 emerged as a biomarker for MGO toxicity, with modifications exclusively observed under cytotoxic MGO levels. Additionally, proteins like serine/threonine-protein kinase SIK2 and calcyphosin, exhibiting comparable or even higher modification levels in control compared to exogenous MGO-treated cells, were defined as biomarkers for endogenous exposure. Bioinformatics analysis revealed that motor proteins, cytoskeleton components, and glycolysis proteins were overrepresented among those highly susceptible to MGO modification. These results identify biomarkers for both endogenous and exogenous MGO exposure and provide insights into the cellular effects of endogenously formed versus externally added MGO.

Keywords: advanced glycation end products; methylglyoxal; neurotoxicity; protein modification; peptide adduct

4.1 Introduction

Advanced glycation end products (AGEs) have received increasing attention over the past years due to growing evidence suggesting their involvement in the pathogenesis of diabetes, kidney diseases, and various age-related diseases including Alzheimer's disease and Parkinson's disease^{6, 182, 183}. AGEs represent a heterogeneous group of compounds that are formed during the non-enzymatic processes initiated by a reaction between the carbonyl groups of reducing sugars or reactive aldehydes and the nucleophilic groups of proteins, lipids, or nucleic acids¹⁸⁴. Methylglyoxal (MGO), an α -oxoaldehyde, is a highly reactive AGE precursor that is generated as a byproduct in several metabolic processes, with glycolysis being the primary source of its production¹⁸⁵. MGO is also abundantly present in exogenous sources such as foods, beverages, and cigarette smoke²². MGO has been reported to be up to 20,000 fold more reactive than glucose in glycation reactions and is considered the major glycation agent in cells⁴⁰. In healthy individuals MGO concentrations are low due to relatively low levels of endogenous formation and efficient detoxication by the glyoxalase system¹⁸⁶. However, factors such as hyperglycemia, inflammation, aging, and exposure to high levels of exogenous glucose may trigger the accumulation of MGO *in vivo*^{10, 73, 74}. The excess MGO induces the increased formation of AGEs by reacting with the nucleophilic sites on DNA and proteins, leading to structural and functional changes in these macromolecules, thereby contributing to cell dysfunction¹⁸⁷. AGEs derived from MGO can also impact cell function by activating the receptor for AGEs (RAGE), which triggers oxidative stress and pro-inflammatory responses¹⁶¹. Understanding the modification targets by MGO and the physiological impact of these modified molecules in different cell types is essential to better define potential biomarkers and etiologic agents of disease.

MGO-mediated protein modifications occur mainly at lysine, arginine, and cysteine residues (see **Figure 4.1** for an overview)^{41, 46}. MGO reacts with lysine and arginine residues in a series of non-enzymatic reactions, initially forming reversible hemiaminal adducts⁴⁶. Further reactions with lysine residues result in the formation of stable AGEs including *N*^ε-carboxyethyl lysine (CEL) and methylglyoxal-lysine dimer (MOLD)¹⁸⁸. Irreversible reactions of the arginine hemiaminal adduct predominantly result in the formation of argpyrimidines, *N*⁷-carboxyethyl arginine (CEA), and hydroimidazolones (MG-H1 and its structural isomers)¹⁸⁹. In addition, MGO reacts with cysteine residues non-enzymatically to form reversible hemithioacetal adducts, potentially functioning as cellular reversibly bound storage for MGO in cells⁴¹. S-carboxyethyl cysteine (CEC) is considered the thiol-derived AGE resulting from MGO modification *in vivo*⁵¹, although the mechanism leading to its formation remains unclear; the

formation of irreversible thiol-derived MGO adducts in cells through enzymatic mediation has been proposed⁵².

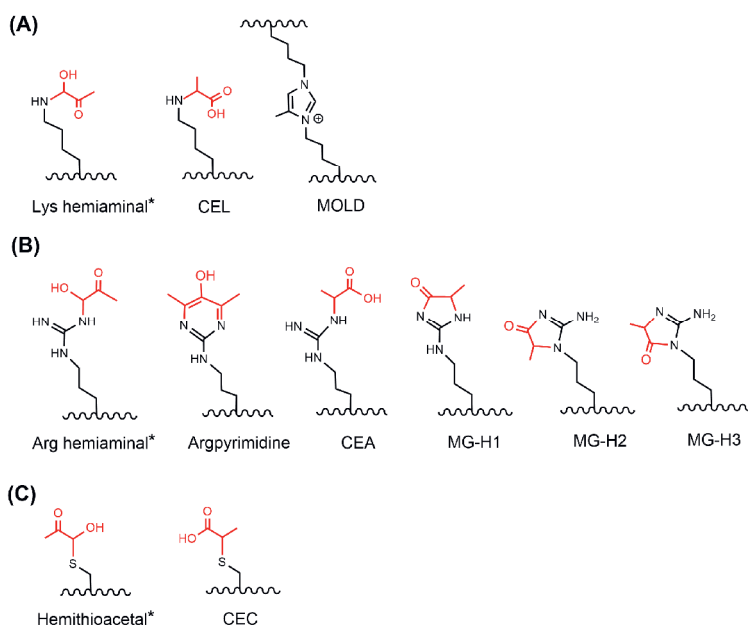


Figure 4.1. Reversible and stable MGO-mediated modifications on lysine (A), arginine (B), and cysteine (C) residues reported in the literature^{41, 46, 51, 188, 189}. Structures with reversible modifications are indicated with an asterisk (*). CEL: N^ε-carboxyethyl lysine, MOLD: methylglyoxal-lysine dimer, CEA: N⁷-carboxyethyl arginine, MG-H: methylglyoxal-derived hydroimidazolone (including 1, 2 and 3), CEC: S-carboxyethyl cysteine.

Although several of the potential modifications (**Figure 4.1**) have been reported to be correlated with the pathogenesis of many diseases such as diabetic complications^{185, 190-193}, the proteins and their specific sites susceptible to MGO modification remain incompletely mapped in biological systems. While detecting these modifications at specific protein sites presents a significant challenge due to their low abundance and heterogeneity, proteomics-based methods have emerged as a potent tool in this realm¹⁰⁴⁻¹⁰⁶. A few studies have highlighted their efficacy in identifying protein modifications by dicarbonyls, with successful applications observed in several cell types such as WIL2-NS B lymphoblastoid cells, HMEC-1 epithelial cells, and HEK293T kidney cells^{104, 106-108}. A study of the protein modifications by MGO in neuronal cells is still absent, although it can be expected to contribute to the elucidation of the mode of action underlying MGO-induced neurotoxicity and the identification of potential biomarkers of exposure and their link to neurological disorders.

In this study we aimed to define the protein modifications induced by MGO in neuronal cells and define potential biomarkers of exposure and toxicity: MGO-induced protein modifications

were qualitatively and quantitatively characterized in control and MGO-exposed cells from the SH-SY5Y human neuroblastoma cell line, a widely recognized neuronal cell model for investigating the pathological effects of neurotoxic compounds¹⁰³. Characterizing protein modifications upon incubation of the cells in the absence or presence of MGO will also provide insight into the effects of endogenously formed versus externally added MGO. A shot-gun proteomic analysis using nanoLC-MS/MS was applied to characterize and quantify the peptide adducts upon digestion of the isolated cellular proteins. Additionally, MGO-mediated modifications of selected potential protein biomarkers for both endogenous and exogenous MGO exposure were further studied in in-vitro cell-free incubation experiments.

4.2 Materials and Methods

4.2.1 Materials

MGO (40% in water), 3-(4,5-dimethylthiazol-2-yl)-2,5-diphenyltetrazolium bromide (MTT, 98%), and dimethyl sulfoxide (DMSO, $\geq 99\%$) were purchased from Merck (Darmstadt, Germany). Dulbecco's Modified Eagle Medium/Nutrient Mixture F-12 (DMEM/F12) with GlutaMAX supplement cell culture medium with and without phenol red, trypsin-EDTA for cell dissociation, phosphate buffered saline (PBS), penicillin/streptomycin, and nonessential amino acids (NEAA) were purchased from Gibco (Paisley, UK). Foetal calf serum (FCS) was purchased from Invitrogen (Breda, The Netherlands). All other reagents in this study were of analytical grade or purer. The recombinant human vimentin and calcyphosin were purchased from Gibco (Paisley, UK) and Prospec-Tany TechnoGene Ltd. (Rehovot, Israel), respectively.

4.2.2 Cell culture

The human neuroblastoma cell line SH-SY5Y (ATCC CRL-2266) was acquired from the American Type Culture Collection (ATCC, Manassas, VA, USA). The cells were cultured in a humidified incubator at 37 °C with 5% CO₂ using DMEM/F12 GlutaMAX medium supplemented with 10% FCS, 1% NEAA, and 1% penicillin/streptomycin. The culture medium was renewed every 4 to 7 days and subculturing was performed at a 1:20 ratio upon reaching confluency, utilizing a 0.05% trypsin-EDTA solution.

4.2.3 Cell viability assay

The MTT method was applied to assess the viability of SH-SY5Y cells after exposure to MGO. Briefly, SH-SY5Y cells were seeded into 96-well plates (Greiner Bio-one, Alphen aan den Rijn, The Netherlands) at a density of 1.5×10^4 cells per well (approximately 4.69×10^4 cells/cm²) and incubated for 24 hours. Subsequently, the cells were exposed to assay medium

(DMEM/F12 without phenol red and FCS supplement) containing various concentrations of MGO (0 (solvent control), 50, 125, 250, 500, 750, 1000, 1250, 1500, 1750, and 2000 μM , final concentration added from 200 times concentrated stock solutions in nano pure water) and incubated for an additional 24 hours. Following the exposure period, an MTT solution was added to each well to achieve a final concentration of 0.5 mg MTT/mL, followed by a 4-hour incubation. Afterward, the produced formazan crystals were dissolved in 100 μL DMSO, and absorbance readings were taken at 562 nm and at a reference wavelength of 620 nm with a microplate reader. Corrected absorbance values were calculated by subtracting the readings at 620 nm from the corresponding values at 562 nm. Cell viability was expressed as a percentage relative to the medium control, which was set at 100%. Six independent biological replicates were collected for all treatments.

4.2.4 Cell sample preparation for label-free quantitative proteomics analysis

SH-SY5Y cells were seeded in T175 flasks (Greiner Bio-one) at a density of 8.2×10^6 cells per flask (4.69×10^4 cells/cm²) and incubated for 24 hours. The cells were then exposed to assay medium (DMEM/F12 without phenol red and FCS supplement) containing MGO at three different concentrations (500, 750, or 1000 μM , final concentration, added from 200 times concentrated stock solutions in nano pure water) or to solvent control (0.5% nano pure water in DMEM/F12 without phenol red and FCS supplement) for 24 hours. Following the exposure period, the cells were washed twice with PBS, after which 1.8 mL of ice-cold PBS was added to the flask. The cells were then carefully scraped from the flask, and the resulting cell/PBS mixture was transferred to a 2-mL protein low binding tube (Eppendorf, Nijmegen, The Netherlands) followed by centrifugation at $500 \times g$ for 2 minutes at 4 °C to obtain cell pellets. The cell pellets were then washed twice with 1.5 mL of ice-cold 100 mM Tris-hydrochloride (Tris-HCl) pH 8 under the same centrifugation conditions. Afterward, the cell pellets were re-suspended in 90 μL 100 mM Tris-HCl pH 8 supplemented with 1% protease inhibitor cocktail (Thermo Fisher Scientific, Bleiswijk, The Netherlands), and the resulting mixture was sonicated in an ice-water bath (Qsonica sonicator, Qsonica, Newtown, USA) for 30 min in a pulse mode (30 s on and 30 s off) at 100% amplitude. The protein concentrations in the samples were determined using a BCA protein assay kit following the manufacturer's instructions (Thermo Fisher Scientific, Bleiswijk, The Netherlands). The protein aggregation capture (PAC) method was applied to further obtain peptide samples for nanoLC-MS/MS analysis¹⁹⁴. The obtained peptide samples were immediately stored at -20 °C until further analysis. Four independent biological replicates were collected for all treatments.

4.2.5 Label-free quantitative proteomics analysis

NanoLC-MS/MS was performed on a Thermo Vanquish Neo nanoLC system coupled to a Thermo Orbitrap Exploris 480 mass spectrometer (Thermo Fisher Scientific, Bremen, Germany). An in-house prepared 0.10 mm × 250 mm analytical column filled with 1.9 µm ReproSil-Pur 120 C18-AQ beads was used. The mobile phase consisted of 0.1 v/v% formic acid in water (eluent A) and 0.1% formic acid in acetonitrile (eluent B), with a 3-step linear gradient: 0 to 9% B in 1 min, 9% to 34% B in 50 min, and 34 to 50% B in 4 min. Then the gradient was kept at 50% B for 1 min and returned to the starting conditions and kept at these conditions for 2.5 column volume at 925 bar before initiating the next injection. The flow rate was 500 nL/min. An electrospray potential of 3.5 kV was applied directly to the eluent before the column. MS and MS/MS automatic gain control targets were set to 300% and 100%, respectively, or maximum ion injection times of 50 ms (MS) and 30 ms (MS/MS) were used. Higher energy collisional dissociation fragmented (isolation width 1.2 m/z , 28% normalized collision energy) MSMS scans in a cycle time of 1.1s were recorded for the most abundant 2-5+ charged peaks in the MS scan in a data-dependent mode at resolution 15,000 (threshold 5e4, with 15 s exclusion duration for the selected $m/z \pm 10$ ppm).

4.2.6 Identification and quantification of MGO-induced modifications in proteins

The MaxQuant software package (2.0.3.0) was used to identify and quantify the peptides. The human (UP000005640) database was downloaded from UniProt¹⁹⁵, and was used together with a contaminants database that contains sequences of common contaminants like Trypsins (P00760, bovine and P00761, porcine). Trypsin was specified as the enzyme and a maximum of two missed cleavages was allowed. Precursor and fragment mass tolerances were 4.5 and 20 ppm, respectively. Arginine and lysine carboxyethylation/hemiaminalization, and cysteine carboxyethylation (+72.021129), arginine methylglyoxal-hydroimidazolone (+54.010565), methionine oxidation (+15.994915), N-terminal acetylation (+42.010565), deamidation (+0.984016) and acrylamide (+71.0371138) were set as variable modifications. Protein and peptide identification false discovery rates were both set at 1%. Modified peptides were further filtered based on the following criteria: scores > 65, localization probability ≥ 0.5, and PEP values ≤ 0.01.

4.2.7 Investigation of MGO-mediated modification on selected proteins in an *in vitro* cell-free system

To further compare the protein biomarkers for exogenous and endogenous MGO exposure as identified in the cell-based study, two proteins, vimentin (VIM) and calpophosin (CAPS), were selected for analysis. Given that intracellular levels of MGO have been reported to range from

1 to 4 μM ¹⁰, the concentration of MGO used in these *in vitro* studies was kept in the low μM range (0-10 μM) to mimic protein modification at background endogenous MGO levels. Furthermore, the intracellular concentration of VIM was estimated to be 1.4 μM , based on our quantitative proteomics data and the “Proteomic Ruler” approach¹⁹⁶. However, quantitative proteomics data for CAPS were not obtained due to the identification of a limited number of CAPS peptides in the samples for reliable quantification of CAPS. We assume its concentration to be analogous to the proteins annexin and calnexin, which share roles in calcium signaling and whose concentrations could be estimated using the aforementioned approach, amounting to 1.1 and 1.0 μM , respectively. Consequently, 1 μM (final concentration) of the commercially available recombinant form of VIM or CAPS was incubated with increasing concentrations of MGO (0, 1, 2, 4, 6, or 10 μM , final concentration) in 100 mM sodium phosphate (pH = 7.4) at 37 °C for 24 h. Following incubation, the protein aggregation capture (PAC) method¹⁹⁴ was employed to prepare peptide samples for subsequent nanoLC-MS/MS analysis. Three independent biological replicates were collected for all treatments.

4.2.8 Statistical analysis

4.2.8.1 Univariate analysis

One-way analysis of variance (ANOVA) was conducted to assess whether cell viability differed among the control and various concentrations of MGO-treated groups. Following this, Dunnett’s post hoc test¹⁹⁷ was applied to compare each MGO-treated group against the control. These data are presented as the mean \pm standard deviation (SD) from six independent experiments.

For the intensity data of MGO-modified peptides, Jonckheere-Terpstra test, a non-parametric method used for identifying ordered differences among groups¹⁰³, was performed to determine if there was a concentration-dependent increase in the intensity of modified peptides in the proteins with increasing concentrations of MGO.

Kruskal-Wallis test¹⁹⁸ was conducted to determine whether there were significant differences in the intensity of MGO-modified peptides among the control group and different concentrations of MGO-treated groups. Following the detection of significant differences, Dunn's post hoc test¹⁹⁹ was applied to perform multiple comparison analysis between each MGO-treated group and the control.

The intensity data for MGO-modified peptides from both *in vitro* cell-based assays and cell-free incubations are presented as medians with interquartile ranges, based on four

independent replicates for the cell-based study and three for cell-free incubations. Tests with p values below 0.05 were considered to be statistically significant.

4.2.8.2 Pathways and network analysis

KEGG pathway enrichment analysis was conducted on proteins highly susceptible to MGO modification using DAVID v2023q4 (<https://david.ncicrf.gov/>, accessed January 2024)²⁰⁰. A protein-protein interaction network with functional annotations was constructed for these proteins utilizing the STRING database 12.0 (<https://string-db.org/>, accessed January 2024)²⁰¹.

4.2.8.3 Data visualization and software

The structural formulas were created using ChemDraw 20. The line charts and bar charts were generated with GraphPad Prism version 9, and heatmaps and KEGG enrichment results were visualized using the online platform at <https://www.bioinformatics.com.cn/>²⁰², accessed January 2024. The statistical analysis for the cell viability data was performed utilizing GraphPad Prism. Jonckheere-Terpstra test was performed using the `jonckheereTest` function from the `PMCMRplus` package (1.9.10)²⁰³ for R software version 4.3.1. Kruskal-Wallis and Dunn's tests were conducted using the `kruskal.test` function from base R and the `dunnTest` function from the `FSA` package (0.9.4)²⁰⁴, respectively.

4.3 Results

4.3.1 Effects of MGO on the viability of SH-SY5Y cells

Exposure of SH-SY5Y cells to MGO for 24 h led to a concentration-dependent decrease in cell viability, with an EC50 value of 1150 μ M, as shown in **Figure 4.2**. The decrease in the viability became statistically significant at concentrations ≥ 1000 μ M MGO. For investigating the protein modifications by MGO, three concentrations (500, 750, and 1000 μ M) were selected. At 500 and 750 μ M, MGO did not reduce cell viability, whereas at 1000 μ M, MGO induced a significant reduction in cell viability, with 68.0% of viability remaining ($p = 0.0007$).

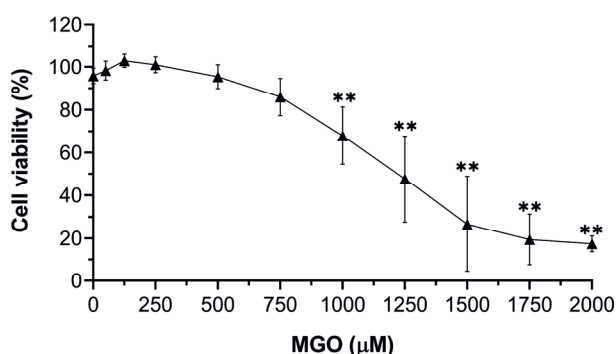


Figure 4.2. Effects of MGO on the viability of SH-SY5Y cells. Data are presented as mean \pm SD calculated over the six independent replicates. Differences between MGO-treated groups and control were assessed with a one-way ANOVA test followed by Dunnett's post hoc test; all observed significant differences had p values less than 0.01, which are denoted by **.

4.3.2 Landscape of MGO-mediated protein modifications in SH-SY5Y cells upon different treatments

Four types of major intracellular MGO-based modifications were investigated and quantified, including arginine methylglyoxal-hydroimidazolone (in short, Arg MG-H), arginine carboxyethylation/hemiaminalization (Arg C-E/H), lysine carboxyethylation/hemiaminalization (Lys C-E/H), and cysteine carboxyethylation (Cys C-E). Due to their identical molecular masses, carboxyethylation and hemiaminalization modifications of a given amino acid cannot be distinguished using LC/MS. However, it should be noted that carboxyethylation might dominate over hemiaminalization due to the possible loss of hemiaminal adducts during sample preparation owing to the reversible nature of hemiaminals. For cysteine, only carboxyethylation was quantified and the reversible hemithioacetals were not considered, as hemithioacetals would be deconjugated due to the use of acrylamide in the proteomics sample preparation method¹⁹⁴.

A total of 153 proteins were identified as modified by MGO in the control and/or MGO-treated cell samples, after applying the filter selection criteria described in **Section 4.2.6**. As shown in **Figure 4.3B**, most of the modified proteins were already detected under basal control conditions, and there was no significant concentration-dependent increase in the number of modified proteins with increasing concentrations of MGO.

Figure 4.4 presents heatmaps showing the modification frequency of each modified protein for each type of modification across all samples. Several proteins exhibited a high frequency of modifications. For instance, serine/threonine-protein kinase SIK2 (SIK2) and calcyphosin (CAPS) were found to be modified in all analyzed samples (**Figure 4.4B**), suggesting a potential

susceptibility to modification by endogenous and potentially also externally added MGO. Conversely, proteins such as histone H2B type 2-F (H2BC18) and tubulin beta-4B chain (TUBB4B) were modified only in cell samples treated with external MGO (**Figure 4.4A**), not in control cells, indicating a specific susceptibility to externally added MGO. In contrast, some proteins were identified as modified in only a limited number of samples and their modification frequencies are not significantly influenced by the increasing amount of MGO added, implying that these proteins are less prone to modification by MGO.

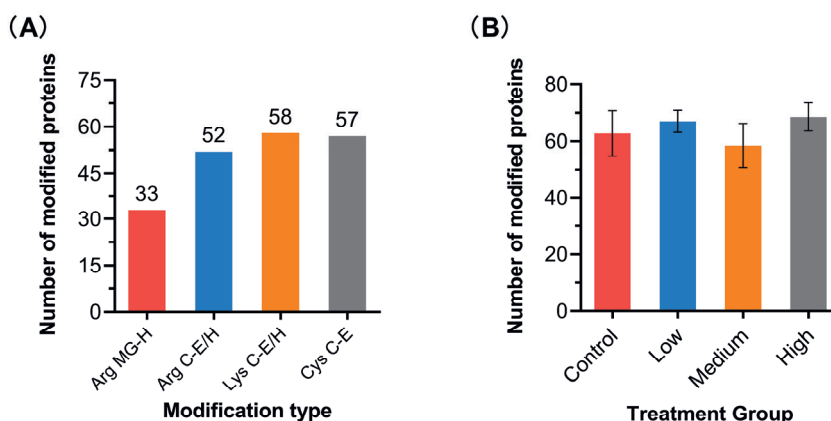


Figure 4.3. Quantitative profile of MGO-induced modifications in SH-SY5Y cells after 24 h incubation in the absence or increasing concentrations of MGO for 24 h: (A) Number of modified proteins for each type of modification and (B) Number of modified proteins in each treatment group. Arg MG-H: arginine methylglyoxal-hydroimidazolone, Arg C-E/H: arginine carboxyethylation/hemiaminalization, Lys C-E/H: lysine carboxyethylation/hemiaminalization, Cys C-E: cysteine carboxyethylation. Treatments are labeled as control (0 μ M MGO), low (500 μ M MGO), medium (750 μ M MGO), and high (1000 μ M MGO). Data are shown as mean \pm SD in panel B calculated over the four independent replicates.

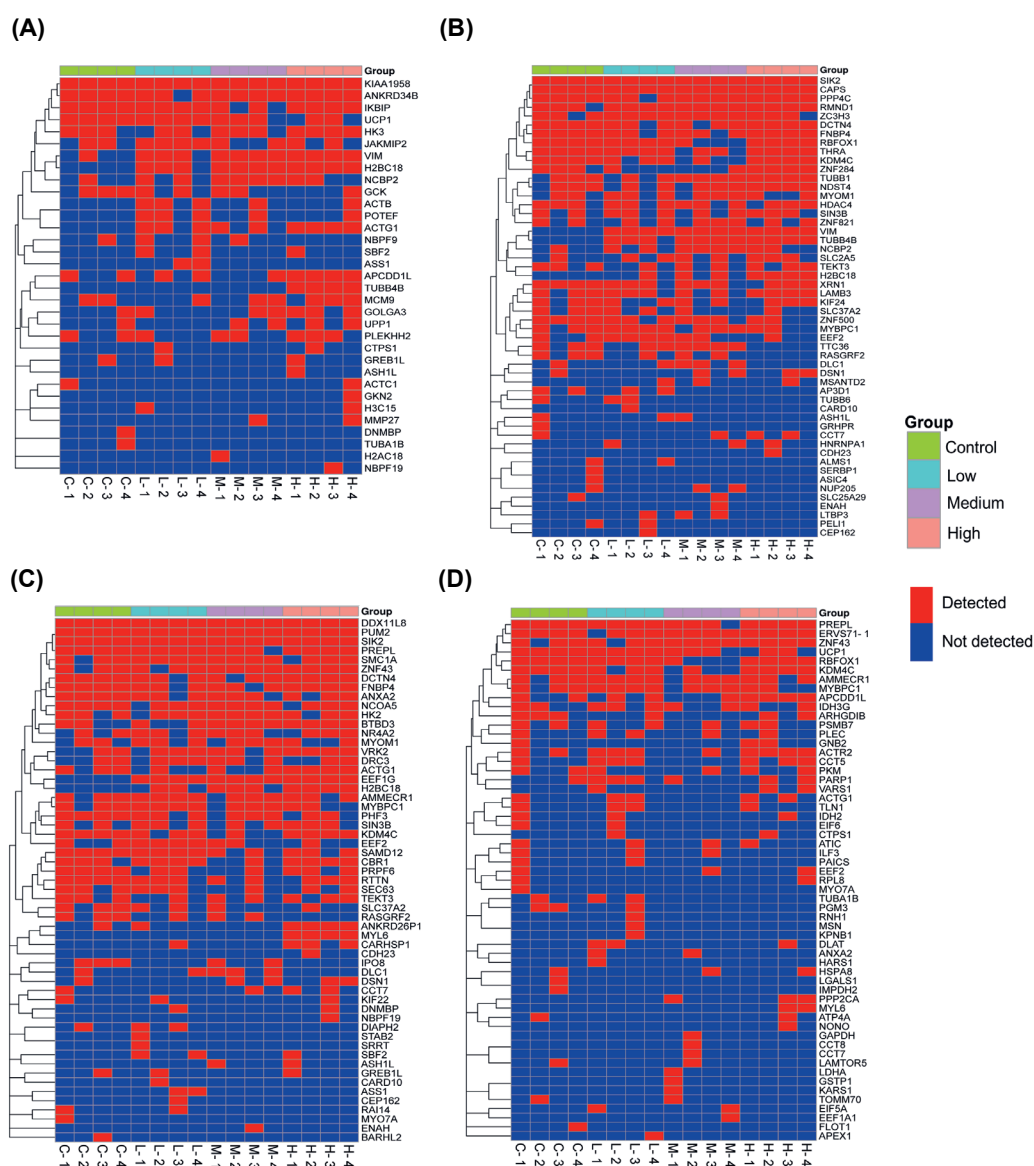


Figure 4.4. Overview of the modification frequency of detected MGO-modified proteins for each modification type—Arg MG-H (A), Arg C-E/H (B), Lys C-E/H (C), and Cys C-E (D) across different treatment groups (4 treatments × 4 replicates). Treatments are labeled as control (C-x) (0 μ M MGO), low (L-x) (500 μ M MGO), medium (M-x) (750 μ M MGO), and high (H-x) (1000 μ M MGO); “x” indicates the replicate number (x=1-4) for each. Red represents modification for the corresponding protein was detected in the sample, and blue indicates modification was not detected.

4.3.3 Screened potential peptide/protein biomarkers for exogenous and endogenous MGO exposure

Given the variability in modification frequency of proteins identified as MGO-modified (**Figure 4.4**), ranging from detection in a single instance to presence in all samples, we have further screened for proteins that exhibit greater sensitivity to MGO modification based on these frequency data. Proteins that were detected in at least three out of the four replicates within any of the treatment groups—control, low, medium, or high—were categorized as highly susceptible to MGO modification, thereby enabling the subsequent definition of biomarkers that respond to either endogenous or exogenous MGO.

4

A total of 77 proteins were selected and defined as highly susceptible to MGO modification based on the predefined selection criteria. A detailed statistical analysis of the intensity of MGO-modified peptides detected in these proteins across each treatment group was then conducted. Jonckheere-Terpstra test was performed to determine if there was a concentration-dependent increase in the total intensity of modified peptides in the proteins with increasing concentrations of MGO.

Proteins with peptides modified in a concentration-dependent manner ($p < 0.05$ in the Jonckheere-Terpstra test, p values can be found in **Table S4.1** in supporting information) were defined as potential biomarkers for exogenous MGO exposure, reflecting their relatively lower modification levels under basal conditions and susceptibility to externally added MGO. Consequently, eight proteins, namely vimentin (VIM), histone H2B type 2-F (H2BC18), actin, cytoplasmic 2 (ACTG1), tubulin beta-4B chain (TUBB4B), elongation factor 1-gamma (EEF1G), calcium-regulated heat-stable protein 1 (CARHSP1), solute carrier family 2, facilitated glucose transporter member 5 (SLC2A5), and myosin light polypeptide 6 (MYL6), exhibiting concentration-dependent modification by MGO, were defined as potential biomarkers for exogenous MGO exposure. The details and intensity levels of these potential biomarkers for exogenous MGO exposure are given in **Table 4.1** and **Figure 4.5**, respectively. Protein MYL6 was additionally defined as a biomarker for the toxicity of MGO as its modified peptide adducts were detected exclusively at cytotoxic MGO levels (**Figure 4.5H**). Kruskal-Wallis test followed by Dunn's post hoc test was applied to assess the differences in the intensity of the modified peptides of these proteins between MGO-treated groups and control. Notably, protein VIM was found to have 14 peptides modified by MGO, with 13 exhibiting a statistically significant increase in intensity in the high-concentration MGO-treated group relative to the control (**Figure 4.5A**), and the total intensity of the modified peptides for VIM was substantially higher than those of other defined biomarker proteins.

The modifications on VIM induced by MGO predominantly occurred at 10 sites and involved Arg MG-H and/or Arg C-E/H modifications (**Table 4.1**). Furthermore, proteins including H2BC18, ACTG1, tubulin TUBB4B, EEF1G, CARHSP1, and MYL6 all had at least one modified peptide with statistically significantly higher intensity in the high-concentration MGO-treated group compared to control. Although the modified peptide from protein SLC2A5 did not exhibit statistically significant changes between control and MGO-treated groups using the Kruskal-Wallis test, it showed an increasing trend as assessed by Jonckheere-Terpstra test and was thus still included as a potential biomarker for exogenous MGO exposure.

Most of other proteins identified as highly susceptible to MGO modification such as serine/threonine-protein kinase SIK2 (SIK2, **Figure 4.6B**) and putative ATP-dependent RNA helicase DDX11-like protein 8 (DDX11L8, **Figure 4.6D**) did not show statistically significant differences in the Jonckheere-Terpstra test (p values in **Table S4.1**), exhibiting similar modification levels in both control and externally MGO-treated groups. However, some proteins like uncharacterized protein KIAA1958 (KIAA1958, **Figure 4.6A**) and calcyphosin (CAPS, **Figure 4.6C**) showed a decreasing trend in the intensity of their modified peptides with increasing MGO concentrations in the Jonckheere-Terpstra test ($p < 0.05$, **Table S4.1**), indicating relatively higher modification levels in the control group compared to the MGO-treated groups.

This decreasing trend observed may be attributed to MGO-induced crosslinking between amino acid residues, which would become more prevalent at higher MGO concentrations for these proteins, leading to reduced detection of modified peptides. Nevertheless, proteins that showed comparable or higher modification levels in control compared to externally MGO-treated groups, were considered to possess the properties necessary for potential endogenous MGO exposure biomarkers due to their sensitivity to endogenous modifications.

Based on these properties, proteins with modification frequencies reaching at least 15 times out of 16 samples and showing consistent modifications in all 4 control samples were selected as highly potential peptide/protein biomarkers for endogenous MGO exposure, as detailed in **Table 4.2** and **Figure 4.6**. Additional proteins that did not meet the criteria for selection as biomarkers for either exogenous or endogenous exposure, as detailed in **Table 4.1** and **Table 4.2**, are outlined in **Figure S4.1 (supporting information)**, with their biomarker potential remaining less certain.

Table 4.1. Screened potential peptide/protein biomarkers for exogenous MGO exposure.

No.	Protein ID	Protein name	Gene name	Modified peptides of each protein	Biological Function
1	P08670	Vimentin	VIM	ISLPLPNFSSLNLR(1, MG-H)ETNLDLPLVDTHSKR ISLPLPNFSSLNLR(1)ETNLDLPLVDTHSKR MFGGPGTASR(0.823, MG-H)PSSSR(0.177, MG-H) QVQSLTCEVDALK(0.132)GTNESLER(0.868) SLYASSPGGVYATR(1)SSAVR SLYASSPGGVYATR(1, MG-H)SSAVR SSVPGVR(1, MG-H)LLQDSVDFSLADINTEFKNTR STR(1)SVSSSSYR STR(1, MG-H)SVSSSSYR SYVTSTR(0.994, MG-H)TYSLGSALR(0.006, MG-H) PST SR(0.001, MG-H) TVETR(1)DGQVINETSQHDDLE TVETR(1, MG-H)DGQVINETSQHDDLE TYSLGSALR(1, MG-H)PSTSR TYSLGSALR(0.143, MG-H)PSTSR(0.857, MG-H) SLYASSPGGVYATR LLLPGLAK(1)HAVSEGK ^a EIQTAVR(1)LLLPGLAK ^a EIQTAVR(1, MG-H)LLLPGLAK ^a IAGEASR(1, MG-H)LAHYNKR ^a C(0.992)PEALFQPSFLGMESC(0.008)GIHETTFNSIM K ^a HQGVMMVGMGQK(1)DSYVGDEAQSKR ^a CDVDIR(1, MG-H)KDLYANTVLSGGTTMYPGIADR ^a LHFFMPGFAPLTSR(0.5)GSQQYR(0.5) ^a LHFFMPGFAPLTSR(0.402, MG-H)GSQQYR(0.598, MG-H) ^a	Maintaining cell structure; regulating cell mechanics, motility, and adhesion; coordinating mechanosensing and signaling ²⁰⁵
2	Q5QNW6	Histone H2B type 2-F	H2BC18	LLLPGLAK(1)HAVSEGK ^a EIQTAVR(1)LLLPGLAK ^a EIQTAVR(1, MG-H)LLLPGLAK ^a IAGEASR(1, MG-H)LAHYNKR ^a	Fundamental to nucleosome assembly
3	P63261	Actin, cytoplasmic 2	ACTG1	C(0.992)PEALFQPSFLGMESC(0.008)GIHETTFNSIM K ^a HQGVMMVGMGQK(1)DSYVGDEAQSKR ^a CDVDIR(1, MG-H)KDLYANTVLSGGTTMYPGIADR ^a LHFFMPGFAPLTSR(0.5)GSQQYR(0.5) ^a LHFFMPGFAPLTSR(0.402, MG-H)GSQQYR(0.598, MG-H) ^a	Involved in various types of cell motility
4	P68371	Tubulin beta-4B chain	TUBB4B	LHFFMPGFAPLTSR(0.5)GSQQYR(0.5) ^a LHFFMPGFAPLTSR(0.402, MG-H)GSQQYR(0.598, MG-H) ^a	Integral component of microtubules
5	P26641	Elongation factor 1-gamma	EEF1G	AFNQKG(1)IFK	Key in translational elongation during protein biosynthesis ²⁰⁶
6	Q9Y2V2	Calcium-regulated heat-stable protein 1	CARHSP1	SK(1)GHGFITPADGGPDIFLHISDVEGEYVPVEGDEVYK	Binding mRNA; regulating stability of target mRNA
7	P22732	Solute carrier family 2, facilitated glucose transporter member 5	SLC2A5	LLVGICAGVSSNVVPMYLGELAPK(0.077)NLR(0.923)	Fructose transporter
8	P60660	Myosin light polypeptide 6	MYL6 ^b	HVLVTLGKMTTEEEVEMLVAGHEDSNGC(1)INYEAFV R NK(1)DQGTIEDYVEGLR	Regulatory light chain of myosin

Note: Numbers in parentheses next to amino acids represent the probability of modification at that site. The probability reflects how well the MS/MS spectrum explains the peptide sequence and the modification localization²⁰⁷. "MG-H" is specifically annotated in parentheses to distinguish between the two types of arginine modifications being studied. Protein IDs and Gene names were retrieved from the UniProt¹⁹⁵. The biological functions of proteins were obtained from UniProt¹⁹⁵ or from the reference cited.

^aAnnotated peptide hits that also match other homologous protein sequences.

^bProtein MYL6 was additionally identified as a biomarker for MGO toxicity, with its modified peptide adducts detected exclusively at cytotoxic MGO levels.

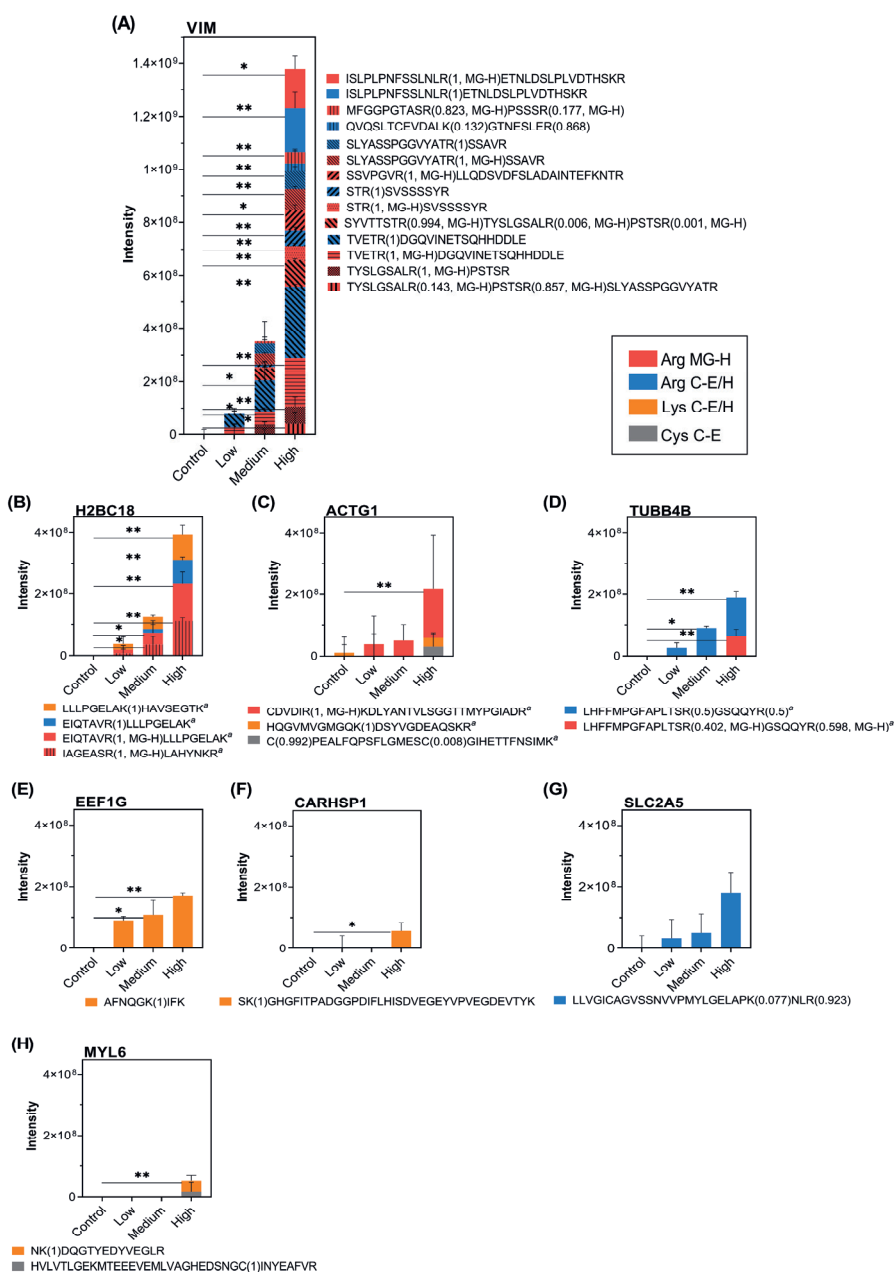


Table 4.2. Selected potential peptide/protein biomarkers for endogenous MGO exposure.

No.	Protein ID	Protein name	Gene name	Modified peptides of each protein	Modification frequency	Biological Function
1	Q8N8K9	Uncharacterized protein KIAA1958	KIAA1958	AGSQER(0.005, MG-H)VCFQDNR(0.995, MG-H)	16/16	Unknown function
2	Q9H0K1	Serine/threonine-protein kinase SIK2	SIK2	LQKK(1)R(1)LFLQK	16/16	Involved in fatty acid oxidation, autophagy, immune response, and glucose metabolism
3	Q13938	Calcyphosin	CAPS	GASGIQGLAR(1)FFR	16/16	Calcium-binding protein
4	A8MPP1	Putative ATP-dependent RNA helicase DDX11-like protein 8	DDX11L8	ASVEVK(1)ATFGPAIAAVQK(1)	16/16	Putative DNA helicase
5	Q8TB72	Pumilio homolog 2	PUM2	GK(1)VLALSQHKFASNVVEK	16/16	RNA-binding repressor
6	A5PLL1	Ankyrin repeat domain-containing protein 34B	ANKRD34B	MLLR(0.5, MG-H)R(0.5, MG-H)QSLQTEQIK	15/16	Involved in promyeloid progenitor cell induction ²⁰⁸
7	P60510	Serine/threonine-protein phosphatase 4 catalytic subunit	PPP4C	QIEQLR(1)R(1)CELIK	15/16	Involved in many processes such as DNA repair, DNA damage response, apoptosis, and cell migration
8	Q4J6C6	Prolyl endopeptidase-like	PREPL	YHLTK(0.519)C(0.519)LQNK(0.962)	15/16	Regulating trans-Golgi network morphology and sorting; potentially involved in synaptic vesicle exocytosis
9	P61550	Endogenous retrovirus group S71 member 1 Env polyprotein	ERV571-1	LAQDC(0.964)WLC(0.016)LK(0.02)	15/16	Involved in receptor recognition during early infection; has lost original fusogenic properties through evolution
10	Q70UQ0	Inhibitor of nuclear factor kappa-B kinase-interacting protein	IKBIP	SFQIIAHLKR(1, MG-H)	14/16	Target of p53/TP53 with pro-apoptotic function
11	Q9UJW0	Dynactin subunit 4	DCTN4	IQLVAVNYIPEVR(1)IMSIPNLR(1)YMK(1)	14/16	Component of the dynactin complex
12	Q8N3X1	Formin-binding protein 4	FNBP4	EGALNGNYLK(1)R(1)	14/16	Involved in the regulation of cytoskeletal dynamics during cell division and migration ²⁰⁹

Note: Numbers in parentheses next to amino acids represent the probability of modification at that site. "MG-H" is specifically annotated in parentheses to distinguish between the two types of arginine modifications being studied. Protein IDs and Gene names were retrieved from the UniProt¹⁹⁵. The biological functions of proteins were obtained from UniProt¹⁹⁵ or the reference cited.

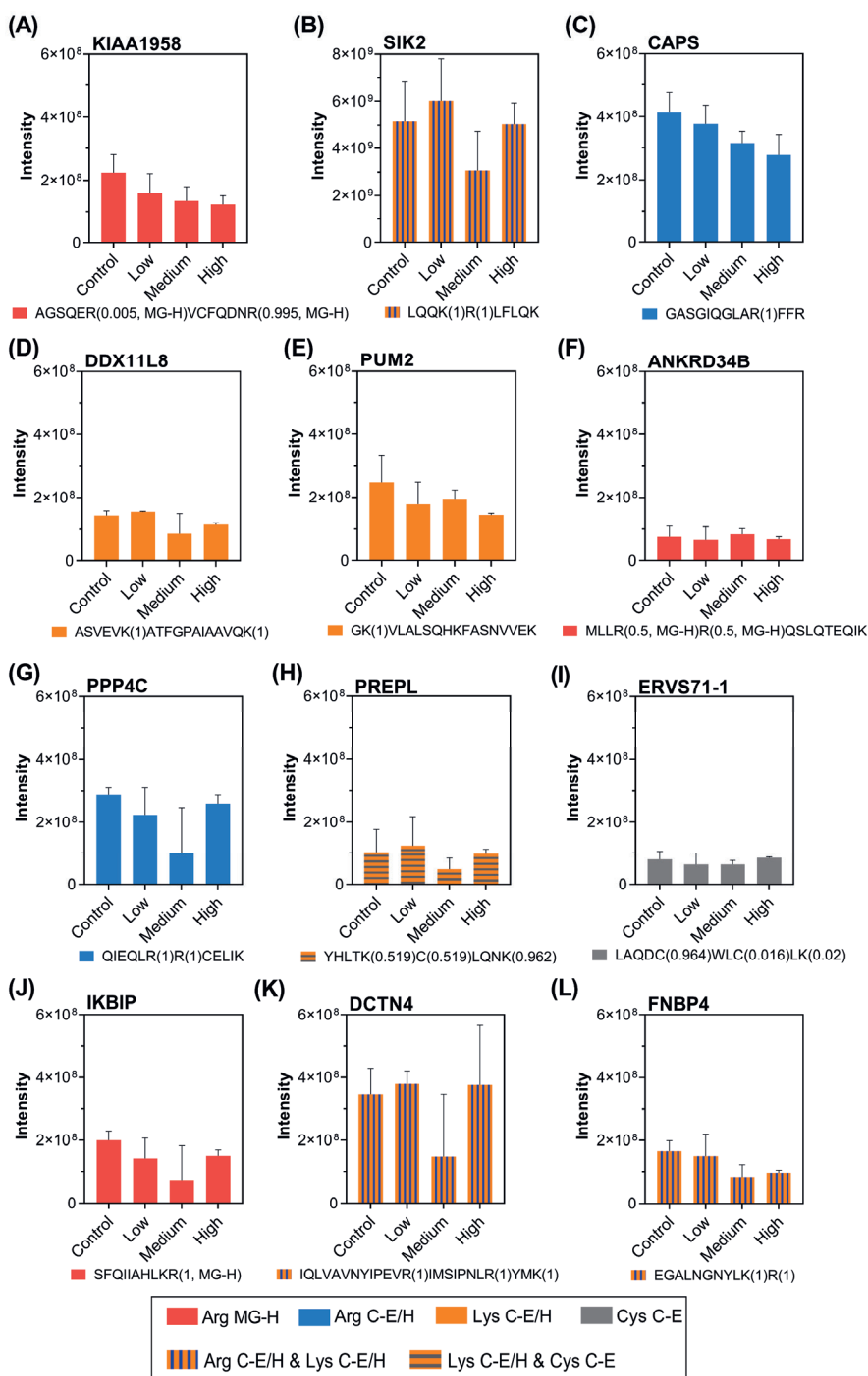


Figure 4.6. Intensity levels of MGO-modified peptides from corresponding proteins identified as potential biomarkers for endogenous MGO exposure in each treatment group. Numbers in parentheses next to amino acids represent the probability of modification at that site. “MG-H” is specifically annotated in parentheses to distinguish between the two types of arginine modifications being studied. Peptides with multiple potential modification types (each having a probability ≥ 0.5) are denoted by pattern fills as indicated in the figure legend. Note the different Y axis in panel B as compared to panels A and C-L.

4.3.4 Functional enrichment and protein-protein interaction (PPI) network analysis of MGO-modified proteins

To understand better the functional consequences of MGO-induced protein modifications in SH-SY5Y cells, we conducted a pathway enrichment analysis on 77 proteins identified as highly susceptible to MGO modification (**Figure 4.7A**). The term “motor protein” emerged as the most significantly enriched category, including 8 proteins such as kinesin-like protein KIF24 (KIF24), dynactin subunit 4 (DCTN4), MYL6, TUBB4B, tubulin beta-1 chain (TUBB1), ACTG1, actin, cytoplasmic 1 (ACTB) and hexokinase-3 (HK3). Furthermore, the results also reveal the enrichment for proteins associated with carbon metabolism (isocitrate dehydrogenase [NAD] subunit gamma, mitochondrial (IDH3G), hexokinase-2 (HK2), HK3, and hexokinase-4 (GCK)), glycolysis/gluconeogenesis (HK2, HK3, and GCK), and carbohydrate digestion and absorption (SLC2A5, HK2, and HK3). Moreover, pathways related to amyotrophic lateral sclerosis and tight junctions were also affected, indicating that modifications of proteins within these pathways may contribute to the neurotoxic effects observed in MGO-exposed SH-SY5Y cells.

A protein-protein interaction network was constructed to explore the relationships among proteins identified as highly susceptible to MGO modification (**Figure 4.7B**). Two main protein clusters were detected, enriched for biological processes of glycolysis and gluconeogenesis (red nodes), and the structural constituents of the cytoskeleton (blue nodes). Three proteins (VIM, ACTB, and TUBB4B) that were classified as biomarkers for exogenous MGO exposure were associated with the structural constituents of the cytoskeleton cluster (**Figure 4.7B**).

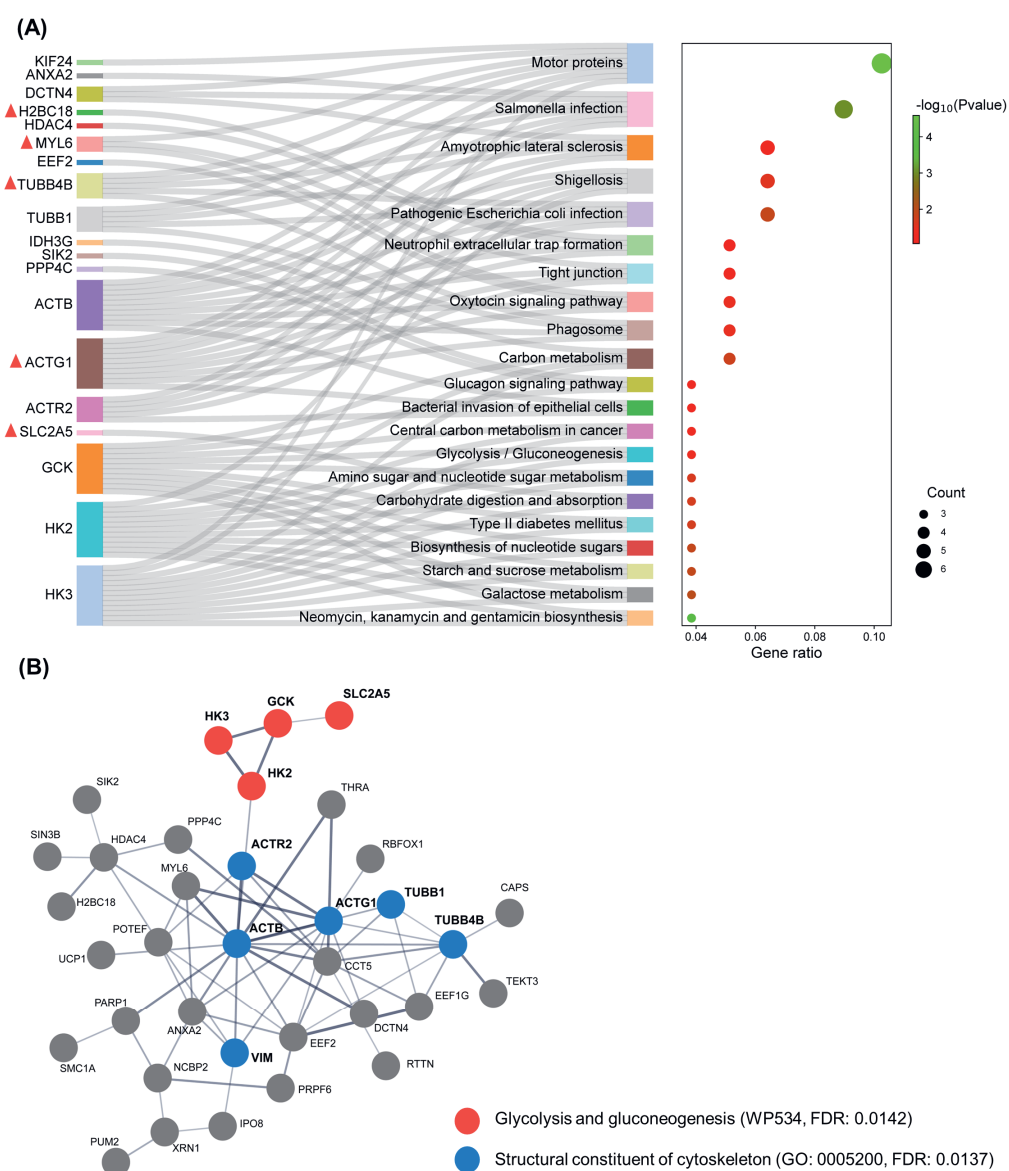


Figure 4.7. Enrichment and protein-protein interaction (PPI) network analysis of proteins susceptible to endogenous and/or exogenous MGO modification. (A) KEGG pathway enrichment analysis using DAVID. Potential biomarkers for exogenous MGO exposure are labeled with triangles. (B) PPI network analysis with functional annotations using STRING database. The edge size indicates the strength of data support. FDR, false discovery rate.

4.3.5 A further study of MGO-mediated modifications on selected proteins in an in-vitro cell-free system

Two proteins, VIM and CAPS, which were respectively identified as biomarkers for exogenous and endogenous exposure to MGO in the cell-based study, were selected for further comparison of their modifications by MGO in an *in vitro* cell-free system. Concentrations of MGO tested in these *in vitro* cell-free systems were in the 0-10 μM range to mimic protein modifications at background endogenous MGO levels¹⁰. In total, 30 peptides for CAPS and 11 peptides for VIM were identified as modified by MGO, respectively. Statistical analyses were further applied to determine which peptides in these two proteins are modified in a concentration-dependent manner with the increasing concentrations of MGO.

As shown in **Figure 4.8A**, 19 peptides in CAPS exhibited a concentration-dependent increase in modification levels ($p < 0.05$, Jonckheere-Terpstra test), including the one (GASGIQGLARFFR) that was also detected as modified in the cell-based study. For VIM (**Figure 4.8B**), only one peptide showed a concentration-dependent increase in modification levels ($p < 0.05$, Jonckheere-Terpstra test), but this modified peptide was not detected in the cell-based study. Although 11 peptide adducts in VIM were identified, including 4 that showed concentration-dependent modifications as detected in the cell-based study, their intensities and modification frequencies across different MGO concentration treatments in the *in vitro* cell-free incubations were not consistent, and were not significant in the Jonckheere-Terpstra test (data not shown). These results from the *in vitro* cell-free incubations reveal that CAPS was much more sensitive than VIM under the low μM range of MGO, reflecting its higher susceptibility to modification by MGO at background cellular MGO level, and further confirming CAPS as a biomarker for endogenous MGO exposure; whereas, for VIM, higher concentrations of MGO may be needed to induce the significant modifications observed in cell-based studies with MGO levels at high μM range, corroborating its role as a sensor for especially high levels of exogenous MGO exposure.

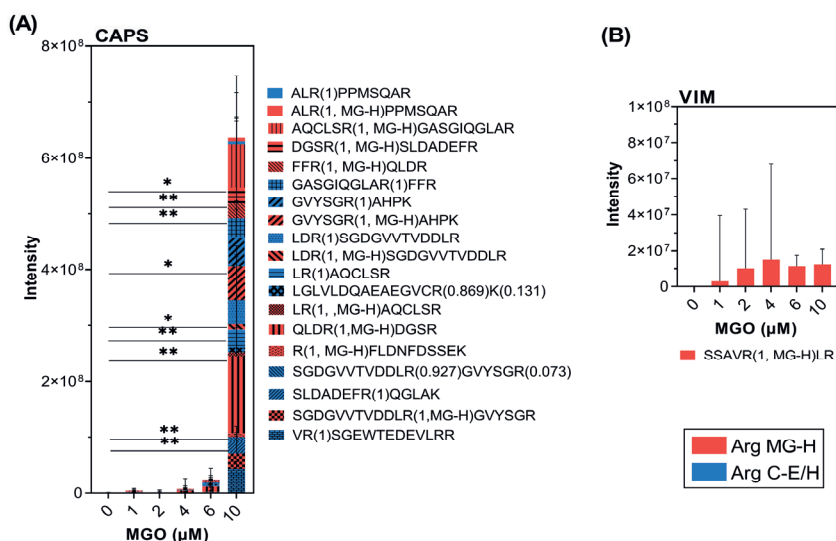


Figure 4.8. Intensity levels of MGO-modified peptides from CAPS (A) and VIM (B) in *in vitro* cell-free incubations treated with increasing concentrations of MGO. Data are presented as medians with interquartile ranges from three independent replicates. Statistically significant differences between the group treated with 10 μM MGO and control were assessed using the Kruskal-Wallis test followed by Dunn's post hoc test, and are indicated as * $p < 0.05$ and ** $p < 0.01$. Note the different scales of the Y-axes.

4.4 Discussion

In this study, we characterized the MGO-induced protein modifications by MGO in SH-SY5Y human neuroblastoma cells, with and without adding external MGO, using a proteomics approach. The modifications investigated included those on arginine, lysine, and cysteine residues, which are the major reaction sites for MGO^{41, 46}. In total 77 proteins were identified as proteins highly susceptible to MGO modification, indicative of non-random or hotspot modifications by MGO. From these, biomarkers for both exogenous and endogenous MGO exposure, as well as markers for MGO toxicity, were defined.

Proteins such as calcyphosin (CAPS) and serine/threonine-protein kinase SIK2 (SIK2) were defined as biomarkers for endogenous MGO exposure. CAPS is a calcium-binding protein involved in cell survival, differentiation, and transformation²¹⁰. It is expressed in most tissues and more intensively in tissues including the lung, colon, and brain²¹¹. The *in vitro* cell-free incubation study further confirmed CAPS as a biomarker for endogenous MGO exposure. Interestingly, 19 modified peptides were detected in the cell-free study, in contrast to only one modified peptide in the cell-based study. This discrepancy may be attributed to the difference in MGO concentrations used and the fact that in a cell-free system modifications may be different from those in cells.

Vimentin (VIM) emerged as a notable biomarker for exogenous MGO exposure, with 14 peptides identified as modified by MGO, displaying a significantly higher modification intensity than that observed in other proteins. As a key cytoskeletal component, VIM is instrumental in maintaining cellular integrity and regulating cell migration, adhesion, and division²¹². A previous study detected glyoxal-induced modifications on the lysine residues of proteins in human dermal fibroblasts, revealing an accumulation of modified VIM in the skin fibroblasts of elderly donors and attributing susceptibility of these lysine residues to modifications primarily to VIM's structural properties²¹³. However, our research revealed that modifications on VIM arginine residues appeared even more prevalent than those on lysine and cysteine residues.

Besides, dicarbonyl-modified VIM was previously shown to accumulate during the replicative senescence of human WI-38 fibroblasts *in vitro*, potentially due to senescence-associated decreased glyoxalase 1 activity, essential for detoxifying dicarbonyl compounds²¹⁴. Additionally, in our study while substantial modifications of VIM by MGO were observed in cell-based experiments at concentrations over 500 μ M, such modifications were not evident at MGO levels at or below 10 μ M, comparable to endogenous background levels, in cell-free *in vitro* experiments. This discrepancy suggests that *in vivo* modifications of vimentin might be more relevant to chronic exposure to higher MGO levels characterized by both elevated levels and prolonged exposure time to MGO, resulting from pathological conditions such as dicarbonyl stress, diminished detoxification efficacy, and higher glucose consumption.

Interestingly, while VIM is typically absent in neurons from the healthy adult brain, it has been reported that neurons may re-express VIM in response to local cellular or tissue damage from trauma and diseases such as Alzheimer's disease, serving as part of the mechanism aimed at repairing neuronal damage²¹⁵⁻²¹⁷. Additionally, neuronal VIM expression is positively correlated with amyloid deposition in the brains of Alzheimer's disease patients²¹⁷, indicating its potential involvement in disease pathophysiology. SH-SY5Y cells, commonly used as models for neuronal function and differentiation, retain characteristics of progenitor cells, including the expression of intermediate filaments like VIM²¹⁸. The modification of VIM by MGO, as observed in SH-SY5Y cells, suggests that such modifications could potentially interfere with the neuronal repair process. Notably, the accelerated accumulation of AGEs in cells and tissues is a prominent feature of Alzheimer's disease, and AGEs can be detected in pathological deposits such as amyloid plaques and neurofibrillary tangles²¹⁹. It is possible that the modification of vimentin, and potentially other biomarker proteins for MGO exposure, could influence amyloidogenic processes, promoting or stabilizing pathological protein aggregates or amyloids. Furthermore, differentiating between endogenous and exogenous

protein biomarkers and their modification levels may reflect underlying pathological conditions and could potentially indicate disease progression.

Structural constituents of the cytoskeleton were notably overrepresented in the PPI network (**Figure 4.7B**), encompassing six proteins including VIM, ACTB, and TUBB4B. Cytoskeletal proteins such as actin and tubulin are essential for neuronal structure and function and are implicated in various neurological disorders²²⁰. Their disruption is associated with pathologies like Alzheimer's disease and amyotrophic lateral sclerosis, due to their critical roles in supporting neural connectivity and modulating nerve signal transmission²²⁰. Comparing the MGO-modified proteins identified in our study with those modified by other electrophiles such as acrolein and 4-hydroxynonenal revealed that cytoskeletal proteins are commonly targeted by these reactive compounds²²¹⁻²²³. Modifications from acrolein and 4-hydroxynonenal typically occur on histidine, lysine, and cysteine residues, with proteins like VIM, TUBB4B, ACTB, and ACTG1 predominantly modified at histidine and lysine sites^{222, 223}. In contrast, modifications on cytoskeletal proteins like VIM and TUBB4B from MGO more frequently target arginine residues. The susceptibility of cytoskeleton proteins to electrophilic modifications, as observed in previous studies and ours, may be partly due to their relatively higher abundance within cells²²⁴. In addition to electrophile-induced modifications, cytoskeletal proteins such as actin and tubulin are also recognized targets for reactive oxygen species (ROS)-mediated oxidative damage²²⁵. Oxidative modifications of these proteins are implicated in regulating their dynamics under both normal physiological conditions and in response to oxidative stress^{225, 226}. For example, oxidative stress might inhibit actin polymerization²²⁷, while physiological levels of ROS are needed for proper cytoskeleton polymerization which may be involved in processes like neurite outgrowth^{228, 229}. Residues C285 and C347 in actin have been suggested to play a protective role against oxidative stress, contributing to the cell's general adaptive response to oxidative conditions²³⁰. Given the inferred dual role of oxidative modifications—both adaptive and potentially harmful—further investigations into the cellular effects of protein modifications induced by MGO and other electrophiles, may illuminate the roles these modifications may play in cellular adaptation and/or dysfunction under various stress conditions.

Enrichment and PPI network analysis also revealed motor proteins, and glycolysis/gluconeogenesis as significantly enriched terms. Motor proteins such as dynein and kinesin play a crucial role in dendritogenesis, facilitating the transport of essential components and signaling molecules within neurons²³¹. MGO-induced modifications on proteins such as KIF24 and DCTN4, observed in this study, might impair their functionality leading to disrupted dendritic growth and branching. With respect to glycolysis/gluconeogenesis, this pathway was also previously shown to be enriched with

MGO-modified proteins identified in WIL2-NS B lymphoblastoid cells¹⁰⁴. Given the glycolysis as the primary intracellular source of MGO, the authors suggested that the modification of glycolytic enzymes by MGO could act as a regulatory mechanism, potentially influencing metabolic pathways by reducing the activity of these enzymes, thus maintaining MGO at physiological concentrations¹⁰⁴. The modification of glycolysis proteins by MGO observed in this previous and our study may be linked to their localization close to where MGO is generated, combined with their relatively higher intracellular abundance. Lastly, exploring other proteins identified as modified by MGO in this study, along with the pathways enriched with these modified proteins, such as amyotrophic lateral sclerosis and tight junctions, is of interest to potentially contribute to elucidating the neurotoxic effects of MGO and their roles in neuronal disorders.

In this study we have successfully identified a set of proteins in SH-SY5Y cells that are susceptible to modifications by endogenous and exogenous MGO. However, the concentrations of exogenous MGO used were significantly above physiological levels. Despite this limitation, the observed modifications provide valuable insights into the cellular impact of protein modifications by MGO. These modifications help highlight the susceptibility of neuronal-like cells to dicarbonyl stress, an important factor in diseases such as Alzheimer's^{10, 95}. The use of high MGO concentrations in *in vitro* models facilitated the identification of robust biomarkers but may not accurately reflect the more subtle biochemical dynamics typical in neurodegenerative conditions, where dicarbonyl stress is chronic but not as intense as those simulated in our *in vitro* models. Future research could employ *in vitro* models that more closely simulate the increased intracellular MGO formation typically seen in pathological states, to further validate and explore these modifications especially under chronic exposure. Additionally, establishing a clearer validated link between these biomarker proteins from normal physiological conditions to pathological states, particularly in neurodegeneration, would enhance our understanding of their potential diagnostic and therapeutic roles in managing such diseases.

In conclusion, this study not only defined biomarkers for endogenous and exogenous MGO exposure but also provided insights into the effects of endogenously formed versus externally added MGO.

Acknowledgments

Liang Zheng is thankful for the financial support provided by the China Scholarship Council, under Grant Number: CSC202008510115.

Supporting information

Table S4.1. Statistical results from the Jonckheere-Terpstra Test for trend analysis of total intensity of detected MGO-modified peptide(s) within each protein with increasing MGO concentrations (Protein IDs and Gene names were retrieved from the UniProt).

No.	Protein ID	Protein name	Gene name	J statistic ^a	p-value
1	P08670	Vimentin	VIM	4.40	0.00001
2	P68371	Tubulin beta-4B chain	TUBB4B	4.37	0.00001
3	Q5QNW6	Histone H2B type 2-F	H2BC18	4.08	0.00004
4	P26641	Elongation factor 1-gamma	EEF1G	4.05	0.00005
5	P60660	Myosin light polypeptide 6	MYL6	2.96	0.00310
6	P63261	Actin, cytoplasmic 2, N-terminally processed	ACTG1	2.29	0.02
7	P22732	Solute carrier family 2, facilitated glucose transporter member 5	SLC2A5	2.25	0.02
8	Q9Y2V2	Calcium-regulated heat-stable protein 1	CARHSP1	2.16	0.03
9	Q08378	Golgin subfamily A member 3	GOLGA3	1.70	0.09
10	Q6NS11	Putative ankyrin repeat domain-containing protein 26-like protein	ANKRD26P1	1.56	0.12
11	Q9Y2F9	BTB/POZ domain-containing protein 3	BTBD3	1.51	0.13
12	Q9NXL9	DNA helicase MCM9	MCM9	1.25	0.21
13	Q8IVE3	Pleckstrin homology domain-containing family H member 2	PLEKHH2	1.05	0.29
14	Q8NCL9	Protein APCDD1-like	APCDD1L	0.98	0.33
15	Q86Y07	Serine/threonine-protein kinase VRK2	VRK2	0.89	0.37
16	P52298	Nuclear cap-binding protein subunit 2	NCBP2	0.88	0.38
17	Q9BXF9	Tektin-3	TEKT3	0.63	0.53
18	P60709	Actin, cytoplasmic 1, N-terminally processed	ACTB	0.63	0.53
19	A5A3E0	POTE ankyrin domain family member F	POTEF	0.63	0.53
20	P48643	T-complex protein 1 subunit epsilon	CCT5	0.57	0.57
21	P61550	Endogenous retrovirus group S71 member 1 Env polyprotein	ERV571-1	0.37	0.71
22	P52790	Hexokinase-3	HK3	0.33	0.74
23	P61160	Actin-related protein 2	ACTR2	0.24	0.81
24	P52179	Myomesin-1	MYOM1	0.14	0.89
25	P09874	Poly [ADP-ribose] polymerase 1	PARP1	0.05	0.96
26	O75182	Paired amphipathic helix protein Sin3b	SIN3B	0.05	0.96
27	P43354	Nuclear receptor subfamily 4 group A member 2	NR4A2	0.05	0.96
28	Q9UJW0	Dynactin subunit 4	DCTN4	0.05	0.96
29	Q9H4B7	Tubulin beta-1 chain	TUBB1	0.00	1.00
30	Q9H3R1	Bifunctional heparan sulfate N-deacetylase/N-sulfotransferase 4	NDST4	-0.05	0.96
31	Q2VY69	Zinc finger protein 284	ZNF284	-0.05	0.96
32	O75541	Zinc finger protein 821	ZNF821	-0.10	0.92
33	Q96QB1	Rho GTPase-activating protein 7	DLC1	-0.17	0.86
34	Q9NWS8	Required for meiotic nuclear division protein 1 homolog	RMND1	-0.19	0.85
35	Q8N8I0	Sterile alpha motif domain containing 12.	SAMD12	-0.19	0.85
36	P51553	Isocitrate dehydrogenase [NAD] subunit gamma, mitochondrial	IDH3G	-0.20	0.85
37	P52789	Hexokinase-2	HK2	-0.23	0.81
38	Q9H069	Dynein regulatory complex subunit 3	DRC3	-0.24	0.81
39	P56524	Histone deacetylase 4	HDAC4	-0.28	0.78
40	Q96AA8	Janus kinase and microtubule interacting protein 2	JAKMIP2	-0.38	0.70
41	P13639	Elongation factor 2	EEF2	-0.47	0.64
42	P60510	Serine/threonine-protein phosphatase 4 catalytic subunit	PPP4C	-0.56	0.58
43	Q9NWB1	RNA binding protein fox-1 homolog 1	RBFox1	-0.56	0.57
44	P17038	Zinc finger protein 43	ZNF43	-0.70	0.48
45	Q5T7B8	Kinesin-like protein KIF24	KIF24	-0.72	0.47
46	A5PLL1	Ankyrin repeat domain 34B	ANKRD34B	-0.75	0.46
47	Q9H0K1	Serine/threonine-protein kinase SIK2	SIK2	-0.75	0.46
48	Q8IZH2	5'-3' exoribonuclease 1	XRN1	-0.80	0.43
49	Q14683	Structural maintenance of chromosomes protein 1A	SMC1A	-0.89	0.37
50	Q92576	PHD finger protein 3.	PHF3	-0.89	0.37
51	Q4J6C6	Prolyl endopeptidase-like	PREPL	-0.93	0.35

(continued on next page)

Table S4.1 (continued)

No.	Protein ID	Protein name	Gene name	<i>J</i> statistic ^a	<i>p</i> -value
52	P16152	Carbonyl reductase [NADPH] 1	CBR1	-0.99	0.32
53	Q00872	Myosin-binding protein C, slow-type	MYBPC1	-1.08	0.28
54	Q86VV8	Rotatin	RTTN	-1.08	0.28
55	P52566	Rho GDP-dissociation inhibitor 2	ARHGDIB	-1.13	0.26
56	Q9HCD5	Nuclear receptor coactivator 5	NCOA5	-1.17	0.24
57	Q13751	Laminin subunit beta-3	LAMB3	-1.27	0.20
58	O94906	Pre-mRNA-processing factor 6	PRPF6	-1.30	0.19
59	P10827	Thyroid hormone receptor alpha	THRA	-1.31	0.19
60	Q70UQ0	IKBKB interacting protein.	IKBIP	-1.50	0.13
61	Q8IXZ2	Zinc finger CCCH domain-containing protein 3	ZC3H3	-1.54	0.12
62	Q9UGP8	Translocation protein SEC63 homolog	SEC63	-1.61	0.11
63	P35557	Hexokinase-4	GCK	-1.65	0.10
64	A8MPP1	Putative ATP-dependent RNA helicase DDX11-like protein 8	DDX11L8	-1.68	0.09
65	Q9Y4X0	AMMECR nuclear protein 1.	AMMECR1	-1.73	0.08
66	P25874	Mitochondrial brown fat uncoupling protein 1	UCP1	-1.78	0.08
67	P07355	AMMECR nuclear protein 1.	ANXA2	-1.83	0.07
68	A6NLP5	Tetratricopeptide repeat domain 36.	TTC36	-1.86	0.06
69	O14827	Ras-specific guanine nucleotide-releasing factor 2	RASGRF2	-1.88	0.06
70	Q8TED4	Glucose-6-phosphate exchanger SLC37A2	SLC37A2	-1.91	0.06
71	O15397	Importin-8	IPO8	-1.94	0.05
72	Q9H3R0	Lysine-specific demethylase 4C	KDM4C	-2.02	0.04
73	Q8TB72	Pumilio homolog 2	PUM2	-2.15	0.03
74	Q8N3X1	Formin binding protein 4.	FNBP4	-2.20	0.03
75	Q8N8K9	Uncharacterized protein KIAA1958	KIAA1958	-2.52	0.01
76	Q13938	Calcyphosin	CAPS	-2.80	0.01
77	O60304	Zinc finger protein 500	ZNF500	-2.87	0.004

^aThe *J* statistic values are ranked in descending order and reflect the direction and magnitude of the trend in intensity of the modified peptides with increasing MGO concentrations. A positive *J* statistic value indicates an upward trend, suggesting that the intensity of protein modification increases as MGO concentration rises. A negative *J* statistic value indicates a downward trend, suggesting a decrease in protein modification intensity with increasing MGO concentrations.

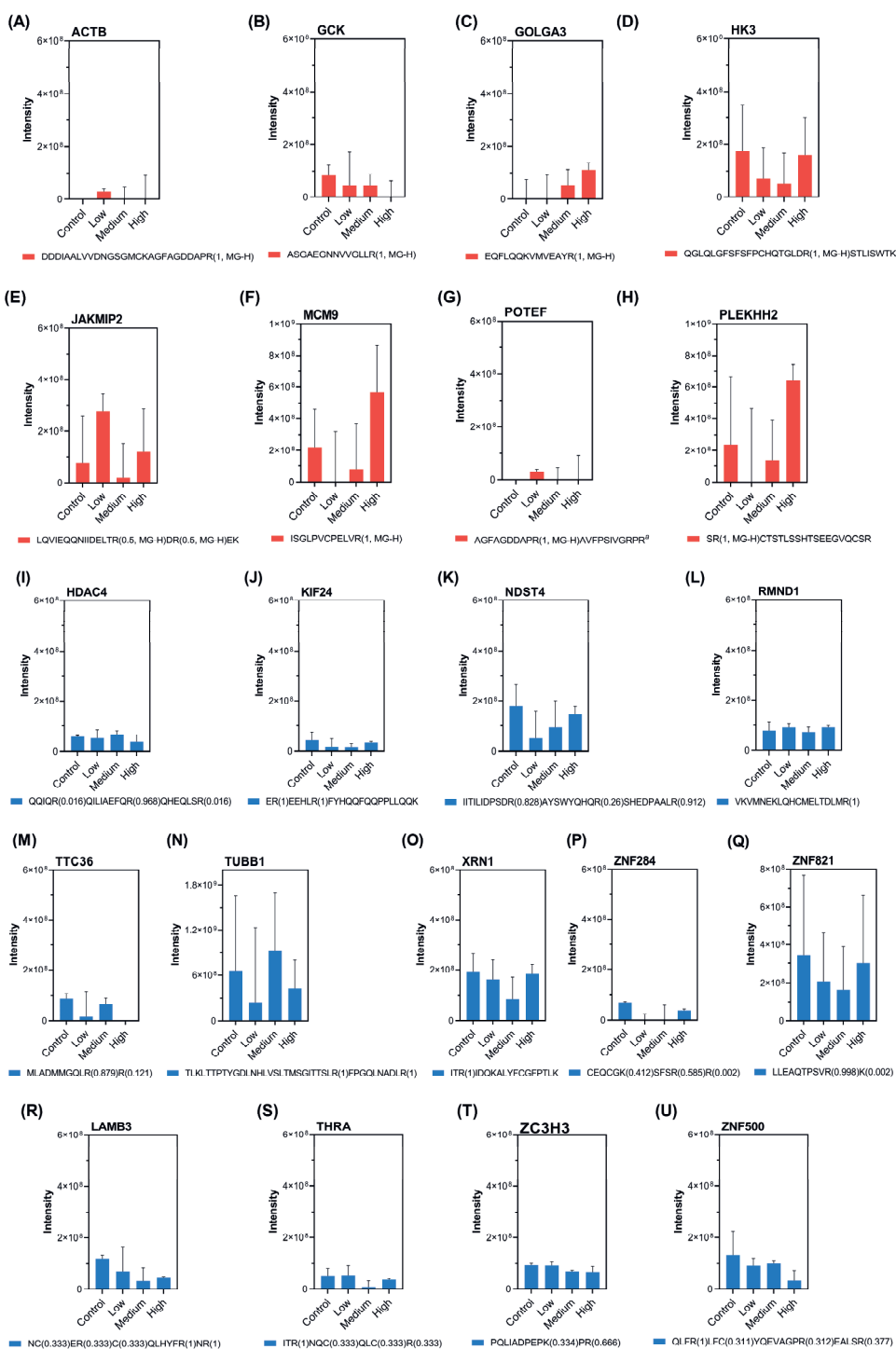


Figure S4.1 (continued)

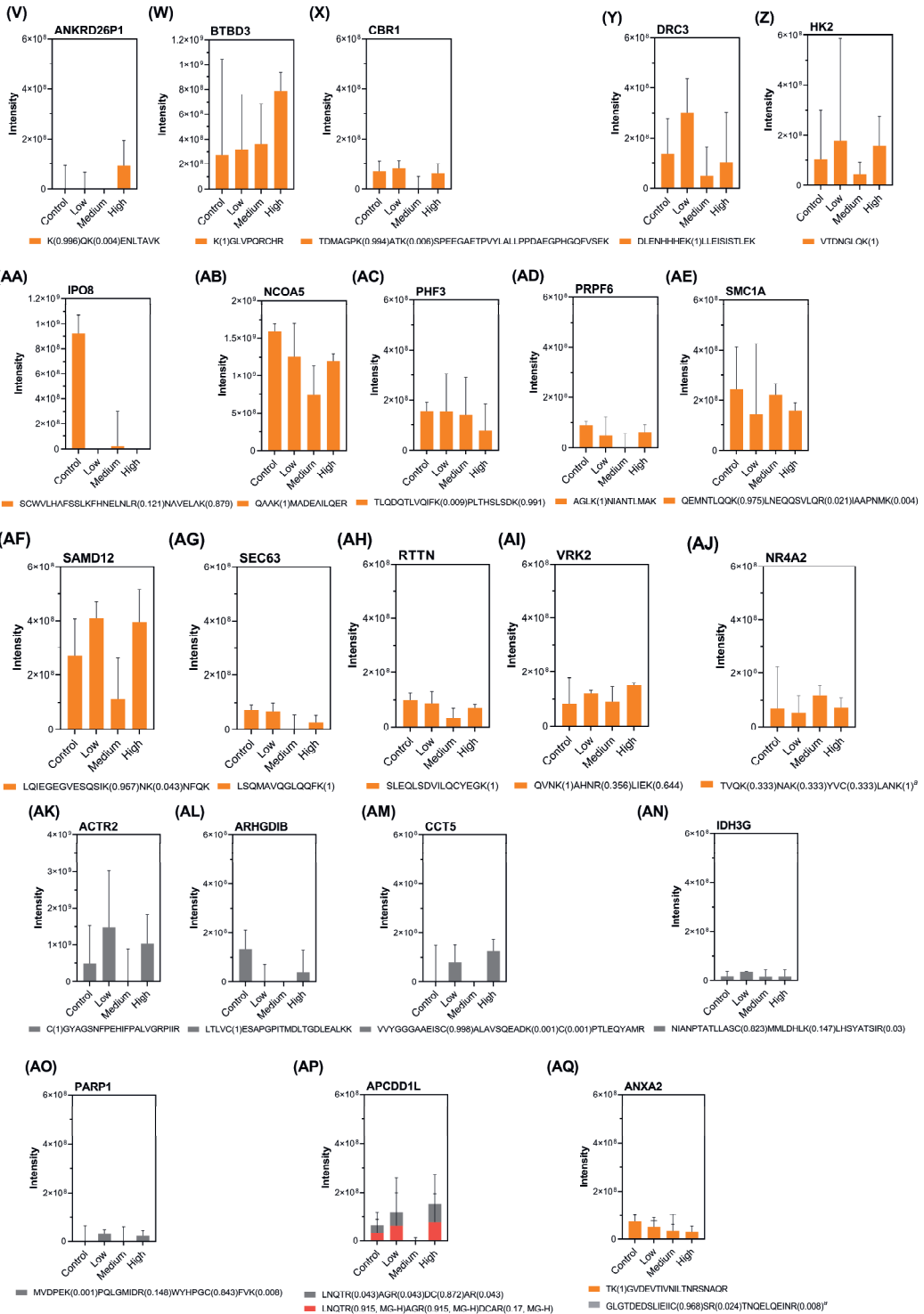


Figure S4.1 (continued)

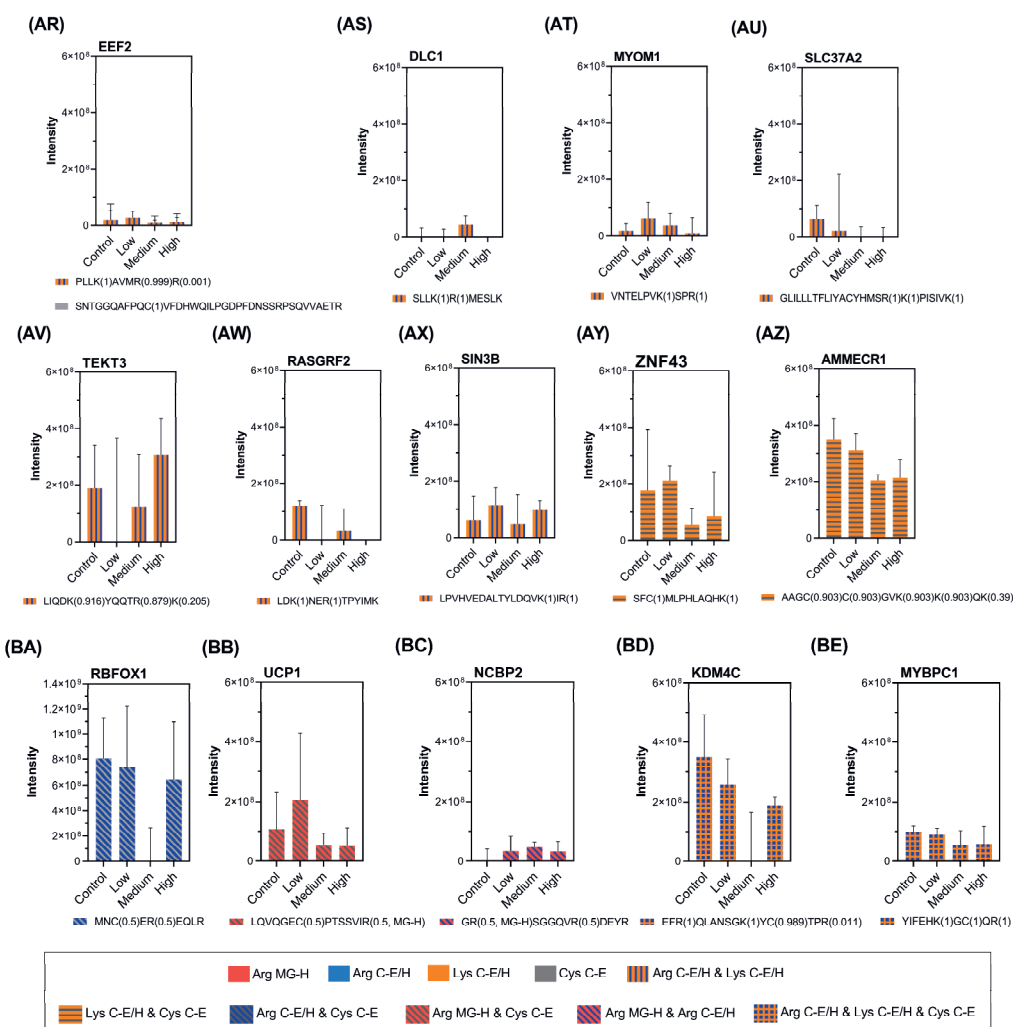


Figure S4.1. Intensity profiles of detected MGO-modified peptides in proteins defined as highly susceptible MGO modification but not meeting biomarker selection criteria. "a" indicates peptide hits that also match additional homologous protein sequences. Numbers in parentheses next to amino acids represent the probability of modification at that site. "MG-H" is specifically annotated in parentheses to distinguish between the two types of arginine modifications being studied. Peptides with multiple potential modification types (each having a probability ≥ 0.5) are denoted by pattern fills as indicated in the figure legend. Data are presented as medians with interquartile ranges, derived from four independent replicates. Note the different Y axis in panels F, H, N, Q, W, AA, AB, AK, and BA as compared to other panels.

5



Chapter 5

An Integrated Proteomics and Metabolomics Analysis of Methylglyoxal-Induced Neurotoxicity in a Human Neuroblastoma Cell Line

This chapter is based on:

Haomiao Wang, Sjef Boeren, Wouter Bakker, Ivonne M. C. M. Rietjens, Edoardo Saccenti*, Liang Zheng*. (2024). An integrated proteomics and metabolomics analysis of methylglyoxal-induced neurotoxicity in a human neuroblastoma cell line. *npj Science of Food* (Accepted).

DOI: 10.1038/s41538-024-00328-0

*Corresponding authors

Abstract

The increased endogenous formation of advanced glycation end products (AGEs) has been linked to many diseases, including neurodegenerative disorders. Methylglyoxal (MGO), extensively found in various food products and also formed endogenously, is the most reactive precursor of AGEs. MGO reacts with cellular free amino acids, proteins, and DNA to form AGEs, leading to structural and functional changes in these molecules, which potentially contribute to neurotoxicity. This study aimed to highlight the molecular and biochemical changes induced by MGO exposure in SH-SY5Y human neuroblastoma cells, and to explore how these changes contribute to neurotoxicity, utilizing integrated proteomics and metabolomics approaches. Using label-free quantitative nanoLC-MS/MS proteomics combined with targeted LC-TQ-MS/MS-based metabolomics, our results revealed that MGO exposure, particularly at cytotoxic levels, significantly altered the proteome and metabolome of SH-SY5Y cells. Analysis of proteomics data showed significant alterations in cellular functions such as protein synthesis, cellular structural integrity, mitochondrial function, and oxidative stress responses. Analysis of metabolomics and integration of metabolomics and proteomics data highlighted significant changes in key metabolic pathways, including arginine biosynthesis, glutathione metabolism, cysteine and methionine metabolism, and the tricarboxylic acid cycle. MGO exposure led to increased endoplasmic reticulum stress, disruptions in cellular adhesion and extracellular matrix integrity, mitochondrial dysfunction, and amino acid metabolism disruption, contributing to cellular toxicity. Conversely, cells exhibited adaptive responses by upregulating protein synthesis, activating the Nrf2 pathway, and reprogramming metabolism to counteract dicarbonyl stress and maintain energy levels. These findings provide insight into the molecular mechanisms underlying MGO-induced neurotoxicity and potential targets for therapeutic intervention.

Keywords: methylglyoxal; proteomics; metabolomics; neurotoxicity

5.1 Introduction

Neurodegenerative disorders, such as Alzheimer's disease (AD) and Parkinson's disease (PD), are increasingly prevalent globally due to aging populations and the lack of effective therapies²³². The pathogenic mechanisms underlying neurodegeneration are complex, involving various characteristics like oxidative stress, mitochondrial dysfunction, inflammation, and protein misfolding and aggregation²³³⁻²³⁵. The process of protein glycation, resulting in irreversible modifications in proteins, has been suggested to play important roles in these multifactorial diseases^{13, 129}. Protein glycation is a post-translational modification wherein reducing sugars or reactive dicarbonyl compounds, notably methylglyoxal (MGO) and glyoxal (GO), react non-enzymatically with amino acid residues on proteins, forming advanced glycation end products (AGEs)²³⁶. These modifications can alter protein structure and dynamics and induce the formation of protein cross-links, potentially promoting or stabilizing pathological protein aggregation, thereby contributing to neurodegeneration^{7, 237}. Furthermore, AGEs could induce cell dysfunction through interacting with the receptor for AGEs (RAGE), triggering oxidative stress and inflammatory responses²³⁸.

MGO, extensively found in various food products and endogenously formed as a by-product primarily from glycolysis, is the most reactive precursor for AGE formation both endogenously and exogenously^{22, 40, 185}. MGO concentrations are typically low in healthy individuals due to the relatively low internal production and effective detoxification by the glyoxalase system¹⁸⁶. Elevated *in vivo* MGO levels can occur under certain pathological conditions, such as hyperglycemia, when the balance in its production and metabolism is disrupted¹⁰. An increase in the steady-state level of reactive dicarbonyls, especially MGO, is the main cause of a dysfunctional metabolic state called dicarbonyl stress, resulting in increased modifications of cellular amino acids and biomacromolecules, including proteins and DNA, forming AGEs¹⁰.

Clinical research has revealed a correlation between elevated serum levels of MGO and accelerated cognitive decline in elderly individuals²³⁹ and found increased levels of MGO and the resulting AGEs in the cerebrospinal fluid of AD patients^{240, 241}. Similarly, increased levels of MGO-derived AGEs have been detected in the nigral neurons of PD patients⁸⁷. In an animal study, aged mice orally treated with 100 mg/kg bw MGO for four weeks developed cognitive impairment, accompanied by increased expression of RAGE and Presenilin-1 (a critical component of the gamma-secretase complex involved in AD) in the hippocampus²⁴². Additionally, in *Caenorhabditis elegans*, long-term dietary exposure to MGO led to AD-related toxicity including reduced locomotive behaviors and promoted amyloid β accumulation²⁴³. These clinical and animal findings underscore the pathological relevance of MGO in the context of neurodegeneration. Furthermore, *in vitro* studies using different neuronal cell

models, such as human SH-SY5Y neuroblastoma cell line and neuronal-like cells transdifferentiated from human mesenchymal stem cells, have shown that exposure of cells to exogenous MGO reduced cell viability and mitochondrial redox activity, as well as increased the production of reactive oxygen species (ROS) and apoptosis^{76, 95, 96, 244}. However, the modes of action underlying these toxic effects induced by MGO, which may play roles in neurodegeneration, remains largely unclear.

Given that the neurotoxic effects of MGO may result from its complex interactions with free cellular amino acids and biomacromolecules, causing damage across the cellular metabolome, proteome, and genome^{41, 245}, traditional toxicological methods that focus on limited endpoints may not adequately capture the broader biological or toxicological impacts of MGO, especially the alterations in gene and protein expression in response to MGO exposure. Omics techniques, such as transcriptomics, proteomics, and metabolomics, offer a more comprehensive view, enabling the analysis of thousands of molecules in a single biological sample¹¹³, which could potentially enhance our understanding of the toxicological mechanisms and adverse outcome pathways associated with MGO exposure. A previous study using 2D fluorescence difference gel electrophoresis coupled with MALDI-TOF-MS identified 49 differentially expressed proteins in MGO-treated SH-SY5Y cells²⁴⁶. However, this gel-based proteomics approach is limited by its inability to detect low-abundance proteins and its ineffectiveness in resolving complex protein mixtures, which could lead to overlooking critical biomarkers²⁴⁷.

In contrast, in the present study we utilized an untargeted, label-free quantitative proteomics approach with nanoLC-MS/MS to explore the cellular mechanisms of neurotoxicity induced by MGO in SH-SY5Y cells, a widely recognized neuronal cell model for investigating the pathological effects of neurotoxic compound¹⁰³. This method substantially broadens the detectable proteome, providing a more detailed and comprehensive proteomic profile that could capture subtle changes, including those involving low-abundance proteins²⁴⁸. Additionally, a targeted metabolomics approach using LC-TQ-MS/MS was applied to investigate the impact of MGO on the cellular metabolome, offering insights into metabolic alterations and the overall metabolic state of the cells. Integrating both proteomics and metabolomics could provide a holistic view of the phenotypic changes and the complex molecular interactions between proteins and metabolites triggered by MGO exposure, enabling a deeper exploration into the disrupted cellular pathways and their potential contributions to MGO neurotoxicity.

5.2 Materials and methods

5.2.1 Chemicals and Reagents

MGO (40 wt % in water) and acetic acid (purity $\geq 99\%$) were purchased from Merck (Darmstadt, Germany). Methanol and acetonitrile (ACN) were obtained from Biosolve BV (Valkenswaard, the Netherlands). Formic acid (purity $\geq 99\%$) was purchased from VWR CHEMICA (Amsterdam, The Netherlands). Dulbecco's Modified Eagle Medium/Nutrient Mixture F-12 (DMEM/F12) with GlutaMAX supplement cell culture medium with and without phenol red, trypsin-EDTA for cell dissociation, phosphate buffered saline (PBS), penicillin/streptomycin, and nonessential amino acids (NEAA) were purchased from Gibco (Paisley, UK). Foetal calf serum (FCS) was purchased from Invitrogen (Breda, The Netherlands). All other reagents in this study were of analytical grade or purer.

5.2.2 Cell culture and MGO treatment

The human neuroblastoma cell line SH-SY5Y (ATCC CRL-2266) was obtained from the American Type Culture Collection (ATCC, Manassas, VA, USA). Cells were maintained in a humidified incubator at 37°C and 5% CO₂. The culture medium consisted of DMEM/F12 GlutaMAX supplemented with 10% fetal calf serum (FCS), 1% non-essential amino acids (NEAA), and 1% penicillin/streptomycin. Medium was refreshed every 4 to 7 days, and cells were subcultured at a 1:20 ratio upon reaching confluency using a 0.05% trypsin-EDTA solution.

For the proteomics and metabolomics studies, three concentrations of MGO—500, 750, and 1000 μM —were used to treat the cells. These concentrations were chosen based on our previous MTT cell viability assay²⁴⁹, which showed that 500 and 750 μM MGO did not significantly affect cell viability, while at 1000 μM , there was a significant reduction, with 68.0% of viability remaining. The cell seeding density for the proteomics and metabolomics studies was the same as that used in the MTT assay.

5.2.3 Label-free quantitative proteomics analysis

5.2.3.1 Proteomic sample preparation

SH-SY5Y cells were seeded in T175 flasks (Greiner Bio-one, Alphen aan den Rijn, The Netherlands) at a density of 4.69×10^4 cells/cm² and incubated for 24 hours. After incubation, the cells were treated with an assay medium (DMEM/F12 without phenol red and FCS supplement) that contained MGO at three concentrations (500, 750, and 1000 μM , final

concentration, added from 200 times concentrated stock solutions in nano pure water) or with a solvent control (0.5% nano pure water in DMEM/F12 without phenol red and FCS supplement) for 24 hours. After exposure, the cells were washed twice with PBS. Subsequently, 1.8 mL of ice-cold PBS was added to each flask, and the cells were gently scraped off. The cell suspension was then transferred into a 2-mL protein low-binding tube (Eppendorf, Nijmegen, The Netherlands) and centrifuged at $500 \times g$ for 2 minutes at 4°C to collect the cell pellets. These pellets were washed twice using 1.5 mL ice-cold 100 mM Tris-hydrochloride (Tris-HCl, pH 8) under identical centrifugation conditions. The washed pellets were resuspended in 90 μL 100 mM Tris-HCl pH 8 with 1% protease inhibitor cocktail (Thermo Fisher Scientific, Bleiswijk, The Netherlands), followed by sonication in an ice-water bath (Qsonica sonicator, Qsonica, Newtown, USA) for 30 minutes using a pulse mode (30 seconds on and 30 seconds off) at 100% amplitude. Protein concentrations were measured using a BCA protein assay kit according to the manufacturer's instructions (Thermo Fisher Scientific, Bleiswijk, The Netherlands). The Protein Aggregation Capture (PAC) method was utilized to prepare peptide samples for nanoLC-MS/MS analysis¹⁹⁴. These peptide samples were immediately stored at -20°C until further analysis. All treatments were conducted in four independent biological replicates.

5.2.3.2 NanoLC-MS/MS based label-free quantitative proteomics analysis

NanoLC-MS/MS analysis was conducted using a Thermo Vanquish Neo nanoLC system connected to a Thermo Orbitrap Exploris 480 mass spectrometer (Thermo Fisher Scientific, Bremen, Germany). An in-house prepared 0.10 mm \times 250 mm analytical column filled with 1.9 μm ReproSil-Pur 120 C18-AQ beads was used. The mobile phase consisted of 0.1 v/v% formic acid in water (eluent A) and 0.1% formic acid in acetonitrile (eluent B). The elution was carried out using a three-step linear gradient, starting from 0 to 9% B over 1 minute, increasing from 9% to 34% B over 50 minutes, and then from 34% to 50% B over 4 minutes. This was followed by maintaining the gradient at 50% B for 1 minute, after which it was returned to the initial conditions and held there for a duration equivalent to 2.5 column volumes at 925 bar to prepare for the next injection. The injection volumes were adjusted to correct for variations in protein concentrations among the samples, based on the BCA assay results, with injection volumes ranging from 1 to 2 μL . The elution flow rate was maintained at 500 nL/min. An electrospray potential of 3.5 kV was applied to the eluent prior to entering the column, and automatic gain control targets for MS and MS/MS were set to 300% and 100%, respectively, with maximum ion injection times capped at 50 ms for MS and 30 ms for MS/MS. Higher energy collisional dissociation was utilized to fragment the most abundant 2-5+ charged peaks identified in the MS scan, employing an isolation width of 1.2 m/z and 28% normalized collision energy, with MS/MS scans conducted in a data-dependent mode at a

resolution of 15,000, applying a threshold of $5e4$ and a 15-second exclusion duration for previously selected $m/z \pm 10$ ppm.

5.2.3.3 Protein Identification and Quantification

The peptides were identified and quantified using the MaxQuant software package (version 2.0.3.0). A human database (UP000005640) retrieved from UniProt ("UniProt: the universal protein knowledgebase in 2021," 2021) along with a contaminants database that contains sequences of common contaminants like Trypsins (P00760, bovine and P00761, porcine) were utilized for analysis. Data were filtered to include only the proteins that were reliably identified by at least two peptides, at least one of which was unique, and one was unmodified and had a false discovery rate (FDR) below 1% on both the protein and peptide level. Reversed hits were removed from the MaxQuant result table.

5.2.4 Targeted metabolomics analysis

5.2.4.1 Metabolite extraction

SH-SY5Y cells were seeded in 6-well plates (Greiner Bio-One) at a density of 4.69×10^4 cells/cm² and incubated for 24 hours. For each well, a parallel setup was implemented: one well designated for metabolite extraction and another for cell counting, with both wells undergoing identical exposure conditions as specified in **Section 5.2.3.1** for the proteomics study. In the wells designated for metabolite extraction, metabolic activity was quenched by adding 500 μ L of 80% methanol (methanol, 80:20 v/v) at -70°C . The cells were then carefully scraped while maintained on dry ice and transferred to a 2-mL tube (Eppendorf). Concurrently, cells in the parallel counting wells were detached using trypsin-EDTA, resuspended in 500 μ L of PBS (2% FCS), and cell numbers and concentrations were determined from a 20 μ L aliquot using a Cellometer (Nexcelom Bioscience, Lawrence, USA). The suspension collected in the 2-mL tube from the wells designated for metabolite extraction was centrifuged at $6000 \times g$ for 5 minutes, and the supernatants were collected in a new 2 mL Eppendorf tube. The cell pellets underwent two additional extractions with 500 μ L of 80% methanol each, with all extracts pooled directly into the same tube. These combined extracts were dried under nitrogen gas, reconstituted in 100 μ L of 50% methanol with 1 μ L acetic acid, and centrifuged at $13000 \times g$ for 5 minutes to remove debris. The prepared samples were then immediately stored at -80°C until LC-MS analysis. All treatments were conducted in four independent biological replicates.

5.2.4.2 LC-TQ-MS/MS based quantification of metabolites

The metabolomics study for the cell metabolite extracts was performed using a Shimadzu Nexera XR LC-20AD XR UHPLC system coupled with a Shimadzu 8050 triple quadrupole mass spectrometer with an electrospray ionization (ESI) interface (Shimadzu Corporation, Kyoto, Japan), accompanied by the LC/MS/MS Method Package for Primary Metabolites ver. 2 (Shimadzu Corporation). This method package offers optimized analytical conditions including chromatogram acquisition, detection of mass spectral peaks via an incorporated mass spectral library, and method files that specify the analytical conditions, which enables simultaneous quantification of 97 metabolites including amino acids, organic acids, nucleosides, and nucleotides. These metabolites are important in central cellular pathways such as the glycolytic system, tricarboxylic acid (TCA) cycle, and amino acid metabolism.

A Supelco Discovery HS F5-3 column (2.1 mm × 150 mm, 3 μm) was employed during the experiment with a flow rate of 0.25 mL/min. Ultrapure water containing 0.1% formic acid (A) and acetonitrile with 0.1% formic acid (B) were used as mobile phase. The following gradient was used: 0-2 min, 100% A; 2-5 min, 100-75% A; 5-11 min, 75-65% A; 11-15 min, 65-5% A; 15-20 min, 5% A; 20-20.1 min, 5-100% A; 20.1-28 min, 100% A. The injection volume was 1 μL. The analysis settings for MS were determined according to the manufacturer's instructions included in the method package for primary metabolites ver. 2 (Shimadzu Corporation).

In addition to the original Shimadzu method which quantifies 97 primary metabolites, we have also incorporated the quantification of methylglyoxal-derived hydroimidazolone 1 (MG-H1). MG-H1 is the most abundant free-form AGE *in vivo*, formed from methylglyoxal and arginine²⁵⁰. It was monitored at the $[M + H]^+$ of precursor to product ion transitions of m/z 229.0 > 114.0 (collision energy = -10 eV).

5.2.5 Statistical analysis

5.2.5.1 Data pre-processing

For proteomics data, zero label-free quantitation (LFQ) intensity values were replaced with a value of 10^7 (slightly lower than the lowest measured value) to facilitate sensible ratio calculations, and LFQ intensities were logarithmically transformed to base 10 for further statistical analysis.

For metabolomics data, peak identification and integration were carried out using LabSolutions software 5.114 (Shimadzu Corporation) to obtain intensity values for detected metabolites. Intensity values of metabolites in each sample were divided by the

corresponding cell count to correct for variations in cell numbers, ensuring comparable metabolite measurements across samples. Data were normalized using a pooled sample from the control group, then log-transformed and mean-centered using MetaboAnalyst 6.0 (<https://www.metaboanalyst.ca/>)²⁵¹.

5.2.5.2 Multivariate analysis

Principal component analysis (PCA) was conducted on the log-transformed LFQ intensities for proteomics data using the `prcomp` function from the `stats` package in R software 4.3.1²⁵², with data centered and scaled to normalize variance across different measurements. For metabolomics data, PCA was performed on the pre-processed data using the same function in R without additional centering and scaling to unit variance.

5.2.5.3 Univariate analysis

The fold change (FC) of proteins and metabolites was calculated as the ratio of the average intensities of each MGO-treated group to that of the control. Student's *t*-test was performed on the respective datasets to compare differences between the control and different concentrations of MGO-treated groups, with *p* values below 0.05 considered statistically significant. Proteomics data were analyzed using Perseus version 1.6.2.1²⁵³, while metabolomics data were analyzed using MetaboAnalyst.

5.2.5.4 Selection of differentially expressed proteins (DEPs) and differential metabolites (DMs)

DEPs and DMs across varying concentrations of MGO-treated groups were identified using the same selection criteria. Both DEPs and DMs were chosen based on FCs greater than 1.2 or less than 0.83, accompanied by *p* values less than 0.05 relative to the control group.

5.2.5.5 Pathway and network analysis

For proteomics data, enrichment analysis for differentially expressed proteins (DEPs) was conducted using DAVID v2023q4 (<https://david.ncifcrf.gov/>, accessed April 2024), including GO terms, KEGG pathways, and WikiPathways²⁰⁰. A protein-protein interaction (PPI) network was constructed for DEPs with a high confidence level set at 0.7 utilizing the STRING database 12.0 (<https://string-db.org/>, accessed April 2024)²⁰¹. Molecular Complex Detection (MCODE) (version 2.0.3)²⁵⁴ in Cytoscape (version 3.10.2)²⁵⁵ was used to identify key functional modules in PPI network with parameters set as follows: degree cutoff = 2, node score cutoff = 0.2, K-core = 2, and max depth = 100. Hub proteins were identified using the CytoHubba plugin with the maximal clique centrality (MCC) method²⁵⁶ in Cytoscape.

For metabolomics data, pathway enrichment analysis of DMs identified from the high-concentration MGO-treated group (1000 μ M MGO) was performed using MetaboAnalyst according to the KEGG database. Pathways with pathway impact greater than 0.20 and p values less than 0.05 were considered significant.

5.2.5.6 Integrated analyses of metabolomics and proteomics

To better understand the interactions between proteins and metabolites, an integrated analysis of metabolomics and proteomics data was conducted, including correlation analysis and joint pathway analysis. Given the large number of DEPs, the correlation analysis focused on all DMs and proteins identified in the top 5 key functional modules in PPI network, both derived from the high-concentration MGO-treated group. Correlation between proteomics and metabolomics data was quantified using Spearman's correlation (`cor.test()` function in R) using only proteins identified in the top 5 key functional modules in PPI network and all DMs. The matrices of median concentrations of each treatment group were merged column-wise before taking pair-wise correlation among proteins and metabolites. Only correlation greater than 0.75 (in absolute value) and with p values < 0.01 were retained for analysis and visualized using Cytoscape.

Subsequently, DEPs and DMs were subjected to joint pathway analysis using MetaboAnalyst based on KEGG database. Pathways with an impact greater than 0.20 and p values less than 0.05 were deemed significant.

5.2.5.7 Data visualization

The bar charts, enrichment results, heatmaps depicting the intensity of DEPs and DMs, and volcano plots illustrating these entities were visualized through the SRplot webserver (www.bioinformatics.com.cn/srplot)²⁰², accessed on April 2024.

5.3 Results

5.3.1 Effects of MGO exposure on the proteome of SH-SY5Y cells

To assess the effects of MGO exposure on the proteomic profile of SH-SY5Y cells and to provide insight into the pathways disturbed by the exposure, quantitative proteomics was performed using MGO concentrations of 500, 750, and 1000 μ M, with the highest concentration being cytotoxic as determined by our previous MTT viability assay²⁴⁹. In total, 3160 proteins were identified and quantified using a 1% false discovery rate filter. PCA was performed on these proteins. The 3D PCA plot, as shown in **Figure 5.1A**, revealed a distinct

separation between the MGO-treated groups and the control group. The PCA accounted for 55.8% of the variation in the protein profiles with PC1, PC2, and PC3. The variation observed suggested that MGO exposure, particularly at the highest MGO concentration, substantially altered the proteome in SH-SY5Y cells compared to the untreated control cells.

Subsequently, DEPs in each MGO treatment group were identified by comparison to the control group (see **Section 5.2.5.4** for selection criteria). As shown in **Figure 5.1B**, there were 93 DEPs (59 upregulated and 34 downregulated) in the low-concentration MGO-treated group (500 μ M), 204 DEPs (108 upregulated and 96 downregulated) in the medium-concentration MGO-treated group (750 μ M), and 453 DEPs (223 upregulated and 230 downregulated) in the high-concentration MGO-treated group (1000 μ M). The volcano plots in **Figure 5.1C** illustrate the distribution of DEPs in each MGO-treated group compared to the control group, and the expression levels of the 453 DEPs identified in the high-concentration MGO-treated group were visualized across all four treatment groups in a clustering heatmap (**Figure 5.1B**). These results indicate that low-concentration MGO exposure (500 μ M) had a lesser impact on the protein profile of SH-SY5Y cells, whereas exposure to higher concentrations, especially the highest tested concentration of 1000 μ M, which is cytotoxic, substantially altered the protein expression profile. Considering the substantial changes in protein profile and the significant reduction in cell viability in the high-concentration MGO-treated group (1000 μ M), subsequent analyses focused on this treatment group to further explore the biological functions and pathways perturbed by MGO, relevant to its neurotoxicity. The *p* values and fold changes of the DEPs identified in the high-concentration MGO-treated group, relative to control, can be found in **Table S5.1**.

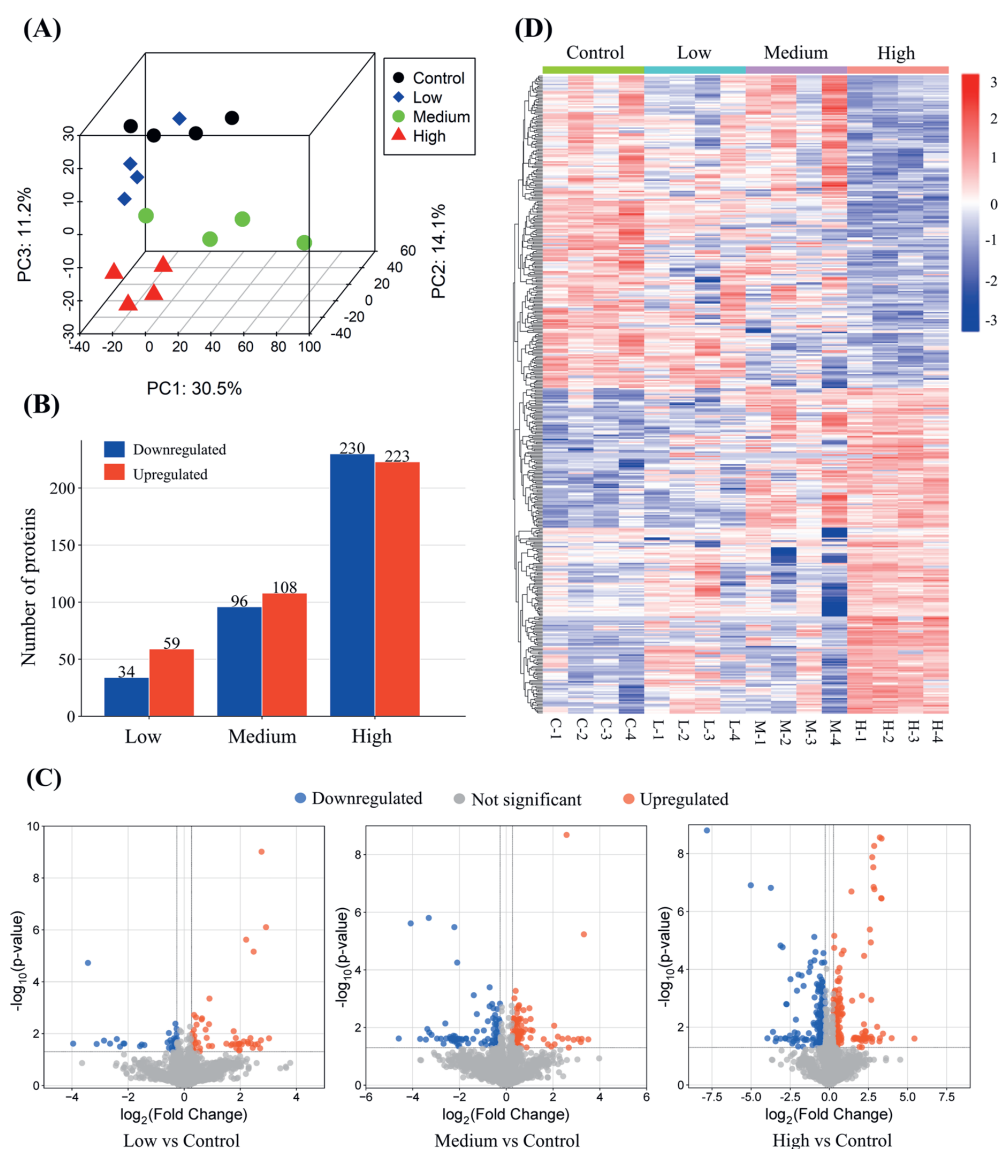


Figure 5.1 Proteomic analysis of SH-SY5Y cells after 24 h exposure to MGO. (A) 3D PCA plot based on the expression levels of 3160 proteins. (B) The number of upregulated and downregulated differentially expressed proteins (DEPs) in different MGO-treated groups. (C) Volcano plot of proteins quantified in different MGO-treated groups (red dots: upregulated DEPs, blue dots: downregulated DEPs, gray dots: proteins with no significant change). (D) Heatmap of the 453 DEPs identified in the high-concentration MGO-treated group presented for all treatment groups. Columns represent groups and rows represent proteins. The color gradient from blue to red indicates the protein expression level from low to high. Treatment groups are labeled as follows: control (C-x) for 0 μ M MGO, low (L-x) for 500 μ M MGO, medium (M-x) for 750 μ M MGO, and high (H-x) for 1000 μ M MGO. The 'x' in each label represents the replicate number, ranging from 1 to 4.

GO, KEGG, and WikiPathways analyses were conducted on DEPs identified in SH-SY5Y cells treated with the high concentration of MGO. The GO enrichment analysis (**Figure 5.2A**) revealed significant impacts on ribosomal RNA processing and ribosome biogenesis, highlighting potential disruptions in protein synthesis. Alterations were also observed in cellular components such as the nucleoplasm and extracellular exosomes, suggesting changes in both intracellular architecture and extracellular communication. Molecular function changes, including those affecting RNA, protein, and nucleosomal DNA binding activities, underscored potential disruptions in molecular interactions. These findings emphasize the extensive cellular and molecular disturbances induced by MGO.

KEGG pathway analysis (**Figure 5.2B**) further demonstrated the impact on ribosome biogenesis and protein processing in the endoplasmic reticulum, essential for proper protein folding and synthesis. Additionally, pathways related to focal adhesion and the regulation of the actin cytoskeleton were also significantly affected, indicating changes crucial for cell morphology and structural integrity. MGO's impact on pathways associated with diabetic cardiomyopathy underscored its potential role in metabolic dysregulation, a common feature in diabetes characterized by elevated MGO levels²⁵⁷. This was further evidenced by significant enrichments in metabolic pathways, biosynthesis of amino acids, and oxidative phosphorylation, all pointing to MGO's extensive impact on cellular metabolism. WikiPathways analysis (**Figure 5.2C**) revealed significant effects of MGO on the cellular oxidative stress response, particularly through the enrichment of the Nrf2 signaling pathway.

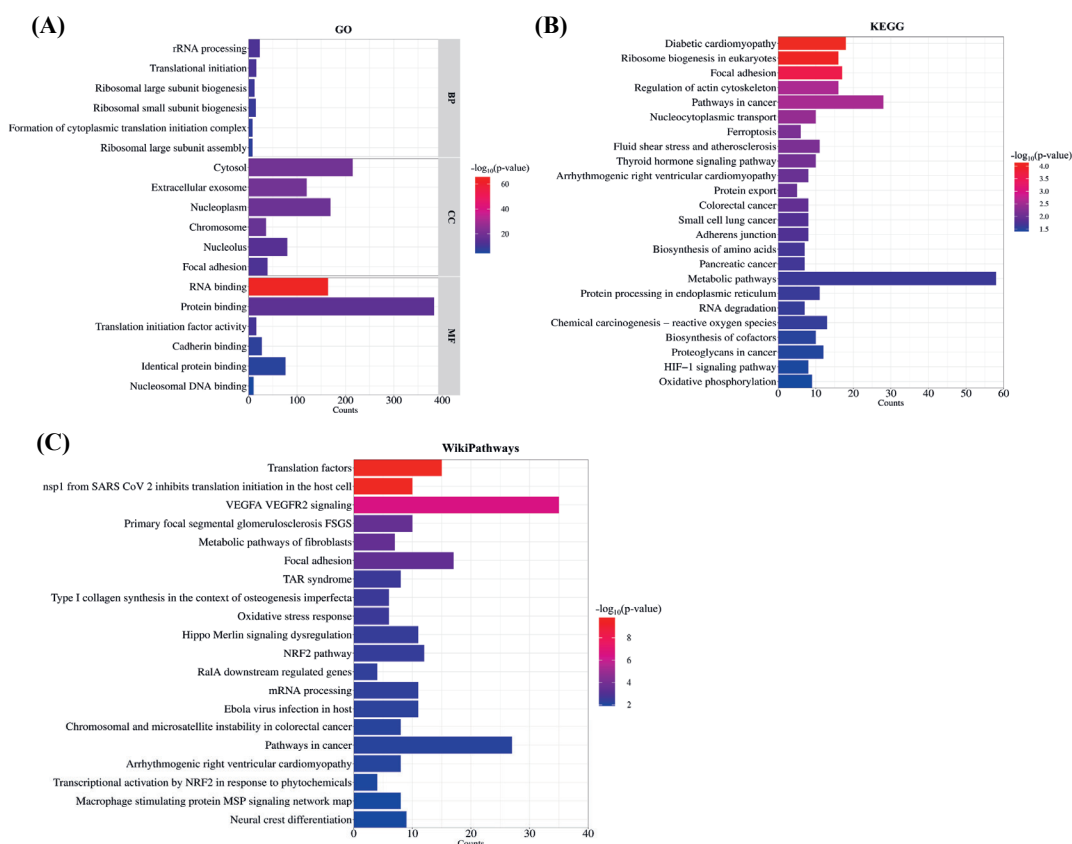


Figure 5.2 Enrichment analysis of differentially expressed proteins (DEPs) identified in the high-concentration MGO-treated group (1000 μ M MGO) compared to control using DAVID. (A) GO enrichment analysis for the categories of biological process (BP), cellular component (CC), and molecular function (MF); the top six enriched terms for each category are shown, selected based on the p values. (B) KEGG pathway enrichment analysis. (C) WikiPathways enrichment analysis (top 20 enriched terms are shown according to the p values).

Protein-protein interaction (PPI) analysis was conducted on DEPs identified from the high-concentration MGO-treated group to delve deeper into the essential proteins and their association with pathways significantly enriched, as analyzed above. The PPI network constructed with DEPs, consisting of 451 nodes and 1681 edges (**Figure S5.1**), was further analyzed using the MCODE plugin in Cytoscape to identify key functional modules. Based on their network scores, the top five densely connected modules were extracted and analyzed for their specific protein compositions (**Figure 5.3**). All selected modules had MCODE scores greater than 3.5. Enrichment analysis was subsequently performed for each module to further elucidate their associated biological functions (**Table 5.1**). Notably, Modules 1 and 2 were both linked to protein synthesis: Module 1 primarily involved proteins related to ribosome biogenesis, such as RBM28, TBL3, UTP4, and WDR3; while Module 2 focused on proteins

involved in translation initiation, including EIF4A1, EIF1AX, and EIF3M. Module 3 was crucial for maintaining cell structure and mediating cell-matrix interactions, featuring proteins like ITGB1, COL1A1, and LAMB1. Module 4 played a key role in energy metabolism and mitochondrial function through oxidative phosphorylation, with proteins such as NDUF7, UQCRB, and COX5B. Finally, Module 5 was linked to oxidative stress responses through the Nrf2 pathway, with critical proteins like NQO1, HMOX1, and GCLM.

Using the CytoHubba plugin in Cytoscape, the top 10 hub proteins (**Figure S5.2**)—PES1, NOC2L, GTPBP4, PDCD11, NOP2, MRTO4, GNL3, GRWD1, RPF2, and TSR1—were identified based on their MCC scores and were all found to be localized in Module 1, indicating the importance of this module.

Overall, the enrichment and PPI network analysis results suggest that exposure of cells to MGO leads to notable changes in several key cellular processes; these changes include abnormal protein synthesis, compromised cellular structure integrity, metabolic dysfunction, and enhanced responses to oxidative stress.

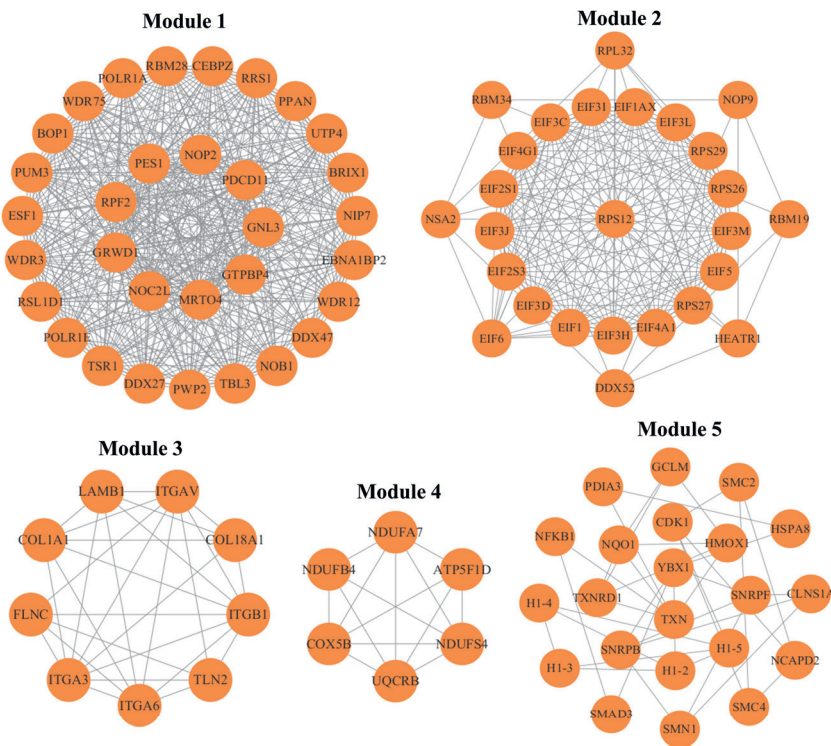


Figure 5.3 Top 5 densely connected modules in the protein-protein interaction network according to the network scores identified using the MCODE plugin in Cytoscape. Enrichment results for each module are presented in Table 5.1.

Table 5.1 Top 5 densely connected modules in the protein-protein interaction network, with enrichment analysis results. Enrichment analysis was conducted using DAVID for each module presented in Figure 5.3. Representative terms were selected for each module to highlight key biological functions. '↑' indicates upregulated protein expression, while '↓' signifies downregulated protein expression.

Modules	Nodes	Edges	Enriched terms	FDR	Proteins
Module 1	32	459	Ribosome biogenesis in eukaryotes (hsa03008)	1.4×10 ⁻¹²	RBM28↑, TBL3↑, UTP4↑, NOB1↓, WDR3↑, WDR75↑, PWP2↑, GTPBP4↑, GNL3↑
			rRNA processing (GO:0006364)	4.8×10 ⁻¹⁷	DDX27↑, DDX47↑, PPAN↑, WDR75↑, BOP1↑, TBL3↑, EBNA1BP2↑, PDCD11↑, NOB1↓, PES1↑, MRTO4↑, ESF1↑, BRIX1↑
Module 2	26	186	Ribosome (hsa03010)	3.2×10 ⁻⁴	RPS26↑, RPS27↓, RPL32↓, RPS29↓, RPS12↑
			Translational initiation (GO:0006413)	7.0×10 ⁻²⁶	EIF4A1↑, EIF1AX↑, EIF2S1↑, EIF1↑, EIF3M↑, EIF2S3↑, EIF6↑, EIF3L↑, EIF3I↑, EIF3J↑, EIF3H↑, EIF3C↑, EIF3D↑, EIF4G1↑
Module 3	9	29	Focal adhesion (hsa04510)	7.7×10 ⁻¹⁰	ITGB1↓, COL1A1↓, ITGA3↓, ITGAV↓, ITGA6↓, LAMB1↓, TLN2↓, FLNC↑
			ECM-receptor interaction (hsa04512)	7.8×10 ⁻⁸	ITGB1↓, COL1A1↓, ITGA3↓, ITGAV↓, ITGA6↓, LAMB1↓
Module 4	6	14	Oxidative phosphorylation (hsa00190)	1.6×10 ⁻⁹	NDUFA7↓, UQCRB↑, NDUFB4↓, NDUFS4↑, COX5B↓, ATP5F1D↑
Module 5	22	37	Nrf2 pathway (WP2884)	6.0×10 ⁻³	NQO1↑, TXNRD1↑, HMOX1↑, TXN↑, GCLM↑

5.3.2 Effects of MGO exposure on the metabolome of SH-SY5Y cells

Considering the effect of MGO on cellular metabolism as revealed in the proteomics study, a targeted metabolomic study using the same exposure conditions as those used in the proteomics study was conducted to further explore the cellular metabolic response upon MGO exposure. In total, 75 out of the 98 compounds were detected and quantified in the samples. The PCA plot showed a distinct separation between the MGO-treated groups and the control (**Figure 5.4A**), indicating MGO exposure, especially at the highest MGO concentration, greatly altered the metabolic profiles in cells. Subsequently, differential metabolites (DMs) in each MGO treatment group were identified by comparison to the control group (see **Section 5.2.5.4** for selection criteria). As shown in **Figure 5.4B**, there were 12 DMs (5 upregulated and 7 downregulated) in the low-concentration MGO-treated group (500 μM), 29 DMs (18 upregulated and 11 downregulated) in the medium-concentration MGO-treated group (750 μM), and 31 DMs (17 upregulated and 14 downregulated) in the

high-concentration MGO-treated group (1000 μ M). The volcano plots in **Figure 5.4C** further illustrate the distribution of DMs in each MGO-treated group compared to the control, and the levels of the 31 DMs identified in the high-concentration MGO-treated group were visualized across all four treatment groups in a clustering heatmap (**Figure 5.4D**). Among all the DMs, MG-H1 that is reported to be the most abundant *in vivo* free-form AGE²⁵⁸, appeared to be the most significantly changed compound in all the three MGO-treated groups compared to control (**Figure 5.4C**). There was an increase of up to 64-fold in the intensity of MG-H1 in the high-concentration MGO treated group compared to control (**Table S5.2**). The *p* values and fold changes for other DMs identified in the high-concentration MGO-treated group can also be found in **Table S5.2**.

To further explore the metabolic pathways influenced by MGO, a pathway analysis based on the KEGG database was conducted on the DMs identified in the high-concentration MGO-treated group. **Figure 5.5A** shows that 9 metabolic pathways were significantly enriched, especially arginine and proline metabolism, cysteine and methionine metabolism, glutathione metabolism, arginine biosynthesis, alanine, aspartate and glutamate metabolism and TCA cycle. These findings suggest that MGO, particularly at cytotoxic levels, induced metabolic dysfunction in SH-SY5Y cells.

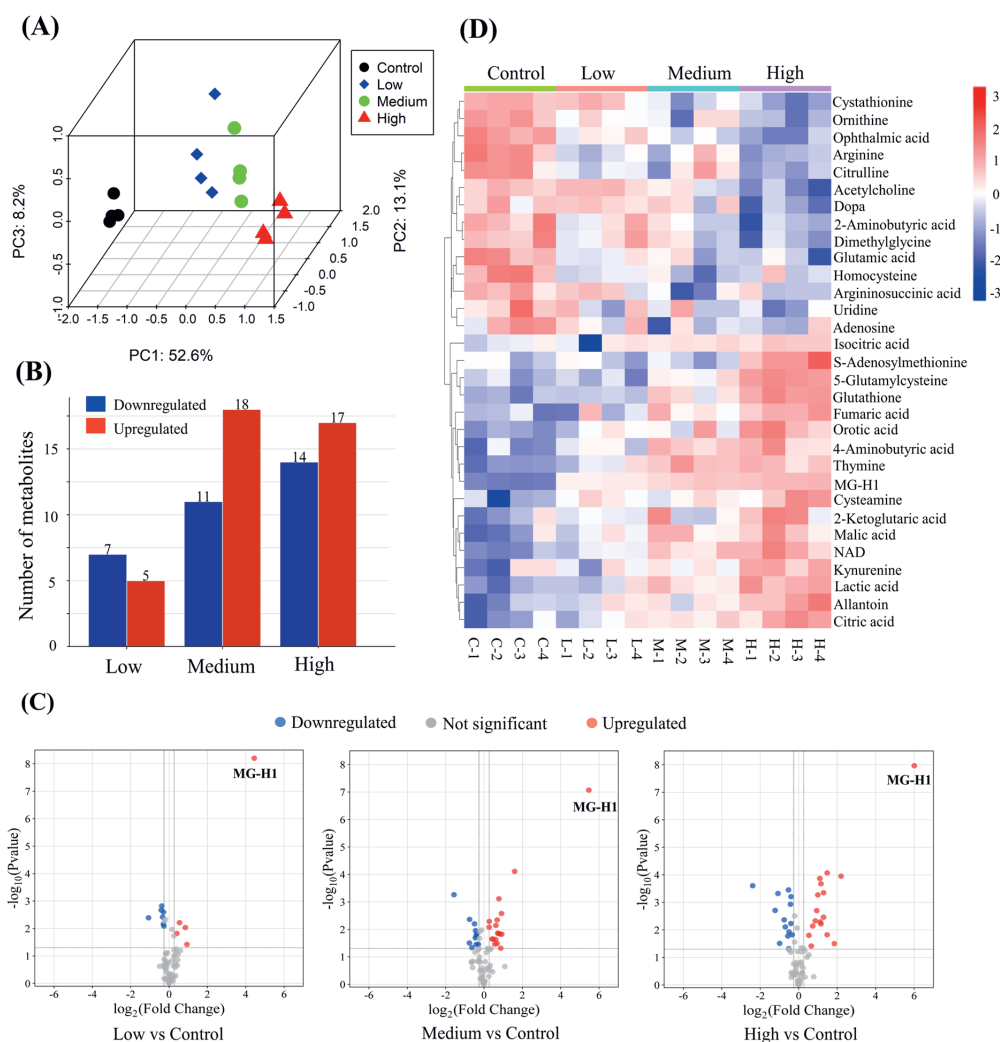


Figure 5.4 Metabolomic analysis of SH-SY5Y cells after 24 h exposure to MGO. (A) 3D PCA plot based on the levels of 75 metabolites. (B) The number of upregulated and downregulated differential metabolites (DMs) in different MGO-treated groups. (C) Volcano plot of metabolites quantified in different MGO-treated groups (red dots: upregulated DMs, blue dots: downregulated DMs, gray dots: proteins with no significant change). (D) Heatmap of the 31 DMs identified in the high-concentration MGO-treated group presented for all treatment groups. The color gradient from blue to red indicates the metabolite level from low to high. Treatment groups are labeled as follows: control (C-x) for 0 μM MGO, low (L-x) for 500 μM MGO, medium (M-x) for 750 μM MGO, and high (H-x) for 1000 μM MGO. The 'x' in each label represents the replicate number, ranging from 1 to 4.

5.3.3 Integrated analyses of proteomics and metabolomics in SH-SY5Y cells after MGO exposure

Integrated analyses of proteomics and metabolomics were conducted to further explore the interactions between differentially expressed proteins (DEPs) and differential metabolites (DMs). Initially, we assessed the correlation between proteins identified in the top 5 key functional modules (**Figure 5.3**) and DMs, both derived from the high-concentration MGO-treated group. The resulting correlation network, depicted in **Figure 5.5B**, revealed a dense web of interactions among the proteins and DMs. Importantly, the network underscored the significant involvement of key metabolic pathways such as glutathione (GSH) metabolism, cysteine and methionine metabolism, and the TCA cycle. Key metabolites highlighted in these pathways include GSH, cystathionine, and various TCA cycle intermediates.

Subsequently, a joint metabolic pathway enrichment analysis was performed to examine the effects of MGO exposure on DEPs and DMs further. This analysis revealed that arginine biosynthesis was the most significantly affected pathway, showing the highest pathway impact and the most notable p value (**Figure 5.5C**). Moreover, the analysis confirmed significant impacts on the TCA cycle, glutathione metabolism, and cysteine and methionine metabolism pathways, corroborating the initial findings suggested by the correlation network. These pathways, affected by MGO exposure in SH-SY5Y cells, are extensively discussed in the discussion section to elucidate their roles in cellular responses.

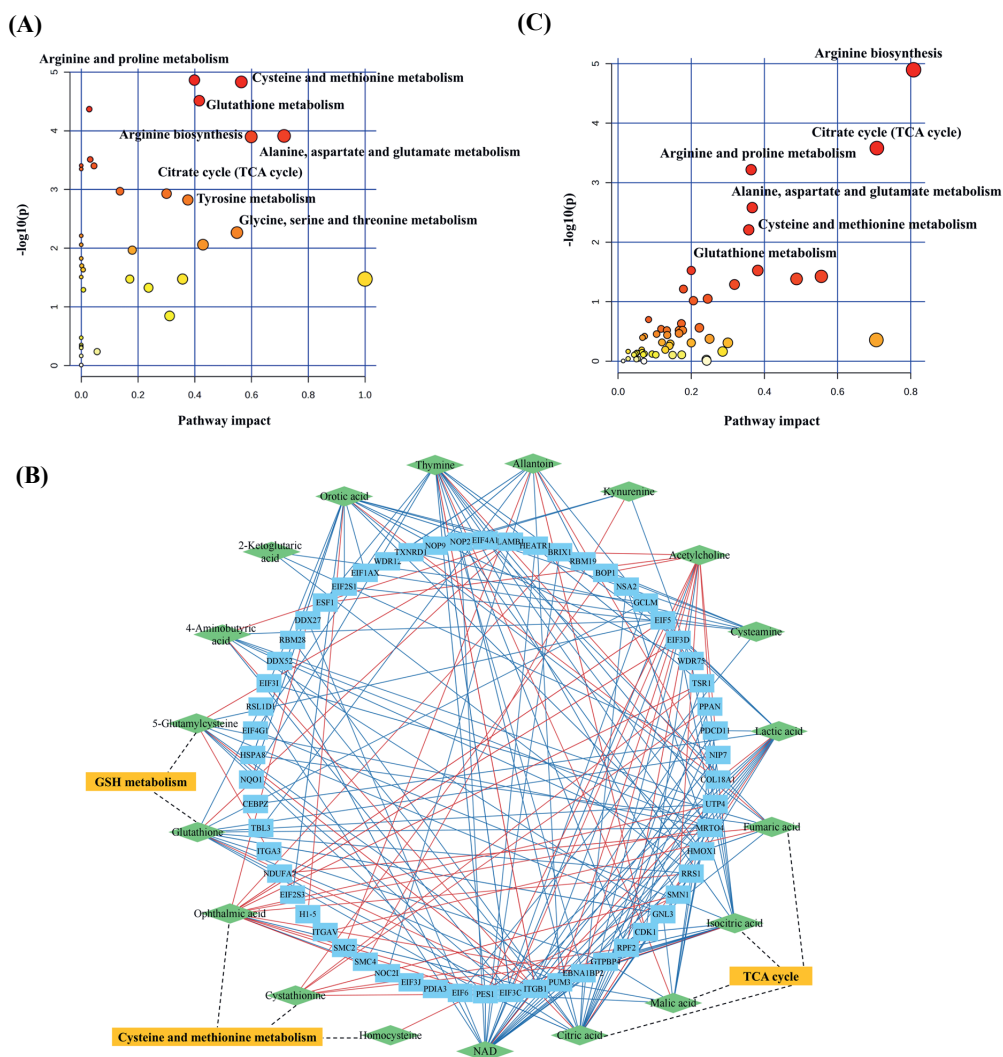


Figure 5.5 Metabolic pathway enrichment analysis of identified differential metabolites (DMs) in the high-concentration MGO-treated group (1000 μ M MGO) (A), followed by integrated analyses of proteomics and metabolomics, including: (B) Correlation network of proteins identified in the top 5 key functional modules and DMs, both identified from high-concentration MGO-treated group. The network was generated based on Spearman's correlation analysis using a significance threshold of $p < 0.01$ and an absolute correlation coefficient > 0.75 . Blue rectangle nodes represent proteins; green diamond nodes represent metabolites. Red edges indicate negative correlations, and blue edges indicate positive correlations; (C) Joint pathway enrichment analysis of differentially expressed proteins (DEPs) and DMs in the high-concentration MGO-treated group. Pathways with a pathway impact greater than 0.20 and a p value less than 0.05 were considered significant.

5.4 Discussion

The objective of this study was to investigate the molecular and biochemical changes induced by MGO exposure in SH-SY5Y human neuroblastoma cells and to elucidate how these changes contribute to neurotoxicity, through integrated proteomics and metabolomics analyses. Our comprehensive analyses revealed that exposure to MGO, especially at cytotoxic level, induced extensive alterations in both the proteome and metabolome of SH-SY5Y cells. Analysis of proteomics data identified a substantial number of DEPs involved in critical cellular functions, including protein synthesis, cellular structural integrity, mitochondrial function, and oxidative stress responses. Analysis of metabolomics and subsequent integration of metabolomics and proteomics data underscored significant changes in key metabolic pathways such as arginine biosynthesis, glutathione metabolism, cysteine and methionine metabolism, and the TCA cycle. These changes may represent cellular adaptations or protective responses to dicarbonyl stress, or they could directly lead to cellular dysfunction and subsequent toxicity.

Firstly, the enrichment and the PPI network analysis indicated significant alterations in protein-synthesis related pathways, such as ribosome biogenesis and translation initiation, upon exposure of cells to MGO. The expression levels of the majority of proteins involved in these pathways were significantly upregulated, indicative of heightened protein synthesis activity (**Table 5.1**). This upregulation is likely a cellular adaptation to meet the increased demand for new proteins and to manage extensive dicarbonyl stress-induced protein damage, crucial for replacing damaged or dysfunctional proteins. However, this enhanced protein synthesis could lead to an increased load of nascent proteins entering the endoplasmic reticulum (ER), elevating the risk of protein misfolding and aggregation—primary indicators of ER stress²⁵⁹. The “protein processing in the endoplasmic reticulum” pathway, significantly enriched in our KEGG enrichment analysis, further corroborated the cellular response to this stress. It highlighted the upregulation of chaperones such as heat shock proteins HSPA8 and HSPH1, which assist in managing misfolded proteins²⁶⁰. Simultaneously, the downregulation of protein disulfide isomerases such as PDIA3, PDIA4, and PDIA6 in the same pathway suggested a compromised ability to maintain protein structural integrity and an enhanced risk of further ER stress²⁶¹. In response to ER stress, the unfolded protein response (UPR) may be activated²⁶². Previous studies indicated that dicarbonyl stress from increased levels of MGO can trigger the UPR, characterized by an increased abundance of not only heat shock proteins but also components like ubiquitin ligases that encapsulate and remove proteins exhibiting misfolding due to dicarbonyl modifications^{107, 262}. While initially protective, prolonged activation of the UPR can lead to cellular dysfunction, as persistent ER stress challenges the cell’s capacity to restore proteostasis and can drive pathways leading to apoptosis and chronic

inflammation¹⁰⁷. Moreover, chronic ER stress and prolonged activation of UPR have been reported to be strongly associated with the pathology of neurodegenerative diseases, exacerbating neuronal loss and synaptic dysfunction which are critical factors in the progression of these disorders²⁶³.

Furthermore, our proteomic analysis revealed significant alterations in cellular adhesion mechanisms, particularly within the focal adhesion and extracellular matrix (ECM)-receptor interaction pathways (**Table 5.1**). There was downregulation of integrins such as ITGB1, ITGAV, ITGA3, and ITGA6, along with crucial ECM components like COL1A1 and LAMB1. These changes suggest substantial alterations in the mechanisms that maintain cellular architecture and mediate signal transduction between the ECM and the cytoskeleton²⁶⁴, potentially underlying the cytotoxic effects induced by MGO. Integrins, serving as critical transmembrane receptors, are pivotal in mediating both physical and biochemical linkages between the extracellular matrix and the cytoskeleton²⁶⁵. Their downregulation can impair cell adhesion, impacting neuronal connectivity and synaptic stability, essential for neural development and function²⁶⁶. Similarly, alterations in COL1A1 and LAMB1 can disrupt the structural integrity and signaling capabilities of cells, potentially contributing to the pathophysiology of neurodegeneration²⁶⁷. Additionally, it is noteworthy that our previous study²⁴⁹ has observed that cytoskeletal proteins, crucial for the structural integrity and functionality of focal adhesion complexes²⁶⁸, appear particularly susceptible to modifications by MGO in SH-SY5Y cells. This observation leads us to hypothesize that MGO-induced modifications to these cytoskeletal proteins could play a role in causing instability and subsequent downregulation of integrins and other adhesion-related proteins.

Moreover, analysis of proteomic data revealed significant alterations in proteins involved in oxidative phosphorylation, indicating changes in mitochondrial function and energy metabolism (**Table 5.1**). Metabolomics and integrated omics analyses confirmed that these changes extend to the TCA cycle, suggesting a comprehensive disruption in energy metabolism (**Figure 5.5**). **Figure 5.6A** specifically depicts the effects of MGO exposure on the energy metabolism in SH-SY5Y cells, beginning with a notable downregulation of glycolytic enzymes such as PFKL and ENO2. This reduction likely compelled the cells to depend more on the TCA cycle, as evidenced by increased intermediates like citric acid and isocitric acid, and enzymes such as IDH3B and IDH3G, responding to higher energy needs or managing oxidative stress. Support from gluconeogenesis and other pathways likely provided necessary substrates. Furthermore, the electron transport chain showed a compromised functionality with significant downregulation of components such as NDUFA7, COQ6, and COX5B, indicating a reduced efficiency. Conversely, the upregulation of components like ATP5F1D suggests compensatory efforts to maintain ATP production despite these inefficiencies.

Previous *in vitro* studies have confirmed that mitochondrial impairments, including reduced mitochondrial membrane potential and the overproduction of ROS mediated by mitochondria, are key contributors to the cytotoxic effects induced by MGO in SH-SY5Y cells^{97, 244}. Our findings provide further evidence at the molecular level of mitochondrial dysfunction's role in these effects within SH-SY5Y cells. It is worth noting that contrasting findings have been reported in different cell types and experimental conditions. For example, exposure to 200 μ M MGO (cytotoxic level) in C2C12 myoblast cells showed a decrease in TCA cycle intermediates without significant glycolysis changes²⁶⁹, while nontoxic MGO concentrations in adipocytes enhanced aerobic glycolysis²⁷⁰. This indicates that metabolic responses may vary with cell type and MGO toxicity levels.

Additionally, the proteomic analysis highlighted significant engagement of the Nrf2 pathway (**Table 5.1**) and alterations in GSH synthesis-related pathways, including cysteine and methionine metabolism and glutathione metabolism, as prominently featured in our metabolomics and integrated omics analyses (**Figure 5.5**). **Figure 5.6B** illustrates the impact of MGO exposure on these pathways. MGO has been reported to activate the Nrf2 pathway directly by modifying Keap1 and potentially indirectly through ROS production induced by MGO^{31, 53}. Consistent with these findings, our study observed the upregulation of several Nrf2-regulated proteins, including HMOX1 and GCLM, with the latter being critical for GSH synthesis²⁷¹. The metabolites detected in the cysteine and methionine metabolism and glutathione metabolism pathways indicated an increased cellular effort to synthesize GSH. For instance, the observed downregulation of glutamate and cystathionine suggested their increased consumption in GSH synthesis. A 2.1-fold increase in GSH levels in the high-concentration MGO-treated cells was observed reflecting the cells' attempt to enhance their detoxification capacity via the GSH-dependent glyoxalase system²⁶². Together, the activation of Nrf2 and the increase in GSH levels can be seen as cellular protective mechanisms against dicarbonyl stress, working to mitigate the cytotoxic effects induced by MGO exposure.

Finally, the metabolomic analysis and integrated omics studies revealed significant alterations in several amino acid metabolism pathways, particularly in the arginine biosynthesis pathway, which plays a critical role in feeding into the urea cycle. Significant downregulation was observed in key metabolites including ornithine, citrulline, arginosuccinate, and arginine—all of which are crucial components of the urea cycle (**Figure 5.6C**). Additionally, glutamate levels were reduced, likely reallocating resources to glutathione synthesis to combat dicarbonyl stress. This reduction in glutamate, a key precursor in both the arginine biosynthesis and the urea cycle, likely contributed to decreased substrate availability for these cycles. The depletion of urea cycle metabolites may also stem from their consumption in the reaction of arginine with MGO to form MG-H1, which was substantially increased. The disruption of this

pathway can compromise nitrogen waste processing and amino acid catabolism²⁷², thereby potentially influencing broader cellular functions and contributing to the neurotoxicity observed in SH-SY5Y cells.

Taking all together, our integrated proteomics and metabolomics analyses provide a comprehensive view of the cellular alterations induced by MGO in SH-SY5Y cells and reveal that MGO exposure induces both toxic effects and adaptive responses in SH-SY5Y neuroblastoma cells. Contributing to toxicity are increased ER stress, disruptions in cellular adhesion and ECM integrity, mitochondrial dysfunction, and disrupted amino acid metabolism, notably in pathways such as arginine biosynthesis which directly impacts the urea cycle. On the adaptive side, cells upregulate protein synthesis, activate the Nrf2 pathway, and reprogram metabolism to counteract dicarbonyl stress and maintain energy levels. These findings enhance our understanding of MGO-induced neurotoxicity and identify potential therapeutic targets for mitigating its harmful effects.

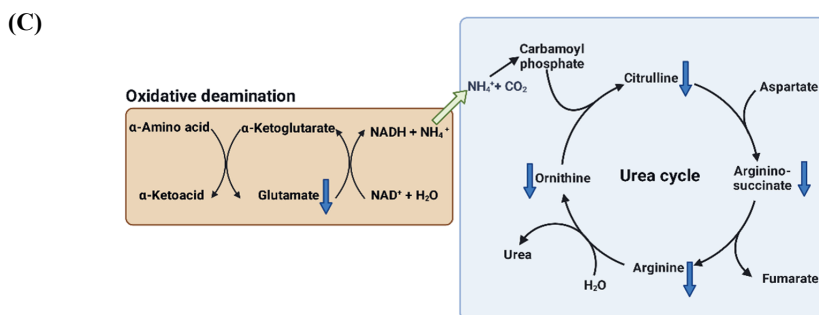
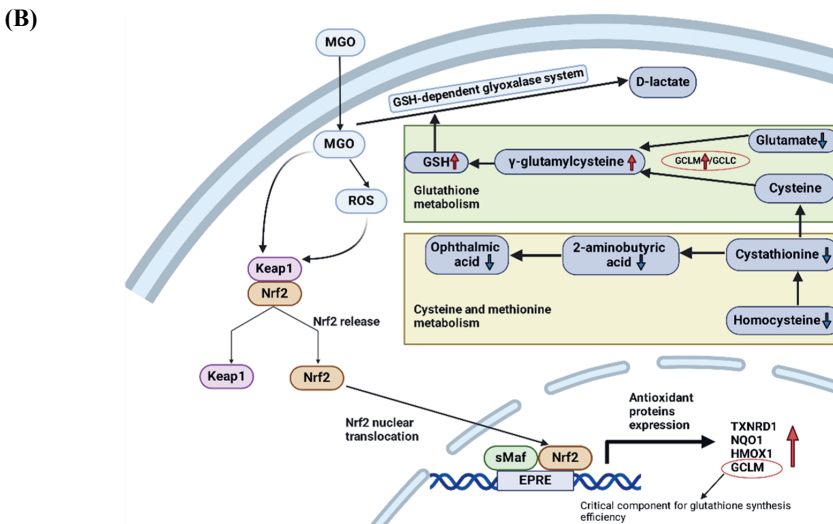


Figure 5.6 Schematic representation of selected impacts of MGO exposure in SH-SY5Y cells, including: (A) energy metabolism, showing disruptions in glycolysis, TCA cycle, and oxidative phosphorylation; (B) Nrf2/GSH axis, depicting activation of the Nrf2 pathway and upregulation of GSH levels; (C) amino acid catabolism, detailing disruptions in arginine biosynthesis and related impacts on the urea cycle induced by MGO. Red arrows indicate upregulation, blue arrows indicate downregulation, based on integrated omics analyses. Figure created with BioRender.com.

Acknowledgments

Haomiao Wang and Liang Zheng are thankful for the financial support provided by the China Scholarship Council, under Grant Numbers CSC202307720061 and CSC202008510115.

Supporting information

Table S5.1 (The 453 differentially expressed proteins (DEPs) identified from the high-concentration MGO-treated group (1000 μ M) and their corresponding *p* values and fold changes) can be accessed at <https://doi.org/10.6084/m9.figshare.26418415> due to its large size, spanning multiple pages. Additional supporting information can be found under this section.

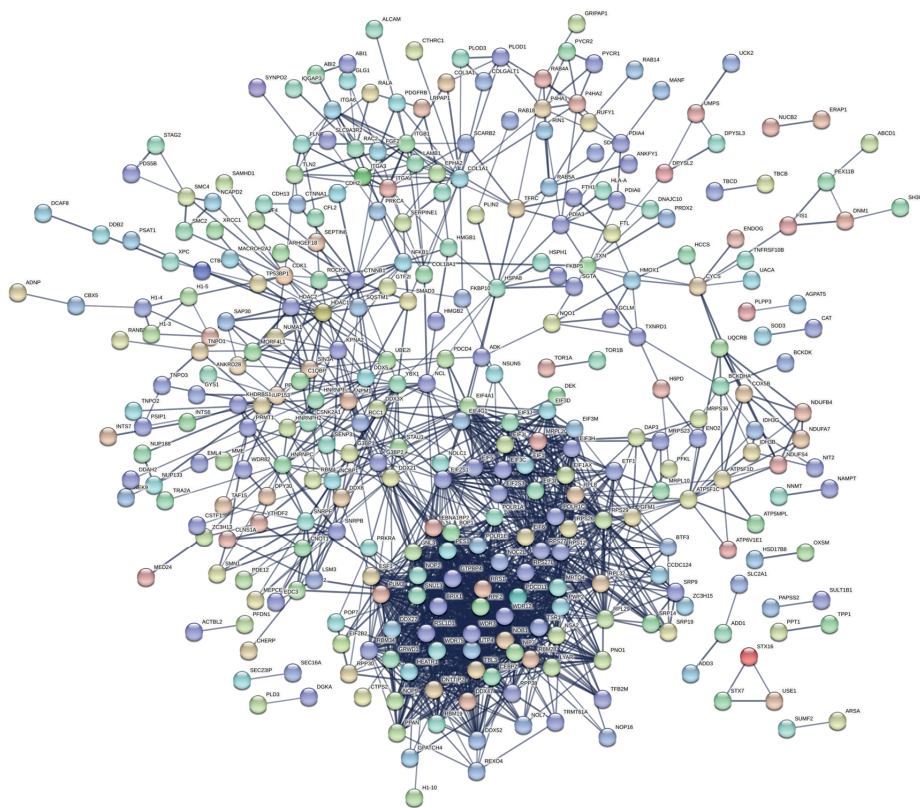


Figure S5.1. Protein-protein interaction (PPI) network of differentially expressed proteins (DEPs) identified from high-concentration of MGO-treated group (1000 μ M MGO) using STRING database. The disconnected nodes were removed from the network.

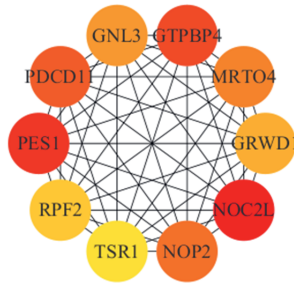
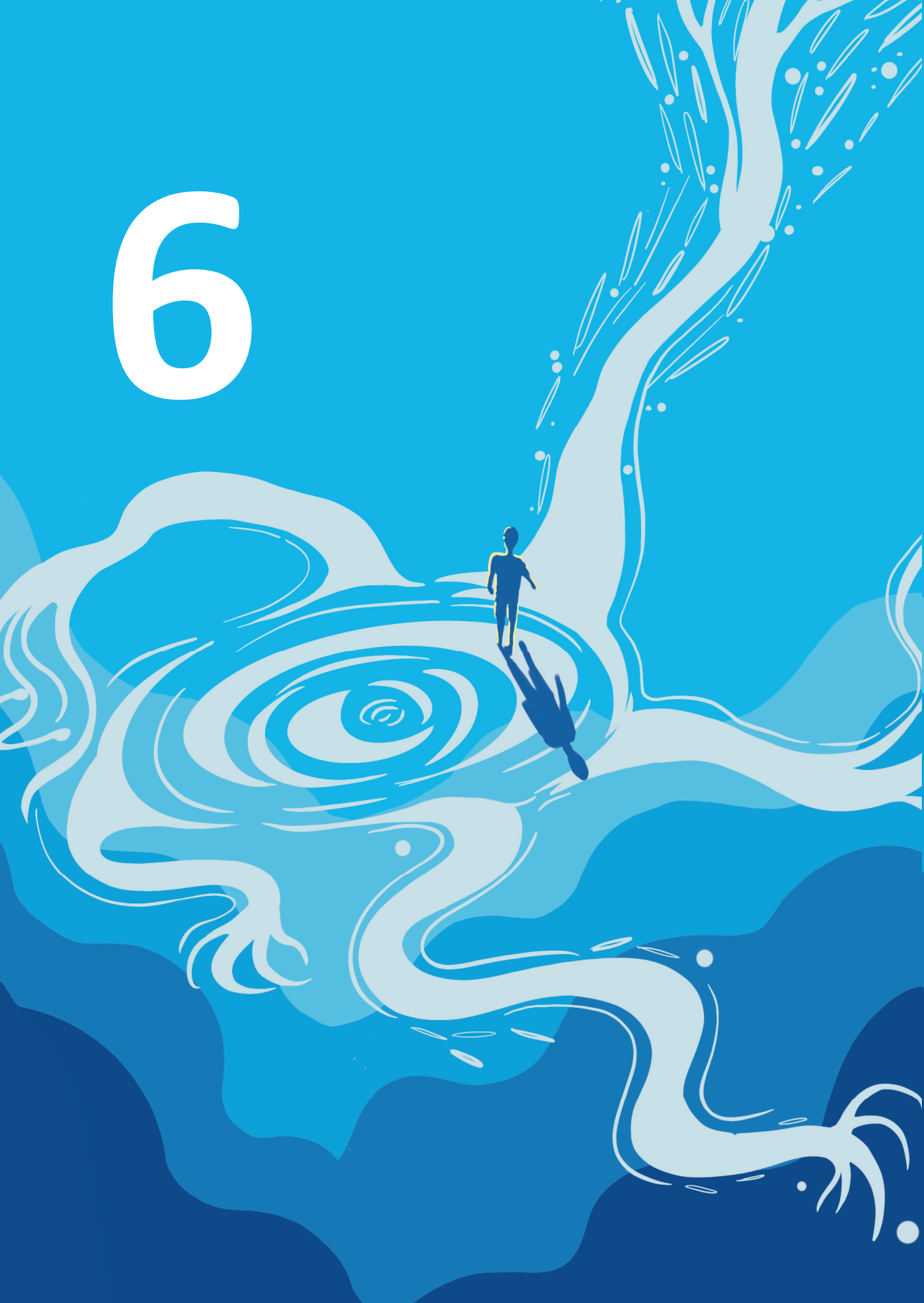


Figure S5.2. The top 10 hub proteins from the PPI network identified using the CytoHubba plugin with the maximal clique centrality (MCC) method in Cytoscape. The proteins were ranked by the MCC score, and the gradient from red to yellow visually represents their rankings, with redder nodes indicating higher prominence in the network.

Table S5.2. The 31 differential metabolites (DMs) identified from the high-concentration MGO-treated group (1000 μ M) and their corresponding *p* values and fold changes.

No.	Metabolite name	<i>p</i> -value	Fold change
1	MG-H1	1.09E-08	64.32109
2	Thymine	8.54E-05	2.788934
3	5-Glutamylcysteine	0.000112	4.593688
4	Glutathione	0.000135	2.136067
5	Orotic acid	0.00021	2.226973
6	Ophthalmic acid	0.000248	0.190017
7	Arginine	0.000353	0.691181
8	Lactic acid	0.000448	2.446483
9	Cystathionine	0.000476	0.473328
10	NAD	0.000537	1.988862
11	Ornithine	0.000621	0.756888
12	Citrulline	0.001167	0.742556
13	Acetylcholine	0.001958	0.426676
14	Fumaric acid	0.001992	1.914462
15	Allantoin	0.003461	2.444271
16	Dimethylglycine	0.004316	0.590982
17	S-Adenosylmethionine	0.004705	1.81475
18	Citric acid	0.005124	2.174811
19	Dopa	0.00587	0.753693
20	Isocitric acid	0.006055	2.227916
21	4-Aminobutyric acid	0.007204	1.653904
22	2-Aminobutyric acid	0.007798	0.615915
23	Glutamic acid	0.011817	0.704374
24	Cysteamine	0.014957	2.78226
25	Argininosuccinic acid	0.01502	0.790889
26	Malic acid	0.015722	1.442335
27	Homocysteine	0.016729	0.675037
28	Uridine	0.030921	0.502816
29	2-Ketoglutaric acid	0.031485	3.606333
30	Kynurenine	0.03856	1.56944
31	Adenosine	0.047881	0.697788

6



Chapter 6

Physiologically Based Kinetic Modeling-Facilitated Reverse Dosimetry to Predict Neurotoxicity and Genotoxicity of Methylglyoxal in Humans from In Vitro Data

This chapter is based on:

Liang Zheng, Xiyu Li, Frances Widjaja, Chen Liu, Ivonne M. C. M. Rietjens. Use of physiologically based kinetic modeling to predict neurotoxicity and genotoxicity of methylglyoxal in humans.

Published in: npj Science of Food. 2024 Oct 6;8:79.

DOI: 10.1038/s41538-024-00322-6.

Abstract

This study aimed to evaluate human neurotoxicity and genotoxicity risks from dietary and endogenous methylglyoxal (MGO), utilizing physiologically based kinetic (PBK) modeling-facilitated reverse dosimetry as a new approach methodology (NAM) to extrapolate *in vitro* toxicity data to *in vivo* dose-response predictions. A human PBK model was defined based on a validated mouse model enabling the translation of *in vitro* toxicity data for MGO from human stem cell-derived neurons and WM-266-4 melanoma cells into quantitative human *in vivo* toxicity data and subsequent risk assessment by the margin of exposure (MOE) approach. The results show that the MOEs resulting from daily dietary intake did not raise a concern for endpoints for neurotoxicity including mitochondrial function, cytotoxicity, and apoptosis, while those for DNA adduct formation could not exclude a concern over genotoxicity. Endogenous MGO formation, especially under diabetic conditions, resulted in MOEs that raised a concern not only for genotoxicity but also for some of the neurotoxicity endpoints evaluated. Thus, the results also point at the importance of taking the endogenous levels into account in risk assessment of MGO.

Keywords: methylglyoxal; neurotoxicity; genotoxicity; PBK model; reverse dosimetry; new approach methodology; risk assessment

6.1 Introduction

Methylglyoxal (MGO), a highly reactive α -oxoaldehyde compound, is extensively found in various foods and beverages, particularly those rich in sugar and fat, as well as in fermented products^{11, 54}. MGO is generated in food through several processes such as the Maillard reaction, autoxidation of sugars, caramelization, lipid oxidation, and/or microbial fermentation during thermal processing and food storage^{22, 24}. In addition to these exogenous sources, MGO is also endogenously formed as a by-product, primarily from glycolysis through the spontaneous degradation of triosephosphate intermediates³⁶. In a healthy adult human, it has been estimated that 3 mmol MGO is formed endogenously each day³⁰. However, the body maintains MGO at relatively low levels, with concentrations reported to be in the range of 0.05-0.6 μ M in plasma and 1-4 μ M in cells, primarily through the GSH-dependent glyoxalase system consisting of the enzymes glyoxalase 1 (Glo1) and glyoxalase 2 (Glo2), which detoxifies MGO into D-lactate (**Figure 6.1**)^{10, 273-275}. Elevated *in vivo* levels of MGO can occur under certain pathological conditions, such as hyperglycemia, that disrupt the balance between the formation and detoxification of MGO¹⁰. It was reported that the plasma levels of MGO in type 2 diabetic patients can be up to 30% higher than in healthy individuals²⁷³.

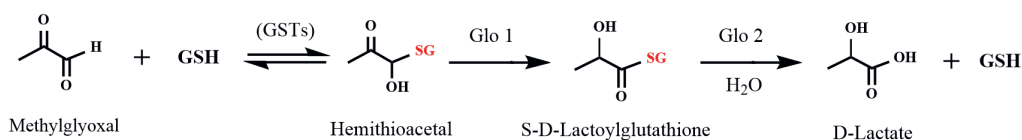


Figure 6.1. Schematic presentation of the intracellular detoxification of MGO by the GSH-dependent glyoxalase system. GSH: glutathione, GSTs: glutathione-S-transferases, Glo1: glyoxalase 1, Glo2: glyoxalase 2.

MGO is a highly reactive precursor for advanced glycation end products (AGEs), whose formation has been linked to various chronic diseases^{22, 129}. Elevated *in vivo* levels of MGO can increase AGE formation by interacting with the nucleophilic sites on DNA and proteins, leading to structural and functional changes in these macromolecules, which contributes to cellular and tissue dysfunction and ultimately could play a role in various diseases, including diabetes and multiple neurodegenerative disorders (e.g., Alzheimer's disease and Parkinson's disease)^{10, 22, 132}. This concern is exacerbated by the dietary intake of exogenous MGO and the resulting AGE formation, which may further increase human exposure and the potential related health risks¹⁶³. However, the extent to which dietary MGO contributes to the total body burden and impacts human health remains unclear.

Clinical studies have shown that higher serum MGO levels are associated with accelerated cognitive decline in older adults²³⁹. In Alzheimer's disease patients, elevated levels of MGO

and the resulting AGEs have been detected in the cerebrospinal fluid^{240, 241}. Similarly, elevated levels of MGO-derived AGEs have been identified in the nigra neurons of Parkinson's disease patients⁸⁷. These clinical findings suggest a pathological role for MGO in the context of neurodegeneration. Moreover, various *in vitro* studies have shown that exposure to exogenous MGO can induce cellular injury and toxicity in different animal and human neuronal cell models^{95, 96, 114, 115, 276, 277}. Neuronal cells, in particular, are susceptible to the toxic effects of MGO, a vulnerability that is potentially related to their high-energy glucose metabolism, combined with relatively lower levels of glutathione (GSH) and lower activities of glyoxalase enzymes compared to what is found in astrocytes²⁷⁸⁻²⁸¹. Exposure of neuronal cells to exogenous MGO has been observed to decrease cell viability and mitochondrial redox activity, as well as to increase reactive oxygen species (ROS) production and apoptosis in *in vitro* studies^{76, 96, 244}. Furthermore, the activation of the receptor for AGEs (RAGE) by AGEs formed in a reaction of DNA and proteins with MGO, is potentially linked to these adverse effects^{244, 282, 283}. These *in vitro* findings reveal the neurotoxicity of MGO and suggest mechanisms underlying its toxicity that may play a role in neurodegeneration. Apart from its well-documented neurotoxicity, the genotoxic potential of MGO represents another critical concern. Studies have shown that DNA adducts induced by MGO could increase the mutation rate in *E. coli* cells, as well as G:C to C:G and T:A transversions in the *supF* gene of simian kidney cells^{284, 285}. Besides, it was found that MGO-derived DNA adducts *N*²-(1-carboxyethyl)-2'-deoxyguanosine (*N*²-CEdG) exhibited a lesion rate of one per 10⁷ nucleosides at an endogenous background level of MGO in WM-266-4 human melanoma cells, and exposure to exogenous MGO resulted in a concentration-dependent increase in these *N*²-CEdG levels¹²².

However, these *in vitro* neurotoxicity and genotoxicity data cannot be applied directly for risk assessment in humans. The concentration-response data obtained from these *in vitro* assays require further translation into dose-response data to determine safe exposure levels in humans. This translation can be achieved using new approach methodologies (NAMs) such as quantitative *in vitro-in vivo* extrapolation (QIVIVE) using physiologically based kinetic (PBK) modeling and reverse dosimetry, methods proven effective in predicting *in vivo* toxicity of various compounds for a variety of endpoints^{116, 117, 119}. The PBK modeling facilitated reverse dosimetry approach contributes to the development of non-animal-based methods and offers a predictive tool to assess whether systemic exposure of the host to MGO might result in internal concentrations that could cause toxicity. This study aimed to use available *in vivo* kinetic mouse data, *in vitro* neurotoxicity and genotoxicity data, and *in vitro-in silico*-based reverse dosimetry for quantitative translation of concentration-response curves for the toxicity of MGO into *in vivo* dose-response predictions in humans. This can help in understanding the effects of exogenous versus endogenous MGO in humans.

In this study, the first step was to develop a mouse PBK model and evaluate the model predictions with the literature available experimental data for blood levels of MGO⁸⁰. Based on the validated mouse model, a human PBK model was developed and applied to translate the concentration-response data from the literature for the toxicity of MGO in human neuronal cells and human melanoma cells to predict *in vivo* dose-response curves for the neurotoxicity and genotoxicity of MGO in humans. Based on these predicted *in vivo* neurotoxicity and genotoxicity data, a risk assessment was performed by the margin of exposure (MOE) approach to evaluate the risks from dietary and endogenous MGO.

6.2 Methods

6.2.1 PBK modeling-facilitated reverse dosimetry approach

The PBK modeling-facilitated reverse dosimetry approach was applied to predict *in vivo* dose-dependent neurotoxicity and genotoxicity induced by MGO. This approach involved the following steps: 1) development of a mouse PBK model for MGO to allow the prediction of the *in vivo* kinetics of MGO in mice, 2) evaluation of the mouse PBK model by comparing predicted kinetic data for MGO with available *in vivo* literature data, 3) defining a human PBK model for MGO based on the mouse PBK model developed, 4) extrapolation of the *in vitro* concentration-response data from the literature for MGO neurotoxicity and genotoxicity to *in vivo* dose-response curves using human PBK model-facilitated reverse dosimetry, 5) risk assessment of MGO from daily dietary intake and endogenous formation via an MOE approach based on the predicted *in vivo* neurotoxicity and genotoxicity data for MGO.

6.2.2 Development of a PBK model for MGO in mice

We utilized our previously developed PBK models for 17 β -estradiol and bisphenol A as the basis to create a new PBK model describing the kinetics of MGO in mice¹¹⁹. The conceptual mouse PBK model for MGO is presented in **Figure 6.2**. This model consisted of separate compartments for the stomach, intestine, liver, fat, blood, rapidly perfused tissue (e.g. brain, lungs, heart, and kidneys), and slowly perfused tissue (muscle, skin, and bone). The PBK model enables the simulation of systemic blood concentrations of MGO following its oral administration. The physiological and anatomical parameters, such as fraction of tissue volumes and blood flows to tissues were obtained from the literature^{286, 287} and are summarized in **Table S6.1**.

This model accounted for stomach emptying following oral administration of MGO and divided the intestinal compartment into seven sub-compartments to simulate intestinal transit of MGO. The apparent permeability coefficient (P_{app}) value for MGO, determined to be 1.09×10^{-6}

⁶ cm/s from Caco-2 transport studies conducted in our lab²⁸⁸, was utilized to define the intestinal absorption of MGO from these sub-compartments. To extrapolate the Caco-2 P_{app} value to an *in vivo* P_{app} value for humans and mice, the following equations were used (eqs 1-2):

$$\text{Log } (P_{app, \text{ human } in \text{ vivo}}) = 0.6836 \times \text{Log } (P_{app, \text{ Caco-2}}) - 0.5579 \quad (1)$$

$$P_{app, \text{ mouse } in \text{ vivo}} = P_{app, \text{ human } in \text{ vivo}}/3.6 \quad (2)$$

in which eq 1 scales the *in vitro* Caco-2 apparent permeability ($P_{app, \text{ Caco-2}}$) to an *in vivo* human effective permeability ($P_{app, \text{ human } in \text{ vivo}}$) for passively absorbed compounds²⁸⁹, and eq 2 scales the human effective permeability ($P_{app, \text{ human } in \text{ vivo}}$) to mouse effective permeability ($P_{app, \text{ mouse } in \text{ vivo}}$) using the equation originally defined for rats²⁹⁰. It was assumed that rat and mouse permeabilities would be the same. The intestinal absorption rate of MGO was subsequently determined using the equation: absorption rate ($\mu\text{mol/h}$) = $P_{app, \text{ mouse } in \text{ vivo}}$ (cm/h) \times surface area of the mouse small intestine (cm^2) \times luminal concentration of MGO ($\mu\text{mol}/\text{cm}^3$)¹¹⁹. The luminal concentration of MGO in each sub-compartment was calculated by dividing the amount of MGO by the volume of the sub-compartment. Additionally, it was reported that blood MGO levels in mice began to rise above basal levels 50-55 minutes following a single oral dose of MGO at 50, 100, or 200 mg/kg bw⁸⁰. Accordingly, a lag time of 55 minutes was included in the model to account for this delayed response.

To describe the distribution of MGO across different tissues, the tissue/blood partition coefficients were estimated using the Rodgers and Rowland method²⁹¹ via the online QIVIVE tool (<https://www.qivivetools.wur.nl/>, accessed January 2024)²⁹². The input parameters for the estimation included the logarithmic octanol-water partition coefficient (LogP) and molecular weight (72.06 g/mol) of MGO. The LogP value used for MGO, 0.196, was sourced from the online platform Chemicalize developed by ChemAxon (<https://chemicalize.com/>, accessed January 2024). The blood-to-plasma ratio was assumed to be 1 for MGO, based on a previous study that reported MGO concentrations in plasma and whole blood to be nearly identical in mice upon oral administration of exogenous MGO⁸⁰. Consequently, correction was not necessary when comparing MGO concentrations in blood and plasma. The assumption was also made that the distribution of MGO in rats mirrors that in mice, and therefore the rat tissue/plasma partition coefficients estimated by the QIVIVE tool were directly applied to the mouse PBK model. The tissue/blood coefficients used for the mouse PBK model are presented in **Table S6.1**.

The *in vivo* clearance or elimination of MGO is primarily mediated through the intracellular glyoxalase system, which is ubiquitously present in the cytoplasm of mammalian cells²⁹³.

Consequently, all tissues possess the capability to metabolize MGO. Given that apparent total body clearance data for MGO in mice are available in the literature, it was assumed that the clearance for each organ could be derived based on its respective tissue volume fraction. Hence, the clearance for each tissue was estimated by multiplying the literature-reported apparent total body clearance (CL_{app}) of MGO with the respective tissue volume fraction⁸⁰, reflecting the individual metabolic contributions of each tissue to the overall clearance of MGO. The reported CL_{app} values for MGO in mice were reported to increase from 7.69 to 8.28 to 15.54 L/h/kg when the oral dose was increased from 50 to 100 to 200 mg/kg bw⁸⁰; consequently, specific CL_{app} values corresponding to each dose were used in the mouse model.

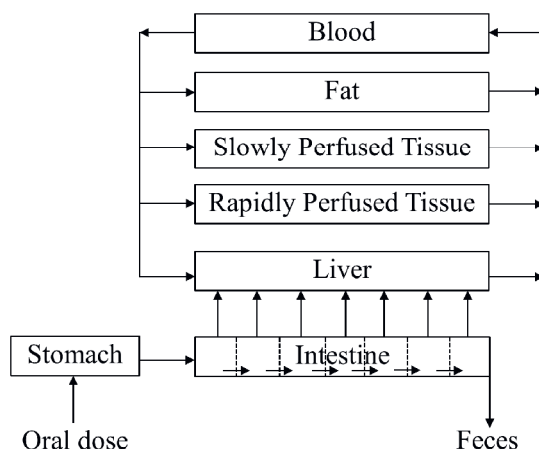


Figure 6.2. Schematic presentation of the PBK model for MGO.

The model equations were coded and numerically integrated into Berkeley Madonna 10.6.1 (UC Berkeley, CA, USA), utilizing Rosenbrock's algorithm for stiff systems. The model code can be found in the Supporting Information.

6.2.3 PBK model evaluation

The performance of the developed mouse PBK model was assessed by comparing model-predicted time-dependent blood concentrations of MGO with reported *in vivo* time-dependent blood concentrations in mice upon a single oral dose of 50, 100, or 200 mg/kg bw of MGO⁸⁰. The software TechDig 2.0 was utilized to digitize and transform graphical data from the cited studies into the numerical format for analysis.

6.2.4 Sensitivity analysis of the PBK model

A sensitivity analysis was conducted to determine which model parameters exert the greatest influence on the predicted maximum blood concentration (C_{\max}) of MGO. Normalized sensitivity coefficients (SCs) were determined using the formula: $SC = (C' - C)/(P' - P) \times (P/C)$, in which C is the initial model output, C' represents the output after parameter adjustment, P represents the initial parameter value, and P' represents the adjusted parameter value²⁹⁴. A 5% increase in each parameter value was implemented to evaluate the impact of parameter adjustments on the C_{\max} predictions of MGO. The sensitivity analysis was conducted for a single oral administration of 50, 100, or 200 mg/kg bw MGO, aligning with the doses used in the *in vivo* kinetic study for model validation. These three doses were all selected for analysis also because the reported apparent total body clearance in mice for each dose differs⁸⁰. Each parameter's influence was examined separately by modifying one parameter at a time while maintaining the others constant.

6.2.5 Human PBK model

Based on the validated mouse PBK model, a human PBK model was developed. The physiological and physicochemical parameters for the human model were obtained from the literature^{287, 292}, and are listed in **Table S6.1**. The *in vivo* P_{app} value for the human model was determined as described in **Section 6.2.2**. The CL_{app} values of MGO for humans were assumed to be the same as those for mice. For further details, the human model script can be found in the Supporting Information. This model was further applied to translate the *in vitro* MGO neurotoxicity and genotoxicity data into *in vivo* dose-response data as further described in **Section 6.2.6**.

6.2.6 Translation of the *in vitro* concentration-response curves for MGO into *in vivo* dose-response curves using the PBK model developed for humans

In vitro concentration-response data on MGO-induced neurotoxicity, utilizing human neuronal cell models, were collected (see Results section). Human primary neuronal-like cells (hNLCs) transdifferentiated from human mesenchymal stem cells exhibited the greatest sensitivity to MGO (see Results section), more accurately reflecting the physiological and biochemical properties of neuronal cells compared to other neuronal cell models⁹⁵. Hence, *in vitro* concentration-response data from hNLCs including effects of MGO on mitochondrial function (measured using the MTT viability assay), cytotoxicity (assessed via the Trypan Blue exclusion method), and apoptosis (evaluated using nuclear staining with Hoechst 33258 dye), were selected for establishing human *in vivo* dose-response relationships for MGO-induced neurotoxicity⁹⁵. Additionally, *in vitro* concentration-response data on MGO-induced DNA

adduct formation in WM-266-4 human melanoma cells reflecting the potential genotoxicity of MGO were also chosen for *in vivo* translation¹²².

In this study, *in vivo* dose-dependent toxicity by MGO was assumed to be dependent on the C_{\max} of MGO reached in blood, and thus the PBK modeling-based reverse dosimetry approach was applied to predict the dose levels that were required to reach the respective effective C_{\max} concentrations of MGO in blood. The translation from the *in vitro* assay concentrations to corresponding exogenous dose levels was performed without correcting for endogenous MGO formation based on the assumption that the endogenous formation of MGO would be comparable in cells *in vitro* and *in vivo*. Indeed intracellular endogenous MGO formation is known to occur *in vivo* but also in *in vitro* cell models²⁷⁴. Additionally, the toxicity of MGO was attributed to the unbound fraction (f_{ub}) of MGO, requiring a correction for protein binding to address differences in f_{ub} between human blood and the *in vitro* assay medium. Consequently, the *in vitro* unbound concentration was set equal to the *in vivo* unbound C_{\max} , and the *in vivo* unbound C_{\max} derived from oral MGO administration was calculated using the equation:

$$C_{in\ vivo} \times f_{un,\ in\ vivo} = C_{in\ vitro} \times f_{un,\ in\ vitro}$$

where $C_{in\ vivo}$ is the maximal total MGO concentration resulting from oral MGO administration, and $C_{in\ vitro}$ is the total MGO concentration used in the *in vitro* assay. The fraction unbound in the assay medium and in blood, $f_{un,\ in\ vitro}$ and $f_{un,\ in\ vivo}$, respectively, take into account the difference in protein binding in the assay medium and human blood. The $f_{un,\ in\ vivo}$ value was calculated using the online QIVIVE tool²⁹² and amounted to 0.71. The $f_{ub,\ in\ vitro}$ value was calculated based on the assumption that the unbound fraction depends linearly on the protein content, and can be derived from the $f_{ub,\ in\ vivo}$ ²⁹⁵. This was determined using the equation: $f_{ub,\ in\ vitro} = 1 - (1 - f_{ub,\ in\ vivo}) \times (\text{protein content } in\ vitro / \text{protein content } in\ vivo)$ ²⁹⁶. In this equation, the protein content in human blood is approximately 8%²⁹⁷, while the protein content in the assay medium used to generate the *in vitro* data intended for *in vivo* translation was considered 0, due to the use of the serum-free medium in these assays.

Based on the above, reverse dosimetry on each effective concentration $C_{in\ vivo}$ was conducted utilizing the developed human PBK model to obtain the corresponding oral MGO dose levels, thereby facilitating the conversion of *in vitro* concentration-response data into *in vivo* dose-response curves.

6.2.7 Determination of points of departure (PODs) based on the predicted *in vivo* dose-response curves

To determine the PODs for MGO, benchmark dose modeling (BMD) analysis was applied to the dose-response curves predicted by the human PBK model. The analysis was conducted using the US EPA's Benchmark Dose Software 3.2. Exponential and hill models were employed due to their suitability for modeling continuous data. The lower and upper 90% confidence limits of the BMD (BMDL₁₀ and BMDU₁₀, respectively), which correspond to an extra 10% response above the background compared to the control, were selected from the model with the best fit, as reflected by the lowest Akaike Information Criterion. The BMDL₁₀ values were used as PODs for MGO risk assessment as further described in **Section 6.2.8**.

6.2.8 Estimation of margins of exposure (MOEs) for MGO resulting from exogenous and endogenous MGO exposure

An MOE approach was employed for risk assessment of both endogenous and exogenous exposure to MGO. MOEs were calculated by dividing the derived PODs (BMDL₁₀) by the estimated daily intake or the estimated endogenous formation of MGO in healthy individuals and diabetic patients. The estimated daily MGO intake levels, as reported by Hellwig et al.²² and Degen et al.⁵⁴, are 0.03 mg/kg bw and 0.07-0.29 mg/kg bw for a 70 kg person, respectively. Levels of daily endogenous MGO formation are estimated at 3.09 mg/kg bw for healthy adult individuals and range from 6.01 to 12.35 mg/kg bw for diabetic patients, as reported by Rabbani & Thornalley³⁰. In the MOE calculations, the highest reported daily intake level of 0.29 mg/kg bw from Degen et al.⁵⁴ and the highest level of estimated daily endogenous formation of 12.35 mg/kg bw for diabetic patients from Rabbani & Thornalley³⁰ were used to represent a conservative, worst-case scenario. For healthy individuals, the reported daily endogenous formation of 3.09 mg/kg bw³⁰ was used.

6.3 Results

6.3.1 PBK model evaluation

Figure 6.3 shows the model-predicted blood concentrations of MGO and their comparisons to the reported blood concentrations of MGO following a single oral dose of 50, 100, or 200 mg/kg bw of MGO to mice. The C_{\max} and T_{\max} of MGO in mouse blood predicted by the PBK model and reported *in vivo* are shown in **Table 6.1**. The PBK model predictions for blood concentrations of MGO matched the reported concentrations well, with predictions falling within a two-fold difference of the *in vivo* data⁸⁰, indicating that the model was able to adequately predict the time-dependent blood concentrations of MGO at the given dose levels.

It is important to note the variations in the reported CL_{app} values for MGO in mice, being 7.69 L/h/kg at 50 mg/kg bw, 8.28 L/h/kg at 100 mg/kg bw, and 15.54 L/h/kg at 200 mg/kg bw⁸⁰. These differences resulted in a similar C_{max} for the 100 mg/kg and 200 mg/kg doses. This reflects that in this dose range clearance appeared to be not linear with the dose. For subsequent human PBK model-based reverse dosimetry, a CL_{app} of 7.69 was used for converted doses below 100 mg/kg bw, and a value of 8.28 was used for doses between 100 and 200 mg/kg bw. Given that the estimated human dietary intake of MGO was reported to be between 5-20 mg/day in a previous study⁵⁴, doses over 200 mg/kg bw were considered unrealistic. Nevertheless, a value of 15.54 was employed for doses above 200 mg/kg bw when needed in the PBK modeling-facilitated reverse dosimetry process.

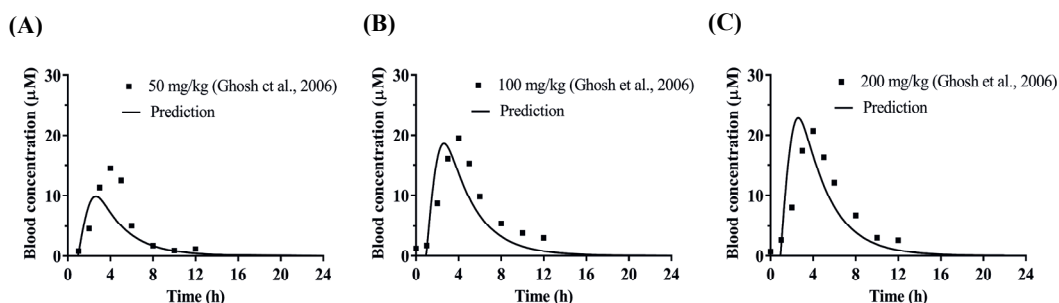


Figure 6.3. Comparison of reported⁸⁰ and PBK model-predicted time-dependent blood concentrations of MGO in mice following a single oral dose of 50 (A), 100 (B), or 200 (C) mg/kg bw MGO. The reported blood concentrations of MGO were corrected for endogenously formed MGO by subtracting the basal *in vivo* level of MGO amounting to 13.7 mM⁸⁰.

Table 6.1. PBK model-predicted C_{max} and T_{max} of MGO compared to *in vivo* mouse data as reported by Ghosh et al.⁸⁰

Dose (mg/kg bw)	Reported C_{max}^a (μ M)	Predicted C_{max} (μ M)	Predicted C_{max} /Reported C_{max}	Reported T_{max} (h)	Predicted T_{max} (h)	Predicted T_{max} /Reported T_{max}
50	13.9 \pm 2.85	9.86	0.71	\approx 4	2.63	0.66
100	18.7 \pm 3.62	18.61	1.00	\approx 4	2.63	0.66
200	19.5 \pm 3.36	22.79	1.17	\approx 4	2.61	0.65

^a The reported C_{max} of MGO was corrected for endogenously formed MGO by subtracting the basal *in vivo* levels of MGO amounting to 13.7 mM⁸⁰.

6.3.2 Sensitivity analysis of the PBK model

The performance of the mouse PBK model was further assessed by a sensitivity analysis to identify the parameters that are most influential on the C_{max} predictions of MGO in blood following a single oral administration of 50, 100, or 200 mg/kg bw. The parameters with an absolute normalized SC value of 0.1 or greater are presented in **Figure S6.1**. The results show that, for all three doses, the C_{max} predictions for MGO appeared to be most sensitive to the

parameters related to gastrointestinal transport and absorption, including the surface area of the intestinal compartment (SA_{in}), the volume for each compartment of intestines (V_{in}), the stomach emptying rate (k_{sto}), the P_{app} value, and the transfer rate to the next compartment within the intestines (k_{in}). Additionally, the CL_{app} value was also identified as one of the influential parameters affecting the C_{max} predictions for MGO.

6.3.3 Translation of the *in vitro* concentration-response curves for neurotoxicity and genotoxicity of MGO to *in vivo* dose-response curves and BMD analysis of predicted dose-response data

Upon evaluating the mouse PBK model for MGO, the model code was adapted to define a human PBK model for predicting MGO-induced neurotoxicity and genotoxicity in humans from *in vitro* data. **Figure 6.4A** summarizes the *in vitro* concentration-response data on MGO-induced neurotoxicity obtained with various human neuronal cell models found in the literature. Human primary neuronal-like cells (hNLCs), were found to be the most sensitive to MGO, displaying the lowest EC_{50} value for the cytotoxicity after 48 hours of exposure, which was 220.8 μM , as detailed in **Table 6.2**. These hNLCs are considered to mimic the physiological and biochemical properties of neuronal cells more accurately than other tested cell models⁹⁵. Consequently, the *in vitro* dataset for hNLCs, which includes the effects of MGO on mitochondrial function, cytotoxicity, and apoptosis, was chosen to establish *in vivo* dose-response data for humans. Furthermore, the dataset from Yuan et al., describing DNA adduct (R- N^2 -CEdG and S- N^2 -CEdG) formation induced by MGO in WM-266-4 cells²⁹⁸, was selected for *in vivo* translation for the genotoxicity of MGO (**Figure 6.4B**). The *in vitro* results in **Figure 6.4** reveal that the toxicity of MGO quantified by cytotoxicity and apoptosis in hNLCs started to occur at concentrations of 10 μM onwards. Mitochondrial dysfunction and cytotoxicity in hNLCs, and DNA adduct formation in WM-266-4 cells appeared to occur at somewhat higher concentrations.

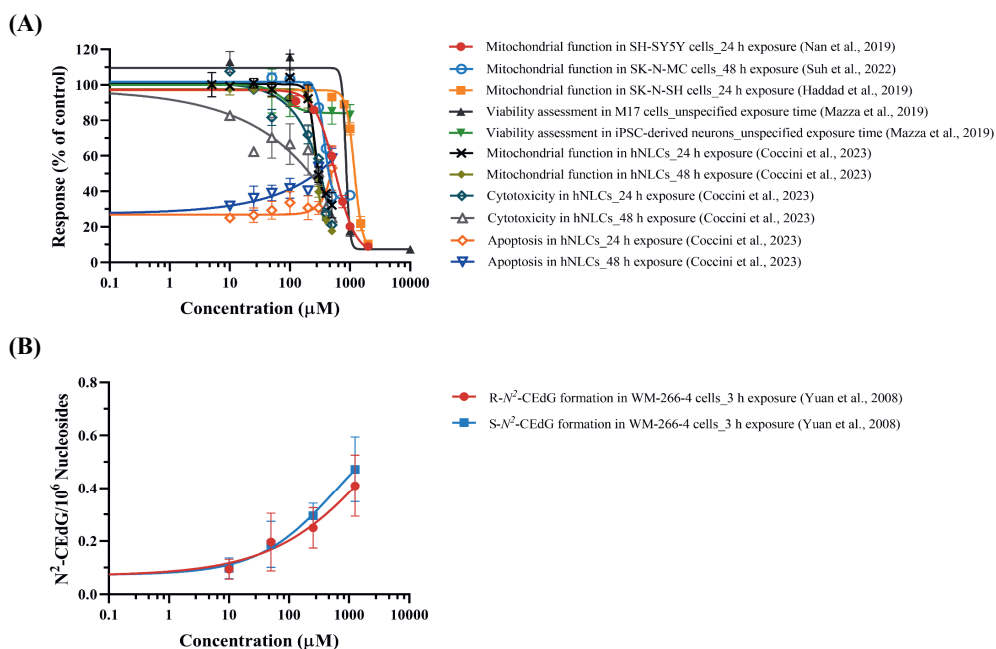


Figure 6.4. Overview of *in vitro* concentration-response data for MGO neurotoxicity and DNA adduct formation found in literature: (A) Neurotoxicity of MGO in various human neuronal cell models including SH-SY5Y cells⁹⁶, SK-N-MC cells²⁷⁷, SK-N-SH cells²⁷⁶, M17 cells and iPSC-derived neurons²⁹⁹, and hNLCs⁹⁵; (B) DNA adduct (R- $\text{N}^2\text{-CedG}$ and S- $\text{N}^2\text{-CedG}$) formation induced by MGO in WM-266-4 cells¹²². Data points are shown as mean \pm (SD or SEM), where available.

Table 6.2. EC_{50} values derived from the *in vitro* data on neurotoxicity of MGO in human neuronal cell models reported in literature

Human neuronal cell models	EC_{50}^a (μM)	Exposure time (h)	Endpoints	References
SH-SY5Y	710.0	24	Mitochondrial function (MTT assay)	96
SK-N-MC	372.9	48	Mitochondrial function (WST assay)	277
SK-N-SH	1179.0	24	Mitochondrial function (Resazurin assay)	276
M17	809.2	unspecified	Viability assessment (method unspecified)	299
Human induced pluripotent stem cell (iPSC)-derived neurons	> 1000	unspecified	Viability assessment (method unspecified)	299
hNLCs	340.5	24	Mitochondrial function (MTT assay)	95
hNLCs	298.3	48	Mitochondrial function (MTT assay)	95
hNLCs	312.1	24	Cytotoxicity (trypan blue exclusion test)	95
hNLCs	220.8	48	Cytotoxicity (trypan blue exclusion test)	95
hNLCs	Not Determined ^b	24	Apoptosis (nuclear staining with Hoechst 33258 dye)	95
hNLCs	Not Determined ^b	48	Apoptosis (nuclear staining with Hoechst 33258 dye)	95

^a EC_{50} values were determined through non-linear regression (variable slope, four parameters) using GraphPad Prism 9, except where specified in the literature.

^b EC_{50} values are not provided due to insufficient data for robust curve fitting.

Figure 6.5 shows the dose-response curves derived from translating the *in vitro* concentration-response data using PBK modeling-facilitated reverse-dosimetry with the developed human PBK model. Subsequent BMD analysis of these predicted *in vivo* dose-response curves revealed BMDL₁₀ values of 216 and 218 mg/kg bw for R-N²-CEdG and S-N²-CEdG formation, respectively, and a somewhat higher BMDL₁₀ of 258 mg/kg bw associated with apoptosis in neuronal cells (48 h exposure). The estimated BMDL₁₀ values for mitochondrial function (48 h exposure) and cytotoxicity (48 h exposure) amounted to 1618 and 481 mg/kg bw, respectively (**Table 6.3**).

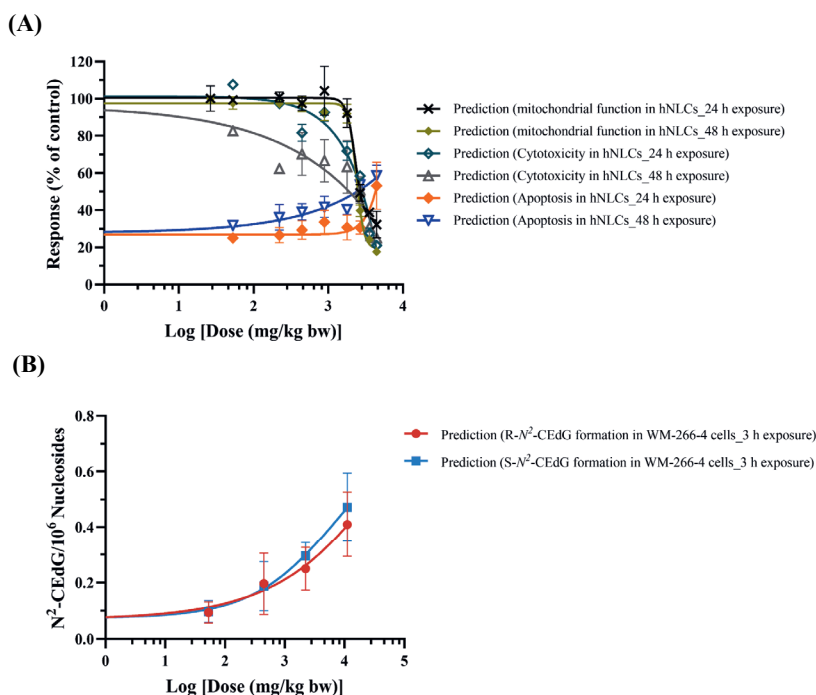


Figure 6.5. Predicted *in vivo* dose-response curves for MGO-induced neurotoxicity and DNA adduct formation upon oral administration of MGO to humans, acquired through PBK modeling-facilitated reverse dosimetry of *in vitro* toxicity data on (A) MGO-induced neurotoxicity in hNLCs reported by Coccini et al.⁹⁵, and (B) DNA adduct formation induced by MGO in WM-266-4 cells reported by Yuan et al.¹²² Data points are shown as mean \pm (SD or SEM), where available.

6.3.4 Risk assessment of exogenous and endogenous exposure to MGO using the MOE approach

Figure 6.6 displays the predicted BMDL₁₀-BMDU₁₀ ranges for MGO-induced neurotoxicity and DNA adduct formation, and also the dose levels at which the MOE relative to the respective BMDL₁₀ is 100 (for mitochondrial function, cytotoxicity, and apoptosis) or 10,000 (for DNA adduct formation) in comparison to the estimated daily dietary intake and endogenous

formation of MGO in humans. The results indicate that both the estimated daily intake and endogenous formation of MGO in healthy and diabetic individuals are below the BMDL_{10} for all the endpoints. Especially, the estimated dietary intake of MGO is approximately three orders of magnitude lower than the predicted BMDL_{10} values. Drawing from the European Food Safety Authority (EFSA)'s risk assessment for acrylamide, which is neurotoxic and genotoxic, this study adopted a similar MOE approach for further risk characterization for MGO³⁰⁰. Accordingly, an MOE of 100 or above for neurotoxicity endpoints including mitochondrial function, cytotoxicity, and apoptosis, was considered of no health concern. This margin accounts for uncertainties and variability within the human population (default uncertainty value of 10) and the incorporation of NAMs (assumed uncertainty value of also 10). Considering that DNA adduct formation implies genotoxicity effects, an MOE of 10,000 or higher for DNA adduct formation was employed, accounting for interindividual variability (value of 10), the use of NAMs (value of 10), uncertainties related to the carcinogenic processes (value of 10), and use of the BMDL_{10} value (value of 10), as indicative of no health concern. The green vertical lines in **Figure 6.6** represent the dose levels where the MOE relative to the respective BMDL_{10} is 100 (for mitochondrial function, cytotoxicity, and apoptosis) or 10,000 (for DNA adduct formation). Comparison of these dose levels to the estimated daily dietary intakes reveals that the estimated daily intake of MGO falls far below the green vertical lines representing the dose levels where the MOE relative to the respective BMDL_{10} is 100 for endpoints including mitochondrial function, cytotoxicity, and apoptosis, indicating that the systematic C_{max} values resulting from daily intake of MGO would not be high enough to cause mitochondrial dysfunction, cytotoxicity, and apoptosis in neuronal cells. However, endogenous MGO levels in healthy individuals, exceed this safety threshold (green vertical line) for apoptosis (48 h exposure), indicating that a potential risk of inducing apoptosis by endogenously formed MGO cannot be excluded. In diabetic patients, endogenous MGO levels not only surpass the dose level where the MOE relative to the BMDL_{10} is 100 for apoptosis but also are above the respective dose levels that result in an MOE of 100 for cytotoxicity, indicating that a concern can no longer be excluded. It is also important to note that for R- N^2 -CEdG and S- N^2 -CEdG formation both the estimated daily intake and the endogenous formation of MGO in healthy and diabetic individuals are above the green vertical lines representing the dose levels where the MOE relative to the respective BMDL_{10} for these endpoints is 10,000, indicating a concern for MGO-induced DNA modification from both dietary intake and endogenous formation cannot be excluded, with concerns for diabetic patients being higher than those for the healthy adult population. The numbers of the calculated MOE values for the dietary intake or endogenous formation of MGO in healthy individuals and diabetic patients for all the endpoints used in this study can be found in **Table 6.3**.

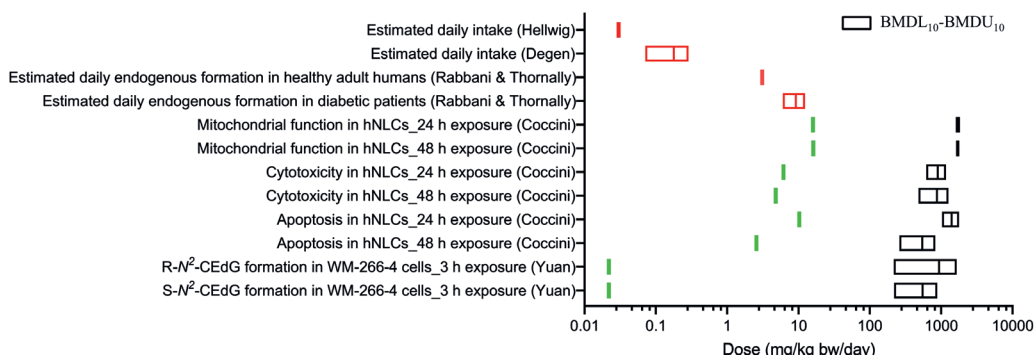


Figure 6.6. Comparison of estimated daily MGO intake and endogenous formation in healthy individuals and diabetic patients with predicted BMDL₁₀ values. The estimated daily MGO intake dose levels were taken from Hellwig et al.²² and Degen et al.⁵⁴ and amount to 0.03 mg/kg bw and 0.07-0.29 mg/kg bw for a 70 kg person, respectively. The estimated daily endogenous MGO formation levels in healthy adult individuals and diabetic patients were taken from Rabbani & Thornalley and amount to 3.09 mg/kg bw, and 6.01-12.35 mg/kg bw for a 70 kg person, respectively³⁰. The green vertical lines represent the dose levels where the MOE relative to the respective BMDL₁₀ is 100 (for mitochondrial function, cytotoxicity, and apoptosis) or 10,000 (for DNA adduct formation). For further details see text.

Table 6.3. Summary of estimated points of departures (PODs) taken as the BMDL₁₀ derived from the predicted dose-response curves and margins of exposure (MOEs) for neurotoxicity (mitochondrial function, cytotoxicity, and apoptosis), and genotoxicity (DNA adduct formation) induced by MGO

Endpoints	BMDL ₁₀ (mg/kg bw/day)	MOEs from dietary MGO exposure ^a	MOEs from endogenous MGO exposure	
			Healthy individuals	Diabetic patients ^b
Mitochondrial function (24 h exposure)	1599	5512	517	129
Mitochondrial function (48 h exposure)	1618	5580	524	131
Cytotoxicity (24 h exposure)	618	2131	200	50
Cytotoxicity (48 h exposure)	481	1659	156	39
Apoptosis (24 h exposure)	1029	3548	333	83
Apoptosis (48 h exposure)	258	891	84	21
R-N ² -CEdG formation (3 h exposure)	216	746	70	18
S-N ² -CEdG formation (3 h exposure)	218	752	71	18

^a MOE calculation for dietary MGO intake used the highest reported value of 0.29 mg/kg bw/day from Degen et al.⁵⁴, representing a worst-case scenario.

^b MOE calculation for diabetic patients' endogenous MGO exposure used the highest reported value of 12.35 mg/kg bw/day from Rabbani & Thornalley³⁰, also representing a worst-case scenario.

6.4 Discussion

PBK modeling-facilitated reverse dosimetry has proven to be a promising NAM for extrapolating *in vitro* data to predict *in vivo* toxicity of chemicals in humans, providing significant potential in chemical risk assessment^{116, 117, 119}. This study aimed to apply the PBK modeling-facilitated reverse dosimetry approach as a NAM to predict the neurotoxicity and genotoxicity of MGO in humans, based on the *in vitro* toxicity data obtained in a human neuronal cell model (hNLCs)⁹⁵, and in WM-266-4 human melanoma cells¹²². The *in vitro* toxicity endpoints evaluated included mitochondrial function, cytotoxicity, apoptosis, and DNA adduct formation.

The human PBK model for MGO presented in this study was developed based on a mouse PBK model. Evaluation of the mouse PBK model performance for MGO demonstrated its adequacy for predicting kinetic data at the given dose levels (50, 100 and 200 mg/kg bw). The kinetic parameters for MGO used in this model, including the P_{app} value and CL_{app} value, were identified as the most influential parameters for the prediction of the C_{max} of MGO in the sensitivity analysis. The absorption rate constant derived from the P_{app} value, determined in our laboratory using the Caco-2 model²⁸⁸, amounted to 0.25 h^{-1} . This value is in line with the average apparent absorption rate constant (k_a) from the reported mouse *in vivo* data⁸⁰ amounting to 0.24 h^{-1} . Since these values are comparable, employing either k_a or the P_{app} value to define MGO's absorption rate in the PBK model does not significantly affect the predicted C_{max} . With respect to the CL_{app} , the reported CL_{app} values for the three doses varied⁸⁰. The CL_{app} at 200 mg/kg bw was around 1.9-fold higher than the one reported at 100 mg/kg bw. This increase might be due to the increased metabolism of MGO by the glyoxalase system. The increase in CL_{app} with increasing dose appeared to be more substantial at dose levels above 100 mg/kg bw and may be less pronounced at lower dose levels. Moreover, although it is challenging to predict the CL_{app} for doses different from the dose levels tested in the *in vivo* kinetic study⁸⁰, the lowest available value of 7.69 appears most suitable for PBK modeling at dose levels in the range of the estimated daily dietary MGO intake. Even when the CL_{app} value would be tenfold lower, it can be calculated (data not shown) that the predicted BMDL₁₀ values for endpoints including mitochondrial function, cytotoxicity, and apoptosis will still be over two orders of magnitude above the estimated daily dietary MGO intake, and the MOEs are still high enough to be of no concern. It is also important to note that the current study assumed that the *in vivo* dose-dependent neurotoxicity induced by MGO is based on the maximal unbound concentration (C_{max}) of MGO in the blood, rather than incorporating a separate compartment for the central nervous system (CNS) in the PBK model to predict the maximal concentration achievable in the CNS. At the present state-of-the-art, the extent to which MGO can enter the CNS is not yet clearly defined. If the transport to the CNS is limited,

the MOEs resulting from daily dietary intake would be even larger than what has now been estimated.

The results reported in the literature and depicted in **Figure 6.6** indicate that the reported endogenous MGO formation in healthy adults (ca. 216 mg equal to 3.09 mg/kg bw for a 70 kg person) exceeds the estimated daily dietary intake of MGO (5-20 mg equal to 0.07-0.29 mg/kg bw for a 70 kg person) by more than tenfold^{30, 54}, indicating that the dietary contribution to the total MGO exposure is relatively low. This observation aligns with findings from a previous study where the consumption of honey containing 37 mg of MGO, a quantity exceeding the estimated daily intake levels and equal to 0.53 mg/kg bw for a 70 kg person, did not result in increased urinary excretion of MGO and its metabolite D-lactate⁸². This suggests that the absorption of dietary MGO might be limited. Furthermore, the results obtained in the current study show that the MOEs resulting from estimated daily dietary intake of MGO for the neurotoxicity endpoints ranged from 258 to 1618, which was above the safety limit of 100, suggesting that the systemic concentrations resulting from daily MGO intake are unlikely to reach levels capable of inducing mitochondrial dysfunction, cytotoxicity, and apoptosis in neuronal cells. In contrast, the MOE value for the apoptosis (48 h exposure) resulting from daily endogenous MGO formation in healthy individuals, amounted to 84, and for diabetic patients, whose endogenous MGO formation is reported to be two to four times higher than that in healthy individuals³⁰, the MOEs for the apoptosis and also for cytotoxicity were below the safety limit of 100 (**Table 6.3**), suggesting neurotoxicity reflected by these two endpoints induced by endogenously formed MGO cannot be excluded. These results are also supported by previous research which linked the progression of diabetic neuropathies, a major complication of diabetes, to increased *in vivo* levels of dicarbonyl compounds³⁰¹, further emphasizing the critical role of endogenous MGO levels in these adverse health outcomes. The MOEs for DNA adduct formation from both dietary intake and endogenous formation in healthy individuals and diabetic patients were all below 10,000, indicating that concerns about MGO's potential to increase the risk of developing cancer via a genotoxic mode of action cannot be excluded, especially not for diabetic patients for which as a result of endogenous MGO formation an MOE of only 18 was obtained. Previous meta-analyses revealed that diabetic patients were at a higher risk of developing several types of cancer³⁰², and endogenous accumulation of AGEs formed from protein and DNA modifications by MGO may potentially be linked to cancer development¹⁸⁵.

It is relevant to note that the average plasma levels from endogenously formed MGO amounted to 0.29 μM for healthy individuals as derived from aggregating data across multiple studies, reporting values of 0.21, 0.13, and 0.52 μM ²⁷³⁻²⁷⁵. In diabetic patients, the plasma MGO levels were found to be more than 30% higher than those in healthy individuals^{273, 275}.

However, it appeared that in the PBK modeling the internal concentrations resulting from an exogenous dose as high as 50, 100 and 200 mg/kg bw were far above the endogenous plasma concentrations (0.29 μ M). This can be attributed to the fact that the dose levels used for the modeling (and used in the mouse kinetic *in vivo* study) are much higher than the dietary intake levels. The PBK model predicted internal C_{\max} levels resulting from realistic estimated daily dietary intake were found to be more than threefold lower than the endogenous plasma MGO levels. This observation also suggests that *in vitro* studies employing MGO concentrations in the high mM range may not accurately reflect realistic dietary exposure to MGO. Besides, considering the more critical role of endogenous MGO levels in potential adverse health effects, future studies could focus on *in vitro* models that mimic increased intracellular MGO formation, aiming to provide deeper insights into the mechanisms underlying how increased endogenous MGO formation contributes to disease processes and identify mitigation strategies, particularly for vulnerable populations like diabetics.

It is also crucial to recognize that while our study suggests the neurotoxicity risk from dietary MGO might be minimal, exposure to other dicarbonyl compounds, such as glyoxal (GO) and 3-deoxyglucosone (3-DG), is also prevalent and could potentially add to the risk of toxicity caused by these dicarbonyl AGE precursors in humans. Among these, MGO was identified as the most reactive in terms of cytotoxicity and ROS formation in a previous study³¹. The estimated worst-case daily intake for glyoxal is around 10 mg³⁰³, whereas, for 3-DG, dietary intake levels are notably higher, ranging from 20 to 160 mg per day⁵⁴. A study found that upon consuming 82 mg 3-DG in a honey matrix, a significant proportion (10–15%) of the ingested 3-DG and its metabolite (3-deoxyfructose) was excreted in the urine⁸¹. This suggests that the contribution of dietary 3-DG to the total *in vivo* 3-DG exposome may be more substantial than what was observed for MGO. Given these findings, it would be of interest for future research to establish relative potency values for GO and 3-DG relative to MGO to more accurately assess the health risks from combined exposure to dicarbonyl compounds.

Taking all together, this study demonstrates a proof of principle on how to integrate *in vitro* data and *in silico* PBK modeling to predict *in vivo* kinetics of dicarbonyl compounds and characterize their dose levels causing toxicity *in vivo* in humans. The results show that the MOEs resulting from daily dietary intake did not raise a concern for endpoints for neurotoxicity including mitochondrial function, cytotoxicity, and apoptosis, while those for DNA adduct formation could not exclude a concern over genotoxicity. In comparison, endogenous MGO formation, especially under diabetic conditions, resulted in MOEs that raised a concern not only for genotoxicity but also for some of the neurotoxicity endpoints evaluated. Thus, the results also point at the importance of taking the endogenous levels into account in risk assessment of MGO.

Acknowledgments

Liang Zheng is thankful for the financial support provided by the China Scholarship Council, under Grant Number: CSC202008510115.

Supporting information

Table S6.3. Physiological and anatomical parameter values (based on Hall et al.²⁸⁶ and Brown et al.²⁸⁷) and the partition coefficients (calculated using the QIVIVE Tool²⁹²) used in the PBK models.

Parameters	Symbols	Mouse	Human
Body weight (kg)	BW	0.03	70
Fraction of tissue volumes			
Fat	VFc	0.070	0.214
Liver	VLc	0.055	0.026
Blood	VBc	0.067	0.079
Rapidly perfused tissue	VRc	0.154	0.068
Slowly perfused tissue	VSc	0.654	0.613
Cardiac output	QC	15.4*BW ^{0.75}	15*BW ^{0.74}
Fraction of blood flow to tissue			
Fat	QFc	0.070	0.052
Liver	QLc	0.158	0.227
Rapidly perfused tissue	QRc	0.630	0.370
Slowly perfused tissue	QSc	0.142	0.351
Tissue/blood partition coefficients			
Fat	PF	0.17	0.17
Liver	PL	0.54A	0.54
Rapidly perfused tissue	PR	0.53	0.53
Slowly perfused tissue	PS	0.48	0.48

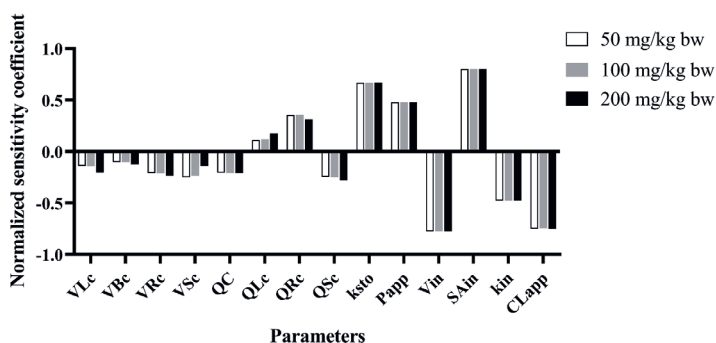


Figure S6.1. Sensitivity analysis for the predicted C_{\max} of MGO after oral administration of 50, 100, or 200 mg/kg bw MGO. Model parameters with an absolute normalized sensitivity coefficient (SC) value ≥ 0.1 are displayed. VLc: fraction of liver tissue, VBc: fraction of blood, VRc: fraction of rapidly perfused tissue, VSc: fraction of slowly perfused tissue, QC: cardiac output, QLc: fraction of blood flow to liver, QRc: fraction of blood flow to rapidly perfused tissue, QSc: fraction of blood flow to slowly perfused tissue, ksto: stomach emptying rate, Papp: apparent permeability coefficient obtained from the Caco-2 model, Vin: volume for each compartment of intestines, SAin: surface area of the intestinal compartment, kin: transfer rate to next compartment within the intestines, CLapp: apparent total body clearance in mice.

Model code for PBK-model built in Berkeley Madonna for mice

```
;Date: December 2023
;Species: Mouse
;Compound: Methylglyoxal (MGO)
;Compiled by: Liang Zheng
;Organization: Wageningen University
;=====
;Physiological parameters
;=====
;tissue volumes286
BW = 0.03           ; body weight mouse (kg)
VFc = 0.07          ; fraction of fat tissue
VLc = 0.055         ; fraction of liver tissue
VBc = 0.067         ; fraction of blood
VRc = 0.154         ; fraction of rapidly perfused tissue
VSc = 0.654         ; fraction of slowly perfused tissue

VF = VFc*BW         ; (L or Kg)           ; volume of fat tissue (calculated)
VL = VLc*BW         ; (L or Kg)           ; volume of liver tissue (calculated)
VB = VBc*BW         ; (L or Kg)           ; volume of blood (calculated)
VR = VRc*BW         ; (L or Kg)           ; volume of richly perfused tissue (calculated)
VS = VSc*BW         ; (L or Kg)           ; volume of slowly perfused tissue (calculated)
;-----
;blood flow rates286

QC = 15.4*BW^0.75   ; (L/hr) ; cardiac output287
QFc = 0.070         ; fraction of blood flow to fat
QLc = 0.158         ; fraction of blood flow to liver
QRc = 0.630         ; fraction of blood flow to rapidly perfused tissue
QSc = 0.142         ; fraction of blood flow to slowly perfused tissue
```

```

QF = QFc*QC ; (L/hr) ; blood flow to fat tissue (calculated)
QL = QLc*QC ; (L/hr) ; blood flow to liver tissue (calculated)
QR = QRc*QC ; (L/hr) ; blood flow to rapidly perfused tissue (calculated)
QS = QSc*QC ; (L/hr) ; blood flow to slowly perfused tissue (calculated)
;=====
;Partition Coefficients
;=====
; Partition coefficients are derived from Rodgers and Rowland291 using the QIVIVE tool
(www.qivivetools.wur.nl)292

PF = 0.17 ; fat/blood partition coefficient
PL = 0.54 ; liver/blood partition coefficient
PR = 0.53 ; rapidly perfused tissue/blood partition coefficient
PS = 0.48 ; slowly perfused tissue/blood partition coefficient
;=====
;Intestinal lumen volumes, surfaces, absorption rates, transfer rates
;=====
;Stomach emptying rate

ksto = 0.36 ; stomach emptying rate (/hr)304

;Papp, Caco-2 = 1.09*1E-6 cm/sec ;from Caco-2 transport studies (Li et al., submitted)

PappCaco2=-5.96 ; Log Papp, Caco-2

;Log (Papp, human) = 0.6836*Log(PappCaco-2)-0.5579 (Sun et al.289)

PappHuman = 10^(0.6836*PappCaco2-0.5579)*3600/10 ; (dm/hr)
PappMouse = PappHuman/3.6 ; interspecies scaling factor290

;7-compartment model for GI-tract based on model bisphenol A and 17β-estradiol by Zhang et al.119

Vin = 0.00012 ; volume for each compartment of intestines (L);
SAin = 0.013 ; surface area (dm2)
kin = 4.17 ; transfer rate to next compartment within the intestines (/hr);
;kabinX = PappMouse*SAinX ; absorption rate constant (L/hr)

Vin1 = Vin ; volume of intestine compartment 1 (L)
SAin1 = SAin ; surface area of intestine compartment 1 (dm2)
kabin1 = PappMouse*SAin1 ; absorption rate constant of intestine compartment 1 (L/hr)
kin1 = kin ; transfer rate to intestine compartment 2 (/hr)

Vin2 = Vin ; volume of intestine compartment 2 (L)
SAin2 = SAin ; surface area of intestine compartment 2 (dm2)
kabin2 = PappMouse*SAin2 ; absorption rate constant of intestine compartment 2 (L/hr)
kin2 = kin ; transfer rate to intestine compartment 3 (/hr)

Vin3 = Vin ; volume of intestine compartment 3 (L)
SAin3= SAin ; surface area of intestine compartment 3 (dm2)
kabin3 = PappMouse*SAin3 ; absorption rate constant of intestine compartment 3 (L/hr)
kin3 = kin ; transfer rate to intestine compartment 4 (/hr)

Vin4 = Vin ; volume of intestine compartment 4 (L)
SAin4 = SAin ; surface area of intestine compartment 4 (dm2)
kabin4 = PappMouse*SAin4 ; absorption rate constant of intestine compartment 4 (L/hr)
kin4 = kin ; transfer rate to intestine compartment 5 (/hr)

```

```

Vin5 = Vin                ; volume of intestine compartment 5 (L)
SAin5 = SAin              ; surface area of intestine compartment 5 (dm2)
kabin5 = PappMouse*SAin5  ; absorption rate constant of intestine compartment 5 (L/hr)
kin5 = kin                 ; transfer rate to intestine compartment 6 (/hr)

Vin6 = Vin                ; volume of intestine compartment 6 (L)
SAin6 = SAin              ; surface area of intestine compartment 6 (dm2)
kabin6 = PappMouse*SAin6  ; absorption rate constant of intestine compartment 6 (L/hr)
kin6 = kin                 ; transfer rate to intestine compartment 7 (hr)

Vin7 = Vin                ; volume of intestine compartment 7 (L)
SAin7 = SAin              ; surface area of intestine compartment 7 (dm2)
kabin7 = PappMouse*SAin7  ; absorption rate constant of intestine compartment 7 (L/hr)
kin7 = kin                 ; transfer rate to co (/hr)

kfe = 0.27                 ; transfer rate to feces (/hr)305
;-----
;Metabolism liver

CLapp = 7.69               ; (L/hr/kg)          ; whole body clearance80
CLhep = CLapp*VL           ; (L/hr)          ; Hepatic clearance
;-----
;Metabolism Fat/Slowly Perfused/Rapidly Perfused/Blood

CLfat = CLapp*VF           ; (L/hr)          ; Fat clearance
CLspt = CLapp*VS           ; (L/hr)          ; Slowly Perfused tissues clearance
CLrpt = CLapp*VR           ; (L/hr)          ; Rapidly Perfused tissues clearance
CLblood = CLapp*VB         ; (L/hr)          ; Blood clearance
;=====
;Run settings
;=====
;Molecular weight

MW = 72.06                 ;Molecular weight MGO (PubChem)
;-----
;Single dose:

;Oral dose is 50 mg/kg bw80
ODOSEmg = 50               ; (mg/kg bw)      ; given oral dose in mg/kg bw
ODOSEumol2 = ODOSEmg*1E-3/MW*1E6 ; (umol/kg bw)    ; recalculated to umol/kg bw
ODOSEumol = ODOSEumol2*BW   ; (umol)          ; given oral dose in umol

;time
Starttime = 0.92           ; (h) lag phase80
Stoptime = 24              ; (h) variable
DTMIN = 1e-6
DTMAX = 1
DTOUT = 0
TOLERANCE = 0.000001
;=====
;Model calculations
;=====
;model of MGO
;-----
;Stomach compartment
;-----
;Single dose

```

```

;Ast = amount of MGO remaining in stomach,  $\mu\text{mol}$ 
Ast' = -ksto*Ast
Init Ast = ODOSEumol
;-----
;intestinal compartment, divided in 7 sub compartments

;Ain1 = Amount MGO in intestine compartment 1 ( $\mu\text{mol}$ )
Cin1 = Ain1/Vin1
Ain1' = ksto*Ast - kin1*Ain1 - kabin1*Cin1
Init Ain1 = 0

;Ain2 = Amount MGO in intestine compartment 2 ( $\mu\text{mol}$ )
Cin2 = Ain2/Vin2
Ain2' = kin1*Ain1 - kin2*Ain2 - kabin2*Cin2
Init Ain2 = 0

;Ain3 = Amount MGO in intestine compartment 3 ( $\mu\text{mol}$ )
Cin3 = Ain3/Vin3
Ain3' = kin2*Ain2 - kin3*Ain3 - kabin3*Cin3
Init Ain3 = 0

;Ain4 = Amount MGO in intestine compartment 4 ( $\mu\text{mol}$ )
Cin4 = Ain4/Vin4
Ain4' = kin3*Ain3 - kin4*Ain4 - kabin4*Cin4
Init Ain4 = 0

;Ain5 = Amount MGO in intestine compartment 5 ( $\mu\text{mol}$ )
Cin5 = Ain5/Vin5
Ain5' = kin4*Ain4 - kin5*Ain5 - kabin5*Cin5
Init Ain5 = 0

;Ain6= Amount MGO in intestine compartment 6 ( $\mu\text{mol}$ )
Cin6 = Ain6/Vin6
Ain6' = kin5*Ain5 - kin6*Ain6 - kabin6*Cin6
Init Ain6 = 0

;Ain7= Amount MGO in intestine compartment 7 ( $\mu\text{mol}$ )
Cin7 = Ain7/Vin7
Ain7' = kin6*Ain6 - kin7*Ain7 - kabin7*Cin7
Init Ain7 = 0

;Aco = Amount MGO in colon ( $\mu\text{mol}$ )
Aco' = kin7*Ain7 - kfe*Aco
Init Aco = 0
ACco' = kin7*Ain7
Init ACco = 0 ; cumulative amount reaching colon
;-----
;Feces

;AFe = amount MGO in feces ( $\mu\text{mol}$ )
AFe' = kfe*Aco
Init AFe = 0
;-----
;Liver compartment

;AL = Amount MGO in liver tissue,  $\mu\text{mol}$ 

```

```

AL' = kabin1*Cin1 + kabin2*Cin2 + kabin3*Cin3 + kabin4*Cin4 + kabin5*Cin5 + kabin6*Cin6 + kabin7*Cin7
+QL*(CB-CVL)-Amhep' ; (μmol/hr)
Init AL = 0
CL = AL/VL
CVL = CL/PL

;Amhep = amount MGO metabolized in liver
Amhep' = CLhep*CVL ; (μmol/hr)
Init Amhep = 0
;-----
;Fat compartment

;AF = Amount MGO in fat tissue (μmol)
AF' = QF*(CB-CVF)-Amfat' ; (μmol/hr)
Init AF = 0
CF = AF/VF
CVF = CF/PF

;Amfat = amount MGO metabolized in Fat
Amfat' = CLfat*CVF ; (μmol/hr)
Init Amfat = 0
;-----
;Tissue compartment rapidly perfused tissues

;AR = Amount MGO in rapidly perfused tissue (μmol)
AR' = QR*(CB-CVR)-Amrpt' ; (μmol/hr)
Init AR = 0
CR = AR/VR
CVR = CR/PR

;Amrpt = amount MGO metabolized in rapidly perfused tissues
Amrpt' = CLrpt*CVR ; (μmol/hr)
Init Amrpt = 0
;-----
;Tissue compartment slowly perfused tissues

;AS = Amount MGO in slowly perfused tissue (μmol)
AS' = QS*(CB-CVS)-Amspt' ; (μmol/hr)
Init AS = 0
CS = AS/VS
CVS = CS/PS

;Amspt = amount MGO metabolized in slowly perfused tissues
Amspt' = CLspt*CVS ; (μmol/hr)
Init Amspt = 0
;-----
;Blood compartment

;AB = Amount MGO in blood (μmol)
AB' = QF*CVF + QL*CVL + QS*CVS + QR*CVR - QC*CB - Amblood' ; (μmol/hr)
Init AB = 0
CB = AB/VB
AUC' = CB ; (μmol*hr/L)
Init AUC = 0

;Amblood = amount MGO metabolized by blood cells
Amblood' = CLblood*CB

```

```

Init Amblood = 0
;=====
;Mass balance calculations
;=====
;single dose

Total = ODOSEumol
Calculated = ASt + Ain1 + Ain2 + Ain3 + Ain4 + Ain5 + Ain6 + Ain7 + Aco + AFe + AL + Amhep + AF + Amfat + AS +
Amspt + AR + Amrpt + AB + Amblood
ERROR=((Total-Calculated)/Total+1E-30)*100
MASSBBAL=Total-Calculated + 1
;=====

```

Model code for PBK-model built in Berkeley Madonna for humans

```

;Date: December 2023
;Species: Human
;Compound: Methylglyoxal (MGO)
;Compiled by: Liang Zheng
;Organization: Wageningen University
;=====
;Physiological parameters
;=====
;tissue volumes287

BW = 70 ; body weight mouse (kg)
VFc = 0.214 ; fraction of fat tissue
VLc = 0.026 ; fraction of liver tissue
VBc = 0.079 ; fraction of blood
VRc = 0.068 ; fraction of rapidly perfused tissue
VSc = 0.613 ; fraction of slowly perfused tissue

VF = VFc*BW ; (L or Kg) ; volume of fat tissue (calculated)
VL = VLc*BW ; (L or Kg) ; volume of liver tissue (calculated)
VB = VBc*BW ; (L or Kg) ; volume of blood (calculated)
VR = VRc*BW ; (L or Kg) ; volume of richly perfused tissue (calculated)
VS = VSc*BW ; (L or Kg) ; volume of slowly perfused tissue (calculated)
;=====
; blood flow rates287

QC = 15*BW^0.74 ; (L/hr) ; cardiac output287
QFc = 0.052 ; fraction of blood flow to fat
QLc = 0.227 ; fraction of blood flow to liver
QRc = 0.370 ; fraction of blood flow to rapidly perfused tissue
QSc = 0.351 ; fraction of blood flow to slowly perfused tissue

QF = QFc*QC ; (L/hr) ; blood flow to fat tissue (calculated)
QL = QLc*QC ; (L/hr) ; blood flow to liver tissue (calculated)
QR = QRc*QC ; (L/hr) ; blood flow to rapidly perfused tissue (calculated)
QS = QSc*QC ; (L/hr) ; blood flow to slowly perfused tissue (calculated)
;=====
;Partition Coefficients
;=====
; Partition coefficients are derived from Rodgers and Rowland291 using the QIVIVE tool
(www.qivivetools.wur.nl)292

```

```

PF = 0.17                ;fat/blood partition coefficient
PL = 0.54                ;liver/blood partition coefficient
PR = 0.53                ;rapidly perfused tissue/blood partition coefficient
PS = 0.48                ;slowly perfused tissue/blood partition coefficient
=====
;Intestinal lumen volumes, surfaces, absorption rates, transfer rates
;=====
;Stomach emptying rate

ksto = 2.8                ; stomach emptying rate (/hr)306

;Papp, Caco-2 = 1.09*1E-6 cm/sec ;from Caco-2 transport studies (Li et al., submitted)

PappCaco2=-5.96          ; Log Papp, Caco-2

;Log (Papp, human) = 0.6836*Log(PappCaco-2)-0.5579 (Sun et al.289)

PappHuman = 10^(0.6836*PappCaco2-0.5579)*3600/10    ; (dm/hr)

;7-compartment model for GI-tract based on model bisphenol A and 17β-estradiol by Zhang et al.119

Vin  = 1.29              ; volume for each compartment of intestines (L);
SAin = 10.3              ; surface area (dm2)
kin  = 2.19              ; transfer rate to next compartment within the intestines (/hr);

;kabinX = PappHuman*SAinX    ; absorption rate constant (L/hr)

Vin1 = Vin                ; volume of intestine compartment 1 (L)
SAin1 = SAin              ; surface area of intestine compartment 1 (dm2)
kabin1 = PappHuman*SAin1   ; absorption rate constant of intestine compartment 1 (L/hr)
kin1 = kin                ; transfer rate to intestine compartment 2 (/hr)

Vin2 = Vin                ; volume of intestine compartment 2 (L)
SAin2 = SAin              ; surface area of intestine compartment 2 (dm2)
kabin2 = PappHuman*SAin2   ; absorption rate constant of intestine compartment 2 (L/hr)
kin2 = kin                ; transfer rate to intestine compartment 3 (/hr)

Vin3 = Vin                ; volume of intestine compartment 3 (L)
SAin3 = SAin              ; surface area of intestine compartment 3 (dm2)
kabin3 = PappHuman*SAin3   ; absorption rate constant of intestine compartment 3 (L/hr)
kin3 = kin                ; transfer rate to intestine compartment 4 (/hr)

Vin4 = Vin                ; volume of intestine compartment 4 (L)
SAin4 = SAin              ; surface area of intestine compartment 4 (dm2)
kabin4 = PappHuman*SAin4   ; absorption rate constant of intestine compartment 4 (L/hr)
kin4 = kin                ; transfer rate to intestine compartment 5 (/hr)

Vin5 = Vin                ; volume of intestine compartment 5 (L)
SAin5 = SAin              ; surface area of intestine compartment 5 (dm2)
kabin5 = PappHuman*SAin5   ; absorption rate constant of intestine compartment 5 (L/hr)
kin5 = kin                ; transfer rate to intestine compartment 6 (/hr)

Vin6 = Vin                ; volume of intestine compartment 6 (L)
SAin6 = SAin              ; surface area of intestine compartment 6 (dm2)
kabin6 = PappHuman*SAin6   ; absorption rate constant of intestine compartment 6 (L/hr)
kin6 = kin                ; transfer rate to intestine compartment 7 (hr)

```

```

Vin7 = Vin                      ; volume of intestine compartment 7 (L)
SAin7 = SAin                    ; surface area of intestine compartment 7 (dm2)
kabin7 = PappHuman*SAin7        ; absorption rate constant of intestine compartment 7 (L/hr)
kin7 = kin                      ; transfer rate to co (/hr)

kfe = 0.27                      ; transfer rate to feces (/hr)305
;-----
;Metabolism liver

CLapp = 7.69                    ; (L/hr/kg)      ; whole body clearance80
CLhep = CLapp*VL                ; (L/hr)      ; Hepatic clearance
;-----
;Metabolism Fat/Slowly Perfused/Rapidly Perfused/Blood

CLfat = CLapp*VF                ; (L/hr)      ; Fat clearance
CLspt = CLapp*VS                ; (L/hr)      ; Slowly Perfused tissues clearance
CLrpt = CLapp*VR                ; (L/hr)      ; Rapidly Perfused tissues clearance
CLblood = CLapp*VB              ; (L/hr)      ; Blood clearance;
;=====
;Run settings
;=====
;Molecular weight

MW = 72.06                     ; Molecular weight MGO (PubChem)
;-----
;Single dose:

;Oral dose is 50 mg/kg bw80
ODOSEmg = 50                   ; (mg/kg bw)   ; given oral dose in mg/kg bw
ODOSEumol2 = ODOSEmg*1E-3/MW*1E6 ; (μmol/kg bw) ; recalculated to μmol/kg bw
ODOSEumol = ODOSEumol2*BW      ; (μmol)      ; given oral dose in μmol

;time
Starttime = 0.92                ; (h) lag phase80
Stoptime = 24                   ; (h) variable
DTMIN = 1e-6
DTMAX = 1
DTOUT = 0
TOLERANCE = 0.000001
;=====
;Model calculations
;=====
;model of MGO
;-----
;Stomach compartment
;-----
;Single dose

;ASt = amount of MGO remaining in stomach, μmol
ASt' = -ksto*ASt
Init ASt = ODOSEumol
;-----
;intestinal compartment, divided in 7 sub compartments

;Ain1 = Amount MGO in intestine compartment 1 (μmol)
Cin1 = Ain1/Vin1
Ain1' = ksto*ASt - kin1*Ain1 - kabin1*Cin1

```


Init Ain1 = 0

;Ain2 = Amount MGO in intestine compartment 2 (μmol)

Cin2 = Ain2/Vin2

Ain2' = $\text{kin1} \cdot \text{Ain1} - \text{kin2} \cdot \text{Ain2} - \text{kabin2} \cdot \text{Cin2}$

Init Ain2 = 0

;Ain3 = Amount MGO in intestine compartment 3 (μmol)

Cin3 = Ain3/Vin3

Ain3' = $\text{kin2} \cdot \text{Ain2} - \text{kin3} \cdot \text{Ain3} - \text{kabin3} \cdot \text{Cin3}$

Init Ain3 = 0

;Ain4 = Amount MGO in intestine compartment 4 (μmol)

Cin4 = Ain4/Vin4

Ain4' = $\text{kin3} \cdot \text{Ain3} - \text{kin4} \cdot \text{Ain4} - \text{kabin4} \cdot \text{Cin4}$

Init Ain4 = 0

;Ain5 = Amount MGO in intestine compartment 5 (μmol)

Cin5 = Ain5/Vin5

Ain5' = $\text{kin4} \cdot \text{Ain4} - \text{kin5} \cdot \text{Ain5} - \text{kabin5} \cdot \text{Cin5}$

Init Ain5 = 0

;Ain6 = Amount MGO in intestine compartment 6 (μmol)

Cin6 = Ain6/Vin6

Ain6' = $\text{kin5} \cdot \text{Ain5} - \text{kin6} \cdot \text{Ain6} - \text{kabin6} \cdot \text{Cin6}$

Init Ain6 = 0

;Ain7 = Amount MGO in intestine compartment 7 (μmol)

Cin7 = Ain7/Vin7

Ain7' = $\text{kin6} \cdot \text{Ain6} - \text{kin7} \cdot \text{Ain7} - \text{kabin7} \cdot \text{Cin7}$

Init Ain7 = 0

;Aco = Amount MGO in colon (μmol)

Aco' = $\text{kin7} \cdot \text{Ain7} - \text{kfe} \cdot \text{Aco}$

Init Aco = 0

ACco' = $\text{kin7} \cdot \text{Ain7}$

Init ACco = 0 ; cumulative amount reaching colon

;Feces

;AFc = amount MGO in feces (μmol)

AFc' = $\text{kfe} \cdot \text{Aco}$

Init AFc = 0

;Liver compartment

;AL = Amount MGO in liver tissue, μmol

AL' = $\text{kabin1} \cdot \text{Cin1} + \text{kabin2} \cdot \text{Cin2} + \text{kabin3} \cdot \text{Cin3} + \text{kabin4} \cdot \text{Cin4} + \text{kabin5} \cdot \text{Cin5} + \text{kabin6} \cdot \text{Cin6} + \text{kabin7} \cdot \text{Cin7} + \text{QL} \cdot (\text{CB-CVL}) \cdot \text{Amhep}'$; ($\mu\text{mol/hr}$)

Init AL = 0

CL = AL/VL

CVL = CL/PL

;Amhep = amount MGO metabolized in liver

Amhep' = $\text{CLhep} \cdot \text{CVL}$; ($\mu\text{mol/hr}$)

Init Amhep = 0

```

;-----
;Fat compartment

;AF = Amount MGO in fat tissue (μmol)
AF' = QF*(CB-CVF)-Amfat' ; (μmol/hr)
Init AF = 0
CF = AF/VF
CVF = CF/PF

;Amfat = amount MGO metabolized in Fat
Amfat' = CLfat*CVF ; (μmol/hr)
Init Amfat = 0
;-----
;Tissue compartment rapidly perfused tissues

;AR = Amount MGO in rapidly perfused tissue (μmol)
AR' = QR*(CB-CVR)-Amrpt' ; (μmol/hr)
Init AR = 0
CR = AR/VR
CVR = CR/PR

;Amrpt = amount MGO metabolized in rapidly perfused tissues
Amrpt' = CLrpt*CVR ; (μmol/hr)
Init Amrpt = 0
;-----
;Tissue compartment slowly perfused tissues

;AS = Amount MGO in slowly perfused tissue (μmol)
AS' = QS*(CB-CVS)-Amspt' ; (μmol/hr)
Init AS = 0
CS = AS/VS
CVS = CS/PS

;Amspt = amount MGO metabolized in slowly perfused tissues
Amspt' = CLspt*CVS ; (μmol/hr)
Init Amspt = 0
;-----
;Blood compartment

;AB = Amount MGO in blood (μmol)
AB' = QF*CVF + QL*CVL + QS*CVS + QR*CVR - QC*CB - Amblood' ; (μmol/hr)
Init AB = 0
CB = AB/VB
AUC' = CB ; (μmol*hr/L)
Init AUC = 0

;Amblood = amount MGO metabolized by blood cells
Amblood' = CLblood*CB
Init Amblood = 0
;=====
;Mass balance calculations
;=====
;single dose

Total = ODOSEumol
Calculated = AS + Ain1 + Ain2 + Ain3 + Ain4 + Ain5 + Ain6 + Ain7 + Aco + AFe + AL + Amhep + AF + Amfat + AS +
Amspt + AR + Amrpt + AB + Amblood

```

$ERROR = ((Total - Calculated) / Total + 1E-30) * 100$


$MASSBAL = Total - Calculated + 1$

7



Chapter 7

General Discussion

An abstract graphic consisting of several overlapping, wavy, horizontal bands of different shades of blue. The bands originate from the left side of the image and flow towards the right, creating a sense of movement and depth. The colors range from a deep navy blue at the bottom to a lighter, sky blue at the top.

7.1 Overview and main findings

α -Dicarbonyl compounds are a special class of low molecular weight electrophiles known for their role as highly reactive precursors in the formation of advanced glycation end products (AGEs)¹⁸. AGEs and their precursors have been linked to a variety of diseases, including diabetes, cardiovascular disease, and neurodegenerative disorders⁶⁻⁸. Methylglyoxal (MGO), glyoxal (GO), and 3-deoxyglucosone (3-DG) are among the most studied and representative dicarbonyls^{10, 11}. Human exposure to these dicarbonyls originates from both dietary intake and endogenous formation within the body^{10, 11}.

The role of α -dicarbonyl compounds in neurotoxicity and neurodegenerative diseases primarily arises from their ability to modify biomolecules within the body⁷. An abnormal increase in the *in vivo* levels of dicarbonyls can lead to a dysfunctional state known as dicarbonyl stress, resulting in the increased formation of AGEs via modification of free amino acids, proteins, and DNA²⁶². These modifications could lead to structural and functional changes of these biomolecules, thereby contributing to neurotoxicity and potentially playing a role in neurodegeneration^{7, 12}. However, the mechanisms by which dicarbonyls drive neurotoxicity remain largely unknown.

The aim of this thesis was to advance our understanding of neurotoxicity and mitigation strategies for α -dicarbonyl precursors of AGEs using new approach methodologies.

In **Chapter 2**, the reactivity of three representative dicarbonyl precursors—MGO, GO, and 3-DG—was compared *in vitro*. This analysis included the comparison of the scavenging capacity of these dicarbonyls by glutathione (GSH) in cell-free incubation experiments. Additionally, the ability of these compounds to induce Nrf2-mediated gene expression and the role of intracellular GSH in counteracting this effect were investigated using a U2OS cell-based reporter gene assay. The results revealed that MGO was the most reactive in terms of GSH-mediated scavenging, reactive oxygen species (ROS) production, induction of Nrf2-mediated gene expression, and the effects of GSH depletion on Nrf2 activation potential. The results also show that endogenous GSH levels play a crucial role in the protection against dicarbonyl stress; depletion of cellular GSH led to increased cell viability loss upon exposure of the cells to the dicarbonyls.

Given the high reactivity of MGO observed in **Chapter 2**, MGO was selected as the model compound for further studies described in this thesis. Considering that dicarbonyl compounds and AGEs are prevalent in our diets, increased dietary exposure to these compounds could elevate the risk of developing related health conditions¹⁵. Moreover, AGE formation induced by dicarbonyls may reduce the nutritional value of foods²⁸. Understanding how to effectively

control the amount of dicarbonyls in food products could potentially prevent both subsequent exogenous and endogenous AGE formation and the resulting adverse effects. Natural polyphenols, especially flavonoids, have been regarded as efficient scavengers of MGO and hold great potential for MGO control in food systems^{16, 27}. In **Chapter 3**, the focus was to investigate the mitigation of dicarbonyls both endogenously and in food. The MGO scavenging capacity of a representative thiol compound (GSH) and a representative flavonoid (kaempferol) were characterized in more detail, with special emphasis on the possible reversible nature of adduct formation and their competition for MGO, in *in vitro* cell-free incubations. Additionally, the safety consequences of their MGO-scavenging effects were evaluated in human SH-SY5Y neuroblastoma cells. The results showed that GSH exhibited immediate and concentration-dependent MGO-scavenging effects, while kaempferol's scavenging effects were both concentration- and time-dependent, with stable adducts forming over time. In a competitive reaction, the GSH adduct gradually disappeared, and kaempferol became the preferred scavenger over time. Furthermore, kaempferol provided better protection than GSH against extracellular MGO of SH-SY5Y cells, which are known to be sensitive to dicarbonyl stress and AGEs. Overall, it is concluded that flavonoids like kaempferol provide better scavengers for food-borne MGO than thiol-based scavengers such as GSH, while, given the endogenous concentrations of both scavengers and the detoxification of the GSH-MGO adduct by the glyoxalase system, GSH will be dominant for intracellular MGO protection. The potential of using flavonoids to mitigate dicarbonyls in foods and *in vivo* will be further discussed in **Section 7.2.1**.

As dicarbonyls can easily modify cellular biomolecules to form AGEs, exploring the specific hotspot modification targets by dicarbonyls within neuronal cells could lead to the identification of potential biomarkers and contribute to understanding the mode of action underlying dicarbonyl-induced neurotoxicity. In **Chapter 4**, a proteomics approach was used to characterize protein modifications induced by MGO in SH-SY5Y cells incubated with and without exogenous MGO. It was found that the majority of proteins identified as modified were already modified under basal control conditions. A total of 77 proteins were categorized as highly susceptible to MGO modification. Among these, eight proteins, including vimentin and histone H2B type 2-F, showed concentration-dependent modifications by externally added MGO and were defined as biomarkers for exogenous MGO exposure. Remarkably, up to 10 modification sites were identified on vimentin. Myosin light polypeptide 6 emerged as a biomarker for MGO toxicity, with modifications exclusively observed under cytotoxic MGO levels. Additionally, proteins like serine/threonine-protein kinase SIK2 and calcyphosin, which exhibited comparable or even higher modification levels in control compared to exogenous MGO-treated cells, were defined as biomarkers for endogenous exposure. Moreover, KEGG pathway and protein-protein network (PPI) analyses revealed that motor proteins,

cytoskeleton components, and glycolysis proteins were overrepresented among those highly susceptible to MGO modification. These results identify biomarkers for both endogenous and exogenous MGO exposure and provide insights into the cellular effects of endogenously formed versus externally added MGO. However, the link between these biomarker proteins and pathological states, particularly neurodegeneration, remains to be established, as further discussed in **Section 7.2.3**.

Chapter 5 deployed an integrated proteomics and metabolomics approach to explore the molecular and biochemical changes induced by MGO exposure in SH-SY5Y cells and how these changes contribute to neurotoxicity. Our results revealed that MGO exposure, particularly at cytotoxic levels, altered significantly the proteome and the metabolome of SH-SY5Y cells. Analysis of proteomics data showed significant alterations in cellular functions such as protein synthesis, cellular structural integrity, mitochondrial function, and oxidative stress responses. Analysis of metabolomics data and integration of metabolomics and proteomics data highlighted significant changes in key metabolic pathways, including arginine biosynthesis, glutathione metabolism, cysteine and methionine metabolism, and the tricarboxylic acid cycle. It was found that MGO exposure led to increased endoplasmic reticulum stress, disruptions in cellular adhesion and extracellular matrix (ECM) integrity, mitochondrial dysfunction, and amino acid metabolism disruption, all contributing to cellular toxicity. Conversely, upon MGO exposure cells exhibited adaptive responses by upregulating protein synthesis, activating the Nrf2 pathway, and reprogramming metabolism to counteract dicarbonyl stress and maintain energy levels. These findings enhance our understanding of MGO-induced neurotoxicity and identify potential therapeutic targets for mitigating its harmful effects, which will be further discussed in **Section 7.2.3**.

To assess human neurotoxicity and genotoxicity risks from dietary and endogenous MGO, **Chapter 6** utilized physiologically based kinetic (PBK) modeling-facilitated reverse dosimetry to extrapolate *in vitro* toxicity data to *in vivo* dose-response predictions. A human PBK model was defined based on a newly developed mouse model, enabling the translation of *in vitro* toxicity data for MGO from human stem cell-derived neurons and WM-266-4 melanoma cells into quantitative human *in vivo* toxicity data and subsequent risk assessment using the margin of exposure (MOE) approach. The results show that the MOEs resulting from daily dietary intake did not raise concerns for endpoints such as neurotoxicity, including mitochondrial function, cytotoxicity, and apoptosis, while those for DNA adduct formation could not exclude a concern over genotoxicity. Endogenous MGO formation, especially under diabetic conditions, resulted in MOEs that raised concerns not only for genotoxicity but also for some of the neurotoxicity endpoints evaluated. The limitations of the current PBK model for MGO risk assessment, along with potential recommendations for model improvements, are discussed

in **Section 7.2.5**. Additionally, future research perspectives on the risk assessment of dietary and endogenously formed dicarbonyls and AGEs are discussed in **Section 7.2.6**.

In the following sections, the results of the current thesis, the limitations, and potential refinements for the current studies, and further recommendations and possibilities for future research are discussed.

7.2 General discussion, future perspectives, and conclusions

The results obtained and the experimental and data analysis approaches developed and applied in the present thesis offer several results that are relevant topics for future research on the toxicity and mitigation of dicarbonyls and the resulting AGEs, as well as on the use of NAMs for the risk assessment of dicarbonyls and AGEs from dietary intake and endogenous formation. These topics include:

- The potential of using flavonoids to mitigate dicarbonyls in foods and *in vivo*
- *In vitro* models to study the neurotoxicity and genotoxicity of MGO
- Impacts of MGO-induced modifications on neuronal cell biomolecules and future directions
- Limitations of omics technologies used in studies on the protein modifications and neurotoxicity of MGO in cells
- Improving PBK modeling in MGO risk assessment
- Future research perspectives for the risk assessment of dicarbonyls and AGEs

7.2.1 The potential of using flavonoids to mitigate dicarbonyls in foods and *in vivo*

In **Chapter 6**, the *in vivo* dose-response curves generated by PBK model-based reverse dosimetry of *in vitro* toxicity data predicted that the dose levels and systemic concentrations resulting from daily dietary intake of MGO are unlikely to reach levels capable of inducing neurotoxicity. However, the study of dicarbonyl scavenging in foods remains relevant and crucial. Dietary dicarbonyls not only induce the formation of AGEs in foods and potentially contribute to the formation of endogenous AGEs upon absorption but they are also implicated in the formation of potentially carcinogenic substances including acrylamide and 4(5)-methylimidazole in foods^{11, 307, 308}. Additionally, dicarbonyl-mediated modification of proteins can affect the digestion and absorption of these proteins, thereby lowering the nutritional value of foods²⁸.

The findings presented in **Chapter 3** indicate that for scavenging MGO in foods, the use of kaempferol and other flavonoids is preferred over GSH and other thiol-based scavengers. This

is attributed to the irreversible nature of MGO scavenging by kaempferol. Although in a competitive reaction, the initial scavenging of MGO by a thiol reagent such as GSH is highly favored over that by kaempferol, the GSH-mediated scavenging of MGO is reversible¹⁷¹. The thiol-based compounds-mediated reversible adduct formation with MGO in foods would provide a way to generate the release of MGO at different locations within the body upon digestion and absorption, thereby providing a way for transient stabilization and transport instead of detoxification.

The application of flavonoids in food products is a promising strategy for controlling the amount of dicarbonyls. However, several concerns need to be addressed prior to the application. Apart from their solubility, the impact of flavonoids on the background flavor and color of the foods may hamper their use³⁰⁹, and the stability and safety of the adducts formed between flavonoids and MGO should be further evaluated. Although in **Chapter 3** it was found that the monoMGO adduct formation of kaempferol was not reversible under physiological conditions, the stability of these adducts and the possibility of release of MGO under the conditions typical of high-temperature food processing or varying pH levels during digestion remain unclear.

Additionally, the results from **Chapter 3** indicate that the scavenging of MGO by kaempferol provided protection against extracellular MGO of SH-SY5Y cells. Similarly, a previous study evaluated the toxicity of oxidized MGO rutin adducts in comparison with rutin and MGO and suggested that the formation of these oxidized adducts significantly decreased the MGO-induced cytotoxicity in several cell types¹⁷⁴. However, in contrast, another study reported that both mono-MGO and di-MGO adducts of quercetin were found to have higher cytotoxic effects than MGO itself¹⁷⁶. The variability of the results highlights the need for safety evaluations of flavonoid-MGO adducts. Further investigation is required to understand to what extent these differences are due to the biological effects of different types of adducts, the specific flavonoids used, or the experimental conditions employed.

On the other hand, due to the involvement of AGE formation in multiple diseases such as diabetes and neurodegenerative disorders, inhibiting the endogenous formation of AGEs with AGE inhibitors has been considered a potential strategy for mitigating their adverse effects in these diseases³¹⁰. Synthetic AGE inhibitors like aminoguanidine have been developed; however, their clinical use has been limited by undesirable side effects³¹¹. Naturally occurring inhibitors, especially flavonoids, have gained increasing attention due to their efficient dicarbonyl scavenging capabilities that have been demonstrated *in vitro* and their potentially relatively low toxicity^{16, 59, 60, 310}.

Physiological levels of flavonoids are generally in the low μM range, primarily due to their poor bioavailability^{180, 181, 312}. After consumption of flavonoid-rich foods, the maximal plasma concentrations of total flavonoids in humans usually reach between 0.06 and 7.6 μM within 1 to 3 hours³¹². Additionally, upon absorption, flavonoids predominantly appear in plasma as conjugated forms, such as glucuronidated and sulfated derivatives, rather than in their free forms³¹³. It remains to be shown whether these conjugates are also effective MGO scavengers. In contrast, the intracellular levels of GSH in mammalian cells are typically much higher, within the range of 0.5 to 10 mM¹⁷⁹. In **Chapter 3**, it was concluded that for endogenous protection against MGO, GSH will be more relevant, not only because of its higher intracellular concentrations but also due to the role of the glyoxalase system in detoxifying GSH-MGO adducts^{29, 179}. However, it is also important to recognize that several studies have demonstrated the potential of flavonoids to protect against MGO/AGE-induced adverse effects in *in vitro* cell and animal models^{79, 314, 315}. For instance, oral administration of hesperetin at a dose of 100 mg/kg body weight in rats led to detectable levels of hesperetin-MGO adducts and their metabolites in plasma within 24 hours, with diMGO adducts being the predominant form, indicating hesperetin's capability to scavenge endogenous MGO³¹⁴. Additionally, diabetic rats treated with oral quercetin for 14 weeks at 90 mg/kg body weight exhibited increased levels of GSH and Glo1 activity and expression in the brain, alongside a decrease in AGE levels and the receptor for AGEs (RAGE)³¹⁵. These effects, including the elevation in GSH levels and Glo1 activity in the brain, are potentially related to quercetin's induction of Nrf2-mediated gene expression^{137, 316}, as also evidenced by *in vitro* studies where pretreatment with flavonoids such as naringenin and apigenin has been shown to protect against MGO- and/or AGE-induced cytotoxicity by promoting GSH synthesis through the Nrf2 signaling pathway^{71, 178}.

Although the direct impact of dicarbonyl scavenging on reducing AGE-induced adverse effects in diseases remains to be elucidated, flavonoids have demonstrated broad beneficial effects, including the induction of Nrf2-mediated gene expression and the regulation of gut microbiota, which could also potentially help counteract the adverse effects of AGEs *in vivo*^{310, 317, 318}. Given these benefits, flavonoids hold great promise for incorporation into daily health regimes to mitigate the risk of chronic diseases. However, their development into pharmaceuticals specifically for endogenous AGE inhibition is hampered by challenges like inadequate permeability and limited bioavailability, which might require high doses for effectiveness³¹⁹. Extensive research is therefore necessary to improve their pharmacokinetic properties and to demonstrate their clinical efficacy and safety in human trials for such use.

7.2.2 *In vitro* models to study the neurotoxicity and genotoxicity of dicarbonyls

Many observational clinical studies have indicated that dicarbonyl stress may play a role in neurodegeneration (as described in **Section 1.6.2**)^{86, 87, 90, 239}. It becomes imperative to further study the underlying mechanisms, and *in vitro* models are considered straightforward and effective for elucidating these mechanisms³²⁰. Neuronal cell death in specific regions of the brain represents a fundamental pathological feature across different neurodegenerative diseases³²¹. Neuronal cells are considered particularly susceptible to dicarbonyl stress, potentially related to their high-energy glucose metabolism; this susceptibility is further compounded by their relatively lower levels of GSH and lower activities of glyoxalase enzymes compared to astrocytes²⁷⁸⁻²⁸¹. Pathological conditions such as hyperglycemia can increase glycolytic flux in neurons, making them prone to the accumulation of dicarbonyls (especially MGO) and resultant AGEs; it has been reported that even a moderate increase in glycolysis within neurons is sufficient to significantly elevate the endogenous levels of MGO and subsequent AGE formation²⁸¹.

7

Various neuronal cell models have been utilized to study the neurotoxicity of dicarbonyls as well as the neuronal protection against their toxicity, particularly focusing on MGO, which has been identified as the most reactive, as confirmed in **Chapter 2**. These neuronal cell models include animal cells (such as rat hippocampal neurons, rat PC12 cells, and mouse neuro2A cells)³²²⁻³²⁴ and human cells (such as human neuroblastoma cells including SH-SY5Y, SK-N-SH, SK-N-MC, and M17 cells, as well as primary neuronal-like cells (hNLCs) transdifferentiated from human mesenchymal stem cells)^{95, 96, 276, 277, 299}. Human cell models are generally preferred over animal cell models due to species differences that can affect the extrapolation of animal data to human conditions.

In further studies, the SH-SY5Y neuronal cell model was chosen to study the neurotoxicity induced by MGO (**Chapters 4 and 5**). This model is the one most widely used for studying the pathological effects of neurotoxic compounds¹⁰³, and several studies have also employed it to examine the effects of MGO^{96, 246, 325}. In **Chapter 6**, to assess the human neurotoxicity risks through PBK model-based reverse dosimetry and quantitative *in vitro* to *in vivo* extrapolation (QIVIVE), the toxicity data of MGO from different neuronal cell models in the literature were compared^{95, 96, 276, 277, 299}. It was found that hNLCs exhibited the greatest sensitivity to MGO. The toxicity of MGO, quantified by cytotoxicity and apoptosis in hNLCs, started to occur at concentrations of 10 μM onwards⁹⁵. Comparison to the cytotoxicity data from human neuroblastoma cells, such as the SH-SY5Y cells in our study (**Chapter 4**), reveals a substantial difference in sensitivity since the SH-SY5Y cells showed significant cell viability loss at concentrations starting from 1000 μM MGO, indicating a substantially lower sensitivity than

that observed in hNLCs. These hNLCs are considered to more accurately mimic the physiological and biochemical properties of neuronal cells than other tested models⁹⁵, making them particularly suitable for the toxicity data selected for QIVIVE. The lower sensitivity of SH-SY5Y cells is likely due to their tumor origin; tumor cells typically possess higher levels of GSH and enhanced glyoxalase system activity³²⁶, enabling them to detoxify dicarbonyls more efficiently than normal tissues or primary cells. As a result, higher concentrations of MGO are required to induce toxic effects in these cells. Nevertheless, for mechanistic studies, SH-SY5Y cells remain a valuable model due to their robustness, cost-effectiveness, and ease of handling. In contrast, stem cell-derived models like hNLCs are time-consuming, non-high-throughput, expensive, and less accessible for some laboratories, presenting substantial barriers to widespread use. However, for generating concentration-response data for QIVIVE, hNLCs appear to be more physiologically relevant. Consequently, in **Chapter 6**, the dose-response curves generated through PBK model-based reverse dosimetry of *in vitro* toxicity data from hNLCs provided a more precise evaluation of the potential human neurotoxicity risks associated with MGO exposure.

Apart from neurons, it is crucial to recognize that neurodegeneration involves various other cell types, including microglia, astrocytes, and microvascular endothelial cells of the blood-brain barrier^{327, 328}. Dicarbonyl stress can impair the functioning of these cells, which in turn may adversely impact neuronal functions^{278, 327}. Microglial cells, as the brain's resident macrophages, are essential for mediating neuroinflammatory responses and can be used to assess dicarbonyl and AGE-induced effects on neuroinflammation³²⁰. Animal studies have shown that MGO can induce a shift in microglia towards a pro-inflammatory phenotype, leading to the secretion of pro-inflammatory and neurotoxic molecules that may potentially compromise neuronal survival^{329, 330}. Activated microglial cells, such as those of the HMO6 cell line, have been observed to synthesize and secrete glycated proteins like glycated albumin, which could promote the death of human primary neurons^{331, 332}.

Astrocytes are essential for maintaining neurovascular communication and supporting neuronal functions³³². Due to their higher GSH and glyoxalase-mediated detoxification capacity, astrocytes exhibit less sensitivity to MGO toxicity²⁸¹. In a co-culture model involving human astrocytes (D384 cell line) and neuronal cells (SH-SY5Y cell line), astrocytes were found to significantly protect neurons from MGO toxicity³³³. Moreover, microvascular endothelial cells, serving as the primary barrier, are instrumental in studies assessing the BBB integrity³³⁴. Exposure of human brain microvascular endothelial cells (BMECs) to exogenous MGO *in vitro* has been shown to cause cell viability loss, cell membrane damage, and apoptosis³³⁵⁻³³⁷. Impaired barrier integrity and increased endothelial barrier permeability were observed at cytotoxic MGO levels in in-vitro BBB functional assays with BMECs^{337, 338}. However, the kinetics

of MGO and other dicarbonyls crossing the BBB are not yet understood, which is crucial for determining how much of the dicarbonyls from peripheral sources can enter the central nervous system and assessing their subsequent impacts. This can be addressed by using *in vitro* BBB models that closely simulate physiological conditions.

Collectively, current studies underscore the complexity of dicarbonyl stress in neurodegeneration, involving multiple cell types and intricate cellular interactions^{327, 328, 339}. Although no model perfectly mimics human brain physiology and pathophysiology, selecting suitable *in vitro* models based on the research objective can streamline investigations. Simpler models such as monocultures of tumor-origin neuronal cells are instrumental in elucidating the fundamental effects of dicarbonyls and AGEs on neuronal dysfunction. Meanwhile, co-culture models that combine neuronal cells with microglia or astrocytes may provide valuable insights into the influence of cellular crosstalk on neurotoxicity. Furthermore, stem cell-derived neurons and 3D human brain organoids, as well as organ-on-chip systems, are expected to offer more physiologically relevant data, thereby enhancing the accuracy of data for QIVIVE.

It is important to note that the concentrations of exogenous MGO used in most studies, including in the present thesis (**Chapters 4 and 5**), when using *in vitro* models to study MGO toxicity, were in the high μM range, substantially above its physiological levels. In **Chapter 6**, the PBK model predicted that internal C_{max} levels resulting from estimated daily dietary MGO intake were more than threefold lower than endogenous plasma MGO levels. This observation suggests that *in vitro* studies employing MGO concentrations in the high μM range may not accurately reflect realistic dietary exposure to MGO. Additionally, findings from **Chapter 4** showed that the majority of proteins identified as modified were already modified in control samples, at levels comparable to or even higher than those in exogenous MGO-treated cells, indicating that the contribution of endogenously formed MGO to protein modification may be more substantial than that resulting from exogenous MGO. Therefore, considering the critical role of endogenous MGO levels in potential adverse health effects, as revealed in **Chapters 4 and 6**, future studies could focus on *in vitro* models that mimic increased intracellular MGO formation, for example, by incubating cells with high glucose to induce dicarbonyl stress. Additionally, while most studies focus on acute toxicity using 24- or 48-hour exposure time, *in vivo* neurodegeneration conditions involve chronic, less intense dicarbonyl stress than those simulated *in vitro*. Future studies might consider long-term and/or repeated exposures in *in vitro* settings to better mimic these conditions.

For the evaluation of genotoxicity risks based on PBK-modelling-based reverse dosimetry in **Chapter 6**, data from the literature were used¹²² quantifying MGO-induced DNA adducts in

WM-266-4 human melanoma cells after a 3-hour exposure to exogenous MGO at concentrations ranging from 0 to 1250 μ M for QIVIVE. It should be noted that, while this data set is the only one currently available for such studies, melanoma cells, as a tumor cell line, appear to be not ideally suited for QIVIVE when assessing genotoxicity. This is due to different basal levels of MGO formation and detoxification capabilities of tumor cells³²⁶, which may affect the *in vitro* effective concentrations. Furthermore, a 3-hour exposure period may not adequately capture the full spectrum of genotoxic effects, which often require longer durations to manifest³⁴⁰. Consequently, future studies should consider using more physiologically relevant *in vitro* models, such as human peripheral blood lymphocytes (HPBLs) from healthy donors, for more accurate assessments of dicarbonyls' genotoxic potential. Nonetheless, our newly defined human PBK model for MGO remains a valuable tool for QIVIVE and subsequent risk assessment for MGO, providing essential insights despite the limitations of the current *in vitro* toxicity data sets available for QIVIVE.

7.2.3 Impacts of MGO-induced modifications on neuronal cell biomolecules and future directions

The toxicity induced by MGO in neuronal cells might result from the modifications it causes to various cellular biomolecules, including free amino acids, proteins, and nucleic acids⁴³. Identifying the principal targets of these modifications is crucial for understanding the mechanisms underlying dicarbonyl-induced toxicity. In **Chapter 4**, using mass spectrometry-based proteomics which is an effective and high-throughput method for identifying protein modifications by electrophiles³⁴¹, several proteins in SH-SY5Y cells that are highly susceptible to modifications by both endogenous and exogenous MGO were successfully identified. However, directly linking these identified protein modifications to biological or toxicological effects, and ultimately to clinically relevant health effects associated with dicarbonyl exposure and neurodegeneration, remains a significant challenge. Establishing this connection is critical for advancing the understanding of the pathophysiological impacts of dicarbonyl-induced modifications and for developing targeted therapeutic interventions. This section will discuss the valuable insights from the studies on protein modifications (**Chapter 4**) and cellular effects characterized through proteomics and metabolomics following MGO exposure (**Chapter 5**), along with possible next steps to establish the relationships between these modifications and functional effects.

Only a few studies have successfully established a direct link between specific dicarbonyl-induced modifications and their functional effects. For instance, the association between diabetic hyperalgesia and MGO is attributed to the modification of the voltage-gated sodium channel Nav1.8³⁴². Similarly, the modification of Keap1 by MGO activates the Nrf2

transcriptional program, providing another well-characterized example of a physiological effect resulting from a protein modification⁵³. While these instances offer valuable insights derived from the study of individual target proteins on a case-by-case basis, the functional implications for the large number of target proteins identified in various cell models in recent years remain largely unclear. However, the fact that many modified proteins are detected, suggests that the traditional approach of analyzing protein modifications one at a time may not be efficient. Proteomics directed at identifying protein modifications combined with bioinformatics analysis, such as pathway enrichment and PPI network analysis, can offer initial insights into the functional consequences of the modified proteins. For example, such an analysis conducted in **Chapter 4**, revealed that motor proteins, cytoskeletal components, and glycolysis-related proteins were significantly overrepresented among those most affected by MGO.

To extend these findings, previous studies suggested that a systems-based approach, involving an integrated analysis of protein modifications with cellular responses characterized through transcriptomics, proteomics, and/or metabolomics, could help generate hypotheses about how specific cellular pathways are influenced by certain electrophile-induced modifications, thereby providing the opportunity to understand the mechanisms of electrophile action and their broader biological impacts more comprehensively³⁴³⁻³⁴⁵. Such a strategy has been applied to 4-hydroxynonenal to establish potential plausible linkages between 4-hydroxynonenal-induced modification of proteins and gene expression changes by bioinformatic analysis of signal transduction networks³⁴⁴. Based on these, the author hypothesized that the modification of heat shock proteins (Hsp70 and Hsp90) by 4-hydroxynonenal is partly responsible for heat shock factor 1 (HSF1)-mediated heat shock response, which was subsequently confirmed to play a protective role against electrophile-induced cell death³⁴⁴.

In **Chapter 5**, proteomics and metabolomics analyses were conducted to investigate cellular responses under the same MGO exposure conditions used in the protein modification study. These analyses revealed that MGO exposure leads to increased endoplasmic reticulum stress, disruptions in cellular adhesion and extracellular matrix (ECM) integrity, mitochondrial dysfunction, and disruptions in amino acid metabolism, all contributing to cellular toxicity. However, cells also exhibited adaptive responses by upregulating protein synthesis, in part by activating the Nrf2-mediated pathway, and reprogramming metabolism to protect themselves from subsequent stress. These observations align with growing evidence that cells are not merely passive targets of electrophilic damage but can actively adapt and protect themselves^{344, 346, 347}. This drives researchers to further explore the role of macromolecular modifications, particularly protein modifications, in sensing and mediating biological

responses to reactive electrophiles, such as the modification of Keap1 by electrophiles that leads to the activation of the Nrf2-mediated protective gene expression^{53, 344, 345}. Additionally, the results highlighted that MGO exposure can induce a variety of changes in cellular signaling, which are possibly related to protein modifications induced by MGO, as identified in **Chapter 4** where protein biomarkers for both endogenous and exogenous MGO exposure were defined. The levels of these modifications may reflect different cellular conditions and potentially play a role in cellular adaptation or dysfunction.

Neuronal cytoskeleton abnormalities have been recognized as one of the hallmarks of neurodegenerative diseases⁴. In **Chapter 4**, it was found that cytoskeletal proteins were significantly overrepresented among those most affected by MGO. These proteins are also targeted by other reactive electrophiles such as acrolein and 4-hydroxynonenal²²¹⁻²²³. By comparing these findings with the protein expression changes observed in **Chapter 5**, it was hypothesized that the modification of cytoskeletal proteins by MGO plays a role in the observed alterations in cellular adhesion mechanisms, potentially contributing to the neurotoxic effects of MGO. This is particularly relevant as cytoskeletal proteins play a key role in maintaining the structural integrity and operational functionality of focal adhesion complexes²⁶⁸.

This hypothesis is based on the protein expression data in **Chapter 5**, which showed significant downregulation of integrins such as ITGB1, ITGAV, ITGA3, and ITGA6, along with crucial extracellular matrix components like COL1A1 and LAMB1. These changes suggest substantial alterations in the mechanisms that maintain cellular architecture and mediate signal transduction between the ECM and the cytoskeleton²⁶⁴, potentially underlying the toxicity induced by MGO. Integrins, serving as critical transmembrane receptors, are pivotal in mediating both physical and biochemical linkages between the ECM and the cytoskeleton²⁶⁵. Their downregulation can impair cell adhesion, impacting neuronal connectivity and synaptic stability, essential for neural development and function²⁶⁶. Similarly, alterations in COL1A1 and LAMB1 can disrupt the structural integrity and signaling capabilities of cells, potentially contributing to the pathophysiology of neurodegeneration²⁶⁷. It is of interest for future studies to further explore and validate this hypothesis, which could enhance the understanding of the role of cytoskeletal protein modifications by MGO in neurotoxicity and neurodegenerative processes.

Besides the hypothesis related to the role of cytoskeletal protein modifications in neurotoxicity, the majority of modified proteins identified in **Chapter 4** have yet to be thoroughly analyzed. Additionally, in **Chapter 5**, 3160 proteins were quantified, of which 453 have been defined as differentially expressed proteins. The interpretation of these protein

expression changes was primarily based on the top 5 functional modules identified in the PPI network (**Figure 5.3 in Chapter 5**). Therefore, further analysis and mining of both protein modification and protein expression data sets from this thesis might be needed, especially using the above-mentioned systems-based approach to establish connections between these data sets and provide insights into the role of MGO-induced modifications on proteins such as motor proteins, which were also significantly overrepresented among those highly susceptible to MGO modification (**Chapter 4**). In future studies this approach can be achieved by using various bioinformatic tools such as WebGestalt (WEB-based Gene SeT AnaLysis Toolkit)³⁴⁸ and GenMAPP (Gene Map Annotator and Pathway Profiler)³⁴⁹, as previously applied for 4-hydroxynonenal³⁴⁴, to bridge the modified proteins with the differentially expressed proteins by shared cellular pathways, providing possible links between these modifications and cellular responses.

7.2.4 Limitations of omics technologies used in studies on the protein modifications and neurotoxicity of MGO in cells

Cell-based omics technologies, as employed in **Chapters 4 and 5** to characterize protein modifications and neurotoxicity induced by MGO, have provided valuable insights into, and great opportunities for further investigation of, the role of MGO-induced protein modifications in cellular adaptation or dysfunction (as discussed in **Section 7.2.3**). However, The studies presented in **Chapters 4 and 5** also have several limitations that should be taken into account in future research.

Firstly, the protein modifications identified by the mass spectrometry-based proteomics are not yet validated, except for CAPS and VIM, which are commercially available and whose modifications have been evaluated in an *in vitro* cell-free system (**Chapter 4**). Although proteins susceptible to MGO, particularly the protein biomarkers for MGO exposure, were defined using a relatively stringent criterion that considered the modification frequency of these proteins across all samples and applied statistical analyses to determine concentration-dependent effects, it should be noted that the identification process used a 1% false discovery rate. This means there is still a possibility of incorrect identifications, and thus validation of these modified proteins through additional experimental methods is necessary. The *in vitro* cell-free system used for the evaluation of the modifications as conducted for CAPS and VIM could provide a way for this purpose. However, given the large number of proteins identified as modified by MGO, this method might not be efficient, as it can only evaluate one protein at a time. Alternatively, such validation can potentially be achieved by using a more sensitive and reliable chemo-proteomic approach using an alkyne-labeled MGO probe (alkMGO), which resembles natural MGO^{350, 351}. This method employs click chemistry and affinity-based

enrichment to isolate proteins modified by dicarbonyls prior to MS analysis³⁵¹. The enrichment process is independent of the type of protein modification, specifically enriching only the modified proteins and enhancing the accuracy of detection^{345, 351}. Moreover, click chemistry provides efficient and selective labeling, significantly reducing background noise and thus improving the reliability of MS analysis, making it a powerful tool for directly identifying and qualitatively validating protein modifications identified in proteomic studies³⁴¹. Additionally, this approach also holds the potential for the identification of cross-linked protein modifications not covered in the present study³⁵².

Secondly, the differentially expressed proteins identified and used for interpreting cellular responses to MGO exposure have not yet been validated, although several findings such as the increased endoplasmic reticulum stress and involvement of the activation of the Nrf2-mediated pathway upon MGO exposure are supported by existing literature^{53, 353}. Different or additional readouts, such as PCR or Western blot, can be used to quantify the differential expression of proteins of interest for further validation.

Additionally, the pathway enrichment and PPI network analyses were conducted using the differentially expressed proteins identified in cells treated with the highest cytotoxic concentration of MGO. The subsequent interpretation of these protein expression changes was primarily based on the top 5 functional modules identified in the PPI network (as also discussed in **Section 7.2.3**). It would also be interesting to analyze protein expression changes in cells treated with non-toxic, lower concentrations of MGO, where adaptive responses may dominate over the cytotoxic effects resulting from biomolecular modifications by MGO. Such analyses could help define the molecular and cellular injury phenotypes that characterize different exposures. Furthermore, in **Chapter 4**, the Jonckheere-Terpstra test was employed to determine if there was a concentration-dependent increase in the intensity of modified peptides in proteins with increasing concentrations of MGO. This statistical approach can be similarly applied to analyze protein expression data, enabling the identification of proteins whose expression levels either increase or decrease with increasing MGO concentrations. This method could pinpoint potentially more sensitive and reliable protein markers, which could be crucial for understanding cellular responses to MGO exposure and may serve as therapeutic targets.

Moreover, in the metabolomic study, only one MGO-modified amino acid adduct was quantified, methylglyoxal-derived hydroimidazolone 1 (MG-H1), which is reported to be the most abundant free AGE²⁵⁰. The observed disruption in the arginine biosynthesis pathway, as revealed by the metabolomic study, is likely related to the consumption of arginine in its reaction with MGO to form MG-H1. This is supported by the substantial increase in MG-H1

levels upon MGO exposure, as observed in **Chapter 5**. Future studies could also quantify other free low molecular mass AGEs in cells in the presence or absence of exogenous MGO to better define the potential impacts of amino acid modifications on amino acid metabolism. Similarly, this approach could be extended to the study of DNA/RNA adducts to investigate the role of dicarbonyl-induced adduct formation in neurotoxicity and neurodegenerative diseases, particularly since DNA and RNA damage are also recognized as pathological hallmarks of neurodegeneration⁴.

7.2.5 Improving PBK modeling in MGO risk assessment

To evaluate human neurotoxicity and genotoxicity risks from dietary and endogenous MGO, human PBK modeling-facilitated reverse dosimetry was utilized as a NAM to extrapolate *in vitro* toxicity data to *in vivo* dose-response predictions as detailed in **Chapter 6**. This human PBK model was defined based on a newly developed and validated mouse model. This section will address the current limitations of both the human and mouse PBK models and propose potential improvements to increase their accuracy and applicability in assessing dicarbonyl risks.

Available *in vivo* kinetic data for MGO are limited, with only one study by Ghosh et al. reporting the kinetics of MGO in mice⁸⁰. Several parameters of the mouse PBK model, including the delay in absorption, the blood-to-plasma ratio, and most importantly, the clearance, were quantified based on the results from this *in vivo* study. The performance of the developed mouse PBK model was evaluated by comparing the model-predicted time-dependent blood concentrations of MGO with the *in vivo* time-dependent blood concentrations reported by Ghosh et al. for mice given a single oral dose of 50, 100, or 200 mg/kg bw⁸⁰. Although the model-predicted blood concentrations matched well with the *in vivo* data, this may partly originate from the fact that several parameters especially the rate constants for clearance used in the mouse PBK model were defined in the study by Ghosh et al. by fitting to the experimental data. To increase the reliability of this model, future studies could independently determine the respective PBK model parameters such as the blood-to-plasma ratio and the rate constant for clearance, which can be determined through *in vitro* assays. Any deviations predicted by this newly parameterized PBK model from the data from the *in vivo* study can then be critically analyzed to further refine the model's predictive accuracy. Especially parameters such as clearance, shown by the sensitivity analysis to be the most influential on C_{\max} predictions, should be quantified with a high level of accuracy.

Moreover, Ghosh et al. conducted an *in vivo* kinetics study using three oral doses of MGO (50, 100, and 200 mg/kg body weight), reporting different apparent total body clearance (CL_{app}) values at the different dose levels: 7.69 L/h/kg, 8.28 L/h/kg, and 15.54 L/h/kg, respectively⁸⁰.

Notably, no significant differences in blood concentrations were observed between the two higher doses⁸⁰. In the current thesis, specific CL_{app} values corresponding to each dose were employed in the mouse PBK model for model evaluation. However, it is important to recognize that organ clearance should ideally be modeled as a function of the local concentration, multiplied by an intrinsic constant that does not vary with the dose. Ghosh et al. calculated these CL_{app} values from the half-life of MGO in 12 mice, and the fact that the value varied with the dose actually suggests that factors other than clearance could influence total circulating concentrations and consequently the half-life. Given the similar maximum blood concentrations (C_{max}) observed after administering 100 and 200 mg/kg body weight MGO, it is likely that there is an influence of saturated uptake or limited gastrointestinal solubility, rather than enhanced clearance with increasing dose. Therefore, using the CL_{app} value from the lowest dose for PBK modeling appears more rational to avoid the complexities introduced by saturation effects at higher doses. For these higher doses, future studies could consider incorporating a fraction absorbed correction to better fit the model to the observed *in vivo* data, rather than using the apparently increasing CL_{app} values at higher doses.

For the sensitivity analysis, parameters such as the surface area of the intestinal compartment (SA_{in}), the volume for each compartment of the intestines (V_{in}), and the CL_{app} value were identified as the most influential parameters on C_{max} predictions. Specifically, for the reasons discussed above, the CL_{app} value may be defined in a better way in future studies. Future studies could also consider running a Monte Carlo simulation taking into account the variability within the population for these influential parameters. Doing so would not only help estimate error margins, thereby enhancing the reliability and robustness of the model's predictions, but it would also aid in understanding how interindividual variability in these parameters impacts the model's outcomes³⁵⁴.

Lastly, in the human PBK model, the same CL_{app} values were used for MGO as those defined for the mouse model, based on the assumption that detoxification of dicarbonyls by the glyoxalase system represents universal basal mammalian physiology³⁵⁵. Comparable blood Glo1 activity has been reported in humans and rats, further supporting this assumption^{356, 357}. However, it would still be beneficial for future studies to compare the detoxification capacities of dicarbonyls across different species using *in vitro* assays, to further validate and support the validity of this assumption made when defining the human PBK model.

7.2.6 Future research perspectives for the risk assessment of dicarbonyls and AGEs

Risk assessments related to dicarbonyl compounds and AGEs have been limited to date. The only report so far is the risk characterization of dietary GO intake for the general population conducted by the World Health Organization (WHO) in 2004³⁰³. This assessment estimated a

daily worst-case GO exposure of 10 mg, corresponding to 0.16 mg GO/kg bw, based on GO concentrations in food and assuming a body weight of 64 kg³⁰³. This level is slightly below the tolerable intake of approximately 0.2 mg/kg body weight per day for lifetime oral exposure, as derived from repeated dose oral toxicity studies on GO in animals, which revealed a no-observed-adverse-effect-level (NOAEL) value of 100 mg/kg body weight per day and used a composite uncertainty factor of 500 to account for interspecies differences (10), interindividual differences (10), and less-than-lifetime exposure (5)³⁰³. Therefore, it is suggested that dietary exposure to GO would not be considered a health risk³⁰³. However, the risks from endogenously formed GO were not assessed. Given that the reported endogenous MGO formation in healthy adults (approximately 216 mg, equal to 3.09 mg/kg bw for a 70 kg person per day) exceeds the estimated daily dietary intake of MGO (5-20 mg, equal to 0.07-0.29 mg/kg bw for a 70 kg person) by more than tenfold^{30, 54}, the endogenously formed MGO and other dicarbonyls may be more important in health risk assessments. Evidence has already linked the increase in endogenously formed MGO under diabetes to the progression of diabetic neuropathies, a major complication of diabetes³⁰¹.

In **Chapter 6**, The neurotoxicity and genotoxicity risks from both dietary and endogenously formed MGO were assessed based on the PBK modeling-facilitated reverse dosimetry. The results show that the MOEs resulting from daily dietary intake did not raise a concern for neurotoxicity, while those for DNA adduct formation could not exclude a concern over genotoxicity. Endogenous MGO formation, especially under diabetic conditions, resulted in MOEs that raised a concern not only for genotoxicity but also for some of the neurotoxicity endpoints evaluated.

These findings underscore the greater risks associated with endogenous than exogenous exposure to MGO, emphasizing the importance of including endogenous MGO levels in risk assessments. A previous study reported that human volunteers who consumed honey containing 37 mg of MGO—a quantity exceeding the estimated daily dietary intake and equal to 0.53 mg/kg bw for a 70 kg person—did not show increased urinary excretion of MGO and its metabolite D-lactate⁸². This suggests that the urinary MGO mainly originates from endogenous formation, that absorption of dietary MGO might be limited, and that its contribution to the total systemic exposome is negligible. However, it is crucial to recognize that the daily exposure typically includes a combination of exogenous dicarbonyls such as MGO, GO, and 3-DG. The co-exposure to these dicarbonyls from dietary intake could potentially amplify the health risks. The estimated daily intake for 3-DG ranges from 20 to 160 mg per day⁵⁴, which is notably higher than the estimated worst-case daily intake for GO at around 10 mg³⁰³, and daily dietary intake of MGO at 5-20 mg³⁰. Furthermore, another study reported that upon a single oral consumption of honey containing a dietary amount of 3-DG

by human volunteers, elevated amounts of 3-DG and its metabolite (3-deoxyfructose) were excreted in the urine, with 10-15% of the ingested 3-DG dose being recovered⁸¹. This indicates that the contribution of dietary 3-DG to the total *in vivo* 3-DG exposome may be more substantial than that observed for MGO. These findings underscore the need for more detailed information on the kinetics of 3-DG to better assess its contributions from dietary and endogenous sources to the total exposome, which is essential for determining whether dietary and endogenously formed 3-DG pose a health risk. Furthermore, given the limited toxicity data on 3-DG compared to MGO, characterizing its impact on biomolecules through proteomics and metabolomics, similar to the analyses conducted for MGO in **Chapters 4 and 5**, would be useful for assessing its risk and for comparison with MGO. Additionally, future studies could consider establishing relative potency values for dicarbonyls including 3-DG and GO relative to MGO to more accurately determine the health risks from combined exposure to these compounds.

Moreover, although melanoma cells may not be the ideal model for genotoxicity evaluation as discussed in **Section 7.2.2**, the concerns arising from both dietary and endogenous MGO exposure with respect to genotoxicity underscore the need to further characterize and define physiologically relevant DNA adduct biomarkers and subsequently determine how much exogenous exposure is required to significantly influence these endogenous biomarker levels.

Compared to dicarbonyls, assessing the potential risks from dietary and endogenously formed AGEs presents greater challenges, despite the accumulation of AGEs *in vivo* being linked to various diseases including cardiovascular and neurodegenerative disorders^{8, 358}. This complexity partly stems from the structural diversity of AGEs, which range from free form and peptide-bound to protein-bound varieties, complicating their characterization and measurement in animal and human studies¹⁵. Additionally, there is no consensus regarding the impact of dietary AGEs on health. While some studies suggest that a high-AGE diet may promote inflammation and oxidative stress^{55, 56}, others do not observe a significant health impact^{359, 360}.

The information on the toxicokinetics and toxicodynamics of AGEs is particularly limited, except for some well-characterized free-form AGEs such as carboxymethyllysine (CML). The kinetic behavior of these compounds can vary with their molecular weight, and it has been suggested that endogenous high molecular mass AGEs (protein-bound) are primarily a result of endogenous formation, whereas low molecular mass AGEs (free-form) may derive from both exogenous and endogenous sources¹⁵. Studies have shown that low molecular mass AGEs such as CML can be absorbed *in vitro* and in rats³⁶¹⁻³⁶³. For example, an increase in protein-bound CML levels in various tissues, including the kidney, heart, lung, pancreas, and

muscle, was observed upon oral administration of free CML to rats for 12 weeks³⁶². In contrast, high molecular mass AGEs may be less efficiently absorbed, requiring their degradation into low molecular mass AGEs before they can be absorbed¹⁵. A previous study has suggested that peptide-bound CML can be released during simulated gastrointestinal digestion of high molecular mass glycated proteins³⁶⁴. This is further supported by an animal experiment where isotope-labeled high molecular mass CML was orally administered to mice, resulting in the retention of isotope-labeled CML in most tissues, especially in the kidneys, intestines, and lungs, although the authors did not distinguish between protein-bound and free CML in the tissues³⁶⁵. The toxicity of AGEs may also vary depending on whether they are in a free or protein-bound form. There is evidence suggesting that protein-bound CML may act as a ligand to RAGE and elicit an inflammatory response, whereas free CML does not appear to bind to RAGE³⁶⁶. The acute oral LD50 of free CML was estimated to be greater than 5000 mg/kg in mice, suggesting low acute toxicity; however, repeated administration was found to induce oxidative damage to the liver and kidneys³⁶⁷.

To further understand whether dietary and endogenously formed AGEs pose risks to human health, the relative contributions of exogenous and endogenously formed AGEs to the total exposome needs to be assessed. Considering that AGEs comprise a wide range of structurally diverse compounds and their kinetics may differ based on their forms, using *in vitro* models to study their kinetics might provide a more cost-effective and efficient method, allowing for the analysis of individual AGEs one at a time and facilitating comparisons of differences between them. For example, to study the absorption of AGEs, *in vitro* cell models such as Caco-2 cell monolayers are particularly useful for determining and comparing the intestinal absorption rates of different forms of AGEs, and the absorption of several free AGEs has been determined using such a model^{361, 368}. Additionally, further defining the relationship between the structures and kinetics of AGEs may help better predict the behaviors of similar compounds and simplify the study of the vast diversity of AGEs. Furthermore, defining relevant outcome measurements for individual low and high molecular mass AGEs remains an area for further investigation. It is also essential for enabling effective risk assessments to consider mixture toxicity and define relative potency factors for relevant endpoints, given that human exposure to AGEs typically occurs as complex mixtures.

7.3 Overall conclusions

In this thesis, the neurotoxicity of dicarbonyl compounds and potential mitigation strategies were explored. The reactivity of three representative dicarbonyls—MGO, GO, and 3-DG—was compared, revealing that MGO is the most reactive in terms of GSH-mediated scavenging, ROS

production, induction of Nrf2-mediated gene expression, and the effects of GSH depletion on Nrf2 activation potential. This prompted the selection of MGO for further detailed studies.

Investigations into the mitigation of dicarbonyls both endogenously and in food concluded that flavonoids like kaempferol provide better scavengers for food-borne MGO than thiol-based scavengers such as GSH. However, given the endogenous concentrations of both scavengers and the detoxification of the GSH-MGO adduct by the glyoxalase system, GSH remains dominant for intracellular MGO protection. Nonetheless, flavonoids hold great promise for incorporation into daily health regimes to mitigate chronic disease risks and for development as pharmaceuticals to inhibit endogenous AGE formation.

In the subsequent studies on the neurotoxicity of MGO, several protein biomarkers for endogenous and exogenous MGO exposure were identified in SH-SY5Y cells using proteomics. Bioinformatics analysis revealed that motor proteins, cytoskeleton components, and glycolysis proteins were overrepresented among those highly susceptible to MGO modification. An integrated proteomics and metabolomics approach revealed that MGO exposure induces both toxic effects and adaptive responses in SH-SY5Y cells. These findings emphasize the need to link protein modifications to cellular responses and ultimately to clinical outcomes.

A human PBK model was developed and used for the risk assessment of MGO from both dietary and endogenous sources. The results revealed that daily dietary intake of MGO did not raise concerns for neurotoxicity, while endogenous MGO formation, especially under diabetic conditions, raised concerns for both genotoxicity and some neurotoxicity endpoints. These findings highlight the importance of considering endogenous levels in the risk assessment of dicarbonyls.

Overall, the insights provided by this thesis pave the way for future studies to elucidate the role of biomolecule modifications by MGO in neurotoxicity and related diseases. Further investigation into the toxicokinetics and toxicodynamics of dicarbonyls, and also of AGEs, is needed for adequate future risk assessment.

R

References

A decorative graphic at the bottom of the page consisting of several overlapping, wavy, horizontal bands of different shades of blue, ranging from a very light sky blue to a deep navy blue. The waves flow from the left side towards the right, creating a sense of movement and depth.

References

1. Li, Z.; Zhang, Z.; Ren, Y.; Wang, Y.; Fang, J.; Yue, H.; Ma, S.; Guan, F., Aging and age-related diseases: from mechanisms to therapeutic strategies. *Biogerontology* **2021**, *22* (2), 165-187.
2. El Ouaamari, Y.; Van den Bos, J.; Willekens, B.; Cools, N.; Wens, I., Neurotrophic factors as regenerative therapy for neurodegenerative diseases: current status, challenges and future perspectives. *International journal of molecular sciences* **2023**, *24* (4), 3866.
3. Forrest, S. L.; Kovacs, G. G., Current Concepts of Mixed Pathologies in Neurodegenerative Diseases. *Canadian Journal of Neurological Sciences* **2023**, *50* (3), 329-345.
4. Wilson, D. M., 3rd; Cookson, M. R.; Van Den Bosch, L.; Zetterberg, H.; Holtzman, D. M.; Dewachter, I., Hallmarks of neurodegenerative diseases. *Cell* **2023**, *186* (4), 693-714.
5. Behl, T.; Makkar, R.; Sehgal, A.; Singh, S.; Sharma, N.; Zengin, G.; Bungau, S.; Andronie-Cioara, F. L.; Munteanu, M. A.; Brisc, M. C.; Uivarosan, D.; Brisc, C., Current Trends in Neurodegeneration: Cross Talks between Oxidative Stress, Cell Death, and Inflammation. *International journal of molecular sciences* **2021**, *22* (14).
6. Heidari, F.; Rabizadeh, S.; Rajab, A.; Heidari, F.; Mouodi, M.; Mirmiranpour, H.; Esteghamati, A.; Nakhjavani, M., Advanced glycation end-products and advanced oxidation protein products levels are correlates of duration of type 2 diabetes. *Life Sciences* **2020**, *260*, 118422.
7. Vicente Miranda, H.; Outeiro, T. F., The sour side of neurodegenerative disorders: the effects of protein glycation. *J Pathol* **2010**, *221* (1), 13-25.
8. Twarda-Clapa, A.; Olczak, A.; Białkowska, A. M.; Koziółkiewicz, M., Advanced glycation end-products (AGEs): Formation, chemistry, classification, receptors, and diseases related to AGEs. *Cells* **2022**, *11* (8), 1312.
9. Rietjens, I.; Michael, A.; Bolt, H. M.; Simeon, B.; Andrea, H.; Nils, H.; Christine, K.; Angela, M.; Gloria, P.; Daniel, R.; Natalie, T.; Gerhard, E., The role of endogenous versus exogenous sources in the exposome of putative genotoxins and consequences for risk assessment. *Arch Toxicol* **2022**.
10. Rabbani, N.; Thornalley, P. J., Dicarbonyl stress in cell and tissue dysfunction contributing to ageing and disease. *Biochemical and biophysical research communications* **2015**, *458* (2), 221-6.
11. Maasen, K.; Scheijen, J.; Opperhuizen, A.; Stehouwer, C. D. A.; Van Greevenbroek, M. M.; Schalkwijk, C. G., Quantification of dicarbonyl compounds in commonly consumed foods and drinks; presentation of a food composition database for dicarbonyls. *Food Chem* **2021**, *339*, 128063.
12. Rabbani, N.; Xue, M.; Thornalley, P. J., Dicarbonyls and glyoxalase in disease mechanisms and clinical therapeutics. *Glycoconjugate journal* **2016**, *33* (4), 513-25.
13. Ramasamy, R.; Vannucci, S. J.; Yan, S. S.; Herold, K.; Yan, S. F.; Schmidt, A. M., Advanced glycation end products and RAGE: a common thread in aging, diabetes, neurodegeneration, and inflammation. *Glycobiology* **2005**, *15* (7), 16R-28R.
14. Vanuopadath, M.; Nair, D.; Gopalakrishnan Nair, B.; Sadasivan Nair, S., Post-translational Modifications of Proteins: Biomarkers and Therapeutic Targets for Diabetes Related Complications. *Current Proteomics* **2016**, *13* (4), 251-270.
15. van Dongen, K. C. W.; Kappetein, L.; Estruch, I. M.; Belzer, C.; Beekmann, K.; Rietjens, I. M. C. M., Differences in kinetics and dynamics of endogenous versus exogenous advanced glycation end products (AGEs) and their precursors. *Food Chem Toxicol* **2022**, *164*, 112987.

16. Zhu, H.; Poojary, M. M.; Andersen, M. L.; Lund, M. N., The effect of molecular structure of polyphenols on the kinetics of the trapping reactions with methylglyoxal. *Food Chemistry* **2020**, *319*, 126500.
17. Zhang, Y.; Chen, Y.; Liu, H.; Sun, B., Advances of nanoparticle derived from food in the control of alpha-dicarbonyl compounds-A review. *Food Chem* **2024**, *444*, 138660.
18. Zheng, J.; Ou, J.; Ou, S., Alpha-Dicarbonyl Compounds. In *Chemical Hazards in Thermally-Processed Foods*, 2019; pp 19-46.
19. Yan, S.; Wu, L.; Xue, X., alpha-Dicarbonyl compounds in food products: Comprehensively understanding their occurrence, analysis, and control. *Comprehensive Reviews in Food Science and Food Safety* **2023**, *22* (2), 1387-1417.
20. Lund, M. N.; Ray, C. A., Control of Maillard reactions in foods: Strategies and chemical mechanisms. *J Agric Food Chem* **2017**, *65* (23), 4537-4552.
21. Kroh, L. W., Caramelisation in food and beverages. *Food chemistry* **1994**, *51* (4), 373-379.
22. Hellwig, M.; Gensberger-Reigl, S.; Henle, T.; Pischetsrieder, M., Food-derived 1,2-dicarbonyl compounds and their role in diseases. *Seminars in Cancer Biology* **2018**, *49*, 1-8.
23. Shibamoto, T., Analytical methods for trace levels of reactive carbonyl compounds formed in lipid peroxidation systems. *Journal of pharmaceutical and biomedical analysis* **2006**, *41* (1), 12-25.
24. Zheng, J.; Guo, H.; Ou, J.; Liu, P.; Huang, C.; Wang, M.; Simal-Gandara, J.; Battino, M.; Jafari, S. M.; Zou, L.; Ou, S.; Xiao, J., Benefits, deleterious effects and mitigation of methylglyoxal in foods: A critical review. *Trends in Food Science & Technology* **2021**, *107*, 201-212.
25. McDonald, S. T., *Role of alpha-dicarbonyl compounds produced by lactic acid bacteria on the flavor and color of cheeses*. The University of Wisconsin-Madison: 1992.
26. Wang, Y.; Ho, C.-T., Dicarbonyl intermediates: a control factor in the Maillard reaction. In *Controlling Maillard pathways to generate flavors*, ACS Publications: 2010; pp 27-34.
27. Zhu, H.; Poojary, M. M.; Andersen, M. L.; Lund, M. N., Effect of pH on the reaction between naringenin and methylglyoxal: A kinetic study. *Food Chem* **2019**, *298*, 125086.
28. Nowotny, K.; Schroter, D.; Schreiner, M.; Grune, T., Dietary advanced glycation end products and their relevance for human health. *Ageing Res Rev* **2018**, *47*, 55-66.
29. Rabbani, N.; Thornalley, P. J., Glyoxalase 1 modulation in obesity and diabetes. *Antioxidants & redox signaling* **2019**, *30* (3), 354-374.
30. Rabbani, N.; Thornalley, P. J., The critical role of methylglyoxal and glyoxalase 1 in diabetic nephropathy. *Diabetes* **2014**, *63* (1), 50-2.
31. Zheng, L.; van Dongen, K. C. W.; Bakker, W.; Miro Estruch, I.; Rietjens, I., The Influence of Intracellular Glutathione Levels on the Induction of Nrf2-Mediated Gene Expression by alpha-Dicarbonyl Precursors of Advanced Glycation End Products. *Nutrients* **2022**, *14* (7).
32. Thornalley, P. J.; Langborg, A.; Minhas, H. S., Formation of glyoxal, methylglyoxal and 3-deoxyglucosone in the glycation of proteins by glucose. *Biochem J* **1999**, *344 Pt 1*, 109-16.
33. Sibbersen, C.; Johannsen, M., Dicarbonyl derived post-translational modifications: chemistry bridging biology and aging-related disease. *Essays Biochem* **2020**, *64* (1), 97-110.
34. Richard, J. P., Mechanism for the formation of methylglyoxal from triosephosphates. *Biochem Soc Trans* **1993**, *21* (2), 549-553.
35. Phillips, S. A.; Thornalley, P. J., The formation of methylglyoxal from triose phosphates: investigation using a specific assay for methylglyoxal. *Eur J Biochem* **1993**, *212* (1), 101-105.

36. Kold-Christensen, R.; Johannsen, M., Methylglyoxal Metabolism and Aging-Related Disease: Moving from Correlation toward Causation. *Trends Endocrinol Metab* **2020**, *31* (2), 81-92.
37. Niwa, T., 3-Deoxyglucosone: metabolism, analysis, biological activity, and clinical implication. *Journal of Chromatography B: Biomedical Sciences and Applications* **1999**, *731* (1), 23-36.
38. Lal, S.; Szwergold, B. S.; Walker, M.; Randall, W.; Kappler, F.; Brown, T.; Beisswenger, P. J., Production and metabolism of 3-deoxyglucosone in humans. In *The Maillard reaction in foods and medicine*, Elsevier: 2005; pp 291-297.
39. Pamplona, R., Advanced lipoxidation end-products. *Chemico-biological interactions* **2011**, *192* (1-2), 14-20.
40. Thornalley, P. J., Dicarbonyl intermediates in the maillard reaction. *Ann N Y Acad Sci* **2005**, *1043*, 111-7.
41. Lo, T. W.; Westwood, M. E.; McLellan, A. C.; Selwood, T.; Thornalley, P. J., Binding and modification of proteins by methylglyoxal under physiological conditions. A kinetic and mechanistic study with N alpha-acetylarginine, N alpha-acetylcysteine, and N alpha-acetyllysine, and bovine serum albumin. *J Biol Chem* **1994**, *269* (51), 32299-32305.
42. Cho, S. J.; Roman, G.; Yeboah, F.; Konishi, Y., The road to advanced glycation end products: a mechanistic perspective. *Current medicinal chemistry* **2007**, *14* (15), 1653-1671.
43. Rabbani, N.; Thornalley, Paul J., Dicarbonyls linked to damage in the powerhouse: glycation of mitochondrial proteins and oxidative stress. *Biochem Soc Trans* **2008**, *36* (5), 1045-1050.
44. Zheng, W.; Li, H.; Go, Y.; Chan, X. H. F.; Huang, Q.; Wu, J., Research Advances on the Damage Mechanism of Skin Glycation and Related Inhibitors. *Nutrients* **2022**, *14* (21).
45. Bidmon, C.; Frischmann, M.; Pischetsrieder, M., Analysis of DNA-bound advanced glycation end-products by LC and mass spectrometry. *Journal of Chromatography B* **2007**, *855* (1), 51-58.
46. Westwood, M. E.; Thornalley, P. J., Molecular characteristics of methylglyoxal-modified bovine and human serum albumins. Comparison with glucose-derived advanced glycation endproduct-modified serum albumins. *Journal of protein chemistry* **1995**, *14*, 359-372.
47. Mittelman, S.; Pischetsrieder, M., Multistep ultrahigh performance liquid chromatography/tandem mass spectrometry analysis for untargeted quantification of glycating activity and identification of most relevant glycation products. *Analytical chemistry* **2011**, *83* (24), 9660-9668.
48. Smuda, M.; Henning, C.; Raghavan, C. T.; Johar, K.; Vasavada, A. R.; Nagaraj, R. H.; Glomb, M. A., Comprehensive analysis of maillard protein modifications in human lenses: effect of age and cataract. *Biochemistry* **2015**, *54* (15), 2500-2507.
49. Thornalley, P. J.; Battah, S.; Ahmed, N.; Karachalias, N.; Agalou, S.; Babaei-Jadidi, R.; Dawnay, A., Quantitative screening of advanced glycation endproducts in cellular and extracellular proteins by tandem mass spectrometry. *Biochemical Journal* **2003**, *375* (3), 581-592.
50. Acimovic, J. M.; Stanimirovic, B. D.; Todorovic, N.; Jovanovic, V. B.; Mandic, L. M., Influence of the microenvironment of thiol groups in low molecular mass thiols and serum albumin on the reaction with methylglyoxal. *Chem Biol Interact* **2010**, *188* (1), 21-30.
51. Mostafa, A. A.; Randell, E. W.; Vasdev, S. C.; Gill, V. D.; Han, Y.; Gadag, V.; Raouf, A. A.; El Said, H., Plasma protein advanced glycation end products, carboxymethyl cysteine, and carboxyethyl cysteine, are elevated and related to nephropathy in patients with diabetes. *Mol Cell Biochem* **2007**, *302* (1-2), 35-42.
52. Van Herreweghe, F.; Mao, J.; Chaplen, F. W.; Grooten, J.; Gevaert, K.; Vandekerckhove, J.; Vancompernelle, K., Tumor necrosis factor-induced modulation of glyoxalase I activities through

phosphorylation by PKA results in cell death and is accompanied by the formation of a specific methylglyoxal-derived AGE. *Proceedings of the National Academy of Sciences* **2002**, 99 (2), 949-954.

53. Bollong, M. J.; Lee, G.; Coukos, J. S.; Yun, H.; Zambaldo, C.; Chang, J. W.; Chin, E. N.; Ahmad, I.; Chatterjee, A. K.; Lairson, L. L.; Schultz, P. G.; Moellering, R. E., A metabolite-derived protein modification integrates glycolysis with KEAP1-NRF2 signalling. *Nature* **2018**, 562 (7728), 600-604.

54. Degen, J.; Hellwig, M.; Henle, T., 1,2-dicarbonyl compounds in commonly consumed foods. *J Agric Food Chem* **2012**, 60 (28), 7071-9.

55. Luévano-Contreras, C.; Garay-Sevilla, M. E.; Wrobel, K.; Malacara, J. M.; Wrobel, K., Dietary advanced glycation end products restriction diminishes inflammation markers and oxidative stress in patients with type 2 diabetes mellitus. *Journal of clinical biochemistry and nutrition* **2013**, 52 (1), 22-26.

56. Clarke, R. E.; Dordevic, A. L.; Tan, S. M.; Ryan, L.; Coughlan, M. T., Dietary Advanced Glycation End Products and Risk Factors for Chronic Disease: A Systematic Review of Randomised Controlled Trials. *Nutrients* **2016**, 8 (3), 125.

57. Ferreira, S. S.; Domingues, M. R.; Barros, C.; Santos, S. A. O.; Silvestre, A. J. D.; Silva, A. M.; Nunes, F. M., Major anthocyanins in elderberry effectively trap methylglyoxal and reduce cytotoxicity of methylglyoxal in HepG2 cell line. *Food Chem X* **2022**, 16, 100468.

58. Zhu, H.; Poojary, M. M.; Andersen, M. L.; Lund, M. N., Trapping of Carbonyl Compounds by Epicatechin: Reaction Kinetics and Identification of Epicatechin Adducts in Stored UHT Milk. *J Agric Food Chem* **2020**, 68 (29), 7718-7726.

59. Comert, E. D.; Gokmen, V., Kinetic evaluation of the reaction between methylglyoxal and certain scavenging compounds and determination of their *in vitro* dicarbonyl scavenging activity. *Food Res Int* **2019**, 121, 257-268.

60. Li, X.; Zheng, T.; Sang, S.; Lv, L., Quercetin inhibits advanced glycation end product formation by trapping methylglyoxal and glyoxal. *J Agric Food Chem* **2014**, 62 (50), 12152-8.

61. Lv, L.; Shao, X.; Chen, H.; Ho, C. T.; Sang, S., Genistein inhibits advanced glycation end product formation by trapping methylglyoxal. *Chem Res Toxicol* **2011**, 24 (4), 579-86.

62. Ou, J.; Teng, J.; El-Nezami, H. S.; Wang, M., Impact of resveratrol, epicatechin and rosmarinic acid on fluorescent AGEs and cytotoxicity of cookies. *Journal of Functional Foods* **2018**, 40, 44-50.

63. Thornalley, P. J., Glyoxalase I--structure, function and a critical role in the enzymatic defence against glycation. *Biochem Soc Trans* **2003**, 31 (Pt 6), 1343-8.

64. Hutschenreuther, A.; Bigl, M.; Hemdan, N. Y. A.; Debebe, T.; Gaunitz, F.; Birkenmeier, G., Modulation of GLO1 expression affects malignant properties of cells. *International journal of molecular sciences* **2016**, 17 (12), 2133.

65. Kammerscheit, X.; Hecker, A.; Rouhier, N.; Chauvat, F.; Cassier-Chauvat, C., Methylglyoxal Detoxification Revisited: Role of Glutathione Transferase in Model Cyanobacterium *Synechocystis* sp. Strain PCC 6803. *mBio* **2020**, 11 (4).

66. Brings, S.; Fleming, T.; Freichel, M.; Muckenthaler, M. U.; Herzig, S.; Nawroth, P. P., Dicarbonyls and advanced glycation end-products in the development of diabetic complications and targets for intervention. *International journal of molecular sciences* **2017**, 18 (5), 984.

67. Xue, M.; Rabbani, N.; Momiji, H.; Imbasi, P.; Anwar, M. M.; Kitteringham, N.; Park, B. K.; Souma, T.; Moriguchi, T.; Yamamoto, M., Transcriptional control of glyoxalase 1 by Nrf2 provides a stress-responsive defence against dicarbonyl glycation. *Biochemical Journal* **2012**, 443 (1), 213-222.

68. Mastrocola, R., AGEs and neurodegeneration: the Nrf2/glyoxalase-1 interaction. *Oncotarget* **2017**, *8* (4), 5645.
69. Wilson, A. J.; Kerns, J. K.; Callahan, J. F.; Moody, C. J., Keap calm, and carry on covalently. *Journal of medicinal chemistry* **2013**, *56* (19), 7463-7476.
70. Nishimoto, S.; Koike, S.; Inoue, N.; Suzuki, T.; Ogasawara, Y., Activation of Nrf2 attenuates carbonyl stress induced by methylglyoxal in human neuroblastoma cells: Increase in GSH levels is a critical event for the detoxification mechanism. *Biochem Biophys Res Commun* **2017**, *483* (2), 874-879.
71. de Oliveira, M. R.; Custodio de Souza, I. C.; Furstenau, C. R., Promotion of mitochondrial protection by naringenin in methylglyoxal-treated SH-SY5Y cells: Involvement of the Nrf2/GSH axis. *Chem Biol Interact* **2019**, *310*, 108728.
72. Rabbani, N.; Thornalley, P. J., Dicarbonyl proteome and genome damage in metabolic and vascular disease. *Biochem Soc Trans* **2014**, *42* (2), 425-32.
73. Haik Jr, G. M.; Lo, T. W.; Thornalley, P. J., Methylglyoxal concentration and glyoxalase activities in the human lens. *Experimental eye research* **1994**, *59* (4), 497-500.
74. Schalkwijk, C. G.; Stehouwer, C. D. A., Methylglyoxal, a Highly Reactive Dicarbonyl Compound, in Diabetes, Its Vascular Complications, and Other Age-Related Diseases. *Physiol Rev* **2020**, *100* (1), 407-461.
75. Hanssen, N. M. J.; Wouters, K.; Huijberts, M. S.; Gijbels, M. J.; Sluimer, J. C.; Scheijen, J. L. J. M.; Heeneman, S.; Biessen, E. A. L.; Daemen, M. J. A. P.; Brownlee, M., Higher levels of advanced glycation endproducts in human carotid atherosclerotic plaques are associated with a rupture-prone phenotype. *European heart journal* **2014**, *35* (17), 1137-1146.
76. Kikuchi, S.; Shinpo, K.; Moriwaka, F.; Makita, Z.; Miyata, T.; Tashiro, K., Neurotoxicity of methylglyoxal and 3-deoxyglucosone on cultured cortical neurons: synergism between glycation and oxidative stress, possibly involved in neurodegenerative diseases. *J Neurosci Res* **1999**, *57* (2), 280-289.
77. Markova, I.; Hüttel, M.; Oliarnyk, O.; Kacerova, T.; Haluzik, M.; Kacer, P.; Seda, O.; Malinska, H., The effect of dicarbonyl stress on the development of kidney dysfunction in metabolic syndrome—a transcriptomic and proteomic approach. *Nutrition & metabolism* **2019**, *16*, 1-10.
78. Stratmann, B., Dicarbonyl stress in diabetic vascular disease. *International Journal of Molecular Sciences* **2022**, *23* (11), 6186.
79. Zhao, Y.; Tang, Y.; Sang, S., Dietary quercetin reduces plasma and tissue methylglyoxal and advanced glycation end products in healthy mice treated with methylglyoxal. *The Journal of Nutrition* **2021**, *151* (9), 2601-2609.
80. Ghosh, M.; Talukdar, D.; Ghosh, S.; Bhattacharyya, N.; Ray, M.; Ray, S., *In vivo* assessment of toxicity and pharmacokinetics of methylglyoxal. Augmentation of the curative effect of methylglyoxal on cancer-bearing mice by ascorbic acid and creatine. *Toxicol Appl Pharmacol* **2006**, *212* (1), 45-58.
81. Degen, J.; Beyer, H.; Heymann, B. r.; Hellwig, M.; Henle, T., Dietary influence on urinary excretion of 3-deoxyglucosone and its metabolite 3-deoxyfructose. *Journal of agricultural and food chemistry* **2014**, *62* (11), 2449-2456.
82. Degen, J.; Vogel, M.; Richter, D.; Hellwig, M.; Henle, T., Metabolic transit of dietary methylglyoxal. *Journal of agricultural and food chemistry* **2013**, *61* (43), 10253-10260.
83. Teleanu, D. M.; Niculescu, A.-G.; Lungu, I. I.; Radu, C. I.; Vladăncenco, O.; Roza, E.; Costăchescu, B.; Grumezescu, A. M.; Teleanu, R. I., An overview of oxidative stress, neuroinflammation, and neurodegenerative diseases. *International journal of molecular sciences* **2022**, *23* (11), 5938.

84. Gulisano, W.; Maugeri, D.; Baltrons, M. A.; Fà, M.; Amato, A.; Palmeri, A.; D'Adamio, L.; Grassi, C.; Devanand, D. P.; Honig, L. S., Role of amyloid- β and tau proteins in Alzheimer's disease: confuting the amyloid cascade. *Journal of Alzheimer's Disease* **2018**, *64* (s1), S611-S631.
85. Wakabayashi, K.; Tanji, K.; Odagiri, S.; Miki, Y.; Mori, F.; Takahashi, H., The Lewy body in Parkinson's disease and related neurodegenerative disorders. *Molecular neurobiology* **2013**, *47*, 495-508.
86. Srikanth, V.; Westcott, B.; Forbes, J.; Phan, T. G.; Beare, R.; Venn, A.; Pearson, S.; Greenaway, T.; Parameswaran, V.; Münch, G., Methylglyoxal, cognitive function and cerebral atrophy in older people. *Journals of Gerontology Series A: Biomedical Sciences and Medical Sciences* **2013**, *68* (1), 68-73.
87. Fan, X.; Sell, D. R.; Hao, C.; Liu, S.; Wang, B.; Wesson, D. W.; Siedlak, S.; Zhu, X.; Kavanagh, T. J.; Harrison, F. E., Vitamin C is a source of oxoaldehyde and glycative stress in age-related cataract and neurodegenerative diseases. *Aging Cell* **2020**, *19* (7), e13176.
88. Vitek, M. P.; Bhattacharya, K.; Glendening, J. M.; Stopa, E.; Vlassara, H.; Bucala, R.; Manogue, K.; Cerami, A., Advanced glycation end products contribute to amyloidosis in Alzheimer disease. *Proceedings of the National Academy of Sciences* **1994**, *91* (11), 4766-4770.
89. Smith, M. A.; Taneda, S.; Richey, P. L.; Miyata, S.; Yan, S.-D.; Stern, D.; Sayre, L. M.; Monnier, V. M.; Perry, G., Advanced Maillard reaction end products are associated with Alzheimer disease pathology. *Proceedings of the National Academy of Sciences* **1994**, *91* (12), 5710-5714.
90. Vicente Miranda, H.; Szegő, É. M.; Oliveira, L. M. A.; Breda, C.; Darendelioglu, E.; De Oliveira, R. M.; Ferreira, D. G.; Gomes, M. A.; Rott, R.; Oliveira, M., Glycation potentiates α -synuclein-associated neurodegeneration in synucleinopathies. *Brain* **2017**, *140* (5), 1399-1419.
91. Ledesma, M. D.; Bonay, P.; Avila, J., τ Protein from Alzheimer's disease patients is glycated at its tubulin-binding domain. *Journal of neurochemistry* **1995**, *65* (4), 1658-1664.
92. Semchyshyn, H., Is carbonyl/AGE/RAGE stress a hallmark of the brain aging? *Pflügers Archiv-European Journal of Physiology* **2021**, *473* (5), 723-734.
93. Miller, M. C.; Tavares, R.; Johanson, C. E.; Hovanesian, V.; Donahue, J. E.; Gonzalez, L.; Silverberg, G. D.; Stopa, E. G., Hippocampal RAGE immunoreactivity in early and advanced Alzheimer's disease. *Brain research* **2008**, *1230*, 273-280.
94. Moreira, A. P.; Vizuete, A. F. K.; Zin, L. E. F.; de Marques, C. O.; Pacheco, R. F.; Leal, M. B.; Gonçalves, C.-A., The methylglyoxal/RAGE/NOX-2 pathway is persistently activated in the hippocampus of rats with STZ-induced sporadic Alzheimer's disease. *Neurotoxicity Research* **2022**, *40* (2), 395-409.
95. Coccini, T.; Schicchi, A.; Locatelli, C. A.; Caloni, F.; Negri, S.; Grignani, E.; De Simone, U., Methylglyoxal-induced neurotoxic effects in primary neuronal-like cells transdifferentiated from human mesenchymal stem cells: Impact of low concentrations. *J Appl Toxicol* **2023**.
96. Nan, F.; Sun, G.; Xie, W.; Ye, T.; Sun, X.; Zhou, P.; Dong, X.; Sun, J.; Sun, X.; Zhang, M., Ginsenoside Rb1 mitigates oxidative stress and apoptosis induced by methylglyoxal in SH-SY5Y cells via the PI3K/Akt pathway. *Mol Cell Probes* **2019**, *48*, 101469.
97. Furstenu, C. R.; de Souza, I. C. C.; de Oliveira, M. R., Tanshinone I Induces Mitochondrial Protection by a Mechanism Involving the Nrf2/GSH Axis in the Human Neuroblastoma SH-SY5Y Cells Exposed to Methylglyoxal. *Neurotox Res* **2019**, *36* (3), 491-502.
98. de Arriba, S. G.; Stuchbury, G.; Yarin, J.; Burnell, J.; Loske, C.; Munch, G., Methylglyoxal impairs glucose metabolism and leads to energy depletion in neuronal cells--protection by carbonyl scavengers. *Neurobiol Aging* **2007**, *28* (7), 1044-50.

99. Morcos, M.; Du, X.; Pfisterer, F.; Hutter, H.; Sayed, A. A. R.; Thornalley, P.; Ahmed, N.; Baynes, J.; Thorpe, S.; Kukudov, G., Glyoxalase-1 prevents mitochondrial protein modification and enhances lifespan in *Caenorhabditis elegans*. *Aging cell* **2008**, *7* (2), 260-269.
100. Pistollato, F.; Madaia, F.; Corvi, R.; Munn, S.; Grignard, E.; Paini, A.; Worth, A.; Bal-Price, A.; Prieto, P.; Casati, S., Current EU regulatory requirements for the assessment of chemicals and cosmetic products: challenges and opportunities for introducing new approach methodologies. *Archives of toxicology* **2021**, *95*, 1867-1897.
101. Zuang, V.; Dura, A.; Ahs, L. E.; Barroso, J.; Batista, L. S.; Berggren, E.; Bopp, S.; Campia, I.; Carpi, D.; Casati, S., *Non-animal methods in science and regulation*. 2022.
102. Carusi, A., Chemicals regulation and non-animal methods: displacing the gold standard. *Wellcome Open Research* **2024**, *9* (167), 167.
103. Iloghen, O. C.; Ceafalan, L. C.; Popescu, B. O., SH-SY5Y cell line *in vitro* models for Parkinson disease research—old practice for new trends. *J Integr Neurosci* **2023**, *22* (1), 20.
104. Donnellan, L.; Young, C.; Simpson, B. S.; Acland, M.; Dhillon, V. S.; Costabile, M.; Fenech, M.; Hoffmann, P.; Deo, P., Proteomic Analysis of Methylglyoxal Modifications Reveals Susceptibility of Glycolytic Enzymes to Dicarbonyl Stress. *Int J Mol Sci* **2022**, *23* (7).
105. Chen, H. J.; Chen, Y. C.; Hsiao, C. F.; Chen, P. F., Mass Spectrometric Analysis of Glyoxal and Methylglyoxal-Induced Modifications in Human Hemoglobin from Poorly Controlled Type 2 Diabetes Mellitus Patients. *Chem Res Toxicol* **2015**, *28* (12), 2377-89.
106. Alhujaily, M.; Abbas, H.; Xue, M.; de la Fuente, A.; Rabbani, N.; Thornalley, P. J., Studies of Glyoxalase 1-Linked Multidrug Resistance Reveal Glycolysis-Derived Reactive Metabolite, Methylglyoxal, Is a Common Contributor in Cancer Chemotherapy Targeting the Spliceosome. *Front Oncol* **2021**, *11*, 748698.
107. Irshad, Z.; Xue, M.; Ashour, A.; Larkin, J. R.; Thornalley, P. J.; Rabbani, N., Activation of the unfolded protein response in high glucose treated endothelial cells is mediated by methylglyoxal. *Sci Rep* **2019**, *9* (1), 7889.
108. Gaffney, D. O.; Jennings, E. Q.; Anderson, C. C.; Marentette, J. O.; Shi, T.; Schou Oxvig, A. M.; Streeter, M. D.; Johannsen, M.; Spiegel, D. A.; Chapman, E.; Roede, J. R.; Galligan, J. J., Non-enzymatic Lysine Lactoylation of Glycolytic Enzymes. *Cell Chem Biol* **2020**, *27* (2), 206-213 e6.
109. Jonckheere, A. R., A distribution-free k-sample test against ordered alternatives. *Biometrika* **1954**, *41* (1/2), 133-145.
110. Shi Jing, L.; Fathiah Muzaffar Shah, F.; Saberi Mohamad, M.; Moorthy, K.; Deris, S.; Zakaria, Z.; Napis, S., A review on bioinformatics enrichment analysis tools towards functional analysis of high throughput gene set data. *Current Proteomics* **2015**, *12* (1), 14-27.
111. Koh, G. C. K. W.; Porras, P.; Aranda, B.; Hermjakob, H.; Orchard, S. E., Analyzing protein–protein interaction networks. *Journal of proteome research* **2012**, *11* (4), 2014-2031.
112. Patil, R.; Satpute, R.; Nalage, D., The application of omics technologies to toxicology. *Toxicol Adv* **2023**, *5* (2), 6.
113. Vailati-Riboni, M.; Palombo, V.; Loor, J. J., What are omics sciences? *Periparturient diseases of dairy cows: a systems biology approach* **2017**, 1-7.
114. Radu, B. M.; Dumitrescu, D. I.; Mustaciosu, C. C.; Radu, M., Dual effect of methylglyoxal on the intracellular Ca²⁺ signaling and neurite outgrowth in mouse sensory neurons. *Cellular and molecular neurobiology* **2012**, *32*, 1047-1057.

115. Hansen, F.; de Souza, D. F.; Silveira, S. d. L.; Hoefel, A. L.; Fontoura, J. B.; Tramontina, A. C.; Bobermin, L. D.; Leite, M. C.; Perry, M. L. S.; Gonçalves, C. A., Methylglyoxal alters glucose metabolism and increases AGEs content in C6 glioma cells. *Metabolic brain disease* **2012**, *27*, 531-539.
116. Louisse, J.; Beekmann, K.; Rietjens, I. M., Use of Physiologically Based Kinetic Modeling-Based Reverse Dosimetry to Predict *in vivo* Toxicity from *in Vitro* Data. *Chem Res Toxicol* **2017**, *30* (1), 114-125.
117. Kiwamoto, R.; Ploeg, D.; Rietjens, I. M.; Punt, A., Dose-dependent DNA adduct formation by cinnamaldehyde and other food-borne alpha,beta-unsaturated aldehydes predicted by physiologically based in silico modelling. *Toxicol In Vitro* **2016**, *31*, 114-25.
118. Wang, D.; Rietdijk, M. H.; Kamelia, L.; Boogaard, P. J.; Rietjens, I., Predicting the *in vivo* developmental toxicity of benzo[a]pyrene (BaP) in rats by an *in vitro*-in silico approach. *Arch Toxicol* **2021**, *95* (10), 3323-3340.
119. Zhang, M.; van Ravenzwaay, B.; Fabian, E.; Rietjens, I.; Louisse, J., Towards a generic physiologically based kinetic model to predict *in vivo* uterotrophic responses in rats by reverse dosimetry of *in vitro* estrogenicity data. *Arch Toxicol* **2018**, *92* (3), 1075-1088.
120. Fragki, S.; Piersma, A. H.; Rorije, E.; Zeilmaker, M. J., *In vitro* to *in vivo* extrapolation of effective dosimetry in developmental toxicity testing: Application of a generic PBK modelling approach. *Toxicol Appl Pharmacol* **2017**, *332*, 109-120.
121. Rietjens, I. M. C. M.; Louisse, J.; Punt, A., Tutorial on physiologically based kinetic modeling in molecular nutrition and food research. *Molecular nutrition & food research* **2011**, *55* (6), 941-956.
122. Yuan, B.; Cao, H.; Jiang, Y.; Hong, H.; Wang, Y., Efficient and accurate bypass of N 2-(1-carboxyethyl)-2'-deoxyguanosine by DinB DNA polymerase *in vitro* and *in vivo*. *Proceedings of the National Academy of Sciences* **2008**, *105* (25), 8679-8684.
123. Johnson, G. E.; Soeteman-Hernández, L. G.; Gollapudi, B. B.; Bodger, O. G.; Dearfield, K. L.; Heflich, R. H.; Hixon, J. G.; Lovell, D. P.; MacGregor, J. T.; Pottenger, L. H., Derivation of point of departure (PoD) estimates in genetic toxicology studies and their potential applications in risk assessment. *Environmental and molecular mutagenesis* **2014**, *55* (8), 609-623.
124. Committee, E. S., Scientific opinion on genotoxicity testing strategies applicable to food and feed safety assessment. *EFSA Journal* **2011**, *9* (9), 2379.
125. Committee, E. S., Statement on the applicability of the Margin of Exposure approach for the safety assessment of impurities which are both genotoxic and carcinogenic in substances added to food/feed. *EFSA Journal* **2012**, *10* (3), 2578.
126. Thornalley, P. J., The glyoxalase system in health and disease. *Mol Aspects Med* **1993**, *14* (4), 287-371.
127. Arribas-Lorenzo, G.; Morales, F. J., Analysis, distribution, and dietary exposure of glyoxal and methylglyoxal in cookies and their relationship with other heat-induced contaminants. *J Agric Food Chem* **2010**, *58* (5), 2966-72.
128. Piskorska, D.; Kopieczna-Grzebieniak, E., Participation of glyoxalases and methylglyoxal in diabetic complication development. *Pol Merkur Lekarski* **1998**, *4* (24), 342-4.
129. Li, J.; Liu, D.; Sun, L.; Lu, Y.; Zhang, Z., Advanced glycation end products and neurodegenerative diseases: mechanisms and perspective. *J Neurol Sci* **2012**, *317* (1-2), 1-5.
130. Chan, W. H.; Wu, H. J.; Hsuuw, Y. D., Curcumin inhibits ROS formation and apoptosis in methylglyoxal-treated human hepatoma G2 cells. *Ann N Y Acad Sci* **2005**, *1042*, 372-8.

131. Kuntz, S.; Rudloff, S.; Ehl, J.; Bretzel, R. G.; Kunz, C., Food derived carbonyl compounds affect basal and stimulated secretion of interleukin-6 and -8 in Caco-2 cells. *Eur J Nutr* **2009**, *48* (8), 499-503.
132. Salahuddin, P.; Rabbani, G.; Khan, R. H., The role of advanced glycation end products in various types of neurodegenerative disease: a therapeutic approach. *Cell Mol Biol Lett* **2014**, *19* (3), 407-37.
133. Matafome, P.; Sena, C.; Seica, R., Methylglyoxal, obesity, and diabetes. *Endocrine* **2013**, *43* (3), 472-84.
134. Yoon, K. D.; Yamamoto, K.; Zhou, J.; Sparrow, J. R., Photo-products of retinal pigment epithelial bisretinoids react with cellular thiols. *Mol Vis* **2011**, *17*, 1839-49.
135. Abordo, E. A.; Minhas, H. S.; Thornalley, P. J., Accumulation of α -oxoaldehydes during oxidative stress: a role in cytotoxicity. *Biochemical Pharmacology* **1999**, *58* (4), 641-648.
136. Masterjohn, C.; Mah, E.; Park, Y.; Pei, R.; Lee, J.; Manautou, J. E.; Bruno, R. S., Acute glutathione depletion induces hepatic methylglyoxal accumulation by impairing its detoxification to D-lactate. *Exp Biol Med (Maywood)* **2013**, *238* (4), 360-9.
137. Lee-Hilz, Y. Y.; Boerboom, A. M.; Westphal, A. H.; Berkel, W. J.; Aarts, J. M.; Rietjens, I. M., Pro-oxidant activity of flavonoids induces EpRE-mediated gene expression. *Chem Res Toxicol* **2006**, *19* (11), 1499-505.
138. van der Linden, S. C.; von Bergh, A. R.; van Vught-Lussenburg, B. M.; Jonker, L. R.; Teunis, M.; Krul, C. A.; van der Burg, B., Development of a panel of high-throughput reporter-gene assays to detect genotoxicity and oxidative stress. *Mutat Res Genet Toxicol Environ Mutagen* **2014**, *760*, 23-32.
139. Sonneveld, E.; Jansen, H. J.; Riteco, J. A.; Brouwer, A.; van der Burg, B., Development of androgen- and estrogen-responsive bioassays, members of a panel of human cell line-based highly selective steroid-responsive bioassays. *Toxicological Sciences* **2005**, *83* (1), 136-148.
140. Sonneveld, E.; van den Brink, C. E.; van der Leede, B. J. M.; Schulkes, R. K. A. M.; Petkovich, M.; van der Burg, B.; van der Saag, P. T., Human retinoic acid (RA) 4-hydroxylase (CYP26) is highly specific for all-trans-RA and can be induced through RA receptors in human breast and colon carcinoma cells. *Cell Growth Differ* **1998**, *9* (8), 629-637.
141. Gijsbers, L.; van Eekelen, H. D.; Nguyen, T. H.; de Haan, L. H.; van der Burg, B.; Aarts, J. M.; Rietjens, I. M.; Bovy, A. G., Induction of electrophile-responsive element (EpRE)-mediated gene expression by tomato extracts *in vitro*. *Food Chem* **2012**, *135* (3), 1166-72.
142. Boerboom, A. M.; Vermeulen, M.; van der Woude, H.; Bremer, B. I.; Lee-Hilz, Y. Y.; Kampman, E.; van Bladeren, P. J.; Rietjens, I. M.; Aarts, J. M., Newly constructed stable reporter cell lines for mechanistic studies on electrophile-responsive element-mediated gene expression reveal a role for flavonoid planarity. *Biochem Pharmacol* **2006**, *72* (2), 217-26.
143. Garcia-Mendoza, D.; Han, B.; van den Berg, H.; van den Brink, N. W., Cell-specific immune-modulation of cadmium on murine macrophages and mast cell lines *in vitro*. *J Appl Toxicol* **2019**, *39* (7), 992-1001.
144. Qanungo, S.; Wang, M.; Nieminen, A. L., N-Acetyl-L-cysteine enhances apoptosis through inhibition of nuclear factor-kappaB in hypoxic murine embryonic fibroblasts. *J Biol Chem* **2004**, *279* (48), 50455-64.
145. Hansen, J. M.; Watson, W. H.; Jones, D. P., Compartmentation of Nrf-2 redox control: regulation of cytoplasmic activation by glutathione and DNA binding by thioredoxin-1. *Toxicol Sci* **2004**, *82* (1), 308-17.
146. Hu, Y. N.; Chen, D.; Zhang, T. Y.; Ding, J.; Feng, Y. Q., Use of ammonium sulfite as a post-column derivatization reagent for rapid detection and quantification of aldehydes by LC-MS. *Talanta* **2020**, *206*, 120172.

147. Wasa, T. M.; Soichiro, Polarographic Behavior of Glyoxal and Its Related Compounds. *Bulletin of University of Osaka Prefecture. Series A, Engineering and natural sciences*. **1970**, *19* (1), 169-180.
148. Rae, C.; Bernersprice, S. J.; Bulliman, B. T.; Kuchel, P. W., Kinetic-Analysis of the Human Erythrocyte Glyoxalase System Using H-1-Nmr and a Computer-Model. *Eur J Biochem* **1990**, *193* (1), 83-90.
149. Nemet, I.; Vikić-Topić, D.; Varga-Defterdarović, L., Spectroscopic studies of methylglyoxal in water and dimethylsulfoxide. *Bioorg Chem* **2004**, *32* (6), 560-70.
150. Weenen, H.; Tjan, S. B., Analysis, Structure, and Reactivity of 3-Deoxyglucosone. In *Flavor Precursors*, 1992; pp 217-231.
151. Wang, Y.; Ho, C. T., Flavour chemistry of methylglyoxal and glyoxal. *Chem Soc Rev* **2012**, *41* (11), 4140-9.
152. Thornalley, P. J.; Yurek-George, A.; Argirov, O. K., Kinetics and mechanism of the reaction of aminoguanidine with the alpha-oxoaldehydes glyoxal, methylglyoxal, and 3-deoxyglucosone under physiological conditions. *Biochem Pharmacol* **2000**, *60* (1), 55-65.
153. Brouwers, O.; Niessen, P. M.; Ferreira, I.; Miyata, T.; Scheffer, P. G.; Teerlink, T.; Schrauwen, P.; Brownlee, M.; Stehouwer, C. D.; Schalkwijk, C. G., Overexpression of glyoxalase-I reduces hyperglycemia-induced levels of advanced glycation end products and oxidative stress in diabetic rats. *J Biol Chem* **2011**, *286* (2), 1374-80.
154. Li, D.; Ma, S.; Ellis, E. M., Nrf2-mediated adaptive response to methyl glyoxal in HepG2 cells involves the induction of AKR7A2. *Chemico-Biological Interactions* **2015**, *234*, 366-371.
155. Liu, Y.; Wang, S.; Ding, Y.; Wang, Q.; Chenheng, W.; Qiao, X., Effects of buthionine sulfoxine on the redox state of human umbilical vein endothelial cells cultured with K562 cells conditioned media. *Chinese Pharmacological Bulletin* **1986**, (04).
156. Zemva, J.; Fink, C. A.; Fleming, T. H.; Schmidt, L.; Loft, A.; Herzig, S.; Kniess, R. A.; Mayer, M.; Bukau, B.; Nawroth, P. P.; Tyedmers, J., Hormesis enables cells to handle accumulating toxic metabolites during increased energy flux. *Redox Biol* **2017**, *13*, 674-686.
157. Ferlita, S.; Yegiazaryan, A.; Noori, N.; Lal, G.; Nguyen, T.; To, K.; Venketaraman, V., Type 2 Diabetes Mellitus and Altered Immune System Leading to Susceptibility to Pathogens, Especially Mycobacterium tuberculosis. *J Clin Med* **2019**, *8* (12).
158. Aoyama, K.; Nakaki, T., Impaired glutathione synthesis in neurodegeneration. *Int J Mol Sci* **2013**, *14* (10), 21021-44.
159. Cepas, V.; Manig, F.; Mayo, J. C.; Hellwig, M.; Collotta, D.; Sanmartino, V.; Carrocera-Pumarino, R.; Collino, M.; Henle, T.; Sainz, R. M., *In Vitro* Evaluation of the Toxicological Profile and Oxidative Stress of Relevant Diet-Related Advanced Glycation End Products and Related 1,2-Dicarbonyls. *Oxid Med Cell Longev* **2021**, *2021*, 9912240.
160. Rogatsky, I.; Trowbridge, J. M.; Garabedian, M. J., Glucocorticoid receptor-mediated cell cycle arrest is achieved through distinct cell-specific transcriptional regulatory mechanisms. *Molecular and cellular biology* **1997**, *17* (6), 3181-3193.
161. Jeong, S. R.; Lee, K. W., Methylglyoxal-Derived Advanced Glycation End Product (AGE4)-Induced Apoptosis Leads to Mitochondrial Dysfunction and Endoplasmic Reticulum Stress through the RAGE/JNK Pathway in Kidney Cells. *Int J Mol Sci* **2021**, *22* (12).
162. Nasu, R.; Furukawa, A.; Suzuki, K.; Takeuchi, M.; Koriyama, Y., The Effect of Glyceraldehyde-Derived Advanced Glycation End Products on beta-Tubulin-Inhibited Neurite Outgrowth in SH-SY5Y Human Neuroblastoma Cells. *Nutrients* **2020**, *12* (10).

163. Garay-Sevilla, M. E.; Rojas, A.; Portero-Otin, M.; Uribarri, J., Dietary AGEs as Exogenous Boosters of Inflammation. *Nutrients* **2021**, *13* (8).
164. Ghassem Zadeh, R.; Yaylayan, V., Interaction pattern of histidine, carnosine and histamine with methylglyoxal and other carbonyl compounds. *Food Chem* **2021**, *358*, 129884.
165. Hamzalioglu, A.; Gokmen, V., Investigations on the reactions of alpha-dicarbonyl compounds with amino acids and proteins during *in vitro* digestion of biscuits. *Food Funct* **2016**, *7* (6), 2544-50.
166. Navarro, M.; Morales, F. J., Mechanism of reactive carbonyl species trapping by hydroxytyrosol under simulated physiological conditions. *Food Chem* **2015**, *175*, 92-9.
167. Ahmed, M. U.; Frye, E. B.; Degenhardt, T. P.; Thorpe, S. R.; Baynes, J. W., Nε-(Carboxyethyl)lysine, a product of the chemical modification of proteins by methylglyoxal, increases with age in human lens proteins. *Biochemical Journal* **1997**, *324* (2), 565-570.
168. Henle, T.; Walter, A. W.; Haeßner, R.; Klostermeyer, H., Detection and identification of a protein-bound imidazolone resulting from the reaction of arginine residues and methylglyoxal. *Zeitschrift für Lebensmittel-Untersuchung und Forschung* **1994**, *199* (1), 55-58.
169. Oya, T.; Hattori, N.; Mizuno, Y.; Miyata, S.; Maeda, S.; Osawa, T.; Uchida, K., Methylglyoxal modification of protein. Chemical and immunochemical characterization of methylglyoxal-arginine adducts. *J Biol Chem* **1999**, *274* (26), 18492-502.
170. de Arriba, S. G.; Krügel, U.; Regenthal, R.; Vissiennon, Z.; Verdaguer, E.; Lewerenz, A.; García-Jordá, E.; Pallas, M.; Camins, A.; Münch, G., Carbonyl stress and NMDA receptor activation contribute to methylglyoxal neurotoxicity. *Free Radical Biology and Medicine* **2006**, *40* (5), 779-790.
171. Andreeva, A.; Bekkhzhin, Z.; Omertassova, N.; Baizhumanov, T.; Yeltay, G.; Akhmetali, M.; Toibazar, D.; Utepbergenov, D., The apparent deglycase activity of DJ-1 results from the conversion of free methylglyoxal present in fast equilibrium with hemithioacetals and hemiaminals. *J Biol Chem* **2019**, *294* (49), 18863-18872.
172. Zhang, Y.; Zhan, L.; Wen, Q.; Feng, Y.; Luo, Y.; Tan, T., Trapping Methylglyoxal by Taxifolin and Its Metabolites in Mice. *J Agric Food Chem* **2022**, *70* (16), 5026-5038.
173. Liu, G.; Xia, Q.; Lu, Y.; Zheng, T.; Sang, S.; Lv, L., Influence of Quercetin and Its Methylglyoxal Adducts on the Formation of alpha-Dicarbonyl Compounds in a Lysine/Glucose Model System. *J Agric Food Chem* **2017**, *65* (10), 2233-2239.
174. Chen, M.; Zhou, H.; Huang, C.; Liu, P.; Fei, J.; Ou, J.; Ou, S.; Zheng, J., Identification and cytotoxic evaluation of the novel rutin-methylglyoxal adducts with dione structures *in vivo* and in foods. *Food Chem* **2022**, *377*, 132008.
175. Moridani, M. Y.; Galati, G.; O'Brien, P. J., Comparative quantitative structure toxicity relationships for flavonoids evaluated in isolated rat hepatocytes and HeLa tumor cells. *Chemico-biological interactions* **2002**, *139* (3), 251-264.
176. Liu, P.; Yin, Z.; Chen, M.; Huang, C.; Wu, Z.; Huang, J.; Ou, S.; Zheng, J., Cytotoxicity of adducts formed between quercetin and methylglyoxal in PC-12 cells. *Food Chem* **2021**, *352*, 129424.
177. Cha, S. H.; Hwang, Y.; Heo, S. J.; Jun, H. S., Diploretohydroxycarmalol Attenuates Methylglyoxal-Induced Oxidative Stress and Advanced Glycation End Product Formation in Human Kidney Cells. *Oxid Med Cell Longev* **2018**, *2018*, 3654095.
178. Zhou, Q.; Cheng, K. W.; Gong, J.; Li, E. T. S.; Wang, M., Apigenin and its methylglyoxal-adduct inhibit advanced glycation end products-induced oxidative stress and inflammation in endothelial cells. *Biochem Pharmacol* **2019**, *166*, 231-241.

179. Meister, A.; Anderson, M. E., Glutathione. *Annual review of biochemistry* **1983**, 52 (1), 711-760.
180. Erlund, I.; Kosonen, T.; Alfthan, G.; Mäenpää, J.; Perttunen, K.; Kenraali, J.; Parantainen, J.; Aro, A., Pharmacokinetics of quercetin from quercetin aglycone and rutin in healthy volunteers. *European journal of clinical pharmacology* **2000**, 56, 545-553.
181. Erlund, I.; Meririnne, E.; Alfthan, G.; Aro, A., Plasma kinetics and urinary excretion of the flavanones naringenin and hesperetin in humans after ingestion of orange juice and grapefruit juice. *The Journal of nutrition* **2001**, 131 (2), 235-241.
182. Dozio, E.; Vettoretti, S.; Lungarella, G.; Messa, P.; Corsi Romanelli, M. M., Sarcopenia in Chronic Kidney Disease: Focus on Advanced Glycation End Products as Mediators and Markers of Oxidative Stress. *Biomedicine* **2021**, 9 (4).
183. D'Cunha, N. M.; Sergi, D.; Lane, M. M.; Naumovski, N.; Gamage, E.; Rajendran, A.; Kouvari, M.; Gauci, S.; Dissanayaka, T.; Marx, W.; Travica, N., The Effects of Dietary Advanced Glycation End-Products on Neurocognitive and Mental Disorders. *Nutrients* **2022**, 14 (12).
184. Poulsen, M. W.; Hedegaard, R. V.; Andersen, J. M.; de Courten, B.; Bugel, S.; Nielsen, J.; Skibsted, L. H.; Dragsted, L. O., Advanced glycation endproducts in food and their effects on health. *Food Chem Toxicol* **2013**, 60, 10-37.
185. Bellier, J.; Nokin, M. J.; Larde, E.; Karoyan, P.; Peulen, O.; Castronovo, V.; Bellahcene, A., Methylglyoxal, a potent inducer of AGEs, connects between diabetes and cancer. *Diabetes Res Clin Pract* **2019**, 148, 200-211.
186. Rabbani, N.; Thornalley, P. J., Methylglyoxal, glyoxalase 1 and the dicarbonyl proteome. *Amino Acids* **2012**, 42 (4), 1133-42.
187. Ahmed, N.; Dobler, D.; Dean, M.; Thornalley, P. J., Peptide mapping identifies hotspot site of modification in human serum albumin by methylglyoxal involved in ligand binding and esterase activity. *J Biol Chem* **2005**, 280 (7), 5724-32.
188. Ahmed, N.; Thornalley, P. J.; Dawczynski, J.; Franke, S.; Strobel, J.; Stein, G.; Haik, G. M., Methylglyoxal-derived hydroimidazolone advanced glycation end-products of human lens proteins. *Invest Ophthalmol Vis Sci* **2003**, 44 (12), 5287-92.
189. Galligan, J. J.; Wepy, J. A.; Streeter, M. D.; Kingsley, P. J.; Mitchener, M. M.; Wauchope, O. R.; Beavers, W. N.; Rose, K. L.; Wang, T.; Spiegel, D. A.; Marnett, L. J., Methylglyoxal-derived posttranslational arginine modifications are abundant histone marks. *Proc Natl Acad Sci U S A* **2018**, 115 (37), 9228-9233.
190. Lai, S. W. T.; Lopez Gonzalez, E. J.; Zoukari, T.; Ki, P.; Shuck, S. C., Methylglyoxal and Its Adducts: Induction, Repair, and Association with Disease. *Chem Res Toxicol* **2022**, 35 (10), 1720-1746.
191. Zheng, Q.; Omans, N. D.; Leicher, R.; Osunsade, A.; Agustinus, A. S.; Fink-Groner, E.; D'Ambrosio, H.; Liu, B.; Chandarlapaty, S.; Liu, S. J. N. C., Reversible histone glycation is associated with disease-related changes in chromatin architecture. **2019**, 10 (1), 1289.
192. Gupta, A.; Khursheed, M.; Arif, Z.; Badar, A.; Alam, K. J. I. J. o. B. M., Methylglyoxal-induces multiple stable changes in human serum albumin before forming nephrotoxic advanced glycation end-products: Injury demonstration in human embryonic kidney cells. **2022**, 214, 252-263.
193. Rabbani, N.; Thornalley, P. J. K. i., Advanced glycation end products in the pathogenesis of chronic kidney disease. **2018**, 93 (4), 803-813.
194. Batth, T. S.; Tollenaere, M. X.; Rütther, P.; Gonzalez-Franquesa, A.; Prabhakar, B. S.; Bekker-Jensen, S.; Deshmukh, A. S.; Olsen, J. V., Protein aggregation capture on microparticles enables multipurpose proteomics sample preparation. *Mol Cell Proteomics* **2019**, 18 (5), 1027a.

195. UniProt: the universal protein knowledgebase in 2021 %J *Nucleic acids research*. **2021**, 49 (D1), D480-D489.
196. Wiśniewski, J. R.; Hein, M. Y.; Cox, J.; Mann, M. J. M.; proteomics, c., A “proteomic ruler” for protein copy number and concentration estimation without spike-in standards. **2014**, 13 (12), 3497-3506.
197. Dunnett, C. W. J. J. o. t. A. S. A., A multiple comparison procedure for comparing several treatments with a control. **1955**, 50 (272), 1096-1121.
198. Kruskal, W. H.; Wallis, W. A. J. J. o. t. A. S. A., Use of ranks in one-criterion variance analysis. **1952**, 47 (260), 583-621.
199. Dunn, O. J. F. t. a. o., Multiple comparisons using rank sums *Technometrics* 6: 241–252. **1964**, 959.
200. Sherman, B. T.; Hao, M.; Qiu, J.; Jiao, X.; Baseler, M. W.; Lane, H. C.; Imamichi, T.; Chang, W., DAVID: a web server for functional enrichment analysis and functional annotation of gene lists (2021 update). *Nucleic acids research* **2022**, 50 (W1), W216-W221.
201. Szklarczyk, D.; Kirsch, R.; Koutrouli, M.; Nastou, K.; Mehryary, F.; Hachilif, R.; Gable, A. L.; Fang, T.; Doncheva, N. T.; Pysalo, S., The STRING database in 2023: protein–protein association networks and functional enrichment analyses for any sequenced genome of interest. *Nucleic acids research* **2023**, 51 (D1), D638-D646.
202. Tang, D.; Chen, M.; Huang, X.; Zhang, G.; Zeng, L.; Zhang, G.; Wu, S.; Wang, Y., SRplot: A free online platform for data visualization and graphing. *PLoS One* **2023**, 18 (11), e0294236.
203. Pohlert, T.; package PMCMRplus, R. J. R. p. a. f. h. c. r.-p. e. c. o. w. p. g. P. p., Calculate pairwise multiple comparisons of mean rank sums extended. **2021**.
204. Ogle, D. H.; Doll, J. C.; Wheeler, A. P.; Dinno, A. J. R. p. v., FSA: simple fisheries stock assessment methods. **2023**, 4.
205. Ridge, K. M.; Eriksson, J. E.; Pekny, M.; Goldman, R. D., Roles of vimentin in health and disease. *Genes Dev* **2022**, 36 (7-8), 391-407.
206. Cristiano, L., The pseudogenes of eukaryotic translation elongation factors (EEFs): Role in cancer and other human diseases. *Genes & Diseases* **2022**, 9 (4), 941-958.
207. Cox, J.; Neuhauser, N.; Michalski, A.; Scheltema, R. A.; Olsen, J. V.; Mann, M., Andromeda: a peptide search engine integrated into the MaxQuant environment. *Journal of proteome research* **2011**, 10 (4), 1794-1805.
208. Al-Shaibi, N.; Ghosh, S. K., A novel cell-surface protein CSP82 on bone marrow stem cells and a cytosolic phosphoprotein DP58 (ankyrinRD 34B) are involved in promyeloid progenitor induction. *Cell Immunol* **2009**, 258 (2), 172-80.
209. Zheng, K.-W.; Zhang, C.-H.; Wu, W.; Zhu, Z.; Gong, J.-P.; Li, C.-M., FNBP4 is a Potential Biomarker Associated with Cuproptosis and Promotes Tumor Progression in Hepatocellular Carcinoma. *International Journal of General Medicine* **2023**, 467-480.
210. Archimandriti, D. T.; Dalavanga, Y. A.; Cianti, R.; Bianchi, L.; Manda-Stachouli, C.; Armini, A.; Koukkou, A.-I.; Rottoli, P.; Constantopoulos, S. H.; Bini, L. J. J. o. P. R., Proteome analysis of bronchoalveolar lavage in individuals from Metsovo, nonoccupationally exposed to asbestos. **2009**, 8 (2), 860-869.
211. Wang, S.; Chen, J.-z.; Zhang, Z.; Huang, Q.; Gu, S.; Ying, K.; Xie, Y.; Mao, Y. J. B.; communications, b. r., Cloning, characterization, and expression of calcyphosine 2, a novel human gene encoding an EF-hand Ca²⁺-binding protein. **2002**, 291 (2), 414-420.
212. Kuburich, N. A.; den Hollander, P.; Pietz, J. T.; Mani, S. A. In *Vimentin and cytokeratin: Good alone, bad together*, Seminars in cancer biology, Elsevier: 2022; pp 816-826.

213. Kueper, T.; Grune, T.; Prah, S.; Lenz, H.; Welge, V.; Biernoth, T.; Vogt, Y.; Muhr, G. M.; Gaemlich, A.; Jung, T.; Boemke, G.; Elsasser, H. P.; Wittern, K. P.; Wenck, H.; Stab, F.; Blatt, T., Vimentin is the specific target in skin glycation. Structural prerequisites, functional consequences, and role in skin aging. *J Biol Chem* **2007**, *282* (32), 23427-36.
214. Ahmed, E. K.; Rogowska-Wrzesinska, A.; Roepstorff, P.; Bulteau, A. L.; Friguet, B., Protein modification and replicative senescence of WI-38 human embryonic fibroblasts. *Aging Cell* **2010**, *9* (2), 252-72.
215. Bignami, A.; Raju, T.; Dahl, D. J. D. b., Localization of vimentin, the nonspecific intermediate filament protein, in embryonal glia and in early differentiating neurons: *In vivo* and *in vitro* immunofluorescence study of the rat embryo with vimentin and neurofilament antisera. **1982**, *91* (2), 286-295.
216. Yen, S.; Gaskin, F.; Fu, S. J. T. A. j. o. p., Neurofibrillary tangles in senile dementia of the Alzheimer type share an antigenic determinant with intermediate filaments of the vimentin class. **1983**, *113* (3), 373.
217. Levin, E. C.; Acharya, N. K.; Sedeyn, J. C.; Venkataraman, V.; D'Andrea, M. R.; Wang, H.-Y.; Nagele, R. G., Neuronal expression of vimentin in the Alzheimer's disease brain may be part of a generalized dendritic damage-response mechanism. *Brain research* **2009**, *1298*, 194-207.
218. Ruangjaroon, T.; Chokchaichamnankit, D.; Srisomsap, C.; Svasti, J.; Paricharttanakul, N. M., Involvement of vimentin in neurite outgrowth damage induced by fipronil in SH-SY5Y cells. *Biochemical and Biophysical Research Communications* **2017**, *486* (3), 652-658.
219. Krautwald, M.; Münch, G., Advanced glycation end products as biomarkers and gerontotoxins – A basis to explore methylglyoxal-lowering agents for Alzheimer's disease? *Experimental Gerontology* **2010**, *45* (10), 744-751.
220. Munoz-Lasso, D. C.; Roma-Mateo, C.; Pallardo, F. V.; Gonzalez-Cabo, P., Much More Than a Scaffold: Cytoskeletal Proteins in Neurological Disorders. *Cells* **2020**, *9* (2).
221. Ravi, S.; Johnson, M. S.; Chacko, B. K.; Kramer, P. A.; Sawada, H.; Locy, M. L.; Wilson, L. S.; Barnes, S.; Marques, M. B.; Darley-Usmar, V. M., Modification of platelet proteins by 4-hydroxynonenal: Potential Mechanisms for inhibition of aggregation and metabolism. *Free Radic Biol Med* **2016**, *91*, 143-53.
222. Geib, T.; Iacob, C.; Jribi, R.; Fernandes, J.; Benderdour, M.; Sleno, L., Identification of 4-hydroxynonenal-modified proteins in human osteoarthritic chondrocytes. *J Proteomics* **2021**, *232*, 104024.
223. Mello, C. F.; Sultana, R.; Piroddi, M.; Cai, J.; Pierce, W. M.; Klein, J. B.; Butterfield, D. A., Acrolein induces selective protein carbonylation in synaptosomes. *Neuroscience* **2007**, *147* (3), 674-679.
224. Klingler-Hoffmann, M.; Mittal, P.; Hoffmann, P. J. P., The emerging role of cytoskeletal proteins as reliable biomarkers. **2019**, *19* (21-22), 1800483.
225. Wilson, C.; González-Billault, C., Regulation of cytoskeletal dynamics by redox signaling and oxidative stress: implications for neuronal development and trafficking. *Frontiers in cellular neuroscience* **2015**, *9*, 381.
226. Gardiner, J.; Overall, R.; Marc, J., The Nervous System Cytoskeleton under Oxidative Stress. *Diseases* **2013**, *1* (1), 36-50.
227. Dalle-Donne, I.; Giustarini, D.; Rossi, R.; Colombo, R.; Milzani, A., Reversible S-glutathionylation of Cys374 regulates actin filament formation by inducing structural changes in the actin molecule. *Free Radical Biology and Medicine* **2003**, *34* (1), 23-32.
228. Munnamalai, V.; Suter, D. M., Reactive oxygen species regulate F-actin dynamics in neuronal growth cones and neurite outgrowth. *Journal of neurochemistry* **2009**, *108* (3), 644-661.

229. Munnamalai, V.; Weaver, C. J.; Weisheit, C. E.; Venkatraman, P.; Agim, Z. S.; Quinn, M. T.; Suter, D. M., Bidirectional interactions between NOX 2-type NADPH oxidase and the F-actin cytoskeleton in neuronal growth cones. *Journal of neurochemistry* **2014**, *130* (4), 526-540.
230. Farah, M. E.; Sirotkin, V.; Haarer, B.; Kakhniashvili, D.; Amberg, D. C., Diverse protective roles of the actin cytoskeleton during oxidative stress. *Cytoskeleton* **2011**, *68* (6), 340-354.
231. Tempes, A.; Weslawski, J.; Brzozowska, A.; Jaworski, J., Role of dynein-dynactin complex, kinesins, motor adaptors, and their phosphorylation in dendritogenesis. *J Neurochem* **2020**, *155* (1), 10-28.
232. Rehman, M. U.; Sehar, N.; Dar, N. J.; Khan, A.; Arafah, A.; Rashid, S.; Rashid, S. M.; Ganaie, M. A., Mitochondrial dysfunctions, oxidative stress and neuroinflammation as therapeutic targets for neurodegenerative diseases: An update on current advances and impediments. *Neurosci Biobehav Rev*. **2023**, *144*, 104961.
233. Jurcau, A., Insights into the pathogenesis of neurodegenerative diseases: Focus on mitochondrial dysfunction and oxidative stress. *Int J Mol Sci*. **2021**, *22* (21), 11847.
234. Gandhi, J.; Antonelli, A. C.; Afridi, A.; Vatsia, S.; Joshi, G.; Romanov, V.; Murray, I. V.; Khan, S. A., Protein misfolding and aggregation in neurodegenerative diseases: a review of pathogeneses, novel detection strategies, and potential therapeutics. *Rev Neurosci*. **2019**, *30* (4), 339-358.
235. Niranjana, R., Recent advances in the mechanisms of neuroinflammation and their roles in neurodegeneration. *Neurochem Int*. **2018**, *120*, 13-20.
236. Chellan, P.; Nagaraj, R. H., Protein crosslinking by the Maillard reaction: dicarbonyl-derived imidazolium crosslinks in aging and diabetes. *Arch Biochem Biophys*. **1999**, *368* (1), 98-104.
237. Sirangelo, I.; Iannuzzi, C., Understanding the role of protein glycation in the amyloid aggregation process. *Int J Mol Sci*. **2021**, *22* (12), 6609.
238. Srikanth, V.; Maczurek, A.; Phan, T.; Steele, M.; Westcott, B.; Juskiw, D.; Munch, G., Advanced glycation endproducts and their receptor RAGE in Alzheimer's disease. *Neurobiol Aging* **2011**, *32* (5), 763-77.
239. Beeri, M. S.; Moshier, E.; Schmeidler, J.; Godbold, J.; Uribarri, J.; Reddy, S.; Sano, M.; Grossman, H. T.; Cai, W.; Vlassara, H., Serum concentration of an inflammatory glycotoxin, methylglyoxal, is associated with increased cognitive decline in elderly individuals. *Mech Ageing Dev* **2011**, *132* (11-12), 583-587.
240. Kuhla, B.; Luth, H. J.; Haferburg, D.; Boeck, K.; Arendt, T.; Munch, G., Methylglyoxal, glyoxal, and their detoxification in Alzheimer's disease. *Ann N Y Acad Sci* **2005**, *1043*, 211-6.
241. Ahmed, N.; Ahmed, U.; Thornalley, P. J.; Hager, K.; Fleischer, G.; Münch, G., Protein glycation, oxidation and nitration adduct residues and free adducts of cerebrospinal fluid in Alzheimer's disease and link to cognitive impairment. *J Neurochem* **2005**, *92* (2), 255-263.
242. Pucci, M.; Aria, F.; Premoli, M.; Maccarinelli, G.; Mastinu, A.; Bonini, S.; Memo, M.; Uberti, D.; Abate, G., Methylglyoxal affects cognitive behaviour and modulates RAGE and Presenilin-1 expression in hippocampus of aged mice. *Food Chem Toxicol*. **2021**, *158*, 112608.
243. Wei, C.-C.; Li, S.-W.; Wu, C.-T.; How, C. M.; Pan, M.-H., Dietary methylglyoxal exposure induces Alzheimer's disease by promoting amyloid β accumulation and disrupting autophagy in *Caenorhabditis elegans*. *J Agric Food Chem*. **2022**, *70* (32), 10011-10021.
244. Wang, Y.-H.; Yu, H.-T.; Pu, X.-P.; Du, G.-H., Myricitrin alleviates methylglyoxal-induced mitochondrial dysfunction and AGEs/RAGE/NF- κ B pathway activation in SH-SY5Y cells. *J Mol Neurosci* **2014**, *53*, 562-570.

245. Suantawee, T.; Cheng, H.; Adisakwattana, S., Protective effect of cyanidin against glucose- and methylglyoxal-induced protein glycation and oxidative DNA damage. *Int J Biol Macromol* **2016**, *93* (Pt A), 814-821.
246. Li, G.; Chang, M.; Jiang, H.; Xie, H.; Dong, Z.; Hu, L., Proteomics analysis of methylglyoxal-induced neurotoxic effects in SH-SY5Y cells. *Cell Biochem Funct* **2011**, *29* (1), 30-5.
247. Rabilloud, T.; Chevallet, M.; Luche, S.; Lelong, C., Two-dimensional gel electrophoresis in proteomics: Past, present and future. *J Proteomics*. **2010**, *73* (11), 2064-2077.
248. Neilson, K. A.; Ali, N. A.; Muralidharan, S.; Mirzaei, M.; Mariani, M.; Assadourian, G.; Lee, A.; Van Sluyter, S. C.; Haynes, P. A., Less label, more free: approaches in label-free quantitative mass spectrometry. *Proteomics* **2011**, *11* (4), 535-553.
249. Zheng, L.; Boeren, S.; Liu, C.; Bakker, W.; Wang, H.; Rietjens, I.; Saccenti, E., Proteomics-based identification of biomarkers reflecting endogenous and exogenous exposure to the advanced glycation end product precursor methylglyoxal in SH-SY5Y human neuroblastoma cells. *Int J Biol Macromol* **2024**, 132859.
250. Arakawa, S.; Suzuki, R.; Kurosaka, D.; Ikeda, R.; Hayashi, H.; Kayama, T.; Ohno, R.-i.; Nagai, R.; Marumo, K.; Saito, M., Mass spectrometric quantitation of AGEs and enzymatic crosslinks in human cancellous bone. *Sci Rep* **2020**, *10* (1), 18774.
251. Pang, Z.; Lu, Y.; Zhou, G.; Hui, F.; Xu, L.; Viau, C.; Spigelman, A. F.; MacDonald, P. E.; Wishart, D. S.; Li, S., MetaboAnalyst 6.0: towards a unified platform for metabolomics data processing, analysis and interpretation. *Nucleic Acids Res.* **2024**, gkae253.
252. Team, R. C., R: A language and environment for statistical computing. R Foundation for Statistical Computing. (*No Title*) **2013**.
253. Tyanova, S.; Temu, T.; Sinitcyn, P.; Carlson, A.; Hein, M. Y.; Geiger, T.; Mann, M.; Cox, J., The Perseus computational platform for comprehensive analysis of (prote) omics data. *Nat Methods*. **2016**, *13* (9), 731-740.
254. Bader, G. D.; Hogue, C. W., An automated method for finding molecular complexes in large protein interaction networks. *BMC bioinformatics* **2003**, *4*, 1-27.
255. Shannon, P.; Markiel, A.; Ozier, O.; Baliga, N. S.; Wang, J. T.; Ramage, D.; Amin, N.; Schwikowski, B.; Ideker, T., Cytoscape: a software environment for integrated models of biomolecular interaction networks. *Genome Res.* **2003**, *13* (11), 2498-2504.
256. Chin, C.-H.; Chen, S.-H.; Wu, H.-H.; Ho, C.-W.; Ko, M.-T.; Lin, C.-Y., cytoHubba: identifying hub objects and sub-networks from complex interactome. *BMC Syst Biol.* **2014**, *8*, 1-7.
257. Vulesevic, B.; McNeill, B.; Giacco, F.; Maeda, K.; Blackburn, N. J. R.; Brownlee, M.; Milne, R. W.; Suuronen, E. J., Methylglyoxal-induced endothelial cell loss and inflammation contribute to the development of diabetic cardiomyopathy. *Diabetes* **2016**, *65* (6), 1699-1713.
258. Arakawa, S.; Suzuki, R.; Kurosaka, D.; Ikeda, R.; Hayashi, H.; Kayama, T.; Ohno, R.-i.; Nagai, R.; Marumo, K.; Saito, M., Mass spectrometric quantitation of AGEs and enzymatic crosslinks in human cancellous bone. *Sci Rep.* **2020**, *10* (1), 18774.
259. Ghemrawi, R.; Khair, M., Endoplasmic reticulum stress and unfolded protein response in neurodegenerative diseases. *Int J Mol Sci.* **2020**, *21* (17), 6127.
260. Duncan, E. J.; Cheetham, M. E.; Chapple, J. P.; van der Spuy, J., The role of HSP70 and its co-chaperones in protein misfolding, aggregation and disease. *Subcell Biochem.* **2015**, 243-273.

261. Victor, P.; Sarada, D.; Ramkumar, K. M., Crosstalk between endoplasmic reticulum stress and oxidative stress: Focus on protein disulfide isomerase and endoplasmic reticulum oxidase 1. *Eur J Pharmacol.* **2021**, *892*, 173749.
262. Rabbani, N.; Xue, M.; Thornalley, P. J., Dicarbonyl stress, protein glycation and the unfolded protein response. *Glycoconj J* **2021**, *38* (3), 331-340.
263. Hetz, C.; Saxena, S., ER stress and the unfolded protein response in neurodegeneration. *Nat Rev Neurol* **2017**, *13* (8), 477-491.
264. Bachir, A. I.; Horwitz, A. R.; Nelson, W. J.; Bianchini, J. M., Actin-based adhesion modules mediate cell interactions with the extracellular matrix and neighboring cells. *Cold Spring Harbor Perspectives in Biology* **2017**, *9* (7), a023234.
265. Hynes, R. O., Integrins: bidirectional, allosteric signaling machines. *cell* **2002**, *110* (6), 673-687.
266. Lilja, J.; Ivaska, J., Integrin activity in neuronal connectivity. *J Cell Sci* **2018**, *131* (12), jcs212803.
267. Soles, A.; Selimovic, A.; Sbrocco, K.; Ghannoum, F.; Hamel, K.; Moncada, E. L.; Gilliat, S.; Cvetanovic, M., Extracellular Matrix Regulation in Physiology and in Brain Disease. *Int J Mol Sci* **2023**, *24* (8).
268. Cronin, N. M.; DeMali, K. A., Dynamics of the actin cytoskeleton at adhesion complexes. *Biology* **2021**, *11* (1), 52.
269. Todoriki, S.; Hosoda, Y.; Yamamoto, T.; Watanabe, M.; Sekimoto, A.; Sato, H.; Mori, T.; Miyazaki, M.; Takahashi, N.; Sato, E., Methylglyoxal Induces Inflammation, Metabolic Modulation and Oxidative Stress in Myoblast Cells. *Toxins (Basel)* **2022**, *14* (4).
270. Komanetsky, S. M.; Hedrick, V.; Sobreira, T.; Aryal, U. K.; Kim, S. Q.; Kim, K. H., Proteomic identification of aerobic glycolysis as a potential metabolic target for methylglyoxal in adipocytes. *Nutr Res* **2020**, *80*, 66-77.
271. Lu, S. C., Glutathione synthesis. *Biochim Biophys Acta.* **2013**, *1830* (5), 3143-3153.
272. Dimski, D. S., Ammonia metabolism and the urea cycle: function and clinical implications. *J Vet Intern Med.* **1994**, *8* (2), 73-78.
273. Scheijen, J. L.; Schalkwijk, C. G., Quantification of glyoxal, methylglyoxal and 3-deoxyglucosone in blood and plasma by ultra performance liquid chromatography tandem mass spectrometry: evaluation of blood specimen. *Clin Chem Lab Med* **2014**, *52* (1), 85-91.
274. Rabbani, N.; Thornalley, P. J., Measurement of methylglyoxal by stable isotopic dilution analysis LC-MS/MS with corroborative prediction in physiological samples. *Nat Protoc* **2014**, *9* (8), 1969-79.
275. Nemet, I.; Varga-Defterdarovic, L.; Turk, Z., Preparation and quantification of methylglyoxal in human plasma using reverse-phase high-performance liquid chromatography. *Clin Biochem* **2004**, *37* (10), 875-81.
276. Haddad, M.; Perrotte, M.; Khedher, M. R. B.; Demongin, C.; Lepage, A.; Fülöp, T.; Ramassamy, C., Methylglyoxal and glyoxal as potential peripheral markers for MCI diagnosis and their effects on the expression of neurotrophic, inflammatory and neurodegenerative factors in neurons and in neuronal derived-extracellular vesicles. *International Journal of Molecular Sciences* **2019**, *20* (19), 4906.
277. Suh, K. S.; Chon, S.; Jung, W. W.; Choi, E. M., Protective effects of sciadopitysin against methylglyoxal-induced degeneration in neuronal SK-N-MC cells. *Journal of Applied Toxicology* **2022**, *42* (2), 274-284.
278. de Almeida, G. R. L.; Szczepanik, J. C.; Selhorst, I.; Cunha, M. P.; Dafre, A. L., The expanding impact of methylglyoxal on behavior-related disorders. *Prog Neuropsychopharmacol Biol Psychiatry* **2023**, *120*, 110635.

279. Manza, P.; Wiers, C. E.; Shokri-Kojori, E.; Kroll, D.; Feldman, D.; Schwandt, M.; Wang, G.-J.; Tomasi, D.; Volkow, N. D., Brain network segregation and glucose energy utilization: relevance for age-related differences in cognitive function. *Cerebral Cortex* **2020**, *30* (11), 5930-5942.
280. Dringen, R., Metabolism and functions of glutathione in brain. *Progress in neurobiology* **2000**, *62* (6), 649-671.
281. Bélanger, M.; Yang, J.; Petit, J.-M.; Laroche, T.; Magistretti, P. J.; Allaman, I., Role of the glyoxalase system in astrocyte-mediated neuroprotection. *Journal of Neuroscience* **2011**, *31* (50), 18338-18352.
282. Thornalley, P. J., Protein and nucleotide damage by glyoxal and methylglyoxal in physiological systems-role in ageing and disease. *Drug metabolism and drug interactions* **2008**, *23* (1-2), 125-150.
283. Gasic-Milenkovic, J.; Loske, C.; Münch, G., Advanced glycation endproducts cause lipid peroxidation in the human neuronal cell line SH-SY5Y. *Journal of Alzheimer's Disease* **2003**, *5* (1), 25-30.
284. Pischetsrieder, M.; Seidel, W.; Münch, G.; Schinzel, R., N2-(1-Carboxyethyl) deoxyguanosine, a nonenzymatic glycation adduct of DNA, induces single-strand breaks and increases mutation frequencies. *Biochemical and biophysical research communications* **1999**, *264* (2), 544-549.
285. Murata-Kamiya, N.; Kamiya, H.; Kaji, H.; Kasai, H., Methylglyoxal induces G: C to C: G and G: C to T: A transversions in the supF gene on a shuttle vector plasmid replicated in mammalian cells. *Mutation Research/Genetic Toxicology and Environmental Mutagenesis* **2000**, *468* (2), 173-182.
286. Hall, C.; Lueshen, E.; Linninger, A. A., Interspecies scaling in pharmacokinetics: A novel whole-body physiologically based modeling framework to discover drug biodistribution mechanisms *in vivo*. *Journal of pharmaceutical sciences* **2012**, *101* (3), 1221-1241.
287. Brown, R. P.; Delp, M. D.; Lindstedt, S. L.; Rhomberg, L. R.; Beliles, R. P., Physiological parameter values for physiologically based pharmacokinetic models. *Toxicology and industrial health* **1997**, *13* (4), 407-484.
288. Li, X.; Bakker, W.; Sang, Y.; Rietjens, I. M. C. M., Absorption and intracellular accumulation of food-borne dicarbonyl precursors of advanced glycation end-product in a Caco-2 human cell transwell model. *Food Chemistry* **2024**, *452*, 139532.
289. Sun, D.; Lennernas, H.; Welage, L. S.; Barnett, J. L.; Landowski, C. P.; Foster, D.; Fleisher, D.; Lee, K. D.; Amidon, G. L., Comparison of human duodenum and Caco-2 gene expression profiles for 12,000 gene sequences tags and correlation with permeability of 26 drugs. *Pharm Res* **2002**, *19* (10), 1400-16.
290. Fagerholm, U.; Johansson, M.; Lennernas, H., Comparison Between Permeability Coefficients in Rat and Human Jejunum. *Pharmaceutical Research* **1996**, *13* (9), 1336-1342.
291. Rodgers, T.; Rowland, M., Physiologically based pharmacokinetic modelling 2: predicting the tissue distribution of acids, very weak bases, neutrals and zwitterions. *Journal of pharmaceutical sciences* **2006**, *95* (6), 1238-1257.
292. Punt, A.; Pinckaers, N.; Peijnenburg, A.; Louisse, J., Development of a web-based toolbox to support quantitative in-vitro-to-in-vivo extrapolations (QIVIVE) within nonanimal testing strategies. *Chemical Research in Toxicology* **2020**, *34* (2), 460-472.
293. Xue, M.; Rabbani, N.; Thornalley, P. J., Glyoxalase in ageing. *Seminars in Cell & Developmental Biology* **2011**, *22* (3), 293-301.
294. Evans, M. V.; Andersen, M. E., Sensitivity analysis of a physiological model for 2, 3, 7, 8-tetrachlorodibenzo-p-dioxin (TCDD): assessing the impact of specific model parameters on sequestration in liver and fat in the rat. *Toxicological sciences* **2000**, *54* (1), 71-80.

295. van Tongeren, T. C.; Moxon, T. E.; Dent, M. P.; Li, H.; Carmichael, P. L.; Rietjens, I. M., Next generation risk assessment of human exposure to anti-androgens using newly defined comparator compound values. *Toxicology in Vitro* **2021**, *73*, 105132.
296. Liu, C.; van Mil, J.; Noorlander, A.; Rietjens, I., Use of Physiologically Based Kinetic Modeling-Based Reverse Dosimetry to Predict *In vivo* Nrf2 Activation by EGCG and Its Colonic Metabolites in Humans. *J Agric Food Chem* **2022**, *70* (43), 14015-14031.
297. Mathew, J.; Sankar, P.; Varacallo, M., *Physiology, Blood Plasma*. StatPearls Publishing, Treasure Island (FL): 2023.
298. Yuan, C.; Mo, Y.; Yang, J.; Zhang, M.; Xie, X., Influences of advanced glycosylation end products on the inner blood–retinal barrier in a co-culture cell model *in vitro*. *Open Life Sciences* **2020**, *15* (1), 619-628.
299. Mazza, M. C.; Shuck, S. C.; Lin, J.; Moxley, M. A.; Termini, J.; Cookson, M. R.; Wilson, M. A., DJ-1 is not a deglycase and makes a modest contribution to cellular defense against methylglyoxal damage in neurons. *Journal of neurochemistry* **2022**, *162* (3), 245-261.
300. Chain, E. P. o. C. i. t. F., Scientific opinion on acrylamide in food. *Efsa Journal* **2015**, *13* (6), 4104.
301. A Shamsaldeen, Y.; S Mackenzie, L.; A Lione, L.; D Benham, C., Methylglyoxal, a metabolite increased in diabetes is associated with insulin resistance, vascular dysfunction and neuropathies. *Current drug metabolism* **2016**, *17* (4), 359-367.
302. Vigneri, P.; Frasca, F.; Sciacca, L.; Pandini, G.; Vigneri, R., Diabetes and cancer. *Endocrine-related cancer* **2009**, *16* (4), 1103-1123.
303. Organization, W. H., Concise International Chemical Assessment Document 57 GLYOXAL. 2004.
304. Roth, W. L.; Freeman, R. A.; Wilson, A. G., A physiologically based model for gastrointestinal absorption and excretion of chemicals carried by lipids. *Risk Analysis* **1993**, *13* (5), 531-543.
305. Crowell, S. R.; Amin, S. G.; Anderson, K. A.; Krishnegowda, G.; Sharma, A. K.; Soelberg, J. J.; Williams, D. E.; Corley, R. A., Preliminary physiologically based pharmacokinetic models for benzo [a] pyrene and dibenzo [def, p] chrysene in rodents. *Toxicology and applied pharmacology* **2011**, *257* (3), 365-376.
306. Mendez-Catala, D. M.; Wang, Q.; Rietjens, I. M., PBK Model-Based Prediction of Intestinal Microbial and Host Metabolism of Zearalenone and Consequences for its Estrogenicity. *Molecular Nutrition & Food Research* **2021**, *65* (23), 2100443.
307. Stadler, R. H.; Gökmen, V., Acrylamide formation mechanisms. In *Acrylamide in food*, Elsevier: 2024; pp 1-17.
308. Jang, H. W.; Jiang, Y.; Hengel, M.; Shibamoto, T., Formation of 4 (5)-methylimidazole and its precursors, α -dicarbonyl compounds, in Maillard model systems. *Journal of agricultural and food chemistry* **2013**, *61* (28), 6865-6872.
309. Ou, J.; Wang, M.; Zheng, J.; Ou, S., Positive and negative effects of polyphenol incorporation in baked foods. *Food chemistry* **2019**, *284*, 90-99.
310. Zhou, Q.; Cheng, K.-W.; Xiao, J.; Wang, M., The multifunctional roles of flavonoids against the formation of advanced glycation end products (AGEs) and AGEs-induced harmful effects. *Trends in Food Science & Technology* **2020**, *103*, 333-347.
311. Smit, A. J.; Lutgers, H. L., The clinical relevance of advanced glycation endproducts (AGE) and recent developments in pharmaceuticals to reduce AGE accumulation. *Current medicinal chemistry* **2004**, *11* (20), 2767-2784.

312. Lotito, S. B.; Frei, B., Consumption of flavonoid-rich foods and increased plasma antioxidant capacity in humans: cause, consequence, or epiphenomenon? *Free Radical Biology and Medicine* **2006**, *41* (12), 1727-1746.
313. Wang, Y.; Ho, C.-T., Metabolism of flavonoids. In *Food Factors for Health Promotion*, Karger Publishers: 2009; Vol. 61, pp 64-74.
314. Zhang, M.; Ge, T.; Huang, W.; He, J.; Huang, C.; Ou, J.; Ou, S.; Zheng, J., Formation of Hesperetin-Methylglyoxal Adducts in Food and *In vivo*, and Their Metabolism *In vivo* and Potential Health Impacts. *Journal of Agricultural and Food Chemistry* **2024**, *72* (19), 11174-11184.
315. Zhu, X.; Cheng, Y.-q.; Lu, Q.; Du, L.; Yin, X.-x.; Liu, Y.-w., Enhancement of glyoxalase 1, a polyfunctional defense enzyme, by quercetin in the brain in streptozotocin-induced diabetic rats. *Naunyn-Schmiedeberg's Archives of Pharmacology* **2018**, *391*, 1237-1245.
316. Lee-Hilz, Y. Y.; Stolaki, M.; van Berkel, W. J. H.; Aarts, J. M.; Rietjens, I. M. C. M., Activation of EpRE-mediated gene transcription by quercetin glucuronides depends on their deconjugation. *Food and Chemical Toxicology* **2008**, *46* (6), 2128-2134.
317. Li, Y.; Peng, Y.; Shen, Y.; Zhang, Y.; Liu, L.; Yang, X., Dietary polyphenols: Regulate the advanced glycation end products-RAGE axis and the microbiota-gut-brain axis to prevent neurodegenerative diseases. *Critical Reviews in Food Science and Nutrition* **2023**, *63* (29), 9816-9842.
318. Kumar Singh, A.; Cabral, C.; Kumar, R.; Ganguly, R.; Kumar Rana, H.; Gupta, A.; Rosaria Lauro, M.; Carbone, C.; Reis, F.; Pandey, A. K., Beneficial effects of dietary polyphenols on gut microbiota and strategies to improve delivery efficiency. *Nutrients* **2019**, *11* (9), 2216.
319. Thilakarathna, S. H.; Rupasinghe, H. P. V., Flavonoid bioavailability and attempts for bioavailability enhancement. *Nutrients* **2013**, *5* (9), 3367-3387.
320. Peng, Y.; Chu, S.; Yang, Y.; Zhang, Z.; Pang, Z.; Chen, N., Neuroinflammatory *in vitro* cell culture models and the potential applications for neurological disorders. *Frontiers in Pharmacology* **2021**, *12*, 671734.
321. Chi, H.; Chang, H.-Y.; Sang, T.-K., Neuronal cell death mechanisms in major neurodegenerative diseases. *International journal of molecular sciences* **2018**, *19* (10), 3082.
322. Di Loreto, S.; Zimmitti, V.; Sebastiani, P.; Cervelli, C.; Falone, S.; Amicarelli, F., Methylglyoxal causes strong weakening of detoxifying capacity and apoptotic cell death in rat hippocampal neurons. *The international journal of biochemistry & cell biology* **2008**, *40* (2), 245-257.
323. Jiang, B.; Le, L.; Pan, H.; Hu, K.; Xu, L.; Xiao, P., Dihydromyricetin ameliorates the oxidative stress response induced by methylglyoxal via the AMPK/GLUT4 signaling pathway in PC12 cells. *Brain research bulletin* **2014**, *109*, 117-126.
324. Huang, S. M.; Chuang, H. C.; Wu, C. H.; Yen, G. C., Cytoprotective effects of phenolic acids on methylglyoxal-induced apoptosis in Neuro-2A cells. *Molecular nutrition & food research* **2008**, *52* (8), 940-949.
325. Koike, S.; Nishimoto, S.; Ogasawara, Y., Cysteine persulfides and polysulfides produced by exchange reactions with H₂S protect SH-SY5Y cells from methylglyoxal-induced toxicity through Nrf2 activation. *Redox Biol* **2017**, *12*, 530-539.
326. Thornalley, P. J.; Rabbani, N. In *Glyoxalase in tumourigenesis and multidrug resistance*, 2011; Elsevier: pp 318-325.
327. Williams, W. M.; Weinberg, A.; Smith, M. A., Protein modification by dicarbonyl molecular species in neurodegenerative diseases. *Journal of Amino Acids* **2011**, *2011* (1), 461216.

328. Berends, E.; van Oostenbrugge, R. J.; Foulquier, S.; Schalkwijk, C. G., Methylglyoxal, a highly reactive dicarbonyl compound, as a threat for blood brain barrier integrity. *Fluids and Barriers of the CNS* **2023**, *20* (1), 75.
329. Wang, J.; Lin, J.; Schlotterer, A.; Wu, L.; Fleming, T.; Busch, S.; Dietrich, N.; Hammes, H.-P., CD74 indicates microglial activation in experimental diabetic retinopathy and exogenous methylglyoxal mimics the response in normoglycemic retina. *Acta diabetologica* **2014**, *51*, 813-821.
330. Schlotterer, A.; Kolibabka, M.; Lin, J.; Acunman, K.; Dietrich, N.; Sticht, C.; Fleming, T.; Nawroth, P.; Hammes, H.-P., Methylglyoxal induces retinopathy-type lesions in the absence of hyperglycemia: studies in a rat model. *The FASEB Journal* **2019**, *33* (3), 4141-4153.
331. Byun, K.; Bayarsaikhan, E.; Kim, D.; Kim, C. Y.; Mook-Jung, I.; Paek, S. H.; Kim, S. U.; Yamamoto, T.; Won, M.-H.; Song, B.-J., Induction of neuronal death by microglial AGE-albumin: implications for Alzheimer's disease. *PloS one* **2012**, *7* (5), e37917.
332. Byun, K.; Bayarsaikhan, E.; Kim, D.; Son, M.; Hong, J.; Jeong, G.-B.; Paek, S. H.; Won, M.-H.; Lee, B., Activated microglial cells synthesize and secrete AGE-albumin. *Anatomy & cell biology* **2012**, *45* (1), 47-52.
333. De Simone, U.; Caloni, F.; Gribaldo, L.; Coccini, T., Human co-culture model of neurons and astrocytes to test acute cytotoxicity of neurotoxic compounds. *International journal of toxicology* **2017**, *36* (6), 463-477.
334. Li, H.; Gao, A.; Feng, D.; Wang, Y.; Zhang, L.; Cui, Y.; Li, B.; Wang, Z.; Chen, G., Evaluation of the protective potential of brain microvascular endothelial cell autophagy on blood-brain barrier integrity during experimental cerebral ischemia-reperfusion injury. *Translational stroke research* **2014**, *5*, 618-626.
335. Fang, L.; Li, X.; Zhong, Y.; Yu, J.; Yu, L.; Dai, H.; Yan, M., Autophagy protects human brain microvascular endothelial cells against methylglyoxal-induced injuries, reproducible in a cerebral ischemic model in diabetic rats. *Journal of neurochemistry* **2015**, *135* (2), 431-440.
336. Lv, Q.; Gu, C.; Chen, C., Venlafaxine protects methylglyoxal-induced apoptosis in the cultured human brain microvascular endothelial cells. *Neuroscience Letters* **2014**, *569*, 99-103.
337. Tóth, A. E.; Walter, F. R.; Bocsik, A.; Sántha, P.; Veszeka, S.; Nagy, L.; Puskás, L. G.; Couraud, P.-O.; Takata, F.; Dohgu, S., Edaravone protects against methylglyoxal-induced barrier damage in human brain endothelial cells. *PloS one* **2014**, *9* (7), e100152.
338. Tóth, A. E.; Tóth, A.; Walter, F. R.; Kiss, L.; Veszeka, S.; Ózsvári, B.; Puskás, L. G.; Heimesaat, M. M.; Dohgu, S.; Kataoka, Y., Compounds blocking methylglyoxal-induced protein modification and brain endothelial injury. *Archives of medical research* **2014**, *45* (8), 753-764.
339. Chrysanthou, M.; Miro Estruch, I.; Rietjens, I. M. C. M.; Wichers, H. J.; Hoppenbrouwers, T., *In vitro* methodologies to study the role of advanced glycation end products (AGEs) in neurodegeneration. *Nutrients* **2022**, *14* (2), 363.
340. Yang, W.; Yu, M.; Fu, J.; Bao, W.; Wang, D.; Hao, L.; Yao, P.; Nüssler, A. K.; Yan, H.; Liu, L., Deoxynivalenol induced oxidative stress and genotoxicity in human peripheral blood lymphocytes. *Food and Chemical Toxicology* **2014**, *64*, 383-396.
341. Yuan, W.; Wang, J.; Zhang, Y.; Lu, H., Sample preparation approaches for qualitative and quantitative analysis of lipid-derived electrophile modified proteomes by mass spectrometry. *Molecular Omics* **2020**, *16* (6), 511-520.

342. Bierhaus, A.; Fleming, T.; Stoyanov, S.; Leffler, A.; Babes, A.; Neacsu, C.; Sauer, S. K.; Eberhardt, M.; Schnölzer, M.; Lasitschka, F., Methylglyoxal modification of Nav1.8 facilitates nociceptive neuron firing and causes hyperalgesia in diabetic neuropathy. *Nature medicine* **2012**, *18* (6), 926-933.
343. Liebler, D. C., Protein damage by reactive electrophiles: targets and consequences. *Chemical research in toxicology* **2008**, *21* (1), 117-128.
344. Jacobs, A. T.; Marnett, L. J., Systems analysis of protein modification and cellular responses induced by electrophile stress. *Accounts of chemical research* **2010**, *43* (5), 673-683.
345. Ullery, J. C.; Marnett, L. J., Protein modification by oxidized phospholipids and hydrolytically released lipid electrophiles: Investigating cellular responses. *Biochimica et Biophysica Acta (BBA)-Biomembranes* **2012**, *1818* (10), 2424-2435.
346. Kumagai, Y.; Akiyama, M.; Unoki, T., Adaptive responses to electrophilic stress and reactive sulfur species as their regulator molecules. *Toxicological Research* **2019**, *35*, 303-310.
347. Itoh, K.; Tong, K. I.; Yamamoto, M., Molecular mechanism activating Nrf2-Keap1 pathway in regulation of adaptive response to electrophiles. *Free Radical Biology and Medicine* **2004**, *36* (10), 1208-1213.
348. Liao, Y.; Wang, J.; Jaehnig, E. J.; Shi, Z.; Zhang, B., WebGestalt 2019: gene set analysis toolkit with revamped UIs and APIs. *Nucleic acids research* **2019**, *47* (W1), W199-W205.
349. Salomonis, N.; Hanspers, K.; Zambon, A. C.; Vranizan, K.; Lawlor, S. C.; Dahlquist, K. D.; Doniger, S. W.; Stuart, J.; Conklin, B. R.; Pico, A. R., GenMAPP 2: new features and resources for pathway analysis. *BMC bioinformatics* **2007**, *8*, 1-12.
350. Sibbersen, C.; Palmfeldt, J.; Hansen, J.; Gregersen, N.; Jørgensen, K. A.; Johannsen, M., Development of a chemical probe for identifying protein targets of α -oxoaldehydes. *Chemical Communications* **2013**, *49* (38), 4012-4014.
351. Sibbersen, C.; Schou Oxvig, A. M.; Bisgaard Olesen, S.; Nielsen, C. B.; Galligan, J. J.; Jorgensen, K. A.; Palmfeldt, J.; Johannsen, M., Profiling of Methylglyoxal Blood Metabolism and Advanced Glycation End-Product Proteome Using a Chemical Probe. *ACS Chem Biol* **2018**, *13* (12), 3294-3305.
352. Camarillo, J. M.; Ullery, J. C.; Rose, K. L.; Marnett, L. J., Electrophilic modification of PKM2 by 4-hydroxynonenal and 4-oxononenal results in protein cross-linking and kinase inhibition. *Chemical research in toxicology* **2017**, *30* (2), 635-641.
353. Chan, C. M.; Huang, D. Y.; Huang, Y. P.; Hsu, S. H.; Kang, L. Y.; Shen, C. M.; Lin, W. W., Methylglyoxal induces cell death through endoplasmic reticulum stress-associated ROS production and mitochondrial dysfunction. *Journal of cellular and molecular medicine* **2016**, *20* (9), 1749-1760.
354. Zhao, S.; Wesseling, S.; Rietjens, I. M.; Strikwold, M., Inter-individual variation in chlorpyrifos toxicokinetics characterized by physiologically based kinetic (PBK) and Monte Carlo simulation comparing human liver microsome and Supersome™ cytochromes P450 (CYP)-specific kinetic data as model input. *Archives of Toxicology* **2022**, *96* (5), 1387-1409.
355. Thornalley, P. J., Glutathione-dependent detoxification of α -oxoaldehydes by the glyoxalase system: involvement in disease mechanisms and antiproliferative activity of glyoxalase I inhibitors. *Chemico-biological interactions* **1998**, *111*, 137-151.
356. Skapare, E.; Konrade, I.; Liepinsh, E.; Makrecka, M.; Zvejniece, L.; Svalbe, B.; Vilskersts, R.; Dambrova, M., Glyoxalase 1 and glyoxalase 2 activities in blood and neuronal tissue samples from experimental animal models of obesity and type 2 diabetes mellitus. *The journal of physiological sciences* **2012**, *62* (6), 469-478.

357. Sakhi, A. K.; Berg, J. P.; Berg, T. J., Glyoxalase 1 enzyme activity in erythrocytes and Ala111Glu polymorphism in type 1-diabetes patients. *Scandinavian Journal of Clinical and Laboratory Investigation* **2013**, *73* (2), 175-181.
358. Grillo, M. A.; Colombatto, S., Advanced glycation end-products (AGEs): involvement in aging and in neurodegenerative diseases. *Amino Acids* **2008**, *35* (1), 29-36.
359. Semba, R. D.; Gebauer, S. K.; Baer, D. J.; Sun, K.; Turner, R.; Silber, H. A.; Talegawkar, S.; Ferrucci, L.; Novotny, J. A., Dietary intake of advanced glycation end products did not affect endothelial function and inflammation in healthy adults in a randomized controlled trial. *The Journal of nutrition* **2014**, *144* (7), 1037-1042.
360. Ames, J. M., Evidence against dietary advanced glycation endproducts being a risk to human health. *Molecular nutrition & food research* **2007**, *51* (9), 1085-1090.
361. Grunwald, S.; Krause, R.; Bruch, M.; Henle, T.; Brandsch, M., Transepithelial flux of early and advanced glycation compounds across Caco-2 cell monolayers and their interaction with intestinal amino acid and peptide transport systems. *British journal of nutrition* **2006**, *95* (6), 1221-1228.
362. Li, M.; Zeng, M.; He, Z.; Zheng, Z.; Qin, F.; Tao, G.; Zhang, S.; Chen, J., Effects of long-term exposure to free N ϵ -(carboxymethyl) lysine on rats fed a high-fat diet. *Journal of agricultural and food chemistry* **2015**, *63* (51), 10995-11001.
363. Li, M.; Zeng, M.; He, Z.; Zheng, Z.; Qin, F.; Tao, G.; Zhang, S.; Chen, J., Increased accumulation of protein-bound N ϵ -(carboxymethyl) lysine in tissues of healthy rats after chronic oral N ϵ -(carboxymethyl) lysine. *Journal of agricultural and food chemistry* **2015**, *63* (5), 1658-1663.
364. Hellwig, M.; Matthes, R.; Peto, A.; Löbner, J.; Henle, T., N- ϵ -fructosyllysine and N- ϵ -carboxymethyllysine, but not lysinoalanine, are available for absorption after simulated gastrointestinal digestion. *Amino acids* **2014**, *46*, 289-299.
365. Tessier, F. J.; Niquet-Léridon, C.; Jacolot, P.; Jouquand, C.; Genin, M.; Schmidt, A. M.; Grossin, N.; Boulanger, E., Quantitative assessment of organ distribution of dietary protein-bound ¹³C-labeled N- ϵ -carboxymethyllysine after a chronic oral exposure in mice. *Molecular nutrition & food research* **2016**, *60* (11), 2446-2456.
366. Xie, J.; Reverdatto, S.; Frolov, A.; Hoffmann, R.; Burz, D. S.; Shekhtman, A., Structural basis for pattern recognition by the receptor for advanced glycation end products (RAGE). *Journal of Biological Chemistry* **2008**, *283* (40), 27255-27269.
367. Liu, X.; Zheng, L.; Zhang, R.; Liu, G.; Xiao, S.; Qiao, X.; Wu, Y.; Gong, Z., Toxicological evaluation of advanced glycation end product N ϵ -(carboxymethyl) lysine: Acute and subacute oral toxicity studies. *Regulatory Toxicology and Pharmacology* **2016**, *77*, 65-74.
368. Hellwig, M.; Geissler, S.; Peto, A.; Knütter, I.; Brandsch, M.; Henle, T., Transport of free and peptide-bound pyrroline at intestinal and renal epithelial cells. *Journal of agricultural and food chemistry* **2009**, *57* (14), 6474-6480.

S

Summary

An abstract graphic consisting of several overlapping, wavy, horizontal bands of different shades of blue. The bands originate from the left side of the image and flow towards the right, creating a sense of movement and depth. The colors range from a deep navy blue at the bottom to a lighter sky blue at the top.

Summary

α -Dicarbonyl compounds, particularly methylglyoxal (MGO), glyoxal (GO), and 3-deoxyglucosone (3-DG), are highly reactive precursor for the formation of advanced glycation end products (AGEs). AGEs and their precursors have been associated with many diseases, including diabetes, cardiovascular disease, and neurodegenerative disorders. Human exposure to dicarbonyl compounds arises from both dietary intake and endogenous formation within the body.

The primary focus of this thesis was on the role of dicarbonyl compounds in neurotoxicity and neurodegenerative diseases. An abnormal increase in the *in vivo* levels of dicarbonyls can induce a dysfunctional state known as dicarbonyl stress, leading to the increased modification of free amino acids, proteins, and DNA, thereby forming AGEs. These modifications can result in structural and functional changes to these biomolecules, contributing to neurotoxicity and potentially playing a role in neurodegeneration. The contribution of dietary intake of dicarbonyl compounds and the resultant AGEs to the adverse effects associated with dicarbonyl stress remains debated. Moreover, the mechanisms by which dicarbonyls promote neurotoxicity are largely unknown. This thesis aimed to advance the understanding of neurotoxicity and mitigation strategies for α -dicarbonyl precursors of AGEs using new approach methodologies.

Chapter 1 began by outlining the background and aim of the thesis. It presented a detailed introduction to α -dicarbonyl compounds and AGEs, specifically focusing on their formation. The chapter then continued with an introduction to the scavenging of exogenous dietary dicarbonyl compounds especially by flavonoids, as well as endogenous pathways for the metabolism of α -dicarbonyl compounds. Furthermore, it presented the current understanding of dicarbonyl stress and its potential implications in neurodegenerative diseases. Lastly, the chapter introduced the new approach methodologies (NAMs) employed in the research, including cell-based proteomics, metabolomics, and physiologically-based kinetic (PBK) modeling.

In **Chapter 2**, the reactivity of three representative dicarbonyl precursors—MGO, GO, and 3-DG—was compared in *in vitro* assays. This analysis included the comparison of the scavenging capacity of these dicarbonyls by glutathione (GSH) in cell-free incubation experiments.

Additionally, the ability of these compounds to induce Nrf2-mediated gene expression and the role of intracellular GSH in counteracting this effect were investigated using a U2OS cell-based reporter gene assay. The study demonstrated that endogenous GSH levels are critical in protecting against dicarbonyl stress. Furthermore, the results showed that MGO exhibited the highest reactivity in terms of GSH-mediated scavenging, reactive oxygen species (ROS) production, induction of Nrf2-mediated gene expression, and the effects of GSH depletion on Nrf2 activation potential. Based on these, MGO was chosen as the model compound for further research presented in this thesis.

In **Chapter 3**, the mitigation of dicarbonyls both endogenously and within food products was explored. The MGO scavenging capacity of a representative thiol compound (GSH) and a representative flavonoid (kaempferol) were characterized in more detail, with special emphasis on the possible reversible nature of adduct formation and their competition for MGO, in in-vitro cell-free incubations. Additionally, the safety consequences of their MGO-scavenging effects were evaluated in human SH-SY5Y neuroblastoma cells. The results showed that GSH exhibited immediate and concentration-dependent MGO-scavenging effects, while kaempferol's scavenging effects were both concentration- and time-dependent, with stable adducts forming over time. The GSH adduct gradually disappeared in a competition reaction with kaempferol, and kaempferol became the preferred scavenger over time. Moreover, kaempferol provided better protection than GSH against extracellular MGO of SH-SY5Y cells. Overall, it is concluded that flavonoids like kaempferol provide better scavengers for food-borne MGO than thiol-based scavengers such as GSH, while, given the endogenous concentrations of both scavengers and the detoxification of the GSH-MGO adduct by the glyoxalase system, GSH will be dominant for intracellular MGO protection.

In **Chapter 4**, the protein modifications induced by MGO in SH-SY5Y cells incubated with and without exogenous MGO were characterized using a proteomics approach. It was found that the majority of proteins identified as modified were already modified under basal control conditions. A total of 77 proteins were categorized as highly susceptible to MGO modification. Among these, eight proteins, including vimentin and histone H2B type 2-F, showed concentration-dependent modifications by externally added MGO, and were defined as biomarkers for exogenous MGO exposure. Remarkably, up to 10 modification sites were identified on vimentin. Myosin light polypeptide 6 emerged as a biomarker for MGO toxicity, with modifications exclusively observed under cytotoxic MGO levels. Additionally, proteins like serine/threonine-protein kinase SIK2 and calcyphosin, which exhibited comparable or

even higher modification levels in control compared to exogenous MGO-treated cells, were defined as biomarkers for endogenous exposure. Moreover, KEGG pathway and protein-protein network analyses revealed that motor proteins, cytoskeleton components, and glycolysis proteins were overrepresented among those highly susceptible to MGO modification. These results identify biomarkers for both endogenous and exogenous MGO exposure and provide insights into the cellular effects of endogenously formed versus externally added MGO.

In **Chapter 5**, the molecular and biochemical changes in SH-SY5Y cells upon exposure to MGO were explored using an integrated proteomics and metabolomics approach to assess how these changes contribute to neurotoxicity. The results revealed that MGO exposure, particularly at cytotoxic levels, significantly altered the proteome and metabolome of SH-SY5Y cells. Analysis of proteomics data showed significant alterations in cellular functions such as protein synthesis, cellular structural integrity, mitochondrial function, and oxidative stress responses. Analysis of metabolomics and integration of metabolomics and proteomics data highlighted significant changes in key metabolic pathways, including arginine biosynthesis, glutathione metabolism, cysteine and methionine metabolism, and the tricarboxylic acid cycle. MGO exposure led to increased endoplasmic reticulum stress, disruptions in cellular adhesion and extracellular matrix integrity, mitochondrial dysfunction, and amino acid metabolism disruption, all contributing to cellular toxicity. Conversely, cells exhibited adaptive responses by upregulating protein synthesis, activating the Nrf2 pathway, and reprogramming metabolism to counteract dicarbonyl stress and maintain energy levels. These findings enhance our understanding of MGO-induced neurotoxicity and identify potential therapeutic targets for mitigating its harmful effects.

In **Chapter 6**, human neurotoxicity and genotoxicity risks from dietary and endogenous MGO were assessed using PBK modeling-facilitated reverse dosimetry. A human PBK model was defined based on a newly developed mouse model, enabling the translation of *in vitro* toxicity data for MGO from human stem cell-derived neurons and WM-266-4 melanoma cells into quantitative human *in vivo* toxicity data and subsequent risk assessment using the margin of exposure (MOE) approach. The results show that the MOEs resulting from daily dietary intake did not raise concerns for endpoints such as neurotoxicity, including mitochondrial function, cytotoxicity, and apoptosis, while those for DNA adduct formation could not exclude a concern over genotoxicity. Endogenous MGO formation, especially under diabetic conditions, resulted in MOEs that raised concerns not only for genotoxicity but also for some of the neurotoxicity

endpoints evaluated. Thus, the results point at the importance of taking the endogenous levels into account in risk assessment of MGO.

In **Chapter 7**, the main findings from previous chapters were synthesized into an integrated discussion, along with recommendations and potential directions for future research. This thesis particularly highlighted the significant potential of flavonoids in mitigating the effects of MGO in food systems and biological contexts. The chapter stressed the importance of using omics approaches to understand the role of MGO-induced damage to cellular biomolecules in cellular adaptation or dysfunction. It emphasized the necessity of considering both dietary and endogenous sources of dicarbonyls in health risk assessments. Lastly, the need for further investigation into the toxicokinetics and toxicodynamics of dicarbonyls, as well as AGEs, was identified as essential for a comprehensive future risk assessment.

A

Acknowledgments

A decorative graphic at the bottom of the page consisting of several overlapping, wavy, horizontal bands of different shades of blue, ranging from a very light sky blue to a deep navy blue. The waves flow from the left side towards the right, creating a sense of movement and depth.

Acknowledgments

I can hardly believe that I have finally made it. Four years ago, after finishing my master's studies in China and starting to work, I knew deep down that I was not ready to settle. Driven by a desire to pursue a PhD and explore more of the world, I decided to commit to this challenging path. Reflecting on my decision and the effort I put into it, I can wholeheartedly say it was all worthwhile. This journey has been filled with joy, happiness, and achievements, yet interspersed with inevitable moments of struggle, stress, and sadness. Every experience has been integral to my growth and has become a precious memory of my journey. The constant support and encouragement from those around me, and the deep friendships I have forged, have been crucial to this journey. I wish to express my deepest gratitude to my mentors, colleagues, friends, and family who witnessed and facilitated my growth. I could not have completed my PhD or achieved such personal growth without you.

My deepest thanks go to my supervisor, **Prof. Ivonne Rietjens**, for your invaluable guidance, support, and encouragement throughout my PhD. Whenever I encountered challenges in my project, your quick, sharp, and expert insights were always there to provide direction and alleviate my worries. I am forever grateful for the opportunity to pursue my PhD under your mentorship, for the trust you placed in me, and for all the support and resources you provided that have helped me grow into the scientist I am today.

I would also like to express my sincere gratitude to my co-promotor, **Dr. Edoardo Saccenti**, who graciously took on the role of second supervisor. It was kind of you to step in and assist during a crucial time. You were always available to answer questions, from which I have learned a lot. Thank you for your expertise and input especially in bioinformatics and data analysis. Your support has greatly improved the quality of our studies.

Additionally, I must extend my gratitude to **Prof. Jacques Vervoort**, who provided invaluable guidance during the first year of my studies. I am very sad that you cannot be present at my defense. I clearly remember July 20th, 2021—the day we had scheduled a morning meeting—but instead, I opened my laptop to the sad news of your passing. I enjoyed working with you. Your encouraging words, kind demeanor, and engaging conversations have left a lasting impression on me. I cherish these memories and hope you are at peace.

Furthermore, I would like to thank all the co-authors who contributed to this thesis, particularly the following individuals: **Ignacio**, thank you for introducing me to the lab on the first day, being my daily supervisor at the beginning of my study, and teaching me many of the skills needed for experiments. **Sjef**, thank you for teaching me the proteomics experiments

and assisting with the LC/MS measurements and data analysis. I learned a lot from you. Your kindness has been truly appreciated. **Wouter**, I am grateful for your help with LC/MS measurements, especially in metabolomics. I enjoyed your humor and our engaging conversations. It was really fun to work with you. **Katja**, I appreciate your collaboration on the second chapter of this thesis. Your generous assistance as a senior peer was instrumental in helping me finish and publish this chapter, bringing me peace of mind during my later studies. **Chen Liu**, thank you for your assistance with the proteomics experiments, and the valuable discussions about our careers. I am looking forward to our future collaborations! Lastly, I want to thank **Frances** for your valuable input in two of my chapters. I truly enjoyed our collaboration and, at the same time, the friendship and fun we shared throughout our PhD. You have been one of my smartest and most humble friends, always an inspiration to me in my studies and my life.

To the current and former staff at TOX: **Hans, Nynke, Nico, Sebas, Laura, Alexandros, Mathias, David, Naomi, Carla, and Gerda**—thank you so much for all your help and support with any questions, along with the enjoyable conversations, jokes, and your genuine personalities. Special thanks to **Hans** for your trust and for offering me a postdoc position at TOX. Thanks to **Nynke** for providing me with a mock interview, which was helpful. My thanks also go to **Carla** and **Gerda** for your administrative support over the past years.

To all the current and former PhDs and Postdocs—**Aafka, Akanksha, Annelies, Chrysanthi, Biyao, Danlei, Donovan, Edith, Frances, Germaine, Ghaliya, Gijs, Haomiao, Hugo, Jiaqi, Jingxuan, Katharina, Kiri, Matteo, Menno, Merel, Mirena, Nina, Nick, Qihui, Rebeka, Rizal, Shivani, Shuo, Sylvia, Tanne, Thijs, Tom, Veronique, Wisse, Xiyu, Xuan, Xukun, Xupeng, Yasser, and Yiming**—thank you for the great years at the department and your companionship. To **Jingxuan** and **Danlei**, thank you both for being my buddies and for all your help, especially when I first arrived here. To **Edith**, I will miss our chats; talking with you was always encouraging. To **Yasser**, thank you for always being there to offer help and support. Your kind and reassuring words were always a source of comfort, and I'm grateful for all the times you helped me, like driving me to the airport and helping me move. **Rebeka**, thank you to you and **Ivan** for helping with the move and for the coolest Halloween party. It was hilarious when you three fell on the grass afterward. To **Nina**, thank you for all the times we shared and encouraged each other through both PhD life and personal experiences. I miss the hotpot with pickled cabbage we had at your place. To the lemon-choco-brownie group (**Hugo, Wisse, Shivani, and Frances**), thank you for the amazing times we shared. It was so much fun to hang out, travel, enjoy dinners, go on beach trips, work out, and play board games together. To the AGE group (**Xiyu and Xukun**), it has been a pleasure meeting, discussing, and learning together with you on similar topics.

To my office mate, **Ghalia**, thank you for always feeding us lots of snacks in the office and for your constant willingness to help. I especially appreciate your kindness and the great help you provided when I had COVID. To **Kiri**, thank you for the nice jokes and for being my Dutch translator in the office. You have a way of cheering people up and reminding them to keep a work-life balance (like telling them to go home). To **Jiaqi**, your enthusiasm, passion, and persistence for science and research are impressive, and it's inspiring to see how you approach life with positivity. Even though we often engage in 'mutual flattery' in the office, I truly believe you will become an outstanding scientist. To **Nick**, welcome to office 4032; finally, I'm not the only guy in the office. I wish you all the best with all the girls!

A big thanks to my paranympths, **Shivani** and **Haomiao**. **Shivani**, I can't believe you became my best friend despite all the times we've been mean to each other and making fun of one another. We know a lot of crazy things about each other. Our 'India vs. China' battles seemed never-ending, but through them, I've learned so many truths and good things about India. Let me be corny just this once for you—thank you for your care and companionship at all times, and most importantly, you helped me through a difficult time and started thinking about being my authentic self. I will miss the gossiping, the parties, the drinks, and all the times we had together, and I will miss this Indian princess. Also, a special thanks to **Vedran** for helping me with the move. I always enjoyed the nice chats with both of you during the many times you invited me over! **Haomiao**, as your former mentor and now colleague, your joining has made my work easier. I never truly understood what it meant to be a supervisor until I met you. Supervising has been a learning process for me as well, and for that, I am grateful. I know I have sometimes pushed you hard, but I believe that when you become a supervisor, you will understand. I hope you stay confident, maybe sleep a little less, and finish your PhD successfully. I am proud and will be proud to see your progress and achievements.

I would like to thank all the friends I met at Wageningen and during my PhD studies. Because of you all, my PhD journey was far from lonely. To **Lucas**, thank you for the moments we shared, from watching Sweet Home and True Beauty to going to Woo sung's concerts, and especially that magical snowy day in Rotterdam. You were a great support during the challenging COVID times, helping me adjust to life in the Netherlands, and we also ventured to so many places together. I truly wish you a fulfilling life where you find your true passions. Please visit China one day; it will be my turn to guide you through new adventures. To **Jingwei**, thank you for being my best friend and gym buddy at Wageningen. Our weekly dinners were always enjoyable. I still remember how you helped me and took me to the airport when I couldn't return home due to COVID. I was truly touched by your kindness. Our trip to Italy was so much fun—hard to believe it's already been two years. To **Xianhui**, my earliest friend in Wageningen, I deeply appreciate how you invited and hosted gatherings, and organized trips for us. Those

moments are truly unforgettable. Sharing our worries and helping each other through difficult times also meant a lot. To **Kaisheng**, it was quite by chance that we met, but I admire your sincerity, diligence, and reliability. Thank you for being my friend. To **Meijun**, through you, I have met many people, some of whom have now become my friends, like Jingwei. You are very sincere, and I thank you for the time we spent in the gym and for sharing each other's troubles and joys. To my mahjong buddies, **Ke Peng**, **Jia Liu**, **Zhengkai**, and **Jielin**, it was always a blast playing mahjong and enjoying food with you all. You made life here far from boring. I would also like to thank **Zhuang Yang**, **Lingfeng**, **Ze Zhu**, **Yili**, **Fengchuan**, **Shiyi**, **Dailing**, and the people from PCC (**Xuefeng**, **Qimeng**, **Qin**, and **Chang**). It was wonderful getting to know you all, and I am grateful for the time we spent together.

I want to express my gratitude to my former supervisors, **Prof. Xiaobo Li** and **Prof. Mengyue Wang**, during my master's studies. Thank you both for your guidance and support. I particularly remember the words Prof. Xiaobo Li shared with me after I finished my master's study: "Accomplish what you want to accomplish; don't wait until you're 80 and lying in bed to have regrets." These words motivated me to decide to pursue my PhD in the Netherlands. I would also like to extend my gratitude to my former managers, **Wenjie** (郭文杰) and **Yan Li** (李岩), and my mentor **Yu Zhong** (钟妤) at Agilent. Thank you for allowing me to work at Agilent and for being such great mentors. I learned a lot from you, which has greatly contributed to my personal and professional growth in the workforce.

I would also like to thank my friends in China. To **Yulong** (张玉龙), no matter how long we go without talking, I know that whenever we do, it will always feel natural, and we'll have endless things to chat about. To **Xin Zhang** (张鑫), my dear junior, thank you for always listening to my trivial matters and for praying for my successful journey abroad when you visited Mount Emei (that was cute). I haven't been able to help you much in return, but I hope we can meet up soon. Was our last meeting really in 2020 when we went to Mount Qingcheng together? To **Bowen** (杨博文), thank you, senior, for your constant encouragement, advice, and support in both my studies and life. You always make me feel secure. To **Zhiqiang** (高智强), **Shu'an** (夏枢安), and all my wonderful colleagues at Agilent, working with you was a lot of fun. Thank you for keeping me in the loop with all the gossip even after I left. To **Guanghao** (周广昊), you are my only friend of the same age in Mingshan. You are humble, generous, cheerful, and warm-hearted. I must admit, I'm a bit jealous that you already have both a career and a family. Thank you for sharing your life with me and trusting me as a friend. To **Christina**, I miss the time we spent together in Chengdu. Thank you for being such a great friend there, and I wish you a happy life with your boyfriend. To **Yinyi** (姚尹伊), my old classmate, thank you for turning my ideas—and, of course, also yours—into this amazing cover. To **Jin Zhou** (周进), I

had such a great time on our road trip in Ya'an and hiking in Bifeng Gorge and Jinfeng Mountain with you. I look forward to exploring more food and life with you, so please wait for me there.

A special thanks to Miss **Rainie Yang**. Your songs and words have always been my spiritual support, helping me through many difficult times. Although I couldn't attend your concert while studying in the Netherlands, I will always support and love you. I always remember your words, "Live your own life well before you come to love me." I think I've done what you said.

Lastly, I want to thank my **parents**. You've supported me unconditionally through every step of my studies and life, always giving me the best. I've taken so much from you throughout this journey, and I know I haven't been able to give back as much (感谢我的爸妈无条件的支持与爱, 我爱你们). I would also like to thank my cousin, **Yumei** (玉梅). It's been nice having you here in the Netherlands, and I wish you all the best in whatever you pursue! To my cousins, **Mimi** (密密), **Haohao** (浩浩), and **Yu Zhou** (周宇), thank you for your companionship during my childhood and for your care and support. I love you all.

As I approach the end of this significant chapter in my life and embark on a new journey, I am reminded that each moment we share is precious. Life, indeed, is a series of meetings and farewells. We continue on our individual paths, not knowing when or where we'll meet again. Though it's upsetting, I look forward to the day our paths cross once more, bringing even more beautiful stories and experiences to share.

A

About the author



Curriculum Vitae

Liang Zheng was born on May 25th, 1994, in Ya'an, Sichuan province, China. In 2012, he completed his high school education at Mianyang Nanshan High School and then studied pharmaceutical sciences of Chinese medicine at Chengdu University of Traditional Chinese Medicine (CDUTCM), a major under China's Double First-Class Initiative for world-class disciplines. He obtained his bachelor's degree in 2016 and was exempted from the national entrance examination for master's programs, allowing him to continue his studies at Shanghai Jiao Tong University (SJTU). At SJTU, he studied pharmaceutical sciences under the supervision of Prof. Xiaobo Li. His master's thesis focused on the



component analysis and metabolic study of the complex system of Chinese medicine. He obtained his master's degree in 2019 and was awarded Excellent Graduate in Shanghai by the Shanghai Municipal Education Committee. After his studies, he worked as a technical service engineer at Agilent Technologies based in Chengdu, where he received comprehensive chromatography technique training. His work involved providing technical service for customers using LC/MS and GC systems. After a year and a half at Agilent, he decided to further his academic career by pursuing a PhD at the Division of Toxicology at Wageningen University and Research (WUR) with financial support from the China Scholarship Council, supervised by Prof. Ivonne Rietjens and Dr. Edoardo Saccenti. His PhD project focused on the neurotoxicity of glycation products using new approach methodologies (NAMs), including cell-based proteomics, metabolomics, and physiologically based kinetic modeling. During his PhD, he followed postgraduate education in toxicology as part of the training required for the registration as a European Toxicologist. Currently, he works as a postdoctoral fellow at the Division of Toxicology at WUR, focusing on the risk assessment of the effects of microplastics on human health under the supervision of Prof. Hans Bouwmeester.

A

List of Publications

This thesis

Zheng, L., van Dongen, K. C., Bakker, W., Miro Estruch, I., & Rietjens, I. M. C. M. (2022). The influence of intracellular glutathione levels on the induction of Nrf2-mediated gene expression by α -dicarbonyl precursors of advanced glycation end products. *Nutrients*, 14(7), 1364.

Zheng, L., Bakker, W., Estruch, I. M., Widjaja, F., & Rietjens, I. M. C. M. (2023). Comparison of the methylglyoxal scavenging effects of kaempferol and glutathione and the consequences for the toxicity of methylglyoxal in SH-SY5Y cells. *Food Chemistry: X*, 20, 100920.

Zheng, L., Boeren, S., Liu, C., Bakker, W., Wang, H., Rietjens, I. M. C. M., & Saccenti, E. (2024). Proteomics-based identification of biomarkers reflecting endogenous and exogenous exposure to the advanced glycation end product precursor methylglyoxal in SH-SY5Y human neuroblastoma cells. *International Journal of Biological Macromolecules*, 132859.

Zheng, L., Li X., Widjaja, F., Liu, C., & Rietjens, I. M. C. M. (2024). Use of physiologically based kinetic modeling to predict neurotoxicity and genotoxicity of methylglyoxal in humans. *npj Science of Food*, 8(1), 79.

Wang H., Boeren, S., Bakker, W., Rietjens, I. M. C. M., Saccenti, E.*, & **Zheng, L.*** (2024). An integrated proteomics and metabolomics analysis of methylglyoxal-induced neurotoxicity in a human neuroblastoma cell line. *npj Science of Food* (Accepted). (*Corresponding authors)

Others

Liu, C.*, Wang D., Rietjens, I. M. C. M. & **Zheng, L.*** Current and emerging issues in chemical food safety. *Submitted*. (*Corresponding authors)

Martati, E., **Zheng, L.***, & Rietjens, I. M. C. M. In vitro and in vivo models for studying the inhibition of the formation of advanced glycation end products (AGEs) by natural compounds. *In preparation*. (*Corresponding author)

Liu, C., Gan, R. Y., Chen, D., **Zheng, L.**, Ng, S. B., & Rietjens, I. M. C. M. (2024). Gut microbiota-mediated metabolism of green tea catechins and the biological consequences: An updated review. *Critical Reviews in Food Science and Nutrition*, 64(20), 7067-7084.

Widjaja, F., **Zheng, L.**, Wesseling, S., & Rietjens, I. M. C. M. (2023). Physiologically based kinetic modeling of senecionine N-oxide in rats as a new approach methodology to define the effects of dose and endpoint used on relative potency values of pyrrolizidine alkaloid N-oxides. *Frontiers in Pharmacology*, 14, 1125146.

Zheng, L., Wang, M., Chen, Z., Hou, J., & Li, X. (2019). Simultaneous quantitation of 13 active components in SimiaoYong'an decoction using high-performance liquid chromatography with diode array detection. *Acta Chromatographica*, 31(3), 216-221.

Zheng, L., Wang, M., Peng, Y., & Li, X. (2017). Physicochemical characterization of polysaccharides with macrophage immunomodulatory activities isolated from red ginseng (*Panax ginseng* CA Meyer). *Journal of Chemistry*, 2017(1), 3276430.

Overview of completed training activities

Discipline specific activities

Courses

Summer Course Glycosciences	VLAG, Wageningen	2021
Advanced Food Analysis	VLAG, Wageningen	2021
Risk Assessment	PET, Wageningen	2021
Neurotoxicology	PET, Utrecht	2022
Cell Toxicology	PET, Leiden	2022
Molecular Toxicology	PET, Amsterdam	2022
Organ Toxicology	PET, Nijmegen	2023
Laboratory Animal Science	PET, Utrecht	2023
NutriNOR Summer School at University of Bergen (UiB)	UiB, Bergen, Norway	2023
Pathobiology & Toxicological Pathology	PET, Utrecht	2023
Immunotoxicology	PET, Utrecht	2023
Epidemiology	PET, Amsterdam	2024

Meetings

63rd Society of Toxicology (SOT) Annual Meeting (poster presentation)	SOT, Salt Lake City, USA	2024
45th Dutch Society of Toxicology Annual Meeting (poster presentation)	NVT, Ede	2024

General courses

VLAG PhD Week	VLAG, Biezenmortel	2021
Introduction to R	VLAG, Wageningen	2021
Chemometrics (Multivariate Statistics)	VLAG, Wageningen	2021
Applied Statistics	VLAG, Wageningen	2021
Adobe Illustrator – Scientific Artwork & Infographics	WGS, Online	2024
Presenting with Impact	WGS, Wageningen	2024

Other activities

Scientific Presentations	TOX-WUR, Wageningen	2020-2024
Preparation of Research Proposal	TOX-WUR, Wageningen	2021
General Toxicology	WUR, Wageningen	2021
Food Toxicology	WUR, Wageningen	2021
Environmental Toxicology	WUR, Wageningen	2022
Organization of PhD Study Tour to United Kingdom	TOX-WUR, Wageningen	2023
Participation of PhD Study Tour to United Kingdom	TOX-WUR, London, UK	2023

Approved by Graduate School VLAG.

The research described in this thesis was financially supported by the China Scholarship Council (No. 202008510115).

Financial support from Wageningen University for printing this thesis is gratefully acknowledged.

Cover design by Yinyi Yao and Liang Zheng

Printed by Proefschriftmaken | proefschriftmaken.nl

